



Design and validation of an fNIRS system to assess functional activity of the prefrontal cortex

Doctoral Thesis presented by
Sergio Molina Rodríguez

Thesis Director: Luis Miguel Martínez Otero
Thesis Co-Director: Joaquin Ibanez Ballesteros

PhD Program in Neuroscience
Neurosciences Institute
University Miguel Hernández of Elche

- 2023 -



This Doctoral Thesis, entitled "Design and validation of an fNIRS system to assess functional activity of the prefrontal cortex" is presented as a compendium of the following publications:

- Molina-Rodríguez, S., Mirete-Fructuoso, M., Martínez, L. M., & Ibáñez-Ballesteros, J. (2022). Frequency-domain analysis of fNIRS fluctuations induced by rhythmic mental arithmetic. *Psychophysiology*, e14063. <https://doi.org/10.1111/psyp.14063>



Sant Joan d'Alacant, 2023

DIRECTOR'S AND CO-DIRECTOR REPORT

Dr. D. *Luis Miguel Martínez Otero*, Director, and Dr. D. *Joaquín Ibáñez Ballesteros*, co-director of the doctoral thesis entitled "Design and validation of an fNIRS system to assess functional activity of the prefrontal cortex".

INFORMS:

That Mr. Sergio Molina Rodríguez has carried out under our supervision the work entitled "Design and validation of an fNIRS system to assess functional activity of the prefrontal cortex" in accordance with the terms and conditions defined in his Research Plan and in accordance with the Code of Good Practice of the University Miguel Hernández of Elche, satisfactorily fulfilling the objectives foreseen for its public defense as a doctoral thesis.

We sign for appropriate purposes, at Sant Joan d'Alacant , 21 of April of 2023.

Thesis director

Dr. D. *Luis Miguel Martínez Otero*

Thesis co-director

Dr D. *Joaquín Ibáñez Ballesteros*

REPORT OF THE DOCTORAL PROGRAMME COORDINATOR

Sant Joan d'Alacant, 2023

Ms. Elvira de la Peña García, Coordinator of the Neurosciences PhD programme at the Institute of Neurosciences in Alicante, a joint centre of the Miguel Hernández University (UMH) and the Spanish National Research Council (CSIC),

INFORMS:

That Mr. Sergio Molina Rodríguez has carried out under the supervision of our PhD Programme the work entitled "Design and validation of an fNIRS system to assess functional activity of the prefrontal cortex" in accordance with the terms and conditions defined in its Research Plan and in accordance with the Code of Good Practice of the University Miguel Hernández de Elche, fulfilling the objectives satisfactorily for its public defense as a doctoral thesis.

Which I sign for the appropriate purposes, in Sant Joan d'Alacant, 2023

Dr Elvira de la Peña García
Coordinator of the PhD Program in Neurosciences

This work has been financially supported by: ayudas para la Formación del Profesorado Universitario (FPU) with reference FPU15/03877 awarded by the Ministerio de Universidades.

A mis padres, mis yayos y a Álvaro.

*Debajo de las multiplicaciones
hay una gota de sangre de pato.*

*Debajo de las divisiones
hay una gota de sangre de marinero.*

Debajo de las sumas, un río de sangre tierna.

Nueva York (Oficina y denuncia). Un poeta en Nueva York

Federico García Lorca

Y cuando la tormenta de arena haya pasado, tú no comprenderás cómo has logrado cruzarla con vida. ¡No! Ni siquiera estarás seguro de que la tormenta haya cesado de verdad. Pero una cosa sí quedará clara. Y es que la persona que surja de la tormenta no será la misma persona que penetró en ella. Y ahí estriba el significado de la tormenta de arena.

Kafka en la orilla

Haruki Murakami

Acknowledgements

A Luis Miguel Martínez Otero por darme la oportunidad de iniciar un doctorado.

A Joaquín Ibáñez Ballesteros por hacer que esta tesis sea posible. Gracias por todas las cosas que me has enseñado, por tu paciencia, tus explicaciones y comprensión en todo momento. Me has instruido en el oficio de hacer ciencia de calidad y en el de enseñar. Ojalá seguir aprendiendo de ti por muchos años.

A mis padres y mi hermana Celia por vuestro apoyo incondicional durante estos años (aún sin saber bien que era esto de una “tesis doctoral” habéis estado siempre al pie del cañón). Papá y mamá gracias por todo (sería imposible transmitir aquí la amplitud y significado de este “todo”). Habéis sido y sois un ejemplo de superación. Celia, quiero agradecerte tu paciencia, tus risas y tu forma de darme ánimo mostrándome la parte positiva de las cosas (a la que muchas veces soy ciego).

Al yayo y la yaya por ser mi refugio preferido.

A mi familia en conjunto. No podría tener una familia mejor y mucho menos tan divertida. Tía Inés gracias por ser un modelo de cómo hacer bien las cosas y enseñarme la importancia del trabajo duro. Tía Loli gracias por nuestra complicidad. Eres un ejemplo de valentía y de lucha incansable por los sueños. Tío Andrés y tía Monse gracias por vuestro apoyo incondicional. A todos mis primos (Fernando, Olga, María, Paula y Sandra) gracias por las risas y los buenos momentos. Verena-madre, gracias por estar siempre ahí para escucharme y darme consejos. Verena-hija, gracias por tus ocurrencias que siempre me roban una sonrisa. Lorenzo eres hermano de esta tesis ya que habéis crecido juntos. Por último, a mi tía Octavia por ser un ejemplo de constancia, fortaleza y sacrificio.

A mi familia política (Juani, Paco, Oscar, Macarena, Francisco y Mari Carmen) gracias por acogerme y hacerme sentir como uno más desde el principio.

A mis amigos por ser una red de seguridad contra las caídas. Sois mis pensamientos cuando convoco un “*patronus*”. La amistad se expresa de muchas formas y por eso quiero daros las gracias uno por uno. Marcos gracias por los momentos únicos de locura, tu genialidad y creer siempre en mis capacidades. Sergey merece una especial mención por sus dotes adivinatorias, su paciencia con mis bromas y su risa contagiosa. Santi gracias por las horas y horas que hemos compartido (y por las que nos quedan). A Estefanía gracias por la locura que te caracteriza y por las conversaciones mientras nos tomábamos un Martini (en las salinas). A Elena por estar siempre ahí sacándome de mis casillas y a la vez siendo la mujer de verde. Recuerda: Tú dame una señal. Yo buscaré un disfraz. Joel gracias por hacerme partícipe de tu vida, por darme lecciones constantes, por tu amistad a lo largo de tantos años, y por ser pluscuamperfecto tal y como eres. Patricia gracias por tu sabiduría ancestral y por rebatirme vehementemente todo lo que digo. María, gracias por tu compañía a lo largo de tantos años. Genie, gracias por ser luz. Arturo gracias por tu amistad incondicional durante todo el doctorado, por ayudarme a mejorar mi pensamiento científico, por tu forma de ser y tus recetas. Titi, gracias por ser mi pilar maestro durante todo el doctorado. Cuando te conocí a través de Arturo supe que nuestra amistad era inevitable. Gracias por las risas, por nuestras aventuras, por acogerme en tu casa, por tus cuidados, por ser siempre comprensiva y saber escuchar. Abraham gracias por estar “ahí” durante todo el doctorado, por tu ayuda en la docencia (y en la vida en general), por apoyarme en los

proyectos más locos, por escuchar mis quejas y transformarlas en carcajadas. La siguiente tesis será la tuya. Las cervezas contigo deberían aparecer en el manual de tratamientos psicológicos eficaces (Nivel de evidencia 1++ y grado de recomendación A). Victoria, gracias por ser prima y amiga a la vez, por todos los momentos que hemos compartido, y por tu amistad extraordinaria. A Virginia y José Manuel, aunque habéis sido los últimos en llegar, siento que os conozco desde siempre. Sois mi familia en Málaga. Virginia gracias por tu bella locura, por hacerme reír hasta que me duele la barriga, y por todos los momentos que nos has hecho vivir. Nota: todos los recuerdan. A José Manuel agradecerle sus recomendaciones de libros, la forma en la que transmite paz y escucha todo lo que digo. Gracias por tu curiosidad inagotable. Tengo mucha suerte de teneros a cada uno de vosotros y vosotras.

A Newmanbrain y sus componentes por el apoyo durante todo el doctorado.

Miguel Ibáñez, mi agradecimiento porque siempre me ha ayudado con cualquier cosa que le he pedido. ¡Gracias por estar ahí!

A mi profesora, compañera y amiga Olga Pellicer, gracias por confiar en mí y por embarcarse conmigo en cualquier proyecto (por disparatado que sea).

Como dice Rainer Maria Rilke, las cosas no son todas tan palpables ni tan expresables como piensa la mayoría de la gente. De hecho, la mayor parte de los acontecimientos son indescriptibles y se desencadenan en un espacio en el que las palabras jamás han puesto un pie. Lo más indescriptible de todo son algunas personas, existencias misteriosas, cuyas vidas y caminos perduran a nuestro lado y se entrelazan milagrosamente junto a nuestra. A ti Álvaro, que eres una de esas existencias misteriosas, gracias por ser una referencia cuando me pierdo, por confiar en mí (cuando ni yo mismo lo he hecho), por animarme a continuar, por escucharme y comprender, por empeñarte en luchar con las distancias insalvables y hacer fácil lo difícil. En definitiva, gracias por todo aquello que solo puedes comprender tú (chumicho). Por último y no menos importante gracias a los “niños” por su apoyo técnico en la redacción de la tesis y por hacernos reír día a día.

Abbreviations	14
List of figures	7
List of tables	20
Resumen.....	11
Abstract	13
1 Introduction.....	15
1.1 <i>Historical perspective</i>	15
1.2 <i>Physical principles</i>	17
1.2.1 Light and tissue interactions.....	17
1.2.2 Chromophores.....	19
1.2.3 Beer-Lambert Law	22
1.2.4 Modified Beer-Lambert Law	23
1.3 <i>Physiological principles of fNIRS.....</i>	26
1.3.1 Regulation of Cerebral blood flow.....	26
1.3.2 Neurovascular unit	27
1.3.3 Functional Neuronal hemodynamic response.....	28
1.4 <i>fNIRS instrumentation.....</i>	31
1.4.1 Different types of fNIRS systems	31
1.4.2 Continuous wave fNIRS and other functional neuroimaging techniques.....	33
1.5 <i>Contamination problem</i>	36
1.5.1 Sources of contamination.....	36
1.5.2 Contamination geometry	39
1.5.3 How much is the NIRS signal contaminated?	50
1.5.4 Dealing with contamination	41
1.6 <i>Functional neuronal hemodynamic response elicitation and detection.....</i>	48
1.6.1 Stimulation paradigms.....	48
1.7 <i>Theia fNIRS device</i>	51
1.8 <i>Frontopolar cortex</i>	53
1.8.1 Characteristics	53
1.8.2 Connectivity:.....	54
1.8.3 Functional specialization	54
1.9 <i>Forehead</i>	57
1.9.1 Characteristics	57
1.9.2 Vascularization	59
1.9.3 Innervation	63
1.10 <i>General validation principles for new NIRS devices</i>	64
2 Material and methods	68

2.1	Participants	68
2.2	fNIRS recordings	68
2.3	Signal quality check - Channels and participants exclusion criteria	80
2.4	Initial testing	80
2.4.1	Light-emitting diode spectral calibration	80
2.4.2	Detection of well-known spontaneous oscillations.....	80
2.4.3	[HbO] and [HbR] cross-talk assessment	71
2.4.4	Limb vascular occlusion test	73
2.5	Experimental validation through a paradigm of mental arithmetic.	75
2.5.1	fNIRS Data Preprocessing	75
2.5.2	Mental task.....	77
2.5.3	Heart rate measurement	78
2.5.4	Heart rate exclusion criteria	78
2.5.5	Identification of task-induced frequencies	79
2.5.6	SS and DS relationships.....	90
2.5.7	Estimating deep component from transfer function.....	82
2.5.8	Simulations	84
2.5.9	Measuring HbO/HbR coupling.....	84
2.5.10	Measuring HbO/ Heart rate coupling.....	85
3	Results	86
3.1	Initial testing	86
3.1.1	Light-emitting diode spectral calibration	86
3.1.2	Detection of well-known spontaneous oscillations.....	87
3.1.3	[HbO] and [HbR] cross-talk assessment	88
3.1.4	Limb vascular occlusion test	89
3.2	Experimental validation through a paradigm of mental arithmetic	100
3.2.1	Assessment of physiological stress responses.....	100
3.2.2	Oscillations alignment to the task frequency	101
3.2.3	SS/DS relationships	93
3.2.4	Neural signal estimation by transfer function	95
3.2.5	Simulation results	96
3.2.6	HbO/HbR coupling.....	97
3.2.7	HbO / Heart rate coupling	99
4	Discussion	100
4.1	Initial testing	100
4.2	Experimental validation through a paradigm of mental arithmetic.	102
5	Conclusions.....	111
6	Conclusiones.....	112
7	References	113
8	Appendixes	151
8.1	Offprint of Frequency-domain analysis of fNIRS fluctuations induced by rhythmic mental arithmetic.....	151
8.2	Supplementary figures	152

8.3 *Informed consent*

form.....1594

Abbreviations

ΔHbO : Oxygenated haemoglobin changes

ΔHbR : Deoxygenated haemoglobin changes

[HbO]: Oxygenated haemoglobin concentration

[HbR]: Deoxygenated haemoglobin concentration

μM : Micromole

BOLD: Blood- Oxygen Level-Dependent

Bpm: Beat per minute

CBF: Cerebral blood flow

CI: Confidence interval

CPSD: Cross-power spectral density

CS: Clean signal

CSF: Cerebrospinal fluid

D: Light detector

DPF: Differential path length

DMN: default-mode network

EEG: Electroencephalography

EKG: Electrocardiogram

Eq: Equation

fMRI: Functional magnetic resonance imaging

fNIRS: Functional near-infrared spectroscopy

FPC: Frontopolar cortex

FT: Fourier transform

GLM: General linear model

Ghz: Gigahertz

HbO: Oxygenated haemoglobin

HbR: Deoxygenated haemoglobin

HR: Heart rate

Hz: Hertz

ICA: Independent component analysis

ISC: Inter-subject correlation

LC: Long channel
LED: light-emitting diode
LFO: Low-frequency oscillations
LS: Long signal
MEG: Magnetoencephalography
Mm: Millimeter
N: Sample size
NBR: negative BOLD response
NIR: Near-infrared
NIRS: Near-infrared spectroscopy
NVC: Neurovascular coupling
NVU: Neurovascular unit
Mhz: Megahertz
mW: Megawatt
OD: Optical density
O₂: oxygen
PC: Personal computer
PCA: Principal component analysis
PET: Positron emission tomography
PFC: Prefrontal cortex
PSD: Power spectral density
rCBF: Regional cerebral blood flow
rCBV: Regional cerebral blood volume
rCMRO₂: Regional cerebral metabolic rate of oxygen
RMSE: Root-mean-square error
ROI: Region of interest
S: Light source
SC: Short channel
SD: Standard deviation
SDD: Source detector distance
SEM: Standard error of the mean
SS: Short signal
t: Student's t-test

TF: Transfer function

VLFO: Very-low-frequency oscillations

- **Figure 1.** Electromagnetic spectrum.
- **Figure 2.** Main phenomena of attenuation of NIR light traveling through tissue.
- **Figure 3.** Water, melanin, HbO, HbR, fat, and Cytochrome-C oxidase absorption spectra at ultraviolet, visible and infrared light spectrum.
- **Figure 4.** Haemoglobin A structure and its oxygen binding process.
- **Figure 5.** Detail of HbO, HbR and water absorption spectra.
- **Figure 6.** Schematic representation of incident and transmitted light.
- **Figure 7.** Schematic representation of NIR light through a head.
- **Figure 8.** Structure of the cerebral cortex, the meninges, and the blood-brain barrier.
- **Figure 9.** Schematic representation of metabolic and hemodynamic changes during neural activation.
- **Figure 10.** Schematic representation of incident and transmitted light in different types of fNIRS systems.
- **Figure 11.** Graphical comparison between the neuroimaging techniques.
- **Figure 12.** Schematic representation of six contributors that are present in any fNIRS signal recorded through the scalp.
- **Figure 13.** Schematic representation of back-reflection geometry of NIR light through a head.
- **Figure 14.** Schematic representation of multi-distance measurements.
- **Figure 15.** Schematic representation of regression based on multi-distance measurements.
- **Figure 16.** Stimulation paradigms in functional neuroimaging and their theoretical hemodynamic responses.
- **Figure 17.** Structure of the Theia device and its placement on the forehead of a participant.
- **Figure 18.** Major subdivisions of the human prefrontal cortex.
- **Figure 19.** Sagittal section of the forehead.
- **Figure 20.** Frontal sinus.
- **Figure 21.** Ophthalmic artery and its main branches involved in the vascularization of the forehead.
- **Figure 22.** Arterial vascularization of the forehead.
- **Figure 23.** Superficial and deep venous drainage systems.

- **Figure 24.** Venous vascularization of the forehead.
- **Figure 25.** Schematic representation of muscle tissue and its blood vessels during venous and arterial occlusion and typical HbO/HbR time courses during the two types of vascular occlusion.
- **Figure 26.** Probe geometry and placement.
- **Figure 27.** Sources and detector estimated location covering frontopolar cortex.
- **Figure 28.** Relationships between both haemoglobins at cardiac frequency
- **Figure 29.** Limb vascular occlusion test experimental setup.
- **Figure 30.** Schematic representation of limb vascular occlusion test.
- **Figure 31.** Schematic representation of the experimental procedure.
- **Figure 32.** 850 nm spectral irradiance at different LED power values.
- **Figure 33.** 740 nm spectral irradiance at different LED power values.
- **Figure 34.** Detection of well-known oscillations in a sample raw signal of HbO from a representative subject.
- **Figure 35.** Comparison of Oxyhaemoglobin (red line) and Deoxyhaemoglobin (blue line) power spectral density (PSD) from a representative subject's short signal.
- **Figure 36.** Deoxyhaemoglobin (blue line) power spectral density (PSD) from a representative subject's short signal.
- **Figure 37.** Time courses of HbO and HbR during venous and arterial occlusion.
- **Figure 38.** Grand average of the normalized PSDs for each ROI, chromophore and signal type in the frequency range 0.005 to 0.08 Hz.
- **Figure 39.** Averaged time courses of HbO and HbR across participants during task (plus a portion of baseline and recovery to the left and right respectively) for each ROI and signal type.
- **Figure 40.** Averaged results across participants of CPSD, MSC and transfer function data between SS and DS for each ROI, comparing baseline and task.
- **Figure 41.** Illustrative comparison of neural signal estimation by regression and phasor analysis in the medial-ROI.
- **Figure 42.** Construction of synthetic data and simulation results.
- **Figure 43.** Averaged CPSDs, MSCs and phases between HbO and HbR for each ROI, comparing baseline and task.
- **Figure 44.** Averaged time courses, CPSDs, MSCs and phases between superficial HbO and heart rate for each ROI, comparing baseline and task.
- **Figure 45.** Shallow fNIRS signals and heart rate changes averaged over all task trials for each participant and for each of the three ROIs.

- **Figure 46.** Deep fNIRS signals and heart rate changes averaged over all task trials for each participant and for each of the three ROIs.
- **Figure 47.** Clean (neural)-signals and heart rate changes averaged over all task trials for each participant and for each of the three ROIs.
- **Figure 48.** Normalized power spectral density of clean-signals for each participant and for each of the three ROIs during task.
- **Figure 49.** Normalized power spectral density of shallow-signals for each participant and for each of the three ROIs during task.
- **Figure 50.** Average time lags across participants between SS and CS for HbO and HbR.

List of tables

- **Table 1.** Comparison between the characteristics of the different types fNIRS systems.
- **Table 2.** Comparison between the neuroimaging techniques.
- **Table 3.** Main contributors of the fNIRS signal.
- **Table 4.** Auxiliary registers and their instrumentation.
- **Table 5.** Different mathematical approaches and their applications with multi-distance and auxiliary registers.
- **Table 6.** Summary of technical specifications Theia devices.
- **Table 7.** PSD descriptive statistics of the cardiac, respiratory and Mayer bands for each chromophore and channel type.
- **Table 8.** Coherence and angle descriptive statistics of the cardiac band for each chromophore and channel type.
- **Table 9.** Averaged heart rate metrics across participants (baseline and task).

La espectroscopía funcional de infrarrojo cercano (fNIRS por sus siglas en inglés) es una tecnología de imagen óptica no invasiva que se ha utilizado ampliamente para medir actividad cortical inferida a través de los cambios de concentración relativa de hemoglobina oxigenada (HbO) y desoxigenada (HbR) gracias al acoplamiento neurovascular. Desafortunadamente, es común que las señales fNIRS se vean afectadas por oscilaciones hemodinámicas (espontáneas y relacionadas con los paradigmas de estimulación) indeseables no relacionadas con la actividad cerebral. Para abordar este problema, se ha propuesto la utilización de mediciones multidistancia como una estrategia particularmente efectiva. El dispositivo Theia es un instrumento fNIRS novedoso de onda continua, equipado con mediciones multidistancia, que ha sido diseñado con el objetivo de cumplir con los estándares de vanguardia en el contexto de sistemas fNIRS aplicados a la neurociencia cognitiva. El objetivo principal de este trabajo es validar el dispositivo Theia para la evaluación de la actividad funcional de la corteza prefrontal. Con este fin se ha aplicado un conjunto de pruebas iniciales (evaluación de ciertos aspectos técnicos, detección de las oscilaciones espontáneas conocidas y un test de oclusión vascular) así como una validación experimental utilizando un paradigma cognitivo basado en aritmética mental. Además, nos propusimos evaluar si la tarea de aritmética mental rítmica podría inducir fluctuaciones hemodinámicas cíclicas adecuadas para llevar a cabo mediciones efectivas en términos de frecuencia. Por otro lado, en un intento por aislar la respuesta cortical provocada por la tarea, investigamos el acoplamiento entre los cambios hemodinámicos que surgen de las capas superficiales (frente) y profundas (corticales) durante el esfuerzo mental. Veinte estudiantes universitarios de entre 18 y 25 años (ocho hombres; edad media: 21,7; SD: 3,8) se sometieron a una tarea de aritmética mental rítmica mientras se monitorizaban los cambios hemodinámicos de la corteza frontopolar a través de la frente utilizando el dispositivo Theia. Demostramos que el rendimiento del dispositivo Theia ha sido óptimo en las diferentes pruebas, cumpliendo con todos los requisitos estipulados en la literatura previa referente a la validación de nuevos instrumentos fNIRS. Además, encontramos que la tarea de aritmética mental propuesta es factible para inducir fluctuaciones hemodinámicas periódicas idóneas para llevar a cabo análisis de frecuencia efectivos. De hecho, esta aproximación permitió aplicar una técnica novedosa (basada en la función de transferencia y el álgebra fasorial) para estimar la actividad cerebral funcional y evaluar la coordinación temporal entre las respuestas cerebrales y extracerebrales. La comparación de la señal cerebral estimada mediante la nueva técnica coincidió con la obtenida por la regresión lineal, la cual es un método consolidado en la literatura

NIRS. En este sentido, ambas aproximaciones coincidieron en señalar que la aritmética mental producía un patrón de oxigenación inversa. En conjunto, nuestros resultados demuestran la viabilidad de utilizar una tarea mental rítmica para imponer un estado oscilatorio útil en la separación de las respuestas funcionales cerebrales de las no cerebrales. Esta diferenciación parece ser esencial para la mejor comprensión de las señales fNIRS y para una evaluación más precisa la dinámica neurovisceral.

Functional near-infrared spectroscopy (fNIRS) is a non-invasive optical imaging technology that has been widely used to measure cortical activity inferred through relative concentration changes in oxygenated (HbO) and deoxygenated (HbR) haemoglobin thanks to neurovascular coupling. Unfortunately, fNIRS signals are commonly impaired by undesirable task-evoked and spontaneous hemodynamic oscillations of non-cerebral activity. To address this issue multi-distance measurements have been proposed as a particularly effective strategy. Theia device is a novel continuous wave-fNIRS instrument with multi-distance measurement, which has been designed with the aim of fulfilling the cutting-edge fNIRS system standard in the context of cognitive neuroscience. The main objective of this work is to validate the Theia device to assess the functional activity of the prefrontal cortex. With this end we have applied a set of initial tests (evaluation of technical aspects, detection of well-known spontaneous oscillations and vascular occlusion test) as well as an experimental validation using a cognitive paradigm of mental arithmetic. In addition, we set out to assess whether the rhythmic mental arithmetic task could induce cyclic hemodynamic fluctuations suitable for effective frequency-resolved measurements. On the other hand, to isolate the task-evoked cortical response, we investigated the coupling between hemodynamic changes arising from superficial (forehead) and deep (cortical) layers during mental effort. Twenty university students aged 18-25 years (eight males; mean age: 21.7; SD: 3.8) underwent an initial testing and a rhythmic mental arithmetic task while hemodynamic changes of the frontopolar cortex were monitored through forehead using Theia device. We demonstrated that the performance of Theia device has been optimal in the different tests, meeting all the requirements stipulated in the previous literature regarding the validation of new fNIRS instruments. In addition, we found that mental arithmetic task proposed here is feasible to induce periodic hemodynamic fluctuations suitable for effective frequency-resolved analyses. In fact, this approximation enabled to apply a novel technique (combination of the transfer function and phasor algebra) in order to estimate the putative functional brain activity and assess the timed-coordination between extracerebral and cerebral responses. The comparison of the estimated brain signal from the novel technique coincides with that produced by a consolidated method in the NIRS literature such as linear regression. In this sense, both methods show agreement in pointing out that mental arithmetic yields an inverse oxygenation pattern. Altogether, our results demonstrate the feasibility of using a rhythmic mental task to impose an oscillatory state useful to separate true brain functional responses from those of non-

cerebral origin. This separation appears to be essential for a better understanding of fNIRS data and to assess more precisely the dynamics of the neuro-visceral link.

1.1 Historical perspective

In the Department of Physiology of Duke University in 1977 Frans Jöbsis carried out various experiments that culminated in the publication of an article entitled “Non-invasive, infrared monitoring of cerebral and myocardial oxygen sufficiency and circulatory parameters” that marks the beginning of near-infrared spectroscopy (NIRS) (Jöbsis, 1977). In this work, Jöbsis pointed out that light between 160 and 865 nm allowed for real-time detection of changes in cortical oxygenation in anesthetized cats (Jöbsis, 1977). Furthermore, this landmark article also showed that it is possible to use the near-infrared range for measurement of brain oxygenation changes associated with voluntary hyperventilation (Ferrari & Quaresima, 2012b; Jöbsis, 1977). Therefore, this report shows for the first time in history that NIRS is an effective non-invasive method to measure oxygenation in vivo in the human brain (Ferrari & Quaresima, 2012b; Jöbsis, 1977; Piantadosi, 2007). Over the next decade, various NIRS devices prototypes were designed to measure the brain of neonates and adult patients (Ferrari & Quaresima, 2012b). During these years the NIRS devices employed in the investigations were created ad hoc by the researchers themselves, however, in 1989 the Hamamatsu photonics company produced the first commercial single-channel NIRS device (Ferrari & Quaresima, 2012b).

Until then, NIRS was used exclusively to monitoring cerebral hemodynamics that allowed clinicians to detect hypoxia or ischemia in the hospital settings (Ferrari & Quaresima, 2012a, 2012b). However, between 1991 and 1993, several papers first demonstrated that NIRS could be applied to capture neural activity associated with mental stimulation, coining the term “functional near-infrared spectroscopy” (fNIRS) (Chance et al., 1993; Hoshi & Tamura, 1993; Kato et al., 1993; Okada et al., 1993; Villringer et al., 1994). For example, Hoshi and Tamura (1993) demonstrated that functional stimulation through an arithmetic task generated changes in the state of oxygenation in the bilateral prefrontal cortex.

The earliest evidence that fNIRS was useful in the field of psychiatry can be traced back to 1994 when Okada, Tokumitsu, Hoshi and Tamura (1994) demonstrated that this technology could be utilized to measure disturbances in inter-hemispheric integration in patients with schizophrenia (Ferrari & Quaresima, 2012). At a later time, Hock et al. (1996) pointed out that fNIRS could also be a valuable method in the quantification of impairment associated with neurodegenerative diseases such as Alzheimer's dementia.

Over time, multichannel fNIRS devices were designed, which allowed the simultaneous acquisition of various cortical areas. Specifically, in 1994 the Hitachi company first introduced a commercial 10-channel fNIRS (Watanabe et al., 1996). In the following year, various multi-channel fNIRS systems broke into the market, considerably improving spatial resolution of this technology (Ferrari & Quaresima, 2012b).

The initial fNIRS devices used fibre optics bundles, which generated discomfort (due to the weight that is exerted on the head) and restricted the movement of the participant, which posed a threat to the ecological validity of the experiments. The first attempts to make fNIRS devices more comfortable and portable occurred since 1998 (Chance et al., 1998; Izzetoglu et al., 2011) and have culminated in the commercialization of more than 8 wearable and wireless systems (Ferrari & Quaresima, 2012b).

Nearly three decades of research at fNIRS have shown that this technique is applicable to fields as diverse as neurology, cognitive neuroscience, rehabilitation, psychiatry, psychology, neurodevelopment, brain-computes interfaces, motor control and education.

1.2 Physical principles

An optical spectrometer or spectroscopy is an instrument that measures properties of light in a certain range of the electromagnetic spectrum. Specifically, NIRS technology measures changes in near-infrared light intensity, which is a type of electromagnetic radiation with wavelengths between 700 and 1400 nm (Figure 1). Currently, fNIRS is a non-invasive optical neuroimaging technique that takes advantage of the physical properties of tissues subjected to near-infrared (NIR) light to infer brain activity through changes in relative concentration changes in oxygenated (HbO) and deoxygenated (HbR) haemoglobin. Some basic physical principles must be reviewed in order to understand how fNIRS technology works.

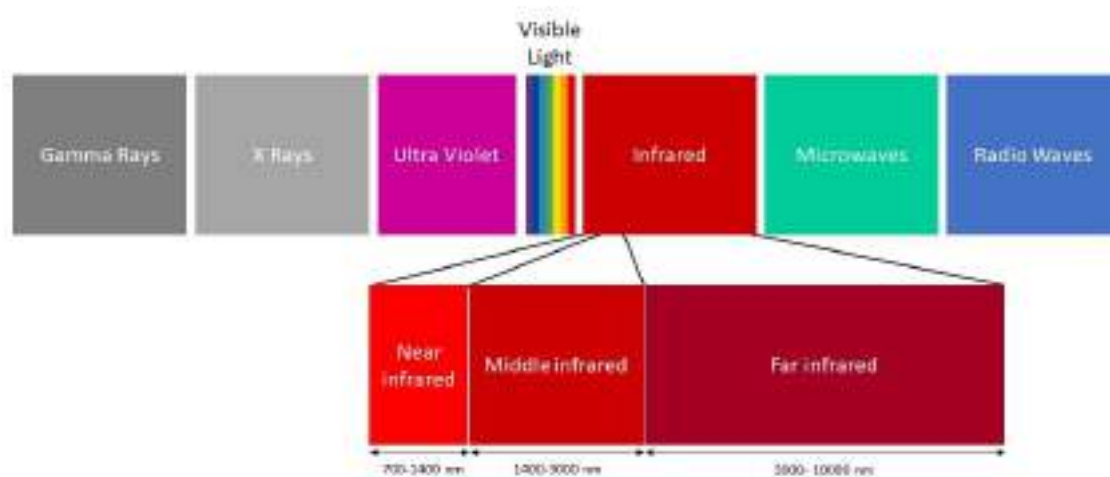


Figure 1. Electromagnetic spectrum. The infrared spectrum is divided into three regions based on its wavelength (near, middle, and far).

1.2.1 Light and tissue interactions

The propagation of light concerns the way in which a certain electromagnetic wave transfers its energy from one point to another. Reflection, scattering and absorption are the main phenomena that determine the attenuation of NIR light during its propagation in biological tissues (Figure 2) (Almajidy et al., 2020; Delpy & Cope, 1997).

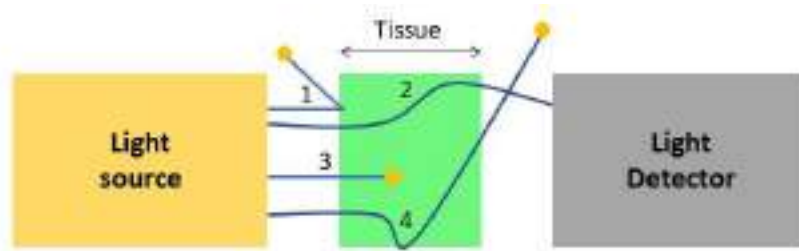


Figure 2. Main phenomena of attenuation of NIR light traveling through tissue. 1. Photon reflected. 2 and 4 Scattered photons. 3. Photon absorbed.

Scattering occurs when NIR light deviates from a straight path, while when NIR light bounces away from the surface it is called reflection (Figure 2). Lastly, absorption is caused when certain molecules in tissues convert light into energy (Almajidy et al., 2020; Pinti, Tachtsidis, et al., 2018). Biological molecules that display specificity in the absorption of certain light's wavelengths are named chromophores (Kumar et al., 2017; León-Carrión & León-Dominguez, 2012). Figure 3 shows the most important chromophores that absorb NIR light in vivo tissues.

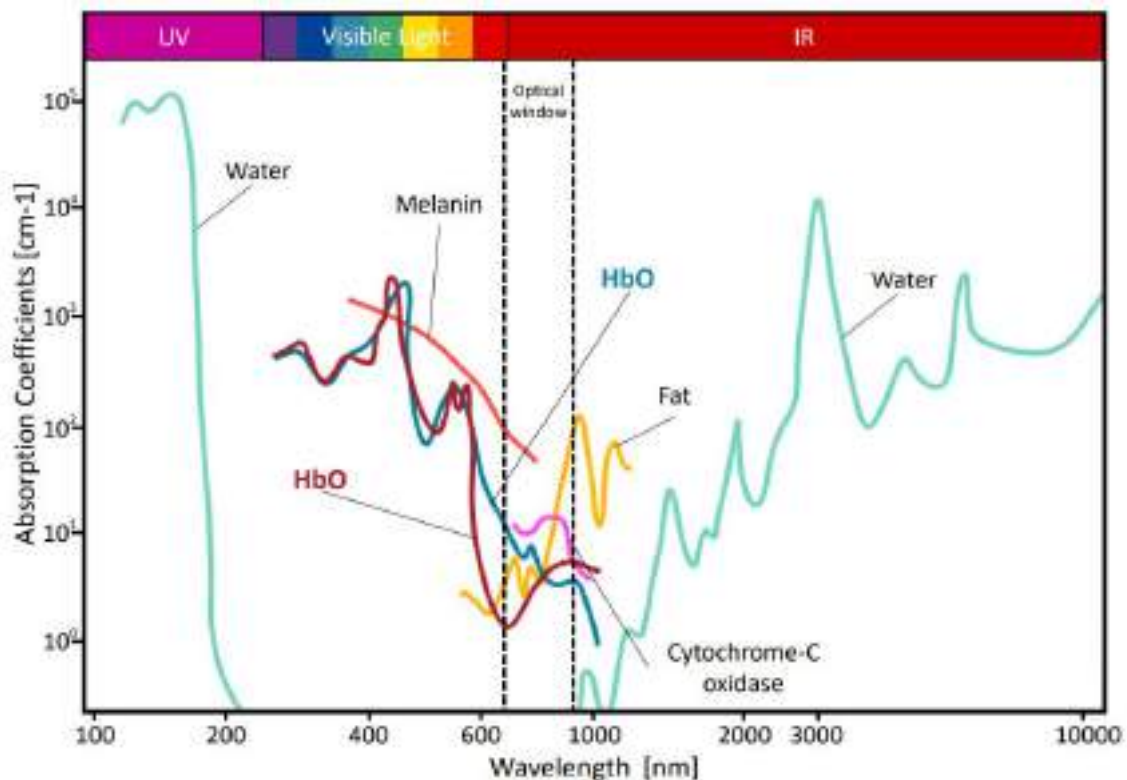


Figure 3. Water, melanin, HbO, HbR, fat, and Cytochrome-C oxidase absorption spectra at ultraviolet, visible, and infrared light spectrum. UV= ultraviolet; IR = infrared; HbO = oxyhemoglobin; HbR = deoxyhemoglobin (Scholkmann et al., 2014).

The wavelength between 700-900 nm is considered the “optical window” since in this range the NIRS light displays an advantageous propagation (being poorly absorbed by water) which allows it to reach deep tissues such as cortex (Figure 3). Although in this spectral range, haemoglobin shows lower absorption coefficients than fat or melanin, it must be considered that the latter are insensitive to brain activity, so they remain constant. Consequently, thanks to the fact that brain activity modifies the amount of haemoglobin in neuronal tissue, we can use NIRS technology as a functional neuroimaging instrument.

1.2.2 Chromophores

In this section we discuss the different chromophores that absorb NIR light, for which we will employ a classification based on whether they are response-dependent or not:

1.2.2.1 Response-dependent chromophore

The response-dependent chromophores are those that can vary their concentrations over time consequently to brain activity. The most relevant response-dependent chromophore that absorbs NIR light in vivo tissues is haemoglobin (Kamran et al., 2018); In fact, it constitutes the primary target of measurement of the fNIRS technology.

1) Haemoglobin is a globular haemoprotein that is present in erythrocytes and whose main function is the transport of oxygen from the lung tissue to the capillaries (Guyton et al., 2011; Lozano-Teruel, 1995; Müller-Esterl & Brandt, 2020). This protein displays a quaternary structure, that is, it is formed by several polypeptide subunits (globins) that are held together by non-covalent interactions. Specifically, the haemoglobin molecule is a tetramer which is composed of four polypeptide subunits with different amino acid sequences (Lozano-Teruel, 1995). Depending on the composition of these subunits, we can differentiate different types of haemoglobin (Haemoglobin A or adult haemoglobin, haemoglobin A2, fetal haemoglobin, glycosylated haemoglobin, etc). However, here we will refer exclusively to haemoglobin A or main haemoglobin in adults made up of two alpha (α) and two beta (β) subunits (Figure 4) (Guyton et al., 2011; Lozano-Teruel, 1995; Müller-Esterl & Brandt, 2020). Each subunit contain a prosthetic group called “heme” (composed of a complex of a pyrrole group, protoporphyrin IX, and a ferrous ion) that can reversibly bind a dioxygen molecule (Figure 4) (Guyton et al., 2011;

Müller-Esterl & Brandt, 2020). Therefore, one haemoglobin molecule can bind four dioxygen molecules (Figure 4).

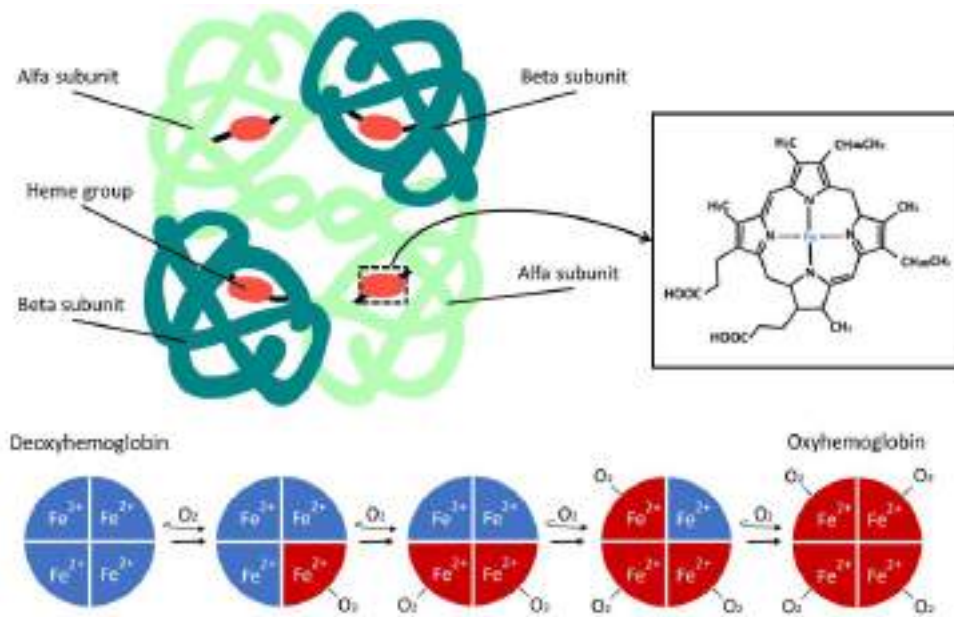


Figure 4. Haemoglobin A structure and its oxygen binding process. At the top, the schematic structure of haemoglobin and the heme group is shown. In the lower part, it can be seen how HbR joins four diatomic oxygen molecules to form HbO.

Classically two haemoglobin forms have been differentiated depending on their oxygenation state (Lozano-Teruel, 1995; Müller-Esterl & Brandt, 2020):

- HbO: the oxygen-loaded structure also known as the R state (relaxed form) in which haemoglobin shows a high affinity for oxygen (Figure 4).
- HbR: The oxygen-unloaded structure is also known as the T (tense form) or reduced state in which haemoglobin shows a low affinity for oxygen (Figure 4).

As seen in Figure 5, the union of the 4 diatomic oxygen molecules confers an HbO and HbR specific absorption profile of NIR light, which enables us to monitor the changes of both chromophores in the neuronal tissues. Specifically, light with wavelengths greater than 800 nm can be employed to infer HbO relative changes. Conversely, light with a wavelength lower than 800 nm can be used to infer HbR relative changes (Pinti et al., 2018). (Figure 5).

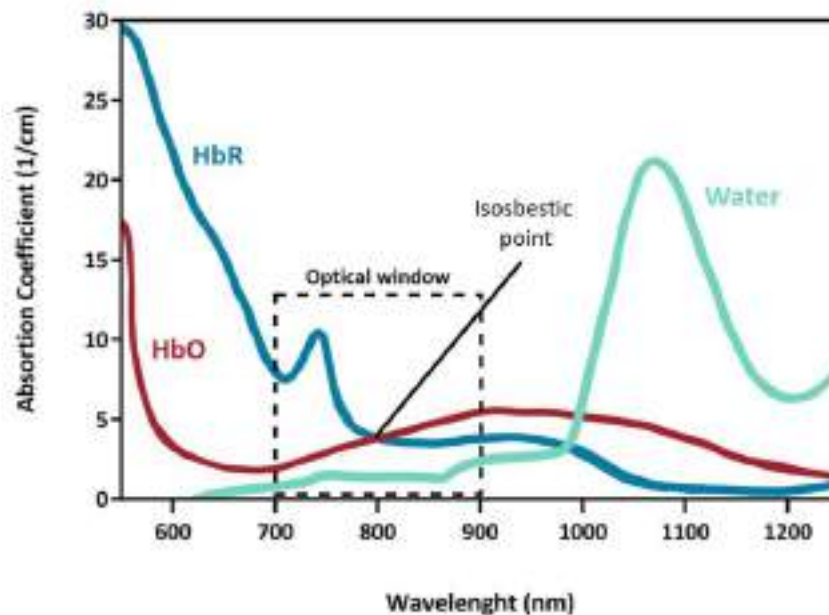


Figure 5. Detail of HbO, HbR and water absorption spectra. The dashed square indicates the wavelengths of the optical window. Around 800 nm the isosbestic point is identified (wavelength in which both chromophores absorb the NIR light with the same intensity). (Scholkmann et al., 2014)

2) Myoglobin is a monomeric haemoprotein made up of a single globin bound to a heme group that is found exclusively in skeletal and cardiac muscle tissue (but not in neuronal tissue) where it acts as an oxygen reservoir (Lozano-Teruel, 1995; Müller-Esterl & Brandt, 2020). Although it is a chromophore that can vary its concentrations over time, these fluctuations are due solely to the increased metabolic demands of muscle tissue. Therefore, although a priori it is response-dependent chromophore, for practical purposes we can ignore its effect on fNIRS measurements in cognitive and emotional contexts.

3) Cytochrome C-oxidase or complex IV is a mitochondrial transmembrane polypeptide that acts as an enzyme in the respiratory electron transport chain, making the chromophore sensitive to neuronal metabolic activity (Bale et al., 2016; de Roever et al., 2017). This enzyme is responsible for catalysing the final step of this set of chemical reactions by receiving electrons from cytochrome C and transferring them to an oxygen molecule, which it reduces to produce a water molecule (Bale et al., 2016). Cytochrome oxidase shows a light absorption peak in 830 nm (Figure 3) which places it close to the wavelength where HbO displays its highest absorption value. However, two factors allow to ignore its participation in the fNIRS measurements: the first one is that the total concentration of cytochrome oxidase remains stable in short periods, in fact,

hours are necessary for its concentration to change. The second one is that the concentration of cytochrome oxidase is very low compared to the two states of oxygenation of haemoglobin (Bale et al., 2016).

1.2.2.2 Response-independent chromophore

These molecules present in biological tissues display a significant near-infrared absorption profile, but their concentrations do not change over time in response to environmental conditions. We can ignore their effect when using fNIRS technology for cerebral activity measurement.

1) Water. Although its proportion varies depending on the tissue, in general terms water constitutes 60-80% of the total body mass (Guyton et al., 2011). As shown in Figure 3, between 200-900 nm there is a region where water absorbs a little of light, which constitutes an optical window that allows us to measure other chromophores present in tissues such as haemoglobin.

2) Lipids. Triglycerides are part of the adipose tissue that is present in the subdermis (Guyton et al., 2011). They are also a fundamental component of the lipid bilayers that form cell membranes and of the myelin that surrounds the axons of neurons (Guyton et al., 2011; Lozano-Teruel, 1995; Müller-Esterl & Brandt, 2020). As shown in Figure 3, fats absorb a little of light at the beginning of the near infrared wavelength, increasing considerably as we approach the mid-infrared spectrum.

3) Melanin is a set of substances derived from the amino-acid tyrosine that give colour to some tissues such as skin, hair, retina, etc (Cafardi, 2012). Melanin shows a great capacity to absorb light in the visible spectrum, decreasing dramatically as we approach the NIR range (Figure 3).

1.2.3 Beer-Lambert Law

The Beer-Lambert law (BLL) was described by French mathematician Pierre Bouguer in 1729 (Bouguer, 1729). However, the discovery of this law is commonly attributed to the Swiss Johann Heinrich Lambert even though this author quotes Bouguer in his works (Lambert, 1760; Scholkmann et al., 2014). Subsequently, the German August Beer improved the law allowing the

quantification of concentrations (Beer, 1852). Although it has been classically denominated Beer-Lambert-Bouguer law in honour of the three authors mentioned above, currently it is called BLL in the fNIRS literature. The BLL relates light attenuation to some physical properties of the medium through which the light is travelling and is expressed as:

$$A^\lambda = -\log_{10} (I^\lambda/I_0^\lambda) = \epsilon^\lambda PL^\lambda c^\lambda \quad (1)$$

The attenuation of light, measured in optical density, through a medium is determined by the logarithmic ratio of the intensity of the transmitted light (I) to the intensity of the incident light (I_0) (Almajidy et al., 2020; Obrig & Villringer, 2003) (Eq. 1). This is equivalent to the product of molar absorptivity of a given chromophore (ϵ) (e.g. HbO or HbR), light pathlength (distance between source-detector) (PL), and the molar concentration of a given chromophore (c) (e.g. HbO or HbR). Note that all parameters are wavelength dependent (λ).

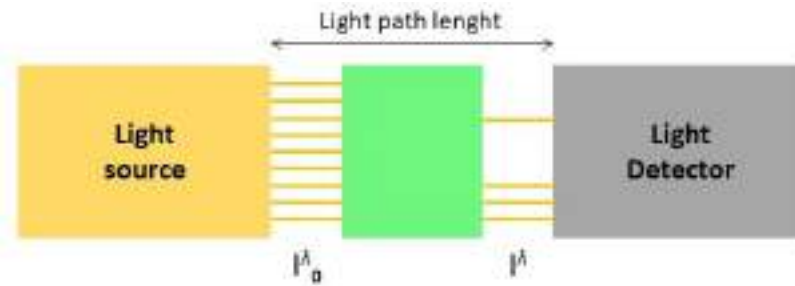


Figure 6. Schematic representation of incident and transmitted light. I^λ = transmitted light. I_0^λ = incident light.

1.2.4 Modified Beer-Lambert Law

BLL does not take into account dispersion of the photons so it cannot be applied to biological tissues in which scattering is the dominant mechanism of light propagation (Almajidy et al., 2020; Scholkmann et al., 2014). To overcome these limitations, two new interdependent aspects were included: photon loss due to dispersion (G) and a scaling factor to represent a more realistic light pathlength (PL). By introducing these improvements in BLL, the new law was called modified BLL (Eq. 2) (Delpy et al., 1988; Huppert et al., 2009; León-Carrión & León-Dominguez, 2012):

$$\Delta OD_{ij}^\lambda = PL_{ij}^\lambda DPF^\lambda (\epsilon_{Hbr}^\lambda \Delta[Hbr] + \epsilon_{HbO}^\lambda \Delta[HbO]) + G^\lambda \quad (2)$$

Where OD is optical density, i and j represent the source and detector respectively, PL is light pathlength (distance between source-detector), DPF is differential path-length factor, ϵ is molar absorptivity, [HbR] is HbR concentration, [HbO] is HbO concentration and G is light attenuation mainly related to scattering. Note that all parameters are wavelength dependent (λ) (Huppert et al., 2009). Usually, the amount of scattered light is unknown and time-invariant. Therefore, G can be neglected in determining changes in optical density (Scholkmann et al., 2014).

The photons do not travel from the source to the detector in a straight line, as each photon follows a random path through the biological tissue (Figure 7) (Hoshi, 2016). In fact, it is assumed that when the photon going through the scalp to a NIR photodetector follows a banana or ellipsoid shaped path due to the scattering phenomena of the different tissue layers (Figure 7) (Dashtestani et al., 2019; Ferrari & Quaresima, 2012b). Therefore, it should be considered that NIR light PL is much longer than the source-detector distance (SDD) (Figure 7). To correct the influence of this phenomenon, the differential PL (DPF) term was included in modified BLL (Eq. 2) (Kamran et al., 2018).

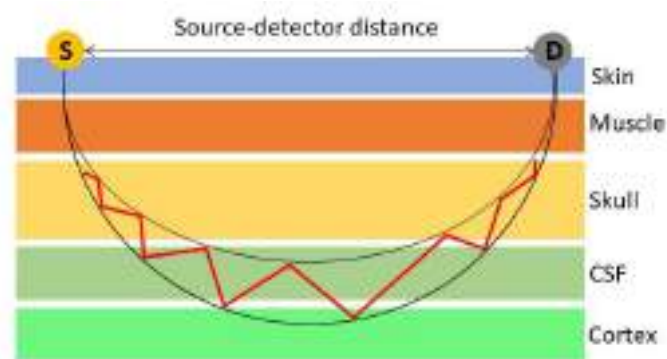


Figure 7. Schematic representation of NIR light through a head. The black line represents the "banana/ellipsoid shape" of the photon path. The red line shows the path of a photon that increases its path length much longer than the source-detector distance. S = light source; D = light detector; CSF = cerebrospinal fluid.

DPF informs us of how many times farther, than of SDD, the photon has travelled due to scattering phenomena (Scholkmann & Wolf, 2013). Note it is only possible to assume that the DPF at a given wavelength is constant because the amount of scattered light (G) changes negligibly during the measurement (Almajidy et al., 2020; Obrig & Villringer, 2003). It is common to apply DPF values between 3 and 6, however it must be considered that DPF varies depending on the chromophore (HbO and HbR), age and sex (Duncan et al., 1995; Kamran et al., 2018; Scholkmann & Wolf, 2013).

In summary, we can use the modified BLL to convert raw NIR light detected into relative changes in [HbR] and [HbO] from which we can indirectly monitor the hemodynamic activity of neuronal tissue.

1.3 Physiological principles of fNIRS

1.3.1 Regulation of Cerebral blood flow

Compared to the rest of the organs, the brain is extremely energy-demanding, monopolizing 15-20% of the cardiac output, even though its mass represents only 2% of the total body (Raichle, 2010; Williams & Leggett, 1989). Despite its high metabolic activity, neuronal tissue shows a low energy storage capacity, so the regulation of blood supply is of paramount importance (Willie et al., 2014). In fact, the cerebrovascular system displays various regulatory mechanisms to meet metabolic demands and protect neuronal tissue against environmental changes:

- 1) Cerebral pressure autoregulation is the process whereby the arterioles modulate their diameter to keep the cerebral blood flow (CBF) invariant despite changes in cerebral perfusion pressure (Claassen et al., 2021; Peterson et al., 2011).

- 2) Neurogenic regulation: there is histological and functional evidence that the perivascular nerve network influences CBF. Two types of perivascular innervation have been identified: (1) When the vessel circulates through the Virchow-Robin space (Figure 8), it receives extrinsic efferences (sympathetic and parasympathetic fibres) that come from the superior cervical, sphenopalatine and trigeminal ganglia. It appears that sympathetic fibres maintain an increased vasoconstrictive tone that facilitates cerebral pressure autoregulation (Hamel, 2006). (2) When the vessels enter the brain parenchyma, it receives intrinsic efferences from the brain tissue itself (Hamel, 2006; Peterson et al., 2011; S. Schaeffer & Iadecola, 2021).

- 3) Local regulation of the cerebrovascular endothelium through the production of chemical substances such as nitric oxide, eicosanoids, etc (Claassen et al., 2021; Peterson et al., 2011).

- 4) Flow-Metabolism Coupling or neurovascular coupling (NVC): it refers to changes in CBF linked to variations in brain metabolism. The ability of neuronal tissue to change CBF based on its energetic demands.

Of all the mechanisms that regulate the CBF, the latter (NVC) is the most important for the fNIRS technology.

1.3.2 Neurovascular unit

The neurovascular unit concept refers to the close structural and functional relationship that exists between neurons and the cerebral microvasculature (Muio et al., 2014; Schaeffer & Iadecola, 2021). Because the elements of NVU (neurons, perivascular astrocytes, smooth muscular cells, pericytes, endothelial cells, basement membrane, and capillaries) maintain reciprocal and complex relationships, they are all considered to constitute a single highly synchronized and coordinated functional unit rather than separated subunits (Bell et al., 2020; Muio et al., 2014; Schaeffer & Iadecola, 2021; Zonta et al., 2003). Since its appearance, this term has been increasingly accepted by the neuroscientific community as it facilitates the understanding and interpretation of some phenomena observed in neuroimaging (Schaeffer & Iadecola, 2021). We will briefly explain each of the NVU components:

- 1) Neurons and perivascular astrocytes. Neurons are capable of constantly sensing the blood supply they receive (nutrients and oxygen). When there are small variations in this supply, the neurons communicate with the surrounding astrocytes to modify the CBF according to its needs (Muio et al., 2014; Zonta et al., 2003). Therefore, astrocytes act by translating neurons' metabolic demands into changes in the vascular tone of blood vessels (Schaeffer & Iadecola, 2021). This vasomotor regulation occurs thanks to the fact that astrocytes have a histological structure called "endfoot" that is in contact with pericytes and smooth muscle cells of the cerebral vessels (Figure 8).

- 2) Pericytes are contractile cells that modify vascular tone depending on the metabolic demands of neuronal tissue (Figure 8).

- 3) Smooth muscle cells are mainly responsible for the change in the diameter of the large vessels.

- 4) Endothelial cells produce chemical messengers that are capable of produce vasodilation and vasoconstriction (Figure 8).

- 5) Vasculature. Neural activity generates two closely coordinated processes: (1) a response of microvessels located in the proximity of active neurons. (2) a less local response that is transmitted upstream to small-caliber arterioles and venules. In fact, it is precisely the capillaries and small-calibre cortical vessels (diameter less than 1 mm) that NIRS technology is capable of recording (because when light propagates into a

medium-calibres vessel the light is completely absorbed) (Hoshi, 2016; Kishi et al., 2003; Liu et al., 1995; Murkin & Arango, 2009; Rasmussen et al., 2007).

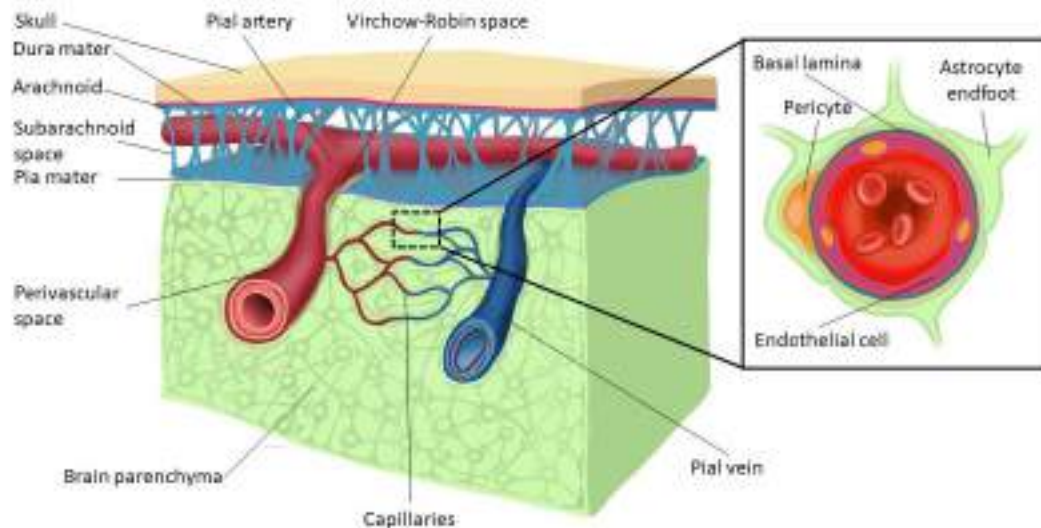


Figure 8. Structure of the cerebral cortex, the meninges, and the blood-brain barrier.

1.3.3 Functional Neuronal hemodynamic response

Neuronal activation produces a growth of the regional cerebral metabolic rate of oxygen ($rCMRO_2$) because metabolically active neurons substantially increase their oxygen consumption (neurometabolic coupling) (Tachtsidis & Scholkmann, 2016). This metabolic demand leads to tissue oxygenation drop, which is rebalanced by the oversupply (functional hyperaemia) through increased regional cerebral blood flow (rCBF) and regional cerebral blood volume (rCBV) (Herold et al., 2018; Pinti, Tachtsidis et al., 2018). The neurovascular coupling (NVC) refers to the tight link in spatial and temporal terms between neuronal metabolism and blood supply, which allows us to map functional brain activity (Steinbrink et al., 2006; Tachtsidis & Scholkmann, 2016).

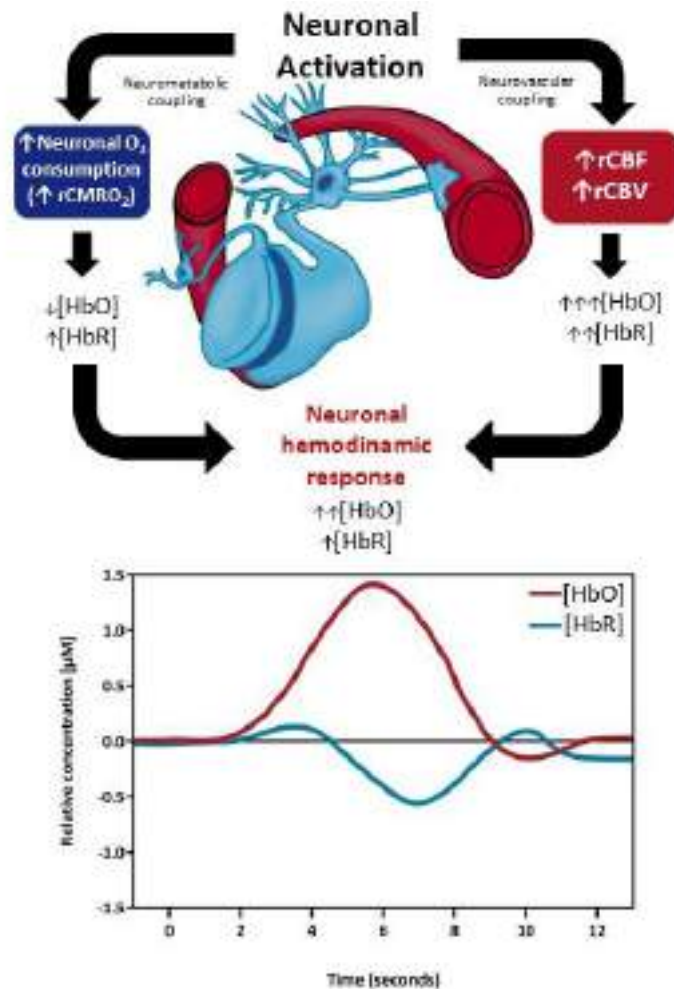


Figure 9. Schematic representation of metabolic and hemodynamic changes during neural activation. rCMRO₂ = regional cerebral metabolic rate of oxygen; rCBF = regional cerebral blood flow; rCBV = regional cerebral blood volume; [HbR] = oxyhaemoglobin concentration; , [HbO] = deoxyhaemoglobin concentration; ↑ = increase; ↓ = decrease.

Because the amount of oxygenated blood that reaches a brain region is greater than the amount of oxygen consumed, the “typical” functional neuronal hemodynamic response associated with neuronal activation is characterized by an increase in HbO and a reciprocal decrease in HbR (Scholkmann et al., 2014; Tachtsidis & Scholkmann, 2016) (Figure 9). Particularly, the changes in [HbO] reach a peak at 5-6 seconds after stimulus onset then an undershoot occurs between 9-11 seconds and goes back to its baseline with a certain delay (12 seconds from the stimulus onset) (Cinciute, 2019; Pinti, Tachtsidis et al., 2018). In parallel, the changes in [HbR] reach a peak at 4 seconds after stimulus onset after an undershoot and an overshoot occur returning to its baseline (12 seconds from the start of stimulation) (Cinciute, 2019).

Until now we have applied the term “neuronal” and “functional” to refer to the hemodynamic response, implying that it is the only form of reaction of the cortex before functional activity. However, some studies indicate that this sequence of changes in [HbO] and [HbR] may not necessarily constitute the only hemodynamic response of neuronal activity (Boas et al., 2001; Holper et al., 2011; Mullinger et al., 2014; Okada et al., 1997; Wylie et al., 2009). For that matter, another type of cortical hemodynamic reaction is the so-called “inverse or negative oxygenation response” (as a counterpoint to neuronal hemodynamic response) which is characterized by decreased HbO and a concomitant increased HbO (Holper et al. 2011). Reverse or inverse oxygenation response has been found in NIRS studies using different stimulation paradigms, such as motor imagery (Abdalmalak et al., 2020; Holper et al., 2011), visual stimulation (Maggioni et al., 2015), n-back (Haeussinger et al., 2014; Kirilina et al., 2012), emotional stimulation (Matsukawa et al., 2018) and mental arithmetic (Bauernfeind, Leeb, Wriessnegger, & Pfurtscheller, 2008; Pfurtscheller, Bauernfeind, Wriessnegger, & Neuper, 2010). Various physiological explanations have been adduced to explain the presence of this type of signal:

1) The “vascular stealing” hypothesis which proposes that the related-task areas are forced to subtract the oxygen from the unrelated-task surrounding areas since the availability of oxygenated blood is limited.

2) The theory called "inhibition hypothesis", which states that the inverse response is triggered by a reduction in neuronal activity (deactivation) that leads to a decrease in oxygen consumption and rCBF.

3) The hypothesis of “activation” defends the idea that neuronal activity triggers the inverted signal due to an increase in CBF in combination with a bigger increase in neuronal oxygen consumption (Maggioni et al. 2015).

Despite the proposed hypotheses, the truth is that the underlying mechanism accounting negative response remains unclear and currently this research topic continues to be the subject of discussion.

1.4 fNIRS instrumentation

1.4.1 Different types of fNIRS systems

Based on the physical principles employed to quantify hemodynamic changes, three different types of fNIRS systems are distinguished:

1) Continuous-wave fNIRS devices. In this type of instruments, the measure of light attenuation at different wavelengths is used to infer relative changes in [HbO] and [HbR]. A laser (with invariable intensity in time) or light-emitting diode (LED) at various wavelengths are deployed as the emission source (Figure 10), while a photodiode is commonly applied as the detection system. Compared to other fNIRS instruments, the continuous wave was the earliest to appear and is the most used in research work (Scholkmann et al., 2014). Among its advantages we can point out its simplicity, inexpensiveness, as well as its low weight and size. However, as a disadvantage we can highlight that these systems cannot determine the optical properties of the biological tissue (light scattering and absorption) and therefore the absolute quantification of [HbO] and [HbR] is not practicable (Ferrari, 2007; Ferrari & Quaresima, 2012; Scholkmann et al., 2014) (Table 1).

2) Frequency-Domain fNIRS devices. This type of fNIR system obtains information about the absorption and scattering of tissues based on the change in amplitude and phase shift of the detected signal with respect to the incident signal (Chance et al., 1998; Delpy & Cope, 1997; Scholkmann et al., 2014; Wabnitz et al., 2010) (Figure 10). Actually, these types of devices are also known as phase modulation spectroscopy, intensity modulated system or frequency resolved (Almajidy et al., 2020). The emission source is usually a LED or laser diode that produces a continuous, but modulated amplitude light (100 Mhz to 1 Ghz). A photon counting device, or a gain-modulated area detector are used as detection apparatus (Almajidy et al., 2020). Determination of the absolute concentrations of chromophore and a good temporal resolution are advantageous features of this device frequently cited whereas the high economic cost and low portability must be considered drawbacks (Ferrari, 2007; Ferrari & Quaresima, 2012b) (Table 1).

3) Time-domain fNIRS devices. This modality of fNIRS instrument employs the temporal broadening of a pulsed light laser through a biological medium to provide

information on tissue absorption and scattering (Torricelli et al., 2014) (Figure 10). Solid-state laser or pulse diode lasers are employed as emission sources due to their ability to produce very short (less than 10 picoseconds) and powerful (1-1000 mW) pulses whereas a streak camera or single photon counters, with high temporal resolution, are implemented to detect the photon distribution of time-of-flight (Delpy & Cope, 1997; Torricelli et al., 2014). In fact, these devices are also called time-of-flight or time-resolved fNIRS (Almajidy et al., 2020). Some notable advantages are the absolute determination of chromophore concentrations and high spatial resolution (Table 1). However, among their drawbacks we could mention that they are cumbersome, bulky, and expensive devices (Almajidy et al., 2020; Delpy & Cope, 1997; Ferrari, 2007; Ferrari & Quaresima, 2012b; Torricelli et al., 2014) (Table 1).

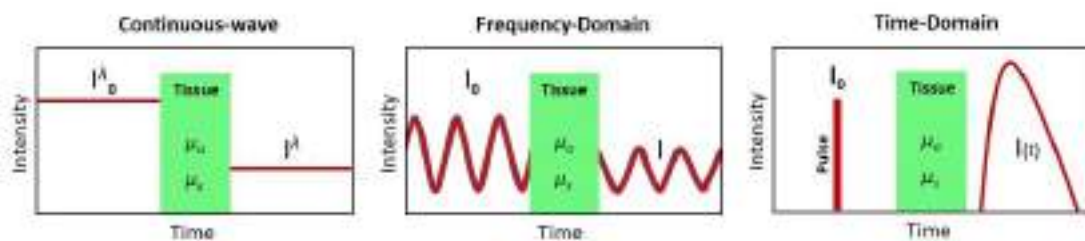


Figure 10. Schematic representation of incident and transmitted light in different types of fNIRS systems. I_0 = incident light; I = transmitted light; μ_a = scattering coefficient; μ_s = absorption coefficient.

Table 1. Comparison between the characteristics of the different types of fNIRS systems (Almajidy et al., 2020; Delpy & Cope, 1997; Ferrari, 2007; Ferrari & Quaresima, 2012; Scholkmann et al., 2014; Torricelli et al., 2014).

Variables	fNIRS system types		
	Continuous-Wave	Frequency-Domain	Time-Domain
Absolute [HbO] and [HbR]	no	yes	yes
Separate scattering and absorbing light	no	yes (medium)	yes (high)
Pathlength measurement	no	yes	yes
Temporal resolution	high	medium	low
Size/weight	small/low	bulky/high	bulky/high
Portability	easy	factible	factible
Telemetry	factible	difficult	difficult
Cost	low-medium	high	high

1.4.2 Continuous wave fNIRS and other functional neuroimaging techniques

fNIRS is one more technique among the multiple existing methods to measure neuronal functional activity, so below we will make a comparison between all of them (Table 2).

1) Positron emission tomography (PET): An injected radiopharmaceutical allows the measurement of regional metabolic changes associated with neuronal activity by means of positron emitting isotope of oxygen using multiple sensors that detect particle disintegration (Boly et al., 2015).

2) Functional magnetic resonance imaging (fMRI): This technique is based on the fact that neuronal activity produces the so-called Blood-Oxygen Level-Dependent (BOLD) response (change in paramagnetic [HbR]) that is detected as a local disturbance in magnetism through of a resonator (Boly et al., 2015; Bunge & Kahn, 2009).

Since fMRI is the neuroimaging technique that is most frequently compared to fNIRS, we will dedicate a few paragraphs to some considerations that must be taking at count. First, fNIRS provides data on [HbO] and [HbR] changes while the BOLD signal is exclusively based on HbR. Furthermore, the temporal resolution of fNIRS is higher compared to fMRI (Table 2) (Figure 11), however, fMRI displays a higher spatial resolution. Finally, some practical aspects should be also considered: fNIRS can be easily placed over the forehead generating scarce physical and psychological discomfort (Bendall et al., 2016) increasing ecological validity (Crum, 2020; Doi et al., 2013; Liu et al., 2016) which is crucial in research with clinical and child populations. Conversely, fMRI imposes an uncomfortable experimental setting (noise, body fixations) that pose a threat for the simulation of real-world environment, which is especially relevant in affective and cognitive neuroscience (Doi et al., 2013).

3) Electroencephalography (EEG): This method detects the electrical dipoles generated by the postsynaptic potentials of cortical neurons thanks to electrodes located on the surface of the scalp.

4) Magnetoencephalography (MEG): detects very low intensity magnetic fields associated with the electrical activity of pyramidal neurons.

Table 2. Comparison between the neuroimaging techniques.

Variables	Neuroimaging techniques					References
	PET	fMRI	EEG	MEG	CW-fNIRS	
Parameters	Regional metabolic changes using positron emitting isotope of oxygen.	Blood-Oxygen Level-Dependent	Dipoles generated by postsynaptic potentials	Magnetic field produced by this electrical activity	[HbO] and [HbR] relative changes	(Bunge & Kahn, 2009; Maestú-Unturbe et al., 2007; Pinti, Tachtsidis, et al., 2018)
Temporal resolution	Low (1 min.)	Medium (6-8 sec.)	High (< 1 sec.)	High (< 1 sec.)	High (< 1 sec.)	(Maestú-Unturbe et al., 2007; Pinti, Tachtsidis, et al., 2018)
Spatial resolution	Medium (5 mm)	High (1mm)	20 mm	15 mm	Low (10-30 mm)	(Gagnon, et al., 2012; Herold et al., 2018; Pinti, Tachtsidis, et al., 2018)
Cortical structures	Yes	Yes	Yes (Cortical gyri and depths of the sulci)	Yes (superficial part of the sulci)	Yes	(Bunge & Kahn, 2009; Gagnon et al., 2012; Pinti, Tachtsidis, et al., 2018)
Subcortical structures	Yes	Yes	No	No	No	(Boly et al., 2015; Finn et al., 2018; Herold et al., 2018; Pfeifer et al., 2018; Pinti, Tachtsidis, et al., 2018)
Size/weight	Bulky	Bulky	Lightweight	Bulky	Lightweight	
Portability	No	No	Yes	No	Yes	
Cost	High	High	Low	High	low	
Setup	Room	Room	Small	Room	Small	
Radioactive tracer	Yes	Not usually	No	No	No	(Boly et al., 2015; Bunge & Kahn, 2009)

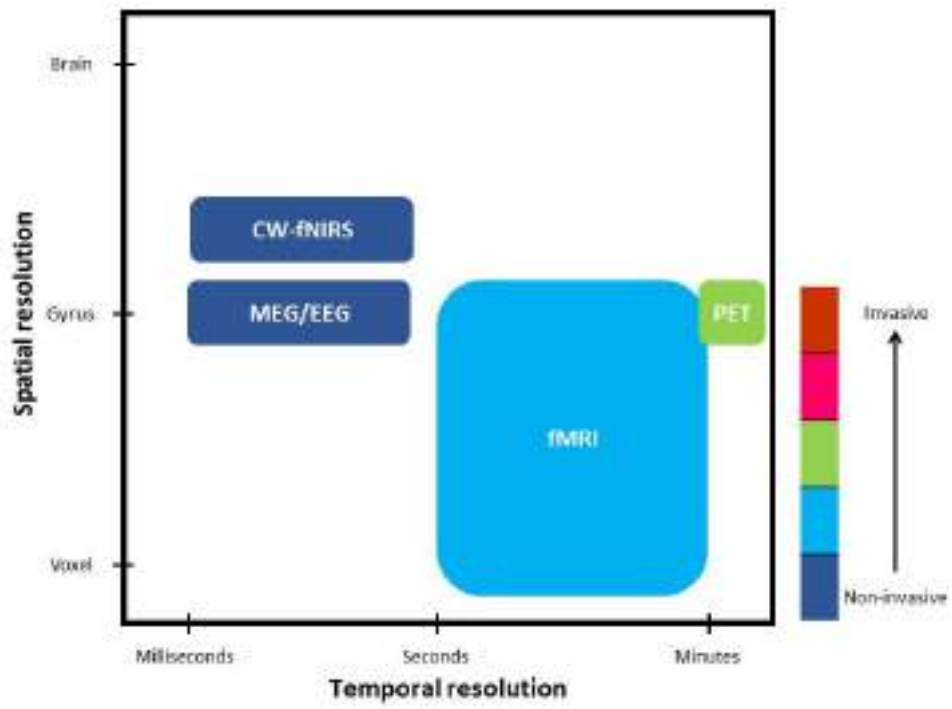


Figure 11. Graphical comparison between the neuroimaging techniques.

1.5 Contamination problem

1.5.1 Sources of contamination

An incorrect assumption is to consider that fNIRS technology only registers changes linked to functional brain activity (Minati et al., 2011). fNIRS signals are the result of various sources as shown in Table 3. These contributors can be classified according to their: (1) compartment (cortical/cerebral versus extracortical/extracerebral) (Figure 12), (2) task involvement (task-related versus non-task related), and (3) drive (neuronal versus systemic) (Scholkmann et al., 2014; Tachtsidis & Scholkmann, 2016). Considering these three variables the classification led to six contributors that are present in any fNIRS signal recorded through the scalp. Unfortunately, the hemodynamic response related to NVC represents only one contributor (Figure 12) while the rest of them represent noise that can mimic or mask the putative cortical signal leading to potential misinterpretations (Tachtsidis & Scholkmann, 2016).

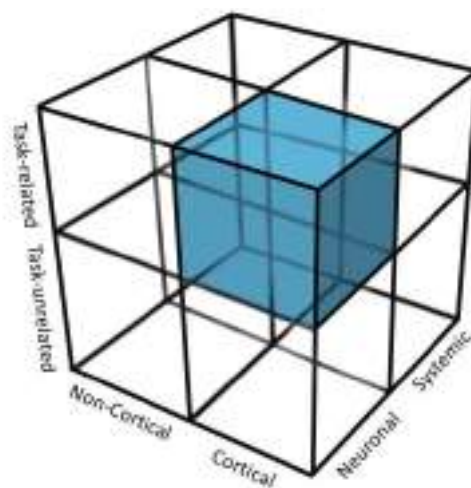


Figure 12. Schematic representation of six contributors that are present in any fNIRS signal recorded through the scalp. The blue cube represents the component of interest in most research in the fNIRS field (Tachtsidis & Scholkmann, 2016).

Table 3. Main contributors of the fNIRs signal
(Scholkmann et al., 2014).

	Task-related		Task-unrelated	
	Neuronal	Systemic	Neuronal	Systemic
Cortical/cerebral compartment	Signal contributor 1: Functional brain activity.	Signal contributor 2: Task-evoked changes in arterial blood pressure, partial pressure of carbon dioxide and heart rate influencing CBF and/or CBV.	Signal contributor 5: Spontaneous brain activity.	Signal contributor 6: Spontaneous oscillations of cortical vessels.
Extracortical/ Extracerebral Compartment (scalp)	Signal contributor 4: Task-evoked activity of the fibres of the autonomic nervous system that innervate the extracortical vessels.	Signal contributor 3: Task-evoked changes in arterial blood pressure, partial pressure of carbon dioxide and heart rate that affects the flow of extracortical vessels.	Signal contributor 8: Spontaneous oscillations of the fibres of the autonomic nervous system that innervate the extracortical vessels.	Signal contributor 7: Spontaneous oscillations of extracortical vessels.

Next, the characteristics of each of the main signal contributors will be reviewed:

Signal contributor 1: Thanks to neurovascular coupling, we can infer task-related regional neuronal activity through neuronal hemodynamic response. It should be considered that typically a task-related hemodynamic response measured by fNIRS is usually small (ΔHbO 0.5-0.7 μM ; ΔHbR \sim 0.2 μM) (Wolf et al., 2002).

Signal contributor 2: cognitive and emotional task can also evoke changes in arterial blood pressure (Jelzow et al., 2011; Minati et al., 2009, 2011; Tachtsidis et al., 2008) , partial

pressure of carbon dioxide and heart rate (Katura et al., 2006) that lead modifications of CBF and CBV.

Signal contributor 3 : The extracortical/extracerebral compartment (skin, subcutaneous tissue, muscle and skull of scalp) show a rich vascularization that is strongly sensitive to task-related systemic fluctuations (Kirilina et al., 2012; Minati et al., 2011; Nishiyasu et al., 1999; Scholkmann et al., 2014; Takahashi et al., 2011; Yücel et al., 2016). In fact, it seems that extracortical vessels are markedly influenced by systemic changes (changes in blood pressure, partial pressure of carbon dioxide and heart rate) since they do not have autoregulation mechanisms like cerebral vessels (Kirilina et al., 2012; Zhang et al., 2002).

Signal contributor 4: Skin forehead has a special autonomic innervation that stands out for its complexity (Matsubayashi et al., 2016; Nolano et al., 2013). In fact, the regulation of flow and volume cutaneous blood depends on at least three mechanisms: 1) vasodilator parasympathetic activity; 2) scarce sympathetic vasoconstrictor tone; 3) sympathetic vasodilator activity (Drummond, 1996; Drummond, 1994; Drummond & Lacnce, 1987). Therefore, these autonomic outflows are responsible for local vasodilation (Takahashi et al., 2011) and vasoconstriction (Haeussinger et al., 2014; Kirilina et al., 2012; Sato et al., 2013) of the forehead vessels during the execution of tasks commonly used in NIRS work. These autonomically mediated changes can lead to misinterpretation of the NIRS signal because changes in skin blood volume and flow are stimulus-locked. Although the literature on this aspect is scarce, probably other tissues of the scalp (such as muscles or the subcutaneous compartment) display autonomic vasomotor activity neurally mediated (Volkening et al., 2016).

Signal contributor 5: Although task-related neuronal activity is usually of primary interest in fNIRS studies (Scholkmann et al., 2014), there are some works that focus on evaluating spontaneous neuronal activity. These types of investigations use fNIRS technology to evaluate resting state connectivity and obtain insight of the functional architecture of brains networks (Hu et al., 2020; Lu et al., 2010).

Signal contributor 6 and 7: There are spontaneous task-unrelated oscillations that affect the hemodynamic of the cortical/cerebral and non-cortical/non-cerebral compartments (Scholkmann et al., 2014). Classically, a series of frequency bands have been differentiated: heart oscillations (≈ 1 Hz), respiratory oscillations (≈ 0.3 Hz), Mayer waves (0.15-0.04 Hz) and very low frequency oscillations related to endothelial vascular function (0.04-0.003 Hz) (Näsi et al., 2011; Obrig et al., 2000; Sassaroli et al., 2012; Scholkmann et al., 2014; Yücel et al., 2016). The physiological origin of each of these systemic and spontaneous oscillations will be briefly

discussed below. Heart oscillation is linked to changes in blood pressure and arterial inflow due to the systole-diastole cycle, which makes it the dominant and ubiquitous fluctuation in comparison with the rest of the systemic oscillations (Fantini, Ruesch, et al., 2018). Another source of measurable systemic spontaneous fluctuations in NIRS signals is the respiration. Respiration leads to modulation of the venous blood volume as follows: Initially during inspiration, the contraction of the diaphragm increases thoracic volume and reduces intrathoracic pressure (to facilitate air entry into the lungs) which increases the volume of peripheral venous return by the vena cava to the right atrium. However, during the expiration phase, the increase in thoracic pressure (to expel air from the lungs) produces a decrease in the amount of venous blood that reaches the right atrium (Fantini, Ruesch, et al., 2018; Kirilina et al., 2013). Therefore, these cyclical changes in thoracic pressure account for the respiration related oscillations of the NIRS signals. Finally, Mayer waves are spontaneous oscillations in blood pressure due to changes in the activity of the autonomic nervous system. Although their origin remains controversial, it is likely that they are induced by the interplay between sympathetic modulation of the heart and sympathetically mediated vasoconstrictor tone (Julien, 2006; Kirilina et al., 2013; Yücel et al., 2016).

Signal contributor 8: the sympathetic and parasympathetic nervous systems are involved in the regulation of blood flow to the skin to maintain and control local temperature as well as blood pressure amplitude in the upright posture (Drummond, 1996, 1997; Kirilina et al., 2012).

1.5.2 Contamination geometry

As we mentioned in previous sections, the photons (sent out by an emitter) going through the scalp to a NIR photodetector follow a banana-shaped path due to the scattering phenomena of the different tissue layers. As can be seen in Figure 13, the emitted photons penetrate all the extracortical layers until they reach the cortex (blue area) and return to transit through said layers to the detector (magenta area). Therefore, a key aspect that must be considered is that the back-reflection geometry imposes double contamination because the extracortical hemodynamic modifies the light as it penetrates and is collected through the scalp (Figure 13) (Gagnon et al., 2012).

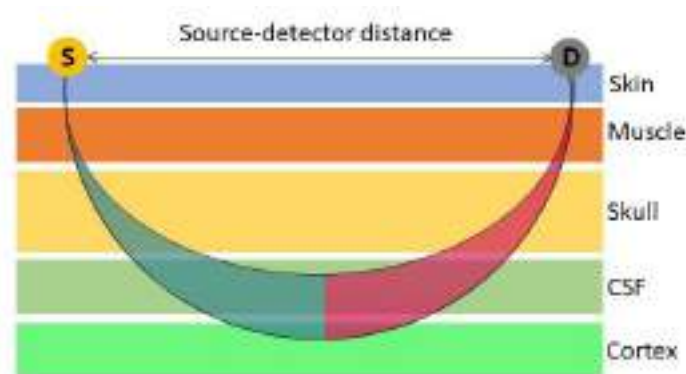


Figure 13. Schematic representation of back-reflection geometry of NIR light through a head. Blue area represents NIR light contamination on the path from source to cortex. Magenta area represents NIR light contamination on the path from the cortex to the detector. S = light source; D = light detector; CSF = cerebrospinal fluid.

1.5.3 How much is the NIRS signal contaminated?

A crucial question is to what extent fNIRS technology is sensitive to extracortical perturbing influence. In general, related investigations have shown that fNIRS displays high sensitivity to hemodynamic changes in extracortical tissues (Al-Rawi et al., 2001; Erdoğan et al., 2014; Haeussinger et al., 2011, 2014; Harris et al., 1994; Kirilina et al., 2012; Miyazawa et al., 2013; Nozawa et al., 2016; Takahashi et al., 2011). Based on the premise that the optodes SDD allows monitoring of hemodynamic activity at different tissue depths, Takahashi et al. (2011) used short-channels (SC) (SDD: 0.5 cm) and long-channels (LC) (SDD: 3.0 cm) to explore extracortical and cortical hemodynamic activity, respectively. Employing this multi-distance approach, it was found that extracortical influence could explain over 90% of the NIRS signal in a verbal fluency experiment. Implementing this same strategy, Nozawa et al. (2016) showed that the temporal correlation of the wavelet transform coherence between a SC (SDD: 1.0 cm) and a LC (SDD: 3.0 cm) averaged 0.5 during a task of cooperative verbal communication. Miyazawa et al., (2013) demonstrated that skin blood flow accounted for 77% of the variance of HbO measured with NIRS during a dynamic exercise task. In addition, Al-Rawi et al. (2001) pointed out that the NIRS technology displayed sensitivities of 87.5% and 13% for changes in flow of the internal and external carotid arteries, respectively, while the specificity values for these same arteries they were 13% and 0%. Using Monte Carlo simulation, Haeussinger et al. (2011) quantified the specific light absorption of the cerebral cortex and of the scalp, skull, and cerebrospinal fluid, determining that fNIRS technology is 20 times more sensitive to the

extracortical compartment than to the cerebral cortex itself. In conclusion, based on the works reviewed in the previous lines, we can conclude that the fNIRS data are clearly dominated by extracortical hemodynamic activity and physiology-based systemic interferences. Therefore, the concern about the presence of contaminants in the NIRS signals is completely justified.

1.5.4 Dealing with contamination

A major challenge in fNIRS research is to reliably disentangle the hemodynamic response due to NVC from other confounding components. To address this particular issue different approaches have been proposed, depending on whether additional instrumentation is available or not.

1.5.4.1 Non-availability of additional instrumentation

When supplementary instrumentation is not accessible other approaches can and should be considered to remove of the physiological noise embedded in the fNIRS signals. Below we will discuss what strategies can be used in these cases:

1) Signal-averaging: this method is based on the idea that cortical activity is task-consistent while extracortical or superficial activity is not, multiple-event averaging was initially proposed to separate functional neural responses from non-cortical confounders (Saager et al., 2011). However, it has been shown that the hemodynamic activity of the non-cortical compartment is stimulus-related (Takahashi et al., 2011), so signal-averaging would accentuate the problem rather than solve it.

2) Frequency-based removal: Band-pass or low-pass filters to suppress high frequency components of systemic interference such as cardiac pulsation (1Hz) and respiration (around 0.2 to 0.3 Hz) (Scholkmann et al., 2014). However, the application of filters is not able to eliminate the noise in low-frequency oscillations (0.04–0.2 Hz, LFO) and very-low-frequency oscillations (0.01–0.04 Hz, VLFO) due to their overlap with the frequency spectrum of the functional neural response (Zhang et al., 2021).

3) Common average reference: This approach is based on re-referencing the signal of the optodes to the inter-optodes common average. In other words, the average value of all signals recorded at each time point is subtracted from each signal at that

time point (Bauernfeind et al., 2014; Raggam et al., 2020). The rationale behind this approach is the assumption that extra-cortical and systemic interference is global and therefore influences all recorded NIRS signals equally (Bauernfeind et al., 2014). However, there is evidence that extra-cortical contamination and systemic interference may not be expressed homogeneously in all NIRS channels (Gagnon et al., 2014; Yücel et al., 2016).

4) Principal component analysis (PCA) and independent component analysis (ICA) are techniques employed to eliminate interference common to all optodes (Tak & Ye, 2014). Although they are useful for separating the mixed components that make up the fNIRS signals, these require additional processing to elucidate which of them are cortical and which are not, which is particularly difficult when extracerebral and cerebral responses are correlated (Zhou et al., 2020).

1.5.4.2 Availability of additional instrumentation

In general, there are two groups of complementary instrumentation, both of which are based on concurrent signal recording: When the co-recorded signal is NIRS, they are called "multidistance measurements" while if the signal has not been acquired using NIRS technology, they are denominated "auxiliary records". Further explanations of these two approaches are provided below:

1) Multi-distance measurements refer to the simultaneous registration of fNIRS signals at various tissue depths, by using different distances between light emitters (source) and photodetectors (detector) in the channel arrangement of the fNIRS probe. Since SDD determines the light penetration in tissues, the assumption is that: (i) SCs (SDD: 5-15 mm) are sensitive only to shallow hemodynamic changes, while (ii) LCs (SDD: 24-40 mm) are sensitive to both shallow and deep activity (Brigadoi and Cooper, 2015). In other words, the short signal (SS) recorded by SC only contains information on the superficial layers (skin, muscle, skull) while the deep signal (DS) measured by LC is a mixture of absorption in the superficial and cortical tissues (Figure 14). Therefore, by using the short-channels' signal as a reference, it is possible to disentangle the actual neuronal signal from the extra-cortical interference (Gagnon et al., 2011; Saager & Berger, 2008; Nozawa, Sasaki, Sakaki, Yokoyama, & Kawashima, 2016).

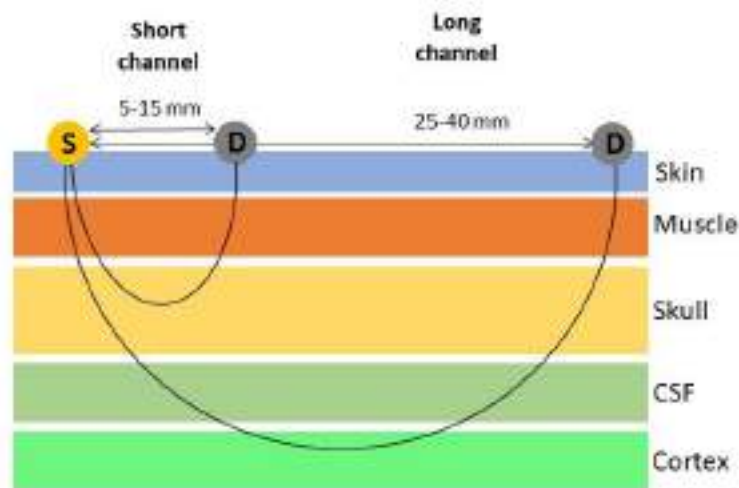


Figure 14. Schematic representation of multi-distance measurements. The black line represents the "banana shape" of the photon path in the short and long channel. S = light source; D = light detector; CSF = cerebrospinal fluid.

Currently, multi-distance measurements are considered a gold standard and commonly accepted as highly effective and accurate approach in treating neuronal hemodynamic response from unwanted sources (Zhou et al., 2020). A relevant issue about this technique is related to the number of optimal SCs. In this regard, previous studies have shown that the scalp is affected by systemic and/or superficial contamination in a spatially heterogeneous way (Erdoğan et al., 2014; Gagnon et al., 2012; Kohno & Hoshi, 2016; Sato et al., 2013; Yücel et al., 2016; Zimeo Morais et al., 2017). In addition, it appears that NIRS recordings made through the forehead show a special propensity to be dominated by contamination (Haeussinger et al., 2014; Takahashi et al., 2011; Zarei et al., 2019), which is a serious problem since the prefrontal cortex is one of the most measured regions. Nowadays, it is assumed that the ideal multi-distance configuration would be to have two SS recorded for each LC. Unfortunately, commercial NIRS devices do not usually have multi-distance measurement, which strongly limits the conclusions of most NIRS investigations (Haeussinger et al., 2014). For all these reasons, fNIRS-systems that incorporate dense arrays with multi-distance measurements into their commercial design could be extremely valuable and eagerly awaited.

2) The auxiliary registers are a set of strategies based on co-registration of fNIRS with an additional non-fNIRS signals (Table 4). Incorporation of auxiliary signals makes it possible to determine which changes in NIRS signals are a result of contamination. Note that not all auxiliary records quantify the same contamination components, for

example measurement of blood pressure signals, respiration rate/amplitude, partial pressure of carbon dioxide, heart rate are useful in managing systemic interference, while recording of skin blood flow assesses the local hemodynamic activity of the most superficial tissue extracerebral compartment (Table 4).

At first glance it may seem that multi-distance recordings are interchangeable with skin laser doppler flowmetry, however several aspects must be considered: first, laser doppler reflects blood volume changes from up to 1 mm deep (Kohno et al., 2007; Takahashi et al., 2011) while a SC (14 mm SDD) detects hemodynamic activity at a depth of 7 mm. This fact is especially relevant considering that LC is contaminated by all the layers of the scalp and not only by the skin. Second, several SCs can be incorporated into the NIRS probe design however the laser doppler must be couple to the participant's scalp producing experimental constraints. Finally, SC provides information on HbO and HbR of the superficial tissues, which allows a good control of the contamination of both chromophores, while the Doppler laser only measures changes in arterial blood flow.

Table 4. Auxiliary registers and their instrumentation

Variable	Instrumentation	Contamination components	Reference
Blood pressure	Continuously and non-invasively measure mean blood pressure	Systemic	(Kirilina et al., 2012; Patel et al., 2011; Tachtsidis et al., 2010)
Respiratory rate and amplitude	Thoracic respiratory belt	Systemic	(Kirilina et al., 2012; Kirilina et al., 2013b)
Partial pressure of carbon dioxide in the arterial blood	Nostril carbon dioxide sensor	Systemic	(Scholkmann et al., 2013; Scholkmann et al., 2013)
Heart rate	Electrocardiogram	Systemic	(Kirilina et al., 2012; Kirilina et al., 2013b; Patel et al., 2011; Tachtsidis et al., 2010)
Skin blood flow	Laser Doppler flowmetry	Extracortical	(Kirilina et al., 2013; Patel et al., 2011; Tachtsidis et al., 2010; Takahashi et al., 2011)

Regardless of the type of instrumentation used, it is always necessary to apply a strategy or mathematical algorithm to separate the neuronal functional response from contamination. In fact, consider that each mathematical method that we will expose can be combined indistinctly with multi-distance measurements or auxiliary registers. In the following we will discuss the different mathematical approaches describing in more detail the linear regression model combined with multi-distance measurements because it is the most applied. In addition, we present a last type of model called transfer function that, although it has been scarcely applied, can be especially useful for the control of surface interference.

1) ICA and PCA are blind source separation techniques frequently used in the NIRS context to recover the functional cortical signal from the noisy mixed signals, assuming statistical independence or orthogonalization between these components, respectively (Table 5). The auxiliary registers or multi-distance measurements can be used to identify which components represent surface and/or systemic contamination for subsequent subtraction (Kohno et al., 2007; Zhang et al., 2005).

2) GLM (general lineal model): The auxiliary register/multi-distance measurement are applied to estimate the global systemic or scalp response that can be incorporated as additional regressors into the GLM to remove undesirable contamination (Gagnon et al., 2011; Sato et al., 2016) (Table 5).

3) Adaptative filtering: Model iteratively or in real time the relationship between the auxiliary record or multi-distance measurement and the NIRS signal to reduce systemic and superficial noises of fNIRS data (Zhang et al., 2009) (Table 5). The coefficients of the adaptive filters vary adapting during their implementation readjusting in each iteration in their learning phase (Nguyen et al., 2018).

4) State-space modelling: this type of recursive methods allows to identify the non-measurable state of a dynamic system that links cortical and extracortical compartments (Table 5). The state-based approach enables accurate identification and feasible elimination of contamination noise embedded in the NIRS signal through two successive steps. In the first step, it uses the prior knowledge of a state to generate a prediction of the possible future state and the associated uncertainty. In the second step, this prediction is modified to update the true state, that is, the estimate is optimized through feedback (Cooper et al., 2012).

5) Linnear regression. Assuming that the DS collected in the LC is sensitive to both extra-cortical and cortical compartment and that the SS measured by the SC is

exclusively sensitive to superficial tissues, we can perform a regression to estimate the cortical signal (Figure 15). The residual (variance of DS not explained by SS) obtained through the regression represents in fact the putative cortical activity (Table 5).

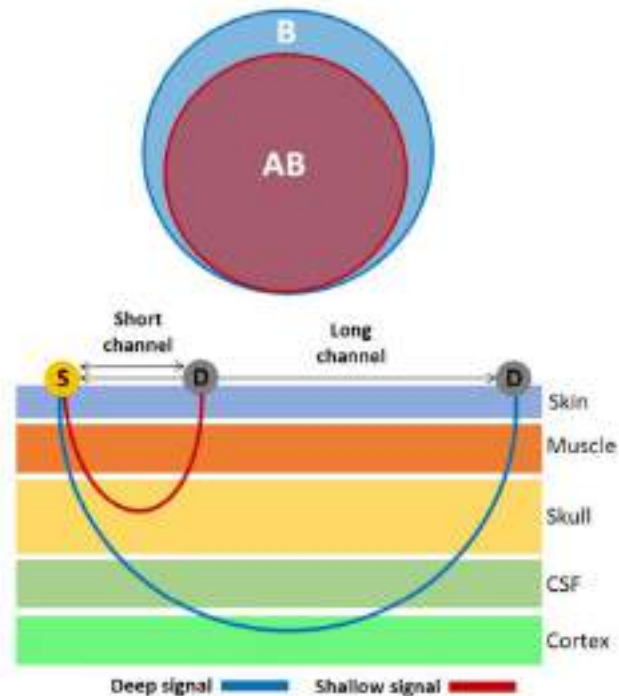


Figure 15. Schematic representation of regression based on multi-distance measurements. In the lower part, the multi-distance measurements are represented (S = light source; D = light detector; CSF = cerebrospinal fluid). The red and blue lines represent SS and DS, respectively. Ven's diagram between DS and SS is displayed at the top. The DS recorded by LC is a mixture of the absorptions in the superficial tissues (skin, muscle, skull) and the cortical ones (AB area). The SS from LS regression allows estimation of cortical activity using the residuals (B area).

6) Transfer function (TF): The extracortical and cortical responses are the result of a coordinated effect produced by different interrelated processes (Caldwell et al., 2016; Tachtsidis & Scholkmann, 2016). Rather than viewing surface fluctuations only as annoying confounders that must be removed, we regard them as carriers of valuable information. Based on this premise, we consider that transfer function models could be useful to assess the timed-coordination between these two systems. A TF describes the dynamic relationship between the output signal of a system and the input signal. Considering SS as input and DS as output, we could use TF to estimate different parameters of how changes in the extracortical compartment affect LC recordings (Table 5). TF models have become a popular approach to investigate the dynamic of

cerebrovascular autoregulation (Jurgen Ahr Claassen et al., 2015; Van Beek, Claassen, Rikkert, & Jansen, 2008), and they have also been used to remove systemic physiological noise from fNIRS signals (Bauernfeind, Böck, Wriessnegger, & Müller-Putz, 2013; Florian & Pfurtscheller, 1997). However, to our knowledge, such an approach has never been previously tested in fNIRS studies with the aim of eliminating the extracortical contamination.

Table 5. Different mathematical approaches and their applications with multi-distance and auxiliary registers.

Mathematical approach	Application examples with multi-distance measurements	Application examples with auxiliary registers
ICA/PCA	(Zhang et al., 2005)	(Kohno et al., 2007; Patel et al., 2011)
GLM	(Gagnon et al., 2011; Sato et al., 2016)	(Tachtsidis et al., 2010)
Adaptative filtering:	(Nguyen et al., 2018; Zhang et al., 2009)	(Morren et al., 2004)
State-space modelling	(Diamond et al., 2006)	(Diamond et al., 2006; Kolehmainen et al., 2003)
Linnear regression	–	(Gratton & Corballis, 1995)
TF	–	(Bauernfeind et al., 2013; Florian & Pfurtscheller, 1997)

1.6 Functional neuronal hemodynamic response elicitation and detection

1.6.1 Stimulation paradigms

Any functional neuroimaging experiment is based on the manipulation or intervention of brain activity through a stimulation paradigm and on the observation of the response that results from this provocation (Amaro & Barker, 2006). Stimulation paradigm makes explicit reference to the temporal organization structure of stimuli during a given experiment. In fNIRS field, 3 different types of stimulation paradigms have been described (summarized in Figure 16) which are inherited from fMRI and PET research.

1) Block-related design is typically composed of a task period and a control period (Figure 16). Both conditions alternate during the experiment as many times as required. During the task period, stimuli of the same category are continuously presented to generate sustained hemodynamic signal associated with the long periods of stimulation (typically between 5 and 30 seconds) (Issard & Gervain, 2018). However, during the control period, the absence of stimulation causes the hemodynamic signal to return to baseline. The different categories of stimuli grouped in blocks (e.g. visual or auditory) are interspersed with control period (Figure 16) (Schaeffer et al., 2014). Therefore, this type of method leads to a sustained hemodynamic response, providing information about cortical areas related to the task (Amaro & Barker, 2006; Donaldson, 2004). Block-related design is frequently used due to their advantages: improves signal-to-noise ratio (Herold et al., 2018), provide robust results (Amaro & Barker, 2006; Miezin et al., 2000), allows signals to revert to their baseline levels during control period before the start of the next stimulation block (Schaeffer et al., 2014), increases statistical power (Amaro & Barker, 2006; Miezin et al., 2000), produce large hemodynamic changes, (Glover, 1999) and it is brief (Amaro and Baker, 2006; Lloyd-Fox, Blasi and Elwell, 2010), which is especially important when working with clinical populations. However, some disadvantages must be considered: Block-related design cannot differentiate between the different types of stimuli within a block (Petersen & Dubis, 2012) and their results may be influenced by anticipation and habituation processes (Orihuela-Espina et al., 2010). In addition, if biphasic hemodynamic responses are given in the same block, they can be cancelled when the block is averaged (Meltzer et al., 2008).

A noteworthy advantage of block-designs is the fact that they can be used to induce hemodynamic oscillations in both cortical and extracortical NIRS signals. In previous studies, a number of protocols have been used to generate hemodynamic oscillations at particular frequencies to investigate cerebrovascular regulation, including cuff inflation-deflation (Aaslid et al., 2007; Kainerstorfer et al., 2014), head-up tilting (Hughson et al., 2001), squat-stand exercises (Claassen et al., 2009), paced breathing (Pierro et al., 2014), and even in visual and motor studies (Obrig et al., 2000; Schroeter, Bücheler, et al., 2004; Wolf et al., 2002). This type of approach could be useful for investigating the coupling between hemodynamic changes arising from the superficial and deep layers during a task and isolating the task-evoked cortical response from other confounders. The rationale behind is the assumption that extracerebral and cerebral responses are the result of a coordinated effect product of different interrelated processes. However, to our knowledge, a cognitive task has never been used for the deliberate generation of oscillations at a specific frequency, which is surprising since this would make it possible to apply well-established frequency-domain methods.

2) Event-related design. This paradigm category is based on the presentation of a single stimulus followed by a period of non-stimulation (Figure 16). Different types of stimuli are presented randomly and sometimes the interval between them varies, facilitating the maintenance of attention throughout the experiment (Amaro & Barker, 2006). The choice of the duration of the intervals between stimuli is critical since they must be long enough to prevent overlapping of the hemodynamic response, which takes between 10 and 12 seconds to return to baseline after the stimulus cessation (Plichta et al., 2007). It is intended to detect a transient hemodynamic response, making possible the temporal characterization of changes associated with events (Amaro & Barker, 2006; Donaldson, 2004), which is especially important to take advantage of the good temporal resolution of NIRS. Although this type of stimulation scheme is time consuming, it provides experimental flexibility, high ecological validity (Schaeffer et al., 2014) and allows us to link in each trial event the cortical hemodynamic with behavioural responses (errors, successes, or emotional subjective rating) (Amaro & Barker, 2006).

3) Mixed designs are comprised of an interesting combination of blocked and event-related methods, distinguishing between sustained and transient hemodynamic responses (Figure 16). Although they provide an ideal way to characterize cortical areas in functional terms (task or item-related), these designs require more assumptions than

the others and produce a haemodynamic response with a poorly defined shape (Amaro & Barker, 2006; Donaldson, 2004).

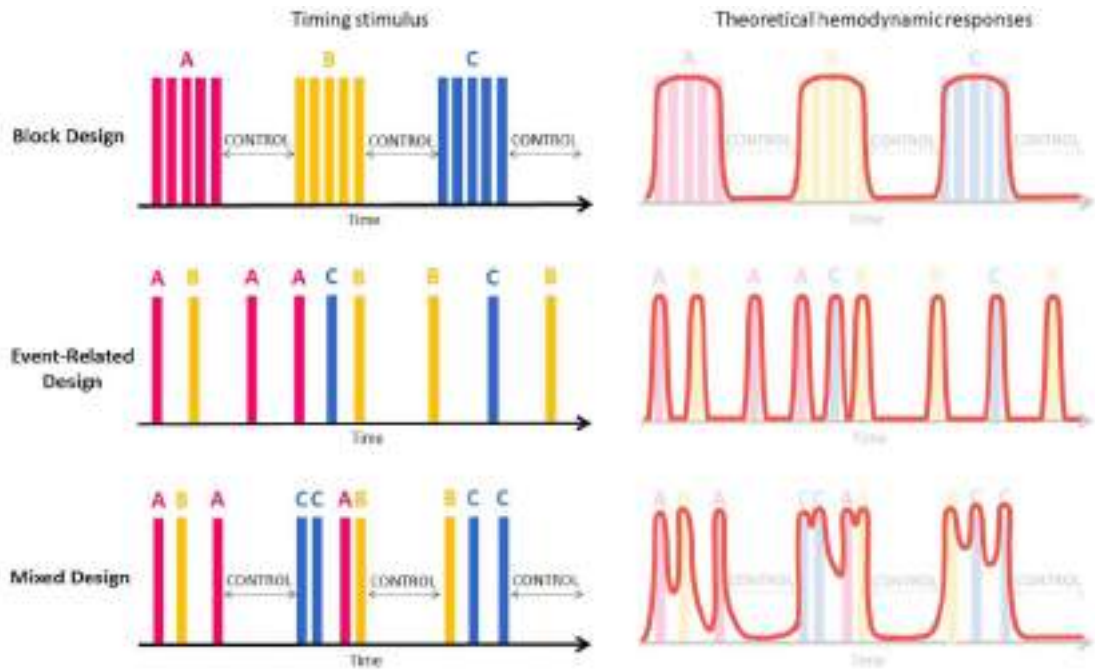


Figure 16. Stimulation paradigms in functional neuroimaging and their theoretical hemodynamic responses. The coloured rectangles identified with letters represent the different categories of stimuli along the types of designs. The red line displays the theoretical hemodynamic HbO response for each type of design.

1.7 Theia fNIRS device

As stated in the title of the thesis, this work is oriented towards the design and validation of a fNIRS system to assess functional activity of the prefrontal cortex. The registered trade name of this fNIRS system is Theia. Consequently, from now on we will refer to the fNIRS device as Theia, which is the subject of this thesis. Theia is a continuous-wave fNIRS device developed by Newmanbrain company for recording the frontopolar area of the prefrontal cortex (PFC). This instrument has been designed with the aim of fulfilling the cutting-edge fNIRS system standard in the context of cognitive neuroscience (Choi et al., 2016; Pinti, Aichelburg, et al., 2018; von Lühmann et al., 2015; Wyser et al., 2017; Wyser et al., 2022; Yaqub et al., 2020; Zhao & Cooper, 2017). Next, we will develop the main aspects of this new instrument:

1) Usability. The flexible probe was specially designed to ensure comfort by adapting to the curvature of the forehead which is crucial for clinical applications and to maintain ecological validity. In addition, the device is held by a comfortable system adjustable to the size of each head, ensuring the accurate optodes placement (Figure 17).

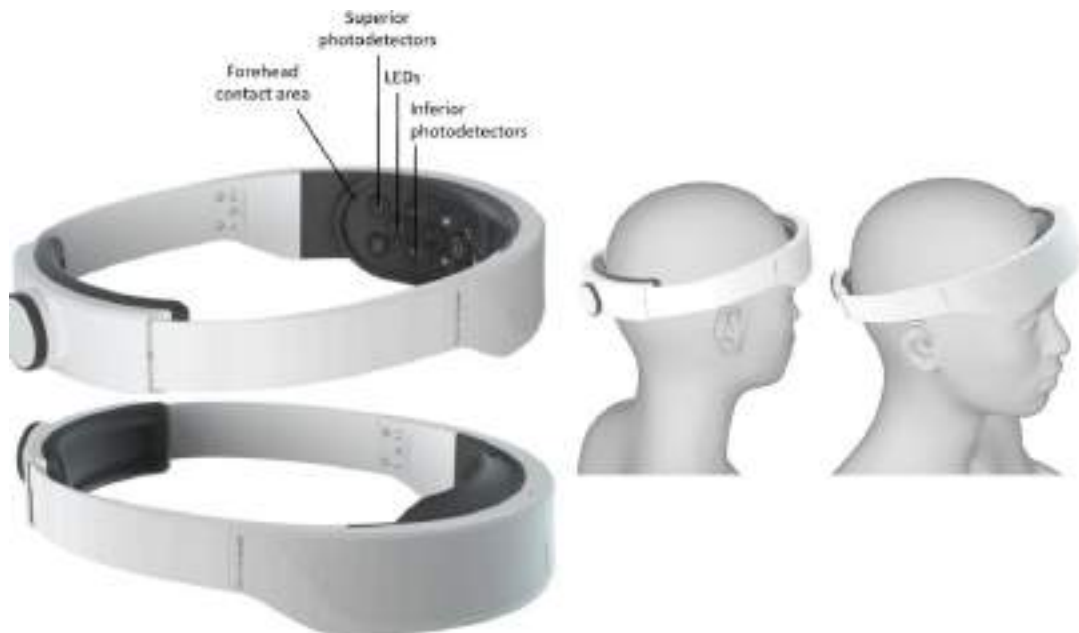


Figure 17. Structure of the Theia device and its placement on the forehead of a participant.

2) Miniaturization. Theia is light-weight and compact allowing the subject to move relatively freely within a normal environment (Table 6).

3) Wireless. This device transmits results in real time to a computer via Bluetooth connection and is battery powered ensuring its portability (Table 6).

4) Safety. Theia is equipped with dual LED light sources that emit harmless light intensities not posing any risk of injury to the skin. Furthermore, this instrument is battery powered so the risk of electrocution is minimal. Finally, the fNIRS device shows multiple layers of safety in both the hardware and firmware design, eliminating the risk of electrical failure.

5) High resolution fNIRS data since Theia displays a sampling rate frequency of 10 Hz (Table 6), which ensures adequate resolution of the signal NIRS signal time courses (whose usual range is 0.1-1.2 Hz) (Wyser et al., 2017)

6) Management of extracortical contamination. Theia is equipped with multi-distance measurement facilitating the elimination of the confounding effect of extracortical contamination. In addition, thanks to a dense array of SC, Theia can cope with heterogeneous extracortical contamination, which is especially important in recordings through the forehead.

7) Accelerometers in three axes for the motion artifacts management.

8) High autonomy. Due to its low energy consumption this device can record hemodynamic activity for 6 hours on a single battery charge without interruption (Table 6).

Table 6. Summary of technical specifications Theia devices.

Parameter	Value
Weight	168 gram
Size	265 x 185x 55 mm
Light sources	LED
Wavelengths	735 and 850 nm
Photodetectors	Photodiodes
Channels	28 (16 short and 12 deep channels)
Source-detector separations	Short channel: 14 mm Long channel: 32 mm
Accelerometer	3 axis
Sampling rate	10 Hz
Communication	Wireless with PC via Bluetooth
Power supplies	AC (Alternating Current) voltage and current: 240 V and 0.5 A Mains frequency: 50/60 Hz DC (Direct Current) voltage and current: 5 V and 1 A
Battery	LiPo 3,7 V, 730 mAh; 6 hours of autonomy

1.8 Frontopolar cortex

The Theia fNIRS device is specially designed to measure the most caudal region of the PFC. For this reason, we will briefly discuss its anatomical relationships, cytoarchitectural characteristics, and its implication in cognitive functioning.

1.8.1 Characteristics

The PFC covers the anterior part of the frontal lobes, extending from the premotor cortex to the frontal pole. Because it is a very large and heterogeneous area (the PFC represents about 30% of the total cortical area), various subdivisions have been functionally differentiated, including the dorsomedial, dorsolateral, ventrolateral, ventromedial, orbitofrontal and anterior cingulate cortices (Carlén, 2017). It has been 20 years since the most anterior part of the frontal lobe, often referred to as the frontopolar cortex (FPC), was recognized as a different part from the dorsolateral PFC in anatomical and functional terms (Kroger & Kim, 2022). The FPC is located in anterior area of the frontal pole, extending in a rostro-caudal axis across the medial, orbital, and lateral surfaces (Figure 18). Currently there is no consensus regarding the name of this region, in fact, in the literature there are various terms that have been used interchangeably (anterior PFC, rostral PFC, etc.), however here we opted to FPC denomination (Burgess et al., 2013; Christoff & Gabrieli, 2000).

Leaving nomenclature aside, the truth is that FPC has some characteristics that make it peculiar compared to other cortical areas: 1) both in relative and absolute terms FPC is larger in humans than in any other animal (Burgess et al., 2013; Ramnani & Owen, 2004). 2) It shows a great cytoarchitectonic complexity which allows it to be subdivided into three regions in a rostro-caudal sense (polar, rostral, and medial) (Öngür et al., 2003) with different functional specializations. 3) It has a low density of cell bodies but a high density of dendritic spines (Bludau et al., 2014). 4) Ontogenetically displays a particularly protracted course of maturation and development that extends into early adulthood (Burgess et al., 2013; Dumontheil et al., 2008).

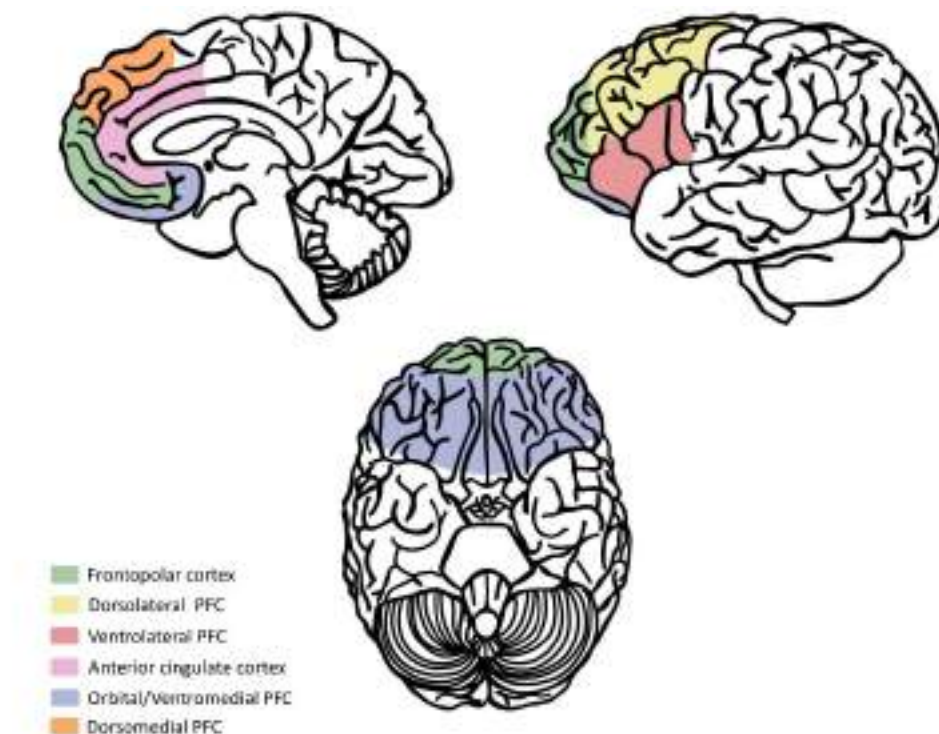


Figure 18. Major subdivisions of the human prefrontal cortex (Raccah, Block, and Fox, 2021).

1.8.2 Connectivity:

FPC shows a large number of intracortical reciprocal connections with other supramodal association cortices such as orbital, medial, and lateral PFC, temporal cortex (especially with the parahippocampal region, dorsal temporal pole, superior temporal gyrus association cortex), thalamus (mediodorsal, anterior ventral and intralaminar) and auditory cortex, cingulate cortex, insular cortex (Burgess et al., 2013; Dumontheil et al., 2008; Kroger & Kim, 2022; Öngür et al., 2003; Peng et al., 2018).

1.8.3 Functional specialization

The functional characterization of FPC is a topic issue in current cognitive neuroscience. It appears that FPC is involved in multiple simple and complex cognitive tasks as well as the regulation of higher-order complex behaviour (Boschin et al., 2015; Burgess et al., 2013; Christoff & Gabrieli, 2000; Dumontheil et al., 2008; Kroger & Kim, 2022; Peng et al., 2018;

Ramnani & Owen, 2004). Below we will briefly discuss some of the functional specializations currently associated with the FPC.

-Multitasking: It can be defined as the ability to sequence the performance of several tasks over time, that is, alternating one with another. In other words, multitasking refers to stopping the execution of a task to perform a new one, but with the intention of returning to the initial task (Burgess et al., 2013; Burgess et al., 2000; Koechlin & Hyafil, 2007). Most of our day-to-day activities involve multitasking to some extent, especially in the work environment. For example, while you are preparing a text document, one of your students appears. Then you must pause the initial task (preparing the text document) to resolve the student's doubts. When the student has left then you can return to the initial task of writing the text document. Multitasking was probably the first recognized functional specialization of FPC, when it was discovered that patients with lesions in the rostral area of the PFC presented impairment in sequencing and alternating various tasks (Burgess et al., 2000). Finally, note that multitasking is not synonymous with "multiple-task performance" since in the latter two tasks are executed at the same time (in parallel), while in the context of multitasking the tasks are always carried out sequentially (Burgess et al., 2013; Burgess et al., 2000).

-Prospective memory: It is referring to the intention to carry out an action in the future, allowing a planned act to be carried out after a certain delay (for example: at 12 noon I have to send an email). A multitude of neuroimaging works have shown a consistent association between FPC activity regardless of task type and difficulty and recall stimuli (Burgess et al., 2013; Ramnani & Owen, 2004).

-Exploration of different alternatives: The FPC activity seems to be related to the evaluation of different alternatives or behavioural options to determine which is the most appropriate in a decision-making context (Burgess et al., 2013; Koechlin & Hyafil, 2007)

-Episodic memory retrieval: The FPC is activated when we try to determine whether or not we know a previously presented stimulus. (Koechlin & Hyafil, 2007).

- Relational reasoning: The FPC seems to be involved in relational reasoning which can be defined as the ability to make general inferences from specific situations. In other words, we use a familiar situation as a source to obtain inferences that can be transported to a less familiar situation, obtaining an abstract scheme that incorporates information about both situations (Burgess et al., 2013; Koechlin & Hyafil, 2007).

-Cognitive branching: It can be defined as a process that requires coordination of cognitive operations associated with sub-goals while holding in mind a main objective for whose achievement it is necessary to combine the result of these intermediate cognitive operations with the active information of the working memory (Burgess et al., 2013; Koechlin et al., 1999; Ramnani & Owen, 2004; Walsh et al., 2009). An example of a task that involves cognitive branching could be iteratively subtracting 20 from 120. To execute this task, the result of the first operation is calculated ($120-20=100$), then the result of this subtraction must be kept in memory in a pending state while the calculations of the second subtraction ($100-20$) are performed. Therefore, in this simple arithmetic task it is necessary to coordinate each of the iterative subtractions (sub-goals), while holding the result of the previous operation in working memory and then combining both to obtain the final result (main goal). There is ample evidence that FPC has a functional specialization closely related to cognitive branching regardless of the paradigm used (Burgess et al., 2013; Koechlin et al., 1999; Ramnani & Owen, 2004; Walsh et al., 2009).

Ultimately it seems that FPC is engaged in tasks that are composed of more than one discrete cognitive process in which the execution of an isolated cognitive operation is not enough to solve the problem, requiring the integration of results from two or more operations to fulfill the higher goal (Ramnani & Owen, 2004). In fact, if we consider the common aspects in the processing of information through these cognitive functions previously reviewed, they all have in common the participation of integration processes. For example, multitasking or different alternatives exploration request cognitive branching participation insofar as it is necessary to explore the different "branches" (switching back and forth between alternatives tasks and options) keeping the other pending. In addition, branching is involved in prospective memory and information retrieval tasks, since it is required to keep information from the past or the future active to be compared with present information. Finally, relational reasoning requires linking new information with pre-existing knowledge, generating a complex relationship that emerges as a result of the integration of results from multiple inferential processes. It is speculated that FPC is responsible for these coordination and integration processes. In fact, this view is consistent with the aforementioned cytoarchitectural and connectivity features of FPC (Burgess et al., 2013; Ramnani & Owen, 2004).

1.9 Forehead

As we have previously commented, the superficial tissues of the forehead strongly contaminate the NIRS signals in comparison with other regions of the scalp (Haeussinger et al., 2014; Takahashi et al., 2011; Zarei et al., 2019). In addition, this interference displays different local characteristics, that is, it is spatially inhomogeneous (Erdoğan et al., 2014; Gagnon et al., 2012; Kohno & Hoshi, 2016; Sato et al., 2013; Yücel et al., 2016; Zimeo Morais et al., 2017). We consider that these facts could be explained by the anatomy as well as the unusual innervation and vascularization that the forehead exhibits, which we will review below.

1.9.1 Characteristics

The forehead is a multi-layered structure that includes (from superficial to deep) skin, subcutaneous tissue, superficial musculoaponeurotic layer, frontalis muscle, areolar connective tissue, periosteum, and frontal bone.

The skin on the forehead is thicker compared to the skin on the rest of the face and is made up of three well-differentiated layers: epidermis, dermis, and hypodermis (Cafardi, 2012; Garritano & Quatela, 2018). The epidermis, made up mainly of keratinocytes, is the most superficial layer. Below, we find the dermis, which is 20 to 30 times thicker than the epidermis and is comprised of fibroblasts and blood vessels that provide support and nutrients to the most superficial layer (Cafardi, 2012). The deepest layer, called the hypodermis, is integrated of subcutaneous adipose tissue and some neurovascular plexuses, which give it the ability to provide thermal insulation and protection against trauma (Cafardi, 2012).

The forehead muscles are covered by a layer of connective tissue that protects and supports blood vessels and nerves called the subcutaneous fascia, which is thinner on the forehead compared to the rest of the scalp (Abramo, 1995; Cafardi, 2012; Garritano & Quatela, 2018; Skaria, 2015; Tan et al., 2011; Wieder & Moy, 1998).

All the muscles of the forehead have in common that they are located superficially and are deeply inserted into the skin where their activity is demonstrated (Abramo, 1995). In fact, since the superficial tissues are strongly adhered to the muscular aponeurosis, their voluntary contractions induce movements in the skin that allow us to express emotions. Although there are several muscle groups related to the forehead, we are going to discuss exclusively the occipitofrontalis because it is the only one that would affect the NIRS measurements made with Theia (Abramo, 1995; Garritano & Quatela, 2018; Tan et al., 2011; Wieder & Moy, 1998).

The occipitofrontalis muscle is made up of two thin muscle bellies (occipital and frontal) that are unified by an intermediate fibrous portion called galea aponeurotica (Abramo, 1995; Garritano & Quatela, 2018; Tan et al., 2011; Wieder & Moy, 1998). This fibrous muscular sheet covers the skull from the supraorbital ridges to the superior nuchal line. Only the frontal belly is of our interest since it is located immediately anterior to the frontal bone of the forehead (Figure 19) (Garritano & Quatela, 2018). The usual frontal belly contraction serves to raise the eyebrows and wrinkle the forehead in a transverse direction (Abramo, 1995; Garritano & Quatela, 2018; Tan et al., 2011; Wieder & Moy, 1998).

The frontal bone consists of a vertical portion that participates in the creation of the roof of the orbit and a horizontal portion that forms the forehead (Figure 19). The innermost face of the horizontal portion is in direct contact with the dura mater while the outer part is in contact with the orbitofrontal muscle. Around the midline there are two asymmetric air-filled cavities called frontal sinuses (Figure 19 and 20). In an anteroposterior axis, the frontal sinuses are located between the external and internal faces of the frontal bone (Figure 19) (McLaughlin et al., 2001; Pondé et al., 2003; Strong, 2009).

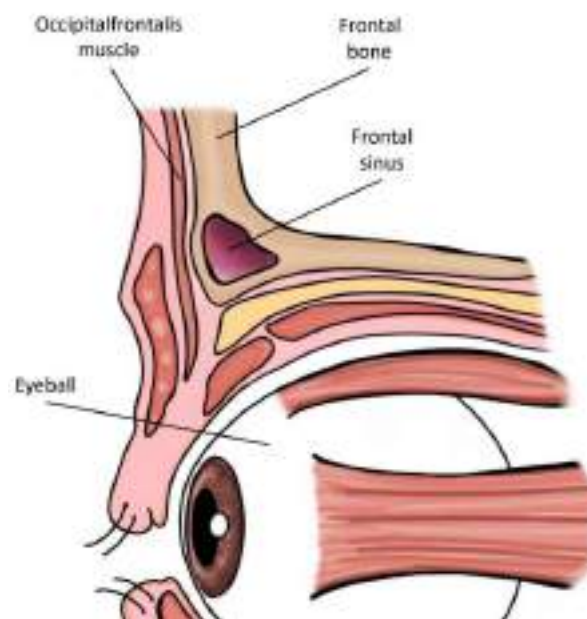


Figure 19. Sagittal section of the forehead(Drake et al., 2020; Gilroy et al., 2013).

Frontal sinus morphology varies considerably between individuals but there are average size values that help us get an idea of its dimensions: 24.3 mm high, 29.0 mm wide and 20.5 mm deep (Holmgaard et al., 2016; Kanat et al., 2015; Kurihara et al., 2012; McLaughlin et al., 2001; Pondé et al., 2003; Strong, 2009). Because they are filled with air it has been suggested that the

frontal sinuses may profoundly impact the optical properties of the NIR-light (Haeussinger et al., 2011; Kurihara et al., 2012).

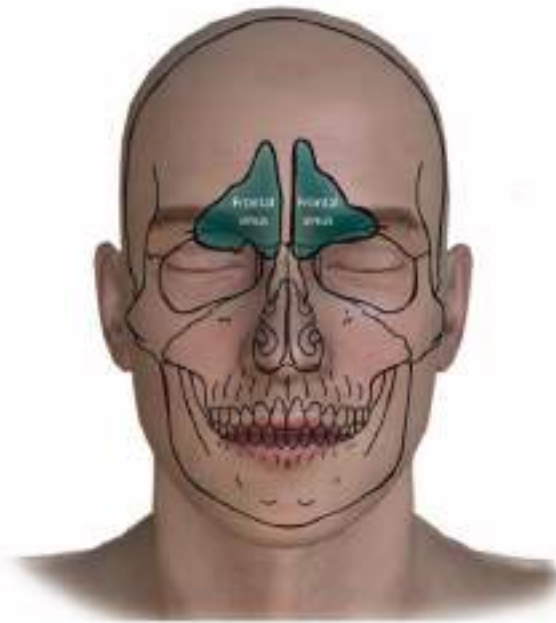


Figure 20. Frontal sinus

(Drake et al., 2020; Gilroy et al., 2013; McLaughlin et al., 2001; Pondé et al., 2003; Strong, 2009).

1.9.2 Vascularization

1.9.2.1 Arteries

There are at least 5 arteries that supply oxygen and nutrients to the forehead tissues (supraorbital artery, supratrochlear artery, frontal branch of the superficial temporal artery, central artery, and paracentral artery). All of them have certain characteristics in common that must be taken into account for a better understanding of the fNIRS records: (1) Most of the arteries show a diameter of less than 1 mm (Kleintjes, 2007), which makes them susceptible to being recorded by NIRS technology (since the volume of blood they contain is not enough to completely absorb light). (2) It is common for these arteries to establish arterio-arterial anastomoses creating a rich vascular arcade (Kelly et al., 2008; Kleintjes, 2007), which could explain the special intensity of surface contamination in fNIRS recordings through the forehead (Haeussinger et al., 2014; Takahashi et al., 2011; Zarei et al., 2019). (3) The supratrochlear and supraorbital arteries are terminal vessels of the ophthalmic branch of the frontopolar artery which supplies the brain (Figure 21). (4) Lastly, the forehead area seems to show arterio-venous anastomoses which are low-resistance connection between arteries and veins that shunt blood

from the arterial territory to the veins (Bergersen, 1993). Taken together, these considerations could explain the lack of homogeneity shown by surface NIRS contamination on the forehead (Erdoğan et al., 2014; Gagnon et al., 2012; Kohno & Hoshi, 2016; Sato et al., 2013b; Yücel et al., 2016; Zimeo Morais et al., 2017). Next, we discuss the origin and trajectory of the main arteries of the forehead:

1) The supraorbital artery originates as a terminal branch of the ophthalmic artery in the interior of the skull (Figure 21). It then exits the skull at the supraorbital rim where it runs medially until it divides into three branches (medial, oblique, and vertical) that anastomose with the frontal branch of the superficial temporal artery and with the supratrochlear artery (Figure 22)(Abramo, 1995; Carruthers & Carruthers, 2018; Erdogmus & Govsa, 2007; Garritano & Quatela, 2018; Kleintjes, 2007).

2) The supratrochlear artery originates as a terminal branch of the ophthalmic artery inside the skull where it runs posterior to the trochlea of the oblique muscle (Figure 21). It then crosses the orbital septum along with the trochlear nerve in the superior and medial area of the orbit to later anastomose with the supraorbital artery (Figure 22)(Abramo, 1995; Agorgianitis et al., 2020; Carruthers & Carruthers, 2018; Garritano & Quatela, 2018; Kelly et al., 2008; Khan et al., 2017; Kleintjes, 2007; Koziej et al., 2019; Skaria, 2015; Tan et al., 2011).

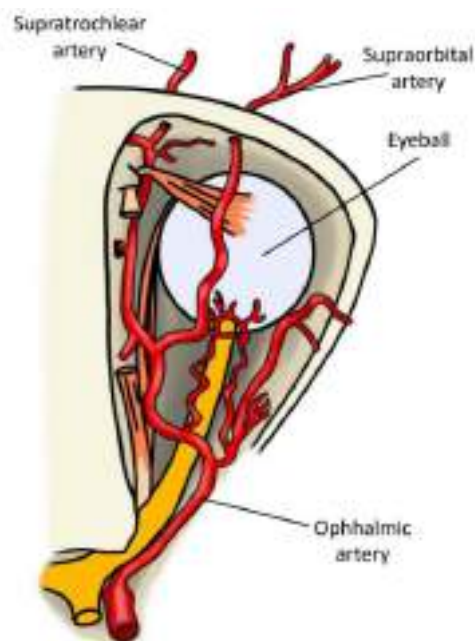


Figure 21. Ophthalmic artery and its main branches involved in the vascularization of the forehead (Drake et al., 2020; Gilroy et al., 2013).

3) The frontal branch of the superficial temporal artery divides into two near the lateral orbital rim, giving rise to an ascending branch (supplying the scalp) and a transverse branch (supplying the forehead). The transverse frontal artery is superficial to the frontalis muscle and as it progresses towards the medial zone it becomes more superficial until it reaches the subdermis (Figure 22) (Garritano & Quatela, 2018; Kleintjes, 2007; Tan et al., 2011).

4) The central artery appears as a branch of the angular artery that ascends along the midline anastomoses with the central artery of the other hemifront and with the supratrochlear artery (Figure 22)(Garritano & Quatela, 2018; Kleintjes, 2007; Koziej et al., 2019; Skaria, 2015).

5) The paracentral artery originates as a branch of the angular artery and anastomoses with the supratrochlear artery (Figure 22) (Garritano & Quatela, 2018; Kleintjes, 2007; Koziej et al., 2019; Skaria, 2015).

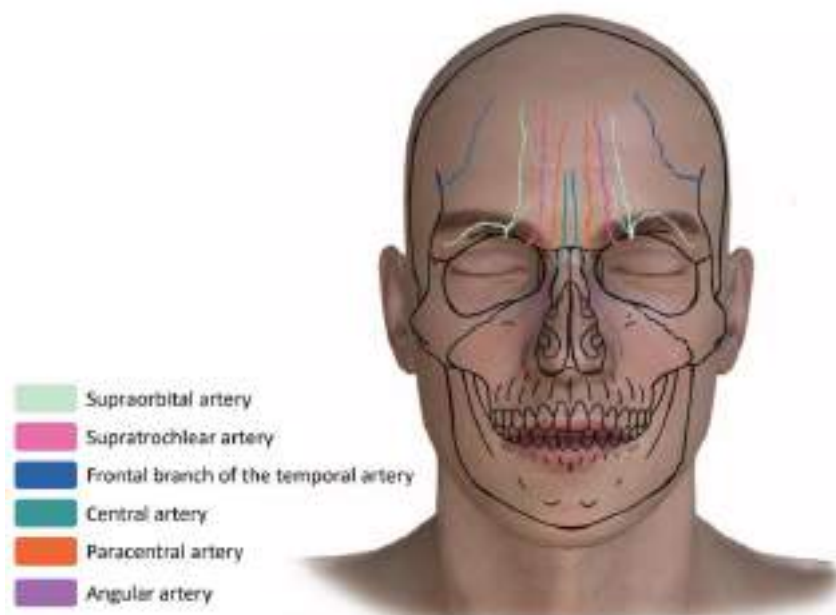


Figure 22. Arterial vascularization of the forehead(Drake et al., 2020; Gilroy et al., 2013; Koziej et al., 2019b; Tan et al., 2011).

1.9.2.2 Veins

In the forehead region there are two venous drainage systems: (1) The superficial drainage system is located between the muscle layer and the skin of the forehead and consists of numerous branching veins that anastomose with each other to create a subdermal venous network of very different shapes and sizes that has received the name of "the polygonal venous network." (Figure 23) (2) The deep system consists of the central, oblique, superior transverse orbital, angular, and facial veins and receives blood from the superficial system and deep tissues to drain into the ophthalmic vein (internal jugular vein) or the facial vein (external jugular vein) (Figure 23) (Shimizu et al., 2013).

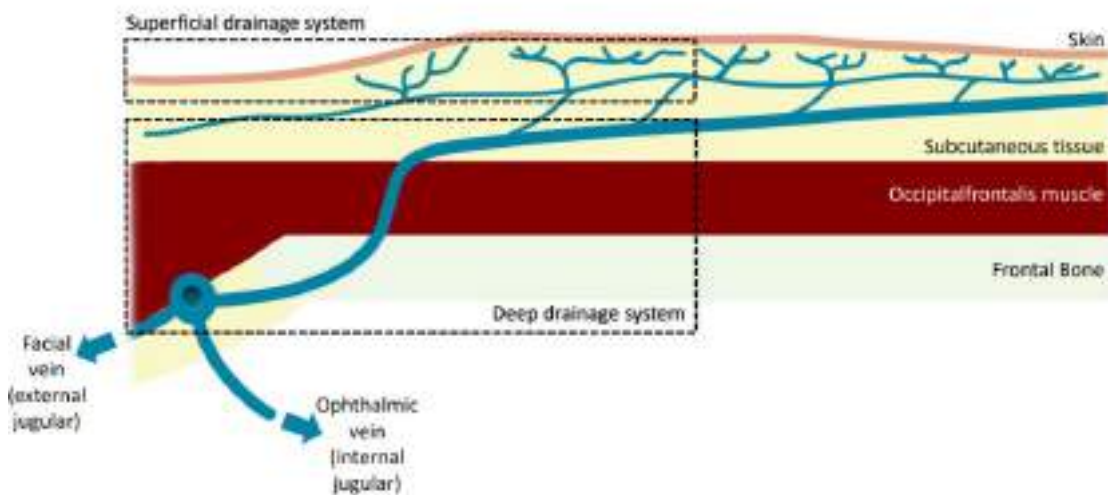


Figure 23. Superficial and deep venous drainage systems (Shimizu et al., 2013).

Below we discuss the origin and trajectory of the main veins of the forehead:

1) The central vein runs parallel to the midline (between the central and paracentral arteries) to end up draining into the angular vein in the lower part of the forehead (Figure 24) (Kleintjes, 2007; Shimizu et al., 2013).

2) The oblique vein descends through the upper part of the medial forehead to the oblique branch of the supraorbital artery to finish draining into the superior transverse orbital vein in the inferior area (Figure 24) (Kleintjes, 2007; Shimizu et al., 2013).

3) The superior transverse orbital vein runs along the superior orbital rim forming a hemi-loop around the orbital along with the angular and facial veins (Figure 24) (Koziej et al., 2019a; Shimizu et al., 2013).

4) The angular vein that drains into two branches, a deep one (into the skull through the ophthalmic vein) and a superficial one that descends transversely to the nose to drain into the facial vein (into the external jugular vein) (Figure 24) (Kleintjes, 2007; Shimizu et al., 2013).

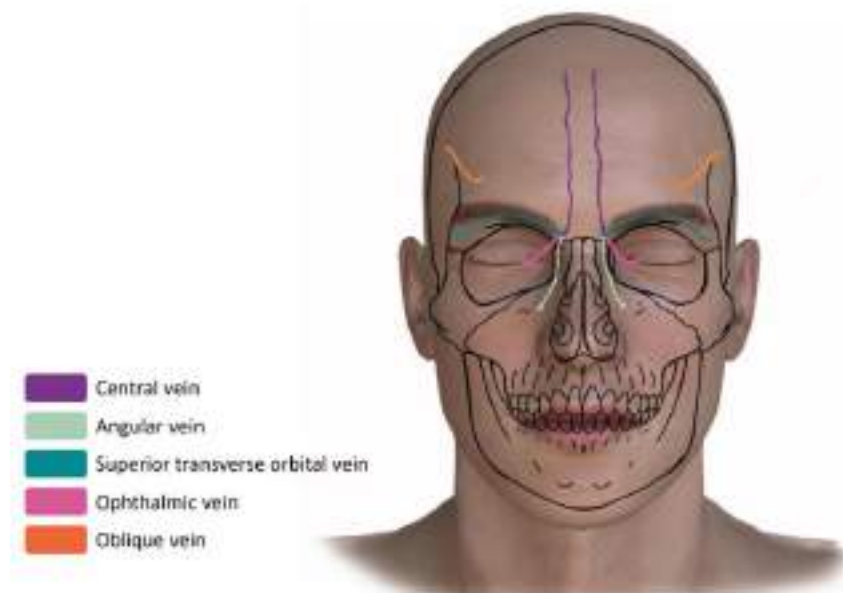


Figure 24. Venous vascularization of the forehead(Drake et al., 2020; Gilroy et al., 2013; Shimizu et al., 2013).

1.9.3 Innervation

Forehead blood vessels are subject to a special and complex autonomic regulation since their flow is controlled in several different ways: 1) Sympathetic vasodilator and vasodilator regulation (supraorbital nerve) 2) Parasympathetic vasodilator control (facial nerves and glossopharyngeal, frontal and nasociliary nerve) 4) Regulation produced by substances released by the vascular endothelium (hormones, vasoactive peptides, etc)(Drummond, 2009; Hosaka et al., 2016; Nolano et al., 2013; Nordin, 1990; Salvesen, 2001). In addition, the autonomic nerve endings and the vascular endothelium release vasoactive substances, modifying the vasomotor tone as a function of the receptors present in the vascular bed, which adds an additional level of control (For example, when adrenaline acts on α_2 receptors, it produces vasoconstriction while produces vasodilation when bound to β receptors) (Salvesen, 2001).

1.10 General validation principles for new NIRS devices

Unfortunately, currently there is no agreed protocol for the validation of new continuous-wave NIRS devices. Usually, the works that seek to demonstrate the proper functioning of new NIRS instruments use two types of complementary approaches:

1. Initial testing:

1.1. The evaluation of the technical aspects constitutes a prerequisite for the rest of the approaches since these consist of the determination of certain basic aspects such as confirming that the light source emits at the wavelengths specified by the manufacturer and quantification of cross-talk (which is a phenomenon that occurs when a genuine concentration change in one of the chromophores generates spurious changes in the measurements of another chromophore) (Orihuela-Espina et al., 2010; Tachtsidis & Scholkmann, 2016).

1.2. The detection of well-known spontaneous oscillations. A high quality fNIRS signal measured through the scalp is characterized by the presence of certain well-known spontaneous oscillations such as the cardiac pulsation (≈ 1 Hz), the respiratory cycle (≈ 0.3 Hz) and the Mayer arterial pressure waves (0.15 Hz). (Liang et al., 2016; Orihuela-Espina et al., 2010; Pollonini et al., 2016; von Lüthmann et al., 2015). The detection of these systemic oscillations has frequently been used as an indicator of NIRS data quality in multiple devices validation (Chiarelli et al., 2020; Liang et al., 2016; Liu et al., 2022; von Lüthmann et al., 2015).

1.3. Application of some paradigm for the elicitation of non-neuronal stereotyped physiological responses such as Valsalva maneuver (Kassab et al., 2018; Liang et al., 2016; G. Liu et al., 2022; Tsow et al., 2021) or limb vascular occlusion test (Liu et al., 2022; Liu et al., 2021; Mohamed et al., 2021; Saikia et al., 2018; Wyser et al., 2017; Yaqub et al., 2020). Although these techniques vary in underlying physiological principles, the rationale common to all is the elicitation of a typical and stereotyped physiological response (which is well characterized in the NIRS literature) to obtain evidence of the validity of the new NIRS instruments (Barstow, 2019; Bezemer et al., 2009; Casavola et al., 2000; Dennis et al., 2021; Gerovasili et al., 2010; Jeffries et al., 2018; Jones et al., 2016; Kooijman et al., 1997; Lacroix et al., 2012, 2012; Lima & Bakker, 2005; Martin et al., 2013; Nioka et al., 2006; Zhang et al., 2020). The Valsalva maneuver is an effort to exhale air while the airway is closed, resulting in a decrease in venous

return to the heart due to increased intrathoracic pressure (Everdell et al., 2013), while the vascular occlusion test consists of applying pressure to modify venous blood flow or arterial. The limb vascular occlusion test is undoubtedly the most frequently used technique because it allows good control and manipulation of the experimental conditions, which is why we will focus on it (Barstow, 2019; Bezemer et al., 2009; Casavola et al., 2000; Dennis et al., 2021; Gerovasili et al., 2010; Jeffries et al., 2018; Jones et al., 2016; Kooijman et al., 1997; Lacroix et al., 2012, 2012; Lima & Bakker, 2005; Martin et al., 2013; Nioka et al., 2006; Zhang et al., 2020). The most common procedure to perform a vascular occlusion test is to place a pneumatic cuff in the proximal area of the limb and the NIRS instrument in the distal area. The pneumatic cuff is inflated to different pressures to produce arterial or venous occlusion while hemodynamic changes in the limb muscle tissue are recorded using the NIRS instrument. Arterial occlusion, both arterial and venous blood flow are obstructed because the cuff pressure exceeds the pressure inside the vessels, yielding a characteristic curve (marked decrease in HbO with consequent increase in HbR) that informs us of local muscle oxygen consumption as long as there are no volume changes (Figure 25) (Jones et al., 2016; Lima & Bakker, 2005).

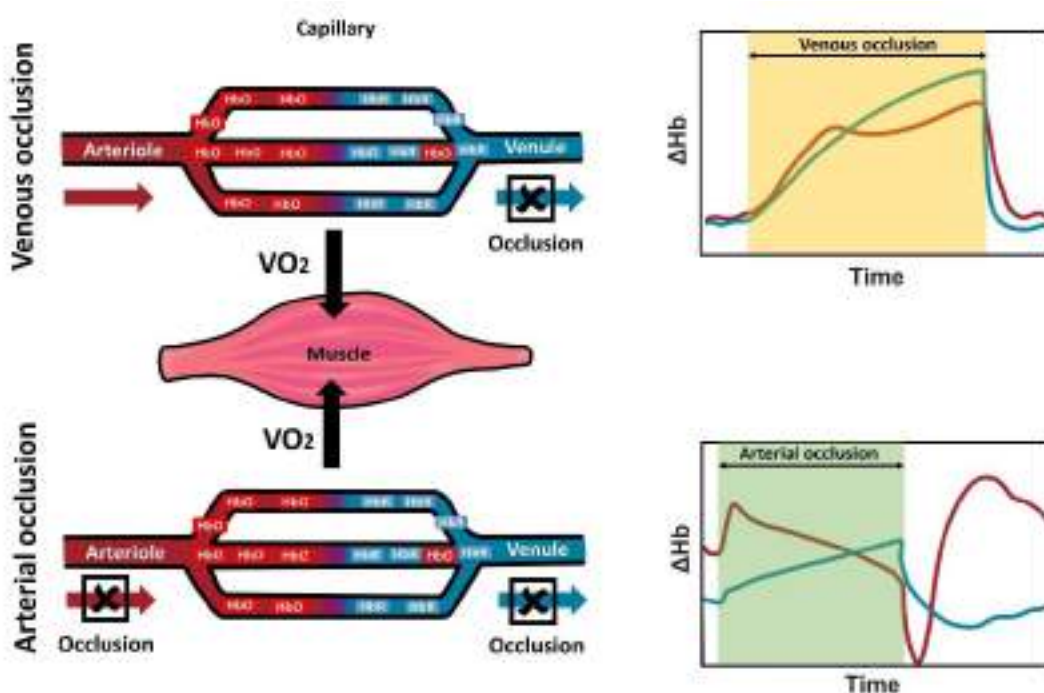


Figure 25. Schematic representation of muscle tissue and its blood vessels during venous and arterial occlusion (on the left) and typical HbO (red line) / HbR (blue line) time courses during the two types of vascular occlusion (on the right) (Jones et al., 2016). VO_2 = oxygen uptake; HbO: oxyhemoglobin; HbR: deoxyhemoglobin.

At the end of the arterial occlusion, the so-called post-occlusive hyperaemic response is observed, operationalized by an increase in HbO and a decrease in HbR (Figure 25). The hyperaemic reaction is produced by vasodilation during the occlusive phase because of deprivation of oxygen and nutrient supply (ischemia) (Gerovasili et al., 2010). However, in venous occlusions the arterial blood flow remains preserved while the venous outflow is stopped because the cuff pressure exceeds only the pressure inside the veins, giving rise to HbO and HbR time-series as the shown in Figure 25 (Jones et al., 2016).

2. Use of a cognitive paradigm to demonstrate that the new NIRS instrument is capable of measuring task-evoked brain activity. The selection of the type of paradigm is dependent on the brain area that is recorded with the NIRS (for example, tapping task is used to record the motor cortex while visual patterns reversal task is applied to the striate cortex) (Chitnis et al., 2016; Lareau et al., 2011; Yaqub et al., 2020; Zhao et al., 2020). However, there is no agreement on what type of cognitive task to deploy to validate fNIRS devices for a multimodal association cortex such as PFC. In this sense, various stimulation paradigms have been applied, such as Stroop tasks, arithmetic, verbal fluency, working memory, etc (Atsumori et al., 2009; Bracken et al., 2019; Tsow et al., 2021; von Lühmann et al., 2015). Amongst others, mental arithmetic tasks yield strong hemodynamic reactions of the frontal areas, so we decided to use this type of paradigm for the validation of the Theia instrument (von Lühmann et al., 2015).

The main objective of this work is to validate the Theia device to assess the functional activity of the PFC. With this end we have applied a set of initial tests (evaluation of technical aspects, detection of well-known spontaneous oscillations and vascular occlusion test) as well as an experimental validation using a cognitive paradigm of mental arithmetic.

In addition, as secondary objectives were considered:

1) To investigate the coupling between hemodynamic changes arising from the superficial (extracerebral) and deep (cerebral) layers during mental effort, as well as to isolate the task-evoked cortical response from other confounders. The rationale behind is the assumption that extracerebral and cerebral responses are the result of a coordinated effect product of different interrelated processes (Caldwell et al., 2016; Tachtsidis & Scholkmann, 2016). Rather than viewing surface fluctuations only as annoying confounders that must be removed, we regard them as carriers of valuable

information. Information, that might prove essential not only to gain a better understanding of the fNIRS data but also, and perhaps as important, to assess the full dynamics of the neuro-visceral link more accurately. This goal, however, is hampered by the inherent difficulty in differentiating spontaneous from task-locked fluctuations. One possible solution is to deliberately induce periodic oscillations through a rhythmic mental arithmetic task, so that they can be easily located and analysed by using well-established frequency-domain methods. To test this idea, the current study was designed to generate an oscillatory state suitable for effective analysis in the frequency-domain. To this end, we employed a mental arithmetic task within a cyclic block-design at a specific frequency, while performing dense multi-distance recordings on the forehead using a newly developed multi-channel NIRS device.

2) To assess the feasibility of using rhythmic cognitive tasks to induce periodic hemodynamic fluctuations suitable for effective frequency-resolved approaches.

3) Identify common task-related oscillatory activity.

4) Estimate the contribution of extracerebral and brain tissue layers to fNIRS signals.

5) Separate task-related extracerebral hemodynamic from the putative cortical response.

6) Measure the relative timing between HbO and HbR changes to better interpret the underlying physiological processes.

7) Use the empirical transfer function as an alternative method to estimate the functional brain activity and assess the timed-coordination between extracerebral and cerebral responses.

2 Material and methods

2.1 Participants

All procedures performed in this study were approved by the Ethics Committee of the University Miguel Hernandez (ADH.NEU.LMO.SMR.23), in accordance with the declarations of Helsinki. Participants did not receive any remuneration. A total of twenty-four healthy young adults volunteered, 10 males and 14 females (mean age: 22.3; SD: 4.2), were recruited for this study. All of them were instructed beforehand about the purpose of the experiment and provided informed written consent prior to study enrollment (Appendixes).

2.2 fNIRS recordings

In this study we used a multichannel, wireless, continuous-wave NIRS device called Theia (Newmanbrain, S.L., Elche, Spain), which employs four sources and ten detectors forming a rectangular grid of 80x20 mm. Each source housed two LED at wavelengths 740 nm and 850 nm. Through a precise switching cycle, the device combines pairs of optodes at different distances, providing 16 SCs and 12 LCs that corresponds to a SDD of 14 and 32 mm respectively (Figure. 26A). The device corrects the ambient light contribution and incorporates a 3-axis accelerometer to account for head motion. It transfers data wirelessly (via Bluetooth) at a sample rate of 10 Hz. The NIRS probe was placed onto the forehead, centered on AFpz according to the international 10-5 system, mainly covering the frontopolar area of the PFC (Figure 26 and 27). The optodes contact the skin through an intermediate convex lens pressing the skin when the probe is held firmly, in order to reduce cutaneous blood flow and, therefore, its hemodynamic interference (Takahashi et al., 2011).

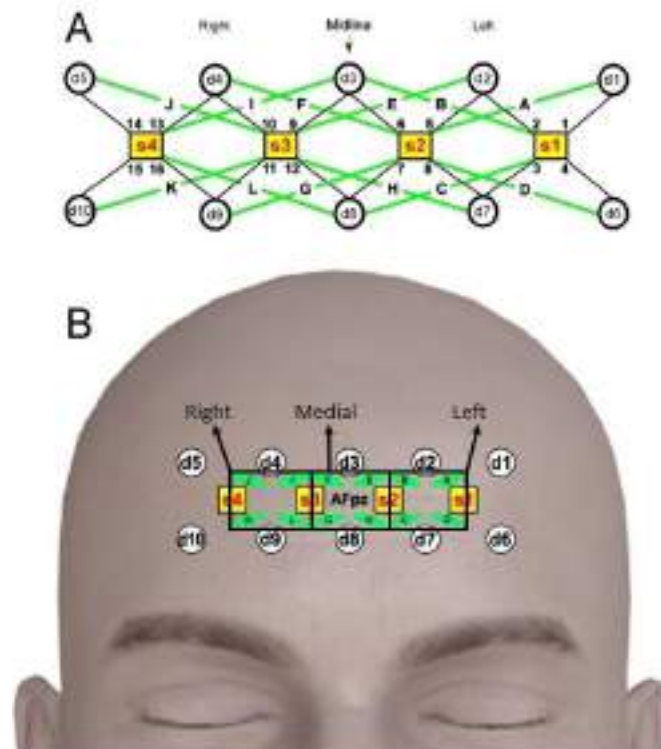


Figure 26. Probe geometry and placement. (a) Optodes arrangement (yellow squares: Sources; white circles: Detectors). Sixteen short-channels (black lines with numbers) and twelve long channels (green lines with letters). (b) Probe position on the forehead. Green shaded areas roughly mark the regions explored by the long-channels. Black rectangles outline the long-channels averaged within each region of interest (right, medial and left).

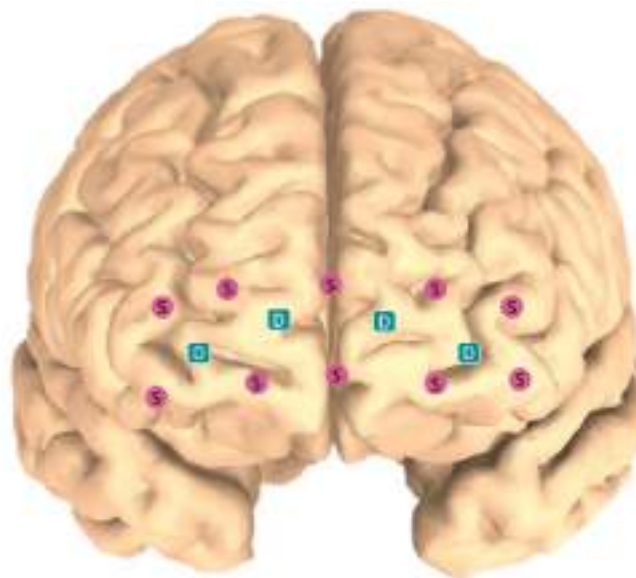


Figure 27. Sources (pink circles) and detector (green squares) estimated location covering frontopolar cortex (Aasted et al., 2015).

2.3 Signal quality check - Channels and participants exclusion criteria

To ensure that only clean signals pass to further analysis, we conducted some preliminary quality tests. To account for instrumental noise (Huppert et al., 2009; Orihuela-Espina et al., 2010) we evaluated first the raw optical data to identify channels exhibiting extreme values (below 5% or above 95% of the device dynamic range), or an excessive coefficient of variation $> 7.5\%$ (calculated as the percentage ratio between the standard deviation and the mean) (Zimeo Morais et al., 2017). Thus, we discarded the recordings suffering from poor signal to noise ratio, saturation or unphysiological noise contamination. By visual inspection, we rejected recordings affected by motion artifacts by identifying sharp changes in the fNIRS signals aligned with abrupt shifts in the accelerometer data. Two participants were excluded for exceeding this limit, leaving a sample of 22.

2.4 Initial testing

2.4.1 Light-emitting diode spectral calibration

Theia fNIRS device features dual-wavelength LEDs that emit at 740 nm and 850 nm. The use of this NIR light source has certain advantages (small size, low cost, and safety), however, since LED technology is based on spontaneously emitted light, it is advisable to check that the spectrum of the emitted light is sharply peaked and invariant (Scholkmann et al., 2014). To verify this aspect, we use an optical fibre placed at 3 mm from the dual-wavelength LED connected to a Stellar-Net Black-Comet spectrometer. Spectral irradiance values were calculated at different LED powers for both wavelengths.

2.4.2 Detection of well-known spontaneous oscillations

A high quality fNIRS signal measured through the scalp is characterized by the presence of certain well-known spontaneous oscillations such as the cardiac pulsation (≈ 1 Hz), the respiratory cycle (≈ 0.3 Hz) and the Mayer arterial pressure waves (0.15 Hz). (Liang et al., 2016; Orihuela-Espina et al., 2010; Pollonini et al., 2016; von Lühmann et al., 2015). Detection of these systemic oscillations as indicators of signal quality has been widely documented in the NIRS literature (Liang et al., 2016; von Lühmann et al., 2015).

In order to evaluate the presence of well-known spontaneous oscillations, we estimate power spectral density (PSD) in the NIRS data of the short and LCs in the baseline condition. The PSDs were computed using the Welch's averaged periodogram method (Welch, 1967) with a hamming window of length 2000 samples and 50% of overlap to achieve a good frequency resolution (0.005 Hz), spectral smoothness and reduced noise variance (Ilvedson, 1998). To allow comparisons, the PSDs were normalized to relative percentage values by calculating the power ratio of each frequency band (cardiac, respiratory and Mayer) to the total power of the entire spectrum (Aarabi & Huppert, 2016). Frequency ranges considered for the band were as follows: cardiac: 0.5-2.5 Hz, respiration: 0.2-0.33 Hz and Mayer waves: 0.06-0.14 Hz (Yücel et al., 2016). Finally, we calculated the mean percentage and standard deviations of all SC and LC within each chromophore type and frequency band.

2.4.3 [HbO] and [HbR] cross-talk assessment

Cross-talk is an undesirable phenomenon that occurs when a genuine concentration changes in one of the chromophores generates spurious changes in the measurements of another chromophore (Orihuela-Espina et al., 2010; Tachtsidis & Scholkmann, 2016). The main cause of cross-talk in NIRS devices is due to wavelength selection. Although Theia's light sources wavelength were carefully selected (740 and 850 nm) taking into account current standards for cross-talk avoidance, we decided to evaluate their possible effect on NIRS measurements (Scholkmann et al., 2014). To this end, we decided to employ cardiac pulsation to assess the cross-talk as it is a dominant and ubiquitous spontaneous oscillation in any NIRS signal. During systole the ejection of blood provides an expansion of the diameter of the arterial vessels due to an increase in arterial pressure. This increase in arterial inflow of vessels results in a rapid rise in HbO and a consequent drop in HbR due to increased venous outflow related to the washout effect. However, during diastole, the fall in arterial pressure and arterial inflow produces a decrease in HbO and an increase in HbR (Fantini et al., 2018).

It is known that during these periodic and spontaneous systole-diastole changes, HbO and HbR are in contra-phase, that is, the cardiac pulsation produces opposite responses in both chromophores, as observed in Figure 28 (Franceschini et al., 2006; Jones et al., 2016; Schmid-Schönbein, 1999). We can take advantage of this fact to evaluate cross-talk between both chromophores. The rationale behind this idea is that in a high cross-talk situation both

haemoglobins would oscillate in phase while in the opposite case we should observe an out-of-phase relationship.

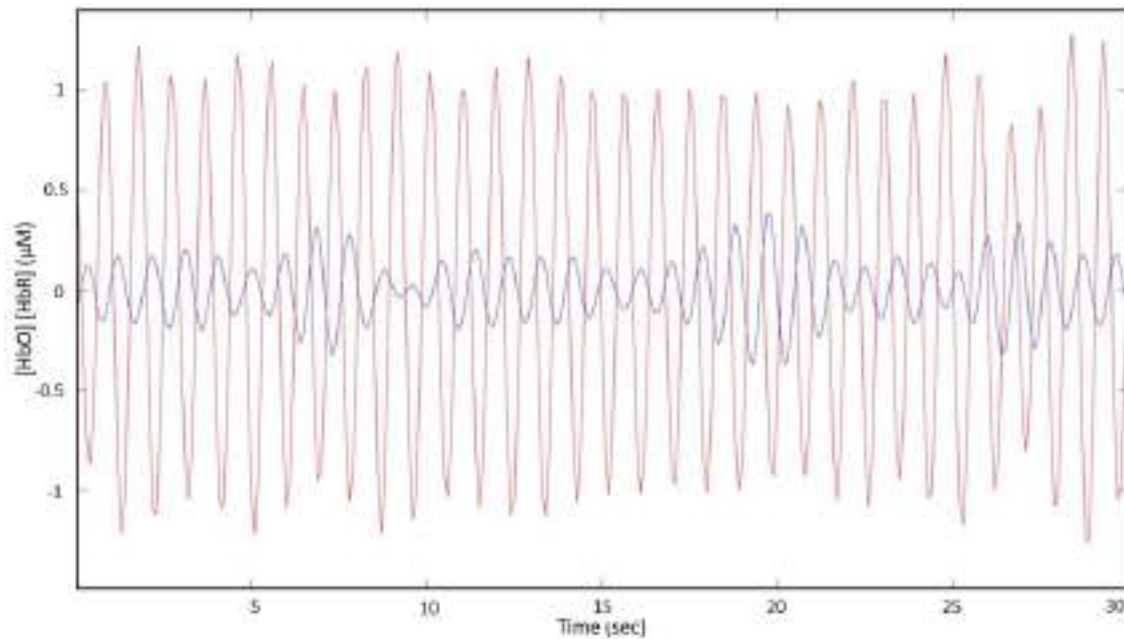


Figure 28. Relationships between both haemoglobins at cardiac frequency

We estimated the cross power spectral density (CPSD) via the MATLAB function “cpsd”, based on the Welch’s averaged periodogram method (Welch, 1967). We used a hamming window of length 2000 samples with a 20% of overlap, to achieve a good frequency resolution (0.005 Hz) and spectral smoothness. Spectral phase was also determined from the complex-valued CPSD result. Since phase estimates from CPSD only have meaning where significant frequency-domain correlation exists, we computed the magnitude squared coherence (MSC) by means of the “mscohere” function (parameterized as for CPSD). MSC, a function of frequency, takes values from 0 (absence of correlation) to 1 (perfect correlation). For each channel, we applied this procedure to the signal pairs HbO- HbR in the baseline period. Phase angles and lags (i.e. time delay) were computed as well from the real and imaginary parts of the complex-valued CPSD (Müller et al., 2003; Reinhard et al., 2006). To deal with phase angles we used the Matlab Toolbox CircStat (Berens, 2009). Thus, we computed the circular mean of phase angles (mean phase difference), and to assess whether it was significantly oriented in a preferred direction, we applied a V-test. From the obtained phase differences, we calculated the mean time delays at the corresponding frequencies (Müller et al., 2003). The HbO-HbR coherence and angle values of the frequency bins between 0.8-2Hz (corresponding 48-120 beats per minute) were added to extract the information related to cardiac pulsation. Finally, we compute the mean and standard deviation of the coherence and angle values within each type of channel.

2.4.4 Limb vascular occlusion test

Limb vascular occlusion test is a useful method for the validation of new NIRS devices because it provides high experimental control. Although the vascular occlusion test does not measure neural activity, it is in fact a quality prerequisite before validating the Theia device in a neuroimaging context. The rationale behind this validation procedure is the fact that it yields stereotyped and reproducible HbO and HbR changes that allow comparison to determine whether an fNIRS meets basic measurement requirements (Dennis et al., 2021; Gerovasili et al., 2010; Martin et al., 2013). Therefore, the purpose of this test is to check if monitoring with Theia of the vascular occlusion test yields the typical vascular occlusion curves described in previous literature (Barstow, 2019; Bezemer et al., 2009; Casavola et al., 2000; Dennis et al., 2021; Gerovasili et al., 2010; Jeffries et al., 2018; Jones et al., 2016; Kooijman et al., 1997; Lacroix et al., 2012, 2012b; Lima & Bakker, 2005; Martin et al., 2013; Nioka et al., 2006; Zhang et al., 2020).

The pneumatic cuff was placed around the leg (5 cm above the patella) while the fNIRS probe was placed in the muscle belly of the medial gastrocnemius (30 cm from the calcaneus) secured with an elastic bandage to prevent movement and intrusion of extraneous light (Jeffries et al., 2018). A manual sphygmomanometer was used to induce pressure changes and to measure blood pressure. The participant was placed in the decubitus prone position on a padded table and was instructed not to move their lower limb during the experimental protocol (Figure 29).

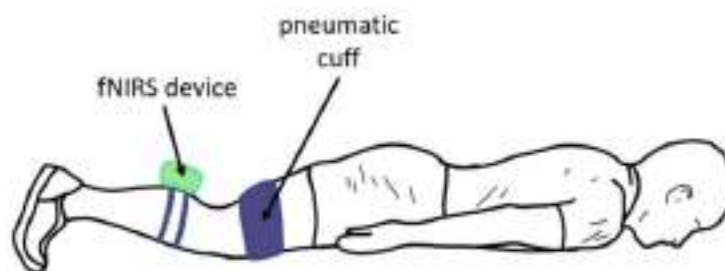


Figure 29. Limb vascular occlusion test experimental setup.

After 180 seconds of the pre-occlusive baseline, a series of 7 of brief occlusions were performed: the first six with a duration of 60 s correspond to different intensities of veno-occlusive pressures (20, 30, 40, 50, 60, 70 mmHg) while the last trial lasting 120 s corresponded to complete arterial occlusion (250 mmHg) (Figure 30). The pressures were chosen based on the recommendations of previous works on NIRS and vascular occlusions (Barstow, 2019). Inter-trial

period duration was not fixed since it lasted as long as necessary to ensure washout of the effect of previous occlusion.



Figure 30. Schematic representation of limb vascular occlusion test. The venous occlusion was depicted by yellow rectangles while arterial occlusion is represented by green ones. The duration of the intertrial period was not constant.

Unlike the rest of the measurements, this test was performed on a single 34-year-old healthy male participant (selected from the 22 participants that make up the full sample). Pre-processing was conducted using the Homer2 NIRS package (Huppert et al., 2009) based in MATLAB. The raw optical data of the LC were converted to optical density, and then into [HbO] and [HbR] relative concentration changes via the modified BLL (Delpy et al., 1988; Kocsis et al., 2006). Since the measurements were made in the lower extremity, a differential pathlength factor of 4 was applied (Barstow, 2019; Jeffries et al., 2018; Lacroix et al., 2012; Zhang et al., 2020).

2.5 Experimental validation through a paradigm of mental arithmetic.

2.5.1 fNIRS Data Preprocessing

Preprocessing was carried out using the Homer2 NIRS package (Huppert et al., 2009) based in MATLAB. The raw optical data were converted to optical density, and then into HbO and HbR relative concentration changes via the modified BLL (Delpy et al., 1988; Kocsis et al., 2006). We used a differential pathlength factor calculated in accordance with the general equation described in (Scholkmann & Wolf, 2013), which considers the participant's age and the wavelength. No partial volume correction was used.

The fNIRS data were digitally low-pass filtered by using a zero-phase, 5th-order Butterworth filter, cut-off 2.5 Hz (MATLAB Signal Processing Toolbox); no high-pass filtering was applied. Therefore, we remove only high-frequency noise while preserving cardiac, respiratory, blood pressure and vasomotor components. After preprocessing, for each chromophore we obtained 16 time-series from the SCs plus 12 from the LCs that we refer to as “shallow-” and “deep-signals” respectively, to indicate how much the light penetrated during their corresponding records. Thus, we had a set of multi-distance recordings to effectively address the problem of extracerebral contamination (Pfeifer et al., 2018; Saager & Berger, 2005; Scholkmann et al., 2014; Yücel et al., 2015), by assuming that short-separation recordings are sensitive only to extra-cerebral changes, while long-separation recordings are sensitive to both extracerebral and cerebral activity (Brigadoi & Cooper, 2015; Saager & Berger, 2005; Scarpa et al., 2013; Yücel et al., 2017).

When using multi-distance recordings regression can be performed assuming that the physiological noise has comparable time courses in both shallow- and deep-signals, and that the focal, task-evoked, cerebral hemodynamics is independent, i.e. uncorrelated (Saager et al., 2011; Saager & Berger, 2008). However, the heterogeneous nature of the local superficial fluctuations cannot be dismissed, which raises the need to collect the shallow-signals at recording sites as close as possible to the deep-signal to be decontaminated from surface hemodynamics (Gagnon et al., 2012). Here, we used a NIRS device that allows each deep-signal to have three shallow-signals that meet the proximity requirements: two obtained close to the long-channel's detector and source respectively and one close to its center (see Figure 26). Adopting the “double short separation measurements” approach recommended in (Gagnon et

al., 2014), we used the combination (the sum) of the two shallow-signals recorded near the detector and source to estimate the extracerebral component to be suppressed from the corresponding deep-signal. Thus, for example, the signal from LC “A” was regressed on the sum of the signals from the SCs 1 and 5 (Figure 26). Over the entire time courses, for all the deep-signals we computed:

$$S_{clean} = S_{deep} - (\beta_0 + \beta_1 S_{shallow}) \quad (3)$$

where β_0 and β_1 are the regression coefficients, S_{deep} is the deep-signal, $S_{shallow}$ is the combined shallow-signal and S_{clean} the desired “clean signal” (in fact, the raw residuals). We solved linear regression by applying the MATLAB function “robustfit”, which uses an iteratively reweighted least squares algorithm and is less sensitive to outliers than ordinary least-squares (Holland & Welsch, 1977). After regression, each S_{deep} have its associated pair S_{clean} and $S_{shallow}$, making a total of 12 signal triplets for each chromophore. Noteworthy, although S_{clean} probably represents the neural component, at this point we prefer the term "clean" without making assumptions about its actual origin. This precaution is based on the fact that, since our mental task attempts to induce periodic oscillations the requirement of non-correlation between extracerebral and cerebral hemodynamics may not be met, compromising the performance of regression (Fantini, Frederick, et al., 2018; Saager & Berger, 2008). Later, in this work, we will apply additional analysis to verify the nature of these regression-estimated signals.

Finally, since the channel positions are not fully consistent across individuals due to the variability in head shape and size (Tak, Uga, Flandin, Dan, & Penny, 2016), the signal-to-noise ratio and signal reliability can be improved by spatial clustering (Plichta et al., 2006; Schecklmann et al., 2008). To this end and to avoid interpreting isolated channels, for every single participant we averaged across the signals belonging to three regions of interest (ROI), left, medial and right (Figure 26). As such, the signal triplets associated to the four leftmost LCs (A, B, C, D) yield the corresponding averages of $S_{shallow}$, S_{deep} and S_{clean} . The same procedure was applied for the medial (E, F, G, H) and the rightmost (I, J, K, L) four LCs (Figure 26). Thus, each of the three ROIs now reduces to just three average signals that, from now on, we denote by SS (shallow), DS (deep) and CS (clean). All further processing was done on these signals, which display comparable signal-to-noise ratio across the three ROIs because they have been obtained by averaging the same number of neighboring signals in each frontopolar region. For each ROI, we computed the averaged time courses of HbO and HbR for the three signals across all the

participants. Furthermore, we obtained the grand average of the trials epoched in the interval -15 to 30-sec relative to the onset (10 trials x 20 participants = 200 trials). Standard error of the mean (SEM) was calculated as well.

2.5.2 Mental task

In this work, the task was based on a block protocol designed as a cyclical pattern of mental effort, alternating phases of mental math with phases of pause of the same duration, i.e. regular repetitions of activation-rest. The idea behind this was to induce periodic hemodynamic changes in the form of cycles of some kind of response followed by a return to basal levels. In this way, such an oscillatory pattern may be analyzed by conventional spectral methods. As illustrated in Figure 31, the experimental session was organized into three consecutive uninterrupted recordings: (i) 300 seconds of baseline in resting condition, (ii) 300 seconds of task, and (iii) 300 seconds of recovery in a relaxed state. The participants practiced the task for 10-15 minutes to make sure they understood and got used to it (to minimize stress responses). They were seated in a comfortable position and were asked to keep their eyes on the screen throughout the experiment. During specific time intervals, an image was presented on the screen to instruct the participants to relax mentally. This image was a soft-colored paint depicting an inanimate scene (it was rated as neutral by the participants in a parallel study with affective pictures; results not shown here). The NIRS probe remained in the same position throughout the session. The task consisted of 10 consecutive 30-second trials. Each trial began with 15 seconds of mental calculation, followed by a 15-second pause of relaxation. To perform the mental math participants were asked to iteratively subtract a small number (between 5 and 9) from a three-digit number (between 100 and 199), as fast as possible. Both numbers, chosen randomly in each trial, were presented on a 21.5" display monitor, 80 cm. away from the participants' eyes. Afterwards, the pause started by presenting the question "Result?" for 5 seconds, which prompted the participants to inform verbally of the final result of their mental calculations (to allow scoring the performance and ensuring that the participants were paying attention), followed by the "relax" image. Two seconds before presenting the subtraction operands, a fixation cross was displayed in the middle of the computer screen to announce the beginning of the mental calculation. Note that the 30-second period of the trials corresponds to a frequency of 0.033 Hz, which we will refer to as f_t (task frequency) throughout this manuscript. This frequency was chosen so that it did not overlap with well-known spontaneous fluctuations such as blood pressure (0.08 - 0.12 Hz) (Huppert et al., 2009; Julien, 2006), or very slow endothelial activity (0.01 - 0.02 Hz) (Stefanovska et al., 1999). Furthermore, the 15-second

duration of mental effort accommodates that of a typical hemodynamic response (Buxton, Uludağ, Dubowitz, & Liu, 2004; K. J. Friston, Josephs, Rees, & Turner, 1998), while the next 15-second pause allows a return to baseline levels, being an optimal inter-event interval to minimize overlaps between consecutive hemodynamic responses (Aarabi et al., 2017; Dale, 1999). Here, we tried to minimize the generation of distress by using a subtraction arithmetic task that was cognitively challenging, but did not exceed the participants' mental abilities. Further, we constantly emphasized the importance of the mental effort, and not the amount or accuracy of the operations performed.



Figure 31. Schematic representation of the experimental procedure.

2.5.3 Heart rate measurement

Electrocardiogram (ECG) was registered using a BIOPAC MP36 physiological monitoring system and the AcqKnowledge software 4.1 (Biopac Systems, Inc., Goleta, CA, USA) at a sampling rate of 500 Hz. ECG was recorded in lead II configuration with disposable electrodes. The MP36R device was digitally synchronized through the I/O port with the PC running the stimuli presentation, so event markers were recorded as well. At the end of the experiment, the raw data was post-processed with AcqKnowledge to: i) create an R-R tachogram from the ECG signal, using the implemented Pan–Tompkins algorithm (Pan & Tompkins, 1985) for R wave detection, and ii) extract the instantaneous heart rate from the reciprocal of the tachogram. Finally, the data was exported to MATLAB and then resampled to 10 Hz using cubic spline interpolation.

2.5.4 Heart rate exclusion criteria

Many studies have investigated how cognitive performance correlates with the stress level induced by mental workload, in most cases through different physiological measures, heart rate being one of common use (Charles & Nixon, 2019; Hakimi, 2018; Mandrick et al., 2016; Tao et al., 2019). However, there is not a clear threshold to differentiate between heart rate changes due to a pure mental effort and those due to a stressful situation. As the present work focuses

on the first, it was necessary to estimate a maximum increase in heart rate, beyond which the influence of stress was considered disproportionate. We took as a reference the results of other studies that applied the Trier Social Stress Test, a standard protocol for stress induction in healthy people (Kudielka et al., 2007). In their review work, (Kudielka et al., 2007) reported that the mean heart rate increases to the test are about 15–25 beats per minute (bpm). (Kirschbaum, Pirke, & Hellhammer, 1993), found increases about 26 bpm during the test. On the basis of the aforementioned literature, we decided to apply a limit well below the reported values. Compared to the mean heart rate at baseline, the threshold was set to a maximum increase of 12 bpm during the task. Two participants were excluded for exceeding this limit. Therefore, the final sample consisted of 20 participants (8 males and 12 females; mean age: 21.7; SD: 3.8). Thus, only those participants showing reasonably stable heart rate throughout the baseline and task periods were further considered. The Wilcoxon signed rank test was used to resolve for differences between the maximum heart rate reached during baseline and task.

2.5.5 Identification of task-induced frequencies

Firstly, we evaluated if the task successfully induced oscillations by estimating the PSD of each participant's NIRS data during the task and the baseline condition. The PSDs were computed using the Welch's averaged periodogram method (Welch, 1967) with a hamming window of length 2000 samples and 50% of overlap to achieve a good frequency resolution (0.005 Hz), spectral smoothness and reduced noise variance (Ilvedson, 1998). To allow comparisons, the PSDs were normalized to relative percentage values by calculating the power ratio of each frequency bin to the total power of the entire spectrum (Aarabi & Huppert, 2016). For further analysis, we focused on the frequency range 0.005 to 0.08 Hz under the assumption that the expected task-induced oscillations would fall within that range.

We assessed the presence of significant task-induced oscillations by contrasting the PSDs during task and baseline. Along frequency bins we performed one-tail paired *t*-tests to check whether within-subject PSD values were statistically higher for the task compared with baseline. The observed *t*-statistics were corrected for multiple comparisons by following the cluster-based nonparametric approach given in (Maris & Oostenveld, 2007). We computed Monte Carlo cluster tests over 1000 permutations of the same *t*-test where the condition, i.e. task and baseline, was randomly shuffled within subject. Then, we estimated the so-called permutation *p*-value from the proportion of random realizations that have larger cluster-statistic than the observed one. We set a critical alpha-level = 0.01 to identify the frequency bins

that showed significantly higher PSD values during the task. Finally, the PSDs were averaged across participants (N=20) to obtain the average normalized PSD of HbO and HbR for each signal type and ROI. In addition, the 95% confidence interval (CI) for the mean at each frequency bin was calculated by bootstrapping over 1000 resamples.

2.5.6 SS and DS relationships

Here, SS data were obtained from fNIRS channels exploring the frontopolar region with a SDD of 14 mm. The scalp-cortex distance is known to be increased in this region (15 mm to 17 mm) compared to more lateral frontal areas (Cui, Bray, Bryant, Glover, & Reiss, 2011; Haeussinger et al., 2011) which, together with the presence of the frontal sinuses, decreases the cerebral fNIRS sensitivity (Haeussinger et al., 2014). Moreover, as pointed out by (Zhang et al., 2015), SCs with a SDD in the range of 14 to 16 mm have a sensitivity to the brain of only about 0.47%. Although it is unlikely that SS picked up cortical signals, it was still important to examine the commonalities and differences between SS and DS to reasonably ensure that SS data are primarily dominated by shallow hemodynamics, while DS also contain deeper components that, likely, stem from the cortical layer. The rationale for this analysis was to demonstrate that the link SS-DS would be altered at the task frequency if another deep oscillatory process (e.g. neurovascular response) appears in the DS signal. To this end, for the time-series pairs HbO_{ss} / HbO_{ds} and HbR_{ss} / HbR_{ds} we performed the following within-subject analysis: (i) cross-spectrum to identify shared fluctuations, (ii) frequency-domain correlation to identify significant covariation, and (iii) transfer function to evaluate the relationship in magnitude and phase. Following the recommendations given in (Jurgen Ahr Claassen et al., 2015) for transfer function analysis, neither detrending nor high-pass filtering was used, and a triangular smoothing window (coefficients $\frac{1}{4}, \frac{1}{2}, \frac{1}{4}$) was applied to both auto- and cross-spectra.

To identify synchrony (or shared fluctuations) in the frequency-domain between shallow and deep signals, a cross-spectrum analysis was performed to compare the two signals. We computed the CPSD of the bivariate time-series using the MATLAB function “cpsd”, based on the Welch’s averaged periodogram method (Welch, 1967); as for PSD we set a hamming window of length 2000 samples and 50% of overlap. From the complex-valued result, we obtained the magnitude and phase values to find the shared power and phase shift between both signals at particular frequencies. The magnitude peaks that showed significantly higher values during the task were located by following the same approach as for PSD in Section 3.5.5.; the values were normalized and averaged in the same way.

To ensure the reliability of the cross-spectral estimates, we evaluated whether the signals showed significant stability in their relative amplitude and phase at particular frequencies. To this end, we estimated their frequency-domain correlation by computing the magnitude-squared coherence (MSC) as a function of the PSDs and the CPSD (Eq. 4) (Zhang, Zuckerman, Giller, & Levine, 1998):

$$MSC_{ssds}(f) = \frac{|CPSD_{ssds}(f)|^2}{PSD_{ss}(f)PSD_{ds}(f)} \quad (4)$$

Coherence values vary between 0 (no correlation) and 1 (perfect correlation), describing the linearity of the relationship between both signals in the frequency domain. The coherence values were also averaged across participants for each signal pair and ROI. Only if significant coherence exists, the cross-spectral estimates have a useful meaning (Jurgen Ahr Claassen et al., 2015). Values of about 0.5 has been commonly considered as a threshold for significance (Sassaroli et al., 2018) but, since the threshold may depend on the frequency, a better alternative for assessing significance is the surrogate data approach (Faes et al., 2004; Paluš, 1997). In this work, following the nomenclature given in (Paluš, 1997), we chose the FT1 surrogates method since it conserves the power spectrum of the original signals (Faes et al., 2004). FT1 surrogates were constructed by substituting the phase of the Fourier transform of the original signals with random values in the range $[-\pi, \pi]$ while the modulus is preserved, and then returning to time-domain by inverting the Fourier transform. We generate 1000 surrogate series and for each one the averaged MSC was computed as for the original signals, realizing the null hypothesis that the averaged MSC stem from pairs of signals that fluctuate asynchronously at the same frequencies of the experimental signals. Afterwards, the mean MSC values obtained from the actual signals were compared with the FT1 distribution to estimate the MSC threshold levels for each frequency bin at $\alpha = 0.05$.

A transfer function describes the dynamic relationship between the output signal of a system and the input signal. Under the assumption of linearity, the transfer function can be estimated from the frequency-domain representation of the experimental input-output signals. Transfer function models have become a popular approach to investigate the dynamic of cerebrovascular autoregulation (Jurgen Ahr Claassen et al., 2015; Van Beek, Claassen, Rikkert, & Jansen, 2008), and they have also been used to remove systemic physiological noise from fNIRS signals (Bauernfeind, Böck, Wriessnegger, & Müller-Putz, 2013; Florian & Pfurtscheller, 1997).

In this work, assuming that SS has energy in the frequency range of interest and contain quasi-periodic oscillations, the transfer function $H(f)$ was approximated from the experimental fNIRS data as (Eq. 5) (Zhang et al., 1998):

$$H(f) = \frac{CPSD_{ssds}(f)}{PSD_{ss}(f)} \quad (5)$$

For each time-series pair, shallow and deep signals were, respectively, the input and output data used to obtain an approximation of the transfer function at particular frequencies (e.g. input HbO_{ss} , output HbO_{ds}). From the complex-valued result, we obtained the magnitude (gain), which represents the relative change in μM between input and output, and the phase that carries their temporal coupling (phase difference or time-lag), while coherence values indicate the reliability of these measures. For reporting, the gain data were converted into percentage values. Then, at the group level and for each signal pair and ROI, we computed the averages of gain and circular phase angle; phase statistics were managed by means of the Matlab Toolbox CircStat (Berens, 2009). In addition, we calculated the 95% CI band around the mean by bootstrapping over 2000 resamples. Finally, to assess whether the task induced a consistent phase coupling across participants, we applied a bootstrapped Rayleigh test (Oden, 1983) on the phase values at the task frequency. Consistent coupling should be reflected as a narrow distribution of phase values around a preferred angle. On the contrary, a poor inter-subject synchronization should display a more uniform distribution throughout the 360° circle.

2.5.7 Estimating deep component from transfer function

We previously expressed some concerns relating to the reliability of the regression-estimated CS signals. To address them, we applied an alternative novel approach to estimate CS from the transfer function. Supposing that DS solely contains the same fluctuations seen in SS, the relation between both signals should be highly linear and coherent, only altered by the small differences in the volume sampled by our SCs and LCs. Therefore, the transfer function should yield fairly constant gain values across frequencies (depending on the fractional part of DS power that is produced by SS) and a phase shift close to zero (in-phase). Furthermore, coherence values should be close to one. However, when another oscillatory process is added to DS we can expect some level of disturbance in gain and/or phase at certain frequencies. At a specific frequency, cyclic hemodynamic oscillations can be approximated as sinusoids, completely defined by their values of amplitude, phase and frequency. Adding two sinusoids of common frequency results

in a sinusoid with same frequency but with amplitude and/or phase altered. In our case, if the task elicits independent cyclic oscillations in both shallow and deep layers, the observed deep sinusoid $X_{ds}(t)$ at the task-frequency would result from the sum of the two contributing sinusoids $X_{ss}(t)$ and $X_{uk}(t)$, i.e.:

$$X_{ds}(t) = X_{ss}(t) + X_{uk}(t), \quad (6)$$

where $X_{ss}(t)$ is the observed shallow sinusoid and $X_{uk}(t)$ is the unknown deep component. All of these sinusoids are characterized by their values of amplitude A , angular frequency ω and phase ϕ , thus, in sinusoidal form:

$$A_{ds} \cos(\omega_{ds}t + \phi_{ds}) = A_{ss} \cos(\omega_{ss}t + \phi_{ss}) + A_{uk} \cos(\omega_{uk}t + \phi_{uk}). \quad (7)$$

Since they represent harmonic oscillations of common frequency (i.e. $\omega_{ds} = \omega_{ss} = \omega_{uk} = \text{task frequency}$), they do not depend on ω or t , but only on A and ϕ , which makes it possible to convert them into phasors (or complex numbers). In exponential form would be:

$$\vec{X}_{ds} = A_{ds}e^{j\phi_{ds}}, \vec{X}_{ss} = A_{ss}e^{j\phi_{ss}} \text{ and } \vec{X}_{uk} = A_{uk}e^{j\phi_{uk}}, \quad (8)$$

where $j = \sqrt{-1}$, while \vec{X}_{ds} , \vec{X}_{ss} and \vec{X}_{uk} are the phasor representation of $X_{ds}(t)$, $X_{ss}(t)$ and $X_{uk}(t)$ respectively. According to phasor algebra:

$$\vec{X}_{ds} = \vec{X}_{ss} + \vec{X}_{uk}, \quad (9)$$

hence, we can estimate the unknown component by computing the subtraction of the two complex numbers corresponding to the known phasors, i.e.:

$$\vec{X}_{uk} = \vec{X}_{ds} - \vec{X}_{ss}. \quad (10)$$

To this end, we firstly obtained the phasors' values for phase and amplitude as follows: (1) We designated \vec{X}_{ss} as the "reference phasor" and, hence, $\phi_{ss} = 0$. (2) From the transfer function we obtained the phase value between SS and DS at the task frequency f_t , so $\phi_{ds} = \arg(H(f_t))$, which indicates the phase-shift of \vec{X}_{ds} with respect to \vec{X}_{ss} . (3) A_{ds} was obtained from the PSD by calculating the RMS amplitude at f_t and converting it to the peak amplitude of

a sinusoid i.e. $A_{ds} = \sqrt{2} \sqrt{PSD(f_t)FR}$, where FR is the frequency resolution (0.005 Hz in our case). Due to spectral leakage, better amplitude estimates are obtained by summing the PSD values within the frequency interval $[f_t - FR, f_t + FR]$. (4) A_{ss} was estimated in the same way and then scaled to the theoretical value that it should reach in DS by itself. This is a crucial step in the procedure. The scaling factor was the gain value of the transfer function at f_t but during “baseline”, which represents the fraction of SS magnitude present in DS when no significant deep component contributes. Thus, A_{ss} was multiplied by the baseline gain to yield its scaled amplitude. Then, we performed the phasor subtraction (Eq. 10) to obtain the amplitude A_{uk} and the phase ϕ_{uk} of the phasor \vec{X}_{uk} . Finally, \vec{X}_{uk} was converted to a sinusoid, which represents the alternative CS estimated by transfer function. This procedure was performed for every single-participant’s signals and averages were computed for each ROI and chromophore.

2.5.8 Simulations

To assess the feasibility of CS estimation by phasors, we performed a fairly realistic simulation by using the actual data during task rather than artificial or baseline signals. SS was used as is. DS was obtained by scaling SS to the amplitude that it should reach in the deep-recording, i.e. multiplying by the transfer function gain during baseline (See Section 3.5.7., step 4). We generated a synthetic neural signal as a sinusoidal wave oscillating at 0.033 Hz, with amplitude and phase obtained from the averaged CSs estimated by regression (amplitude = 0.05 μM and 0.04 μM , time-lag = 13 and -9.5 sec for HbO and HbR respectively and relative to CS) (See Results 4.2.2. and Figure 39). Then, the sinusoid was added to DS to build the simulated deep-signal. This procedure was applied to the medial-ROI data of every participant and then subjected to both regression and phasor estimation of the neural component. Since phasor-estimated result represents the average over the task, the regression-estimated signal was averaged across trials to allow intra-subject comparisons. The quality of the neural estimates was quantified using the root mean square error (RMSE) between the true synthetic signal and the recovered one. A paired t-test was applied to resolve for statistical differences.

2.5.9 Measuring HbO/HbR coupling

To investigate significant frequency-domain correlation between HbO and HbR, we computed their MSC and CPSD during the baseline and task conditions. In this case, we were only interested in the SS and CS signals because we assume that DS is nothing more than the linear combination of the first two. MSC and CPSD data, as well as their averages and significance thresholds, were obtained by the same procedure previously detailed. In addition, from the complex-valued CPSD we extracted the phase data (Müller et al., 2003; Reinhard et al., 2006) at the task-frequency to assess the temporal relation (time-shift) between both chromophores. As usual, this procedure was applied for every single participant. Next, we computed the circular mean of phase angles at the group level and then, to assess whether it was significantly oriented in a preferred direction, we applied a bootstrapped Rayleigh test (Oden, 1983) through 2000 resamples. The 95% CI was also computed by bootstrapping.

2.5.10 Measuring HbO/ Heart rate coupling

As in Section 3.5.9., we investigated the relationships between HbO and heart rate by MSC and CPSD. We only used the HbO data of the SS signals because the coupling between heart rate and the rest of signals can be inferred from the results obtained in other previously performed tests.

3.1 Initial testing

3.1.1 Light-emitting diode spectral calibration

The manufacturer's specifications indicated that LEDs had an emission spectrum located at 740nm and 850nm. The spectral irradiance figures confirm this aspect since for both wavelengths the spectrum of the emitted light is sharply peaked and invariant despite power modifications (Figure 32 and 33).

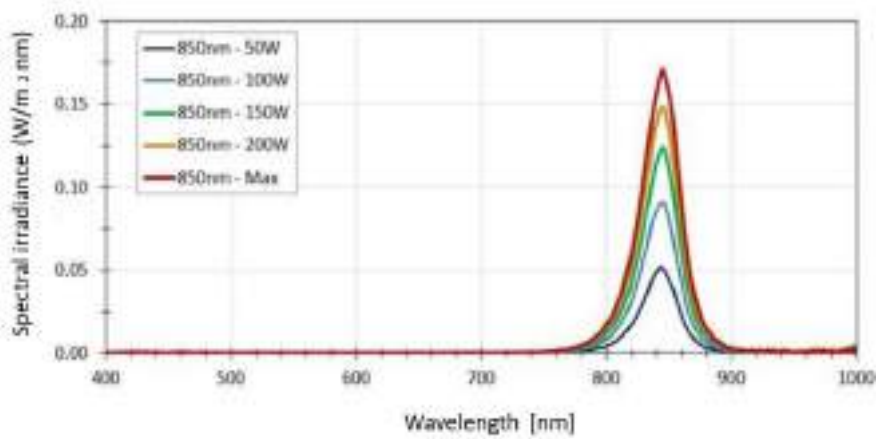


Figure 32. 850 nm spectral irradiance at different LED power values.

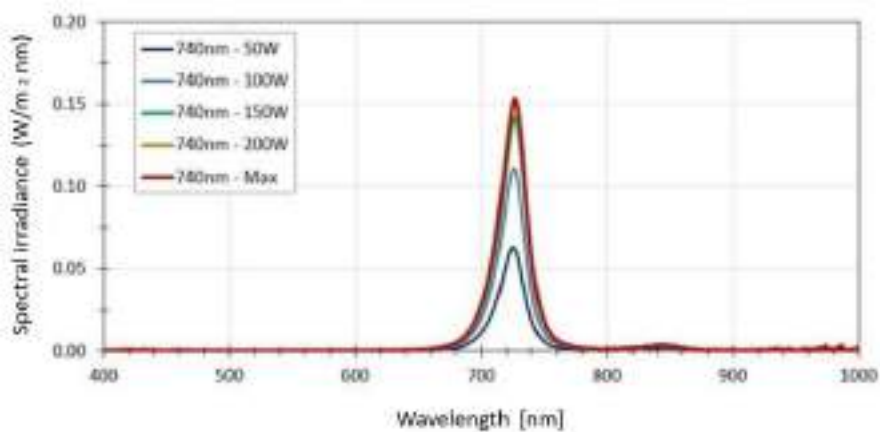


Figure 33. 740 nm spectral irradiance at different LED power values.

3.1.2 Detection of well-known spontaneous oscillations

As shown in Table 7, the cardiac band is the one with the highest percentage of PSD displays, followed by the Mayer band and the respiratory band, regardless of the type of chromophore and channel. Comparing both chromophores, we observe that HbO generally shows higher percentages of PSD in the cardiac and Mayer band than HbR, while in the respiratory band HbR presents slightly higher values than HbO (Table 7). Moreover, NIRS raw signals clearly show cardiac pulsation and respiratory cycle waveforms (Figure 34). This fact is corroborated by the appearance of a HbO and HbR characteristic power spectrum confirming that the signals acquired with Theia display the typical oscillatory components of quality NIRS signals (Figures 35 and 36).

Table 7. PSD descriptive statistics of the cardiac, respiratory and Mayer bands for each chromophore and channel type.

Channel	Chromophore	Cardiac band	Respiratory band	Mayer band
		M (SD)	M (SD)	M (SD)
Short	HbO	27.32% (18.10)	1.20% (1.02)	21.26% (13.34)
	HbR	11.75% (8.48)	1.89% (1.05)	9.86% (8.70)
Long	HbO	19.71% (12.71)	1.46% (0.80)	12.03% (9.77)
	HbR	9.57% (5.26)	1.88% (0.97)	5.35% (4.11)

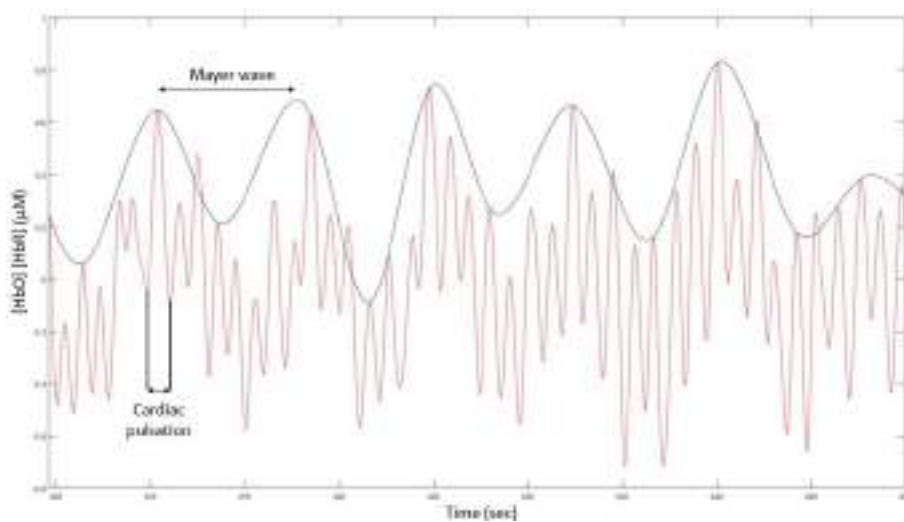


Figure 34. Detection of well-known oscillations in a sample raw signal of HbO from a representative subject. NIRS raw signals clearly show cardiac pulsation and Mayer waves. Different well-known oscillations characteristic of a NIRS signal are indicated by arrows.

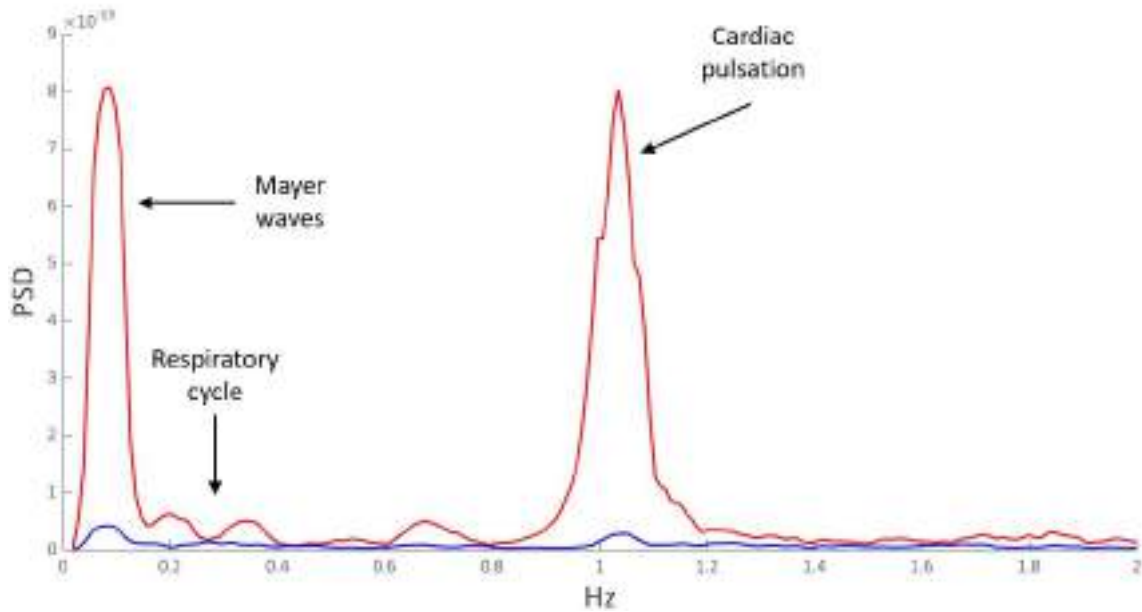


Figure 35. Comparison of Oxyhaemoglobin (red line) and Deoxyhaemoglobin (blue line) power spectral density from a representative subject's short signal. Different well-known oscillations characteristic of a NIRS signal are indicated by arrows.

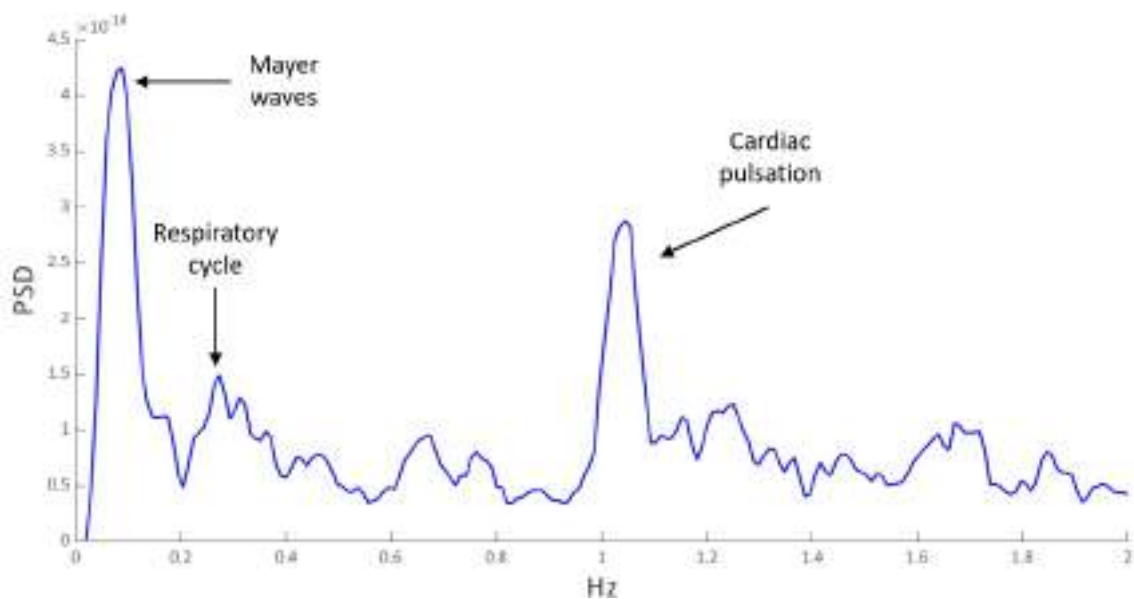


Figure 36. Deoxyhaemoglobin (blue line) power spectral density from a representative subject's short signal. Different well-known oscillations characteristic of a NIRS signal are indicated by arrows.

3.1.3 [HbO] and [HbR] cross-talk assessment

First evidence of the absence of cross-talk is the fact that HbO shows higher PSD values in the cardiac and Mayer band compared to HbR, which proves certain independence in the measurements of both chromophores. However, we should check this fact specifically through

the coherence values between HbO and HbR and their angles (Table 8). Coherence levels are particularly high in the two types of channels studied, while the angular values are concentrated around 130 on average, which implies that the HbO and HbR signals oscillate almost in counterphase at cardiac band (Table 8).

Table 8. Coherence and angle descriptive statistics of the cardiac band for each chromophore and channel type.

Channel	Chromophore	Coherence	Angle
		M (SD)	M (SD)
Short	HbO-HbR	0.70 (0.10)	111.6 (67.7)
Long	HbO-HbR	0.68 (0.09)	163.8 (54.1)

3.1.4 Limb vascular occlusion test

In venous occlusions, the pneumatic cuff reached pressures between 20-70 mmHg, preventing venous outflow but keeping arterial inflow intact. In NIRS signals the cuff inflations were followed by a marked rapid increase in HbR due to increased venous blood volume (Figure 37). In arterial occlusion, the pneumatic cuff reached a pressure of 250 mmHg, blocking the venous outflow and arterial inflow. Since the tissues continue to consume oxygen, this situation results in an HbO decrease and a matching HbR increase. After deflation of the occluding cuff a typically reactive hyperaemic post-occlusive response was observed in the Figure 37 (rapid HbO increase and consequent HbR washout) which reflects the rapid restoration of blood flow.

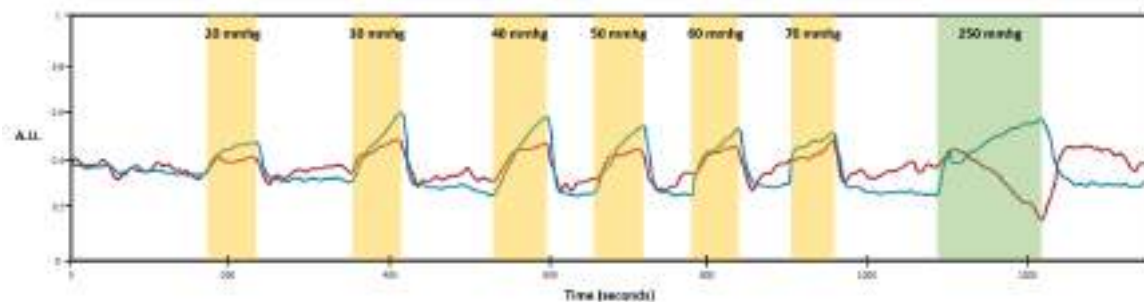


Figure 37. Time courses of HbO (red line) and HbR (blue line) during venous (yellow rectangles) and arterial (green rectangles) occlusion.

3.2 Experimental validation through a paradigm of mental arithmetic

3.2.1 Assessment of physiological stress responses

We analyzed how fNIRS signals fluctuate in response to a cyclic mental arithmetic task, which can induce physiological stress responses (Charles & Nixon, 2019; Kudielka et al., 2007). To reduce any putative stress response that could have influenced our results we have taken several cautions. First, we have used a non-strenuous task duration, only 30 seconds, including a calculation and a recovery phase. Second, volunteers practiced the task for 10-15 minutes to make sure they understood and got used to it and the experimental setting. Third, the participants included in this study had a stable mental performance and reasonably low heart-rate fluctuations during the entire experimental session. In fact, they showed no significant differences between their heart rate values across the two conditions (baseline and task) of the experiment, (Wilcoxon's signed rank test, $p = .091$). On average, during task, the mean heart rate increased only slightly, 7 bpm (9%), with respect to the baseline (Table 9).

Table 9. Averaged heart rate metrics across participants (baseline and task).

All sample (20 participants)	Maximum	Mean
	Range	Range
Baseline	98 (62–127)	77 (53–104)
Task	103 (66–140)	84 (55–116)

3.2.2 Oscillations alignment to the task frequency

fNIRS signals showed clear oscillations in accordance with the task frequency and such oscillations were consistently observed, over multiple ROIs, on both shallow and deep layers. Figure 38 shows the results of the PSD analysis at the group level. The normalized PSDs were averaged across participants for each of the three ROIs, for each signal type and for each condition (baseline and task). The DC component (frequency = 0) was set to zero and the upper value of the displayed frequency range was limited to 0.08 Hz. A ubiquitous peak can be seen at ~ 0.01 Hz both at rest (Figure 38, black traces) and during mental task (Figure 38, colored traces), although the cluster-permutation test found no significant differences between both conditions. However, a clear peak at f_t was detected exclusively during the task and marked as significant

by the cluster-test ($p < 0.01$) (Figure 38, shaded vertical rectangles). This peak corresponds closely to the task frequency and was observed in all ROIs and signal types. In some cases, a secondary peak around 0.066 Hz was also found, which most likely represents a harmonic of the fundamental task-frequency. It seems obvious that the task successfully induced cyclic fluctuations of the HbO and HbR, which were present in the shallow-signals (Figure 38 SS), deep-signals (Figure 38 DS) and in clean-signals (Figure 38 CS).

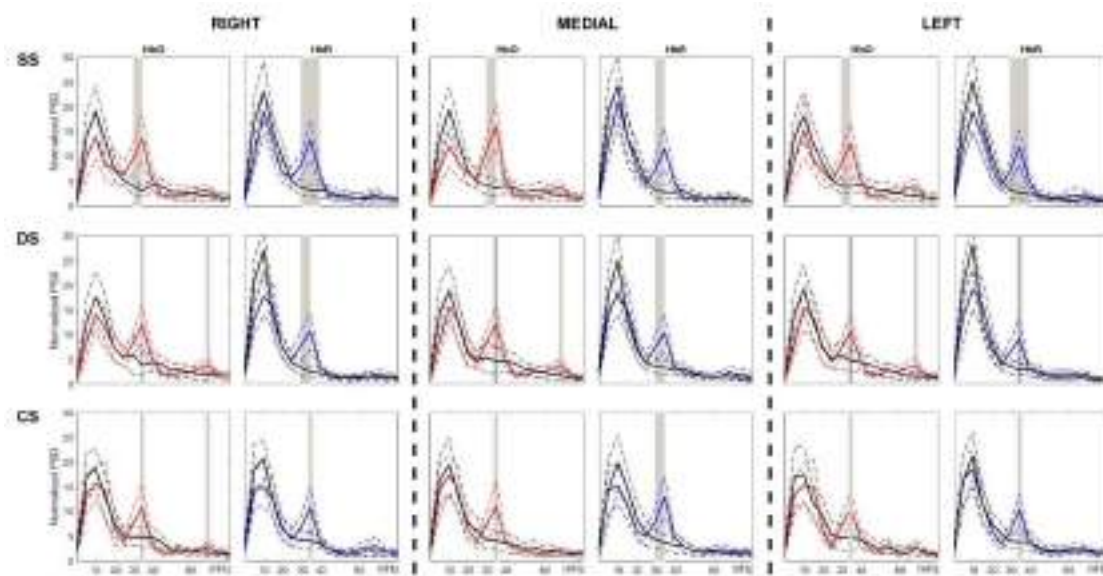


Figure 38. Grand average (20 participants) of the normalized PSDs for each ROI (right, medial and left), chromophore and signal type in the frequency range 0.005 to 0.08 Hz. Solid black curves refer to baseline and colored curves to task. Dashed lines represent the 95% CI of the mean. Shaded rectangles delimit the frequency ranges that show significantly higher power during task. (SS) results for shallow-signals. (DS) deep-signals. (CS) clean-signals.

Figure 39 shows the group-level averaged temporal traces of HbO and HbR after band-pass filtering around the task frequency, using a filter width of 0.015 Hz. It can be seen how SSS (Figure 39 SS) start to oscillate in sync with the task-trials, although showing an evident time-shift between both chromophores. Figure 39 also depicts the grand averages of the trials across participants (smaller plots next to temporal traces), which for SS display a common response consisting of: (i) shortly before the trial onset, the HbO strongly increases reaching a maximum at ~ 11.2 sec, (ii) then HbO gently returns to previous levels during the subsequent rest, and (iii) HbR changes were less pronounced and lead HbO by ~ 4 seconds. Regarding the DSS, a similar periodic response can be observed (Figure 39 DS), but HbO peaks are slightly anticipated to SS (~ 0.3 sec) while HbR lags SS by ~ 2 sec. Finally, CSS also show cyclic fluctuations aligned to the

task (Figure 40 CS), but in this case HbO oscillates in counter-phase with respect to SS. Furthermore, HbO and HbR show similar amplitudes ($\sim 0.05 \mu\text{M}$) and evolve anti-correlated with each other, HbO showing a valley at ~ 12.6 sec and HbR a peak at ~ 18.5 sec. At this point, it seems likely that the observed time-shift in DS, relative to SS, is due to the summation of the CS component. Interestingly, the pattern seen in CS would correspond to an inverted HbO/HbR response, i.e. decrease in HbO together with an increase in HbR. Noteworthy, the inverted pattern does not appear immediately but progressively reaches stability during the first few trials. This observation might be of interest for a tentative physiological interpretation (see 5.2. section).

Since fNIRS signals can be highly individual-specific, we have provided additional information about hemodynamic response and spectral data for each participant in the Supplementary figures (8.1. section) , with the aim of illustrating the individual differences and the variable contribution of surface tissues to the fNIRS signals in different regions of the forehead.

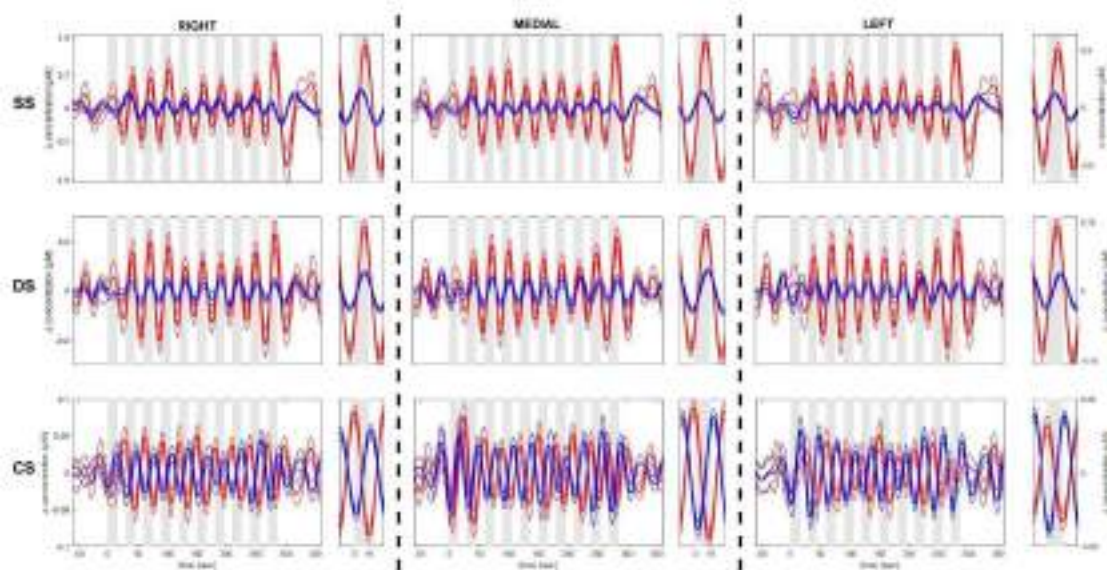


Figure 39. Averaged time courses of HbO (red traces) and HbR (blue traces) across participants during task (plus a portion of baseline and recovery to the left and right respectively) for each ROI and signal type. The small plots next to time courses show the grand average of trials. SEMs are depicted by thin lines. Gray boxes mark the 15-sec of mental math of each trial. Each row show the results for shallow (SS), deep (DS) and clean-signals (CS) for the three ROIs (right, medial and left).

3.2.3 SS/DS relationships

To answer the question of to what extent shallow fluctuations, contribute to deep-signals, we performed coherence, cross-spectra and a transfer function estimate between SS and DS data (Figure 40). The analysis revealed a significant cross-spectral peak during the task centered at f_t ($p < 0.01$), and that was present in all ROIs for HbO and HbR (Figure 40 A, left axis). These peaks indicate that SS and DS oscillate at the task frequency with a remarkable shared power. Moreover, a higher peak was located at ~ 0.01 Hz but showing no differences during task compared to baseline.

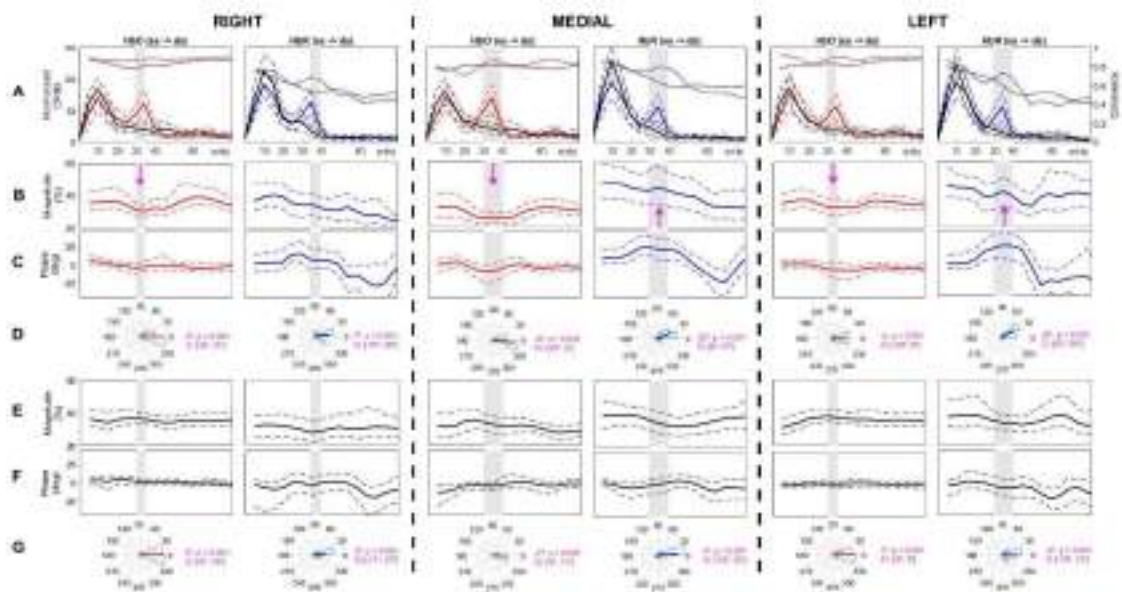


Figure 40. Averaged results across participants of CPSD, MSC and transfer function data between SS and DS for each ROI, comparing baseline and task. (a) CPSDs are drawn on the left axis and MSC on the right axis. Thick black curves correspond to baseline and the colored ones to task (HbO in red and HbR in blue). Dashed lines depict the 95% CI of the mean. Gray boxes indicate the frequencies that showed significantly higher cross-power during task. (b) Averaged gain values for task. Arrows point to frequencies showing clear disturbances in gain. (c) Averaged phase values for task. (d) Circular histograms of phase angles for task plus mean angles, p-values for the bootstrapped Rayleigh test and 95% CIs. (e–g) same as (b)–(d) but for baseline results.

Coherence values were above the significance threshold along the entire range of explored frequencies in both conditions (Figure 40 A, right axis), describing a consistent linear relationship between SS and DS in the frequency domain. Coherence levels were particularly high for HbO (on average > 0.8), indicating a stronger correlation and, likely, that HbO is more

influenced by shallow hemodynamics than HbR. It should be noted that coherence also peak during the task around f_t (quite evident for HbR), meaning that the task-induced oscillations were more coherent than the spontaneous ones.

During the task, transfer function analysis revealed a decrease in magnitude around f_t for HbO, especially pronounced in the medial ROI (Figure 40B). Phase values also showed certain perturbation at the same frequency (Figure 40C). HbR exhibited a slight increase in magnitude, mainly observed in the medial and left ROIs (Figure 40B), in parallel with strong disturbances in the phase values (Figure 40C). Again, the resting condition did not show such changes. A t-test revealed no differences at the group-level between gain values of HbO and HbR during rest ($p = 0.2$). However, during task the gain values were significantly lower for HbO ($p < 0.01$) in medial and left ROIs, which agrees with the decreasing gain values shown in Figure 40B. The paired t-test showed no differences for either HbO or HbR when comparing task with rest, indicating that on average the change during task is very subtle.

Circular histograms show that during rest the phase angles concentrates around 0° at the task frequency in all the cases (Figure 40G), being the Rayleigh test highly significant ($p < 0.01$) and the 95% CI quite narrow. This implies that SS and DS oscillate almost in-phase at that frequency (no time-lags). However, during the task the phases of HbR were shifted clearly to positive values (DS lags SS) in the medial and left ROIs by 22° and 30° respectively (Rayleigh test, $p < 0.01$), which correspond to time-lags of 1.8 and 2.5 sec at f_t (Figure 40D). Phase changes in HbO were less apparent than those of HbR, a slight shift to negative values (DS leads SS) was observed in the same ROIs (-8° and -4° , time-lags 0.6 and 0.3 sec). Noteworthy, the time-lags calculated from the phase values coincide with those obtained from the averaged time-series (see Figure 39).

As expected, these results corroborate that shallow- and deep-signals are highly correlated, underlining the strong influence of surface hemodynamics on deep recordings, which is particularly true for HbO (also observable within a single individual, compare Figure 45 and 46 of 8.1. section). Fortunately, the analysis also disclosed changes in magnitude and phase related to the task, pointing to the contribution of a deep component, uniquely present in DS, as responsible for the observed disturbances. Therefore, these findings confirm that our deep recordings captured other oscillatory processes that are different from the superficial ones.

3.2.4 Neural signal estimation by transfer function

We applied an alternative method to estimate the putative neural signal by using phasor representations of the magnitude and phase data obtained from transfer function. Under the assumption that signals were quasi-stationary over the short period of time determined by the task, we modeled them as sinusoids oscillating at 0.033 Hz, i.e. the task frequency. Phasor algebra was used to extract the hidden deep component that explained the disturbances observed in DS.

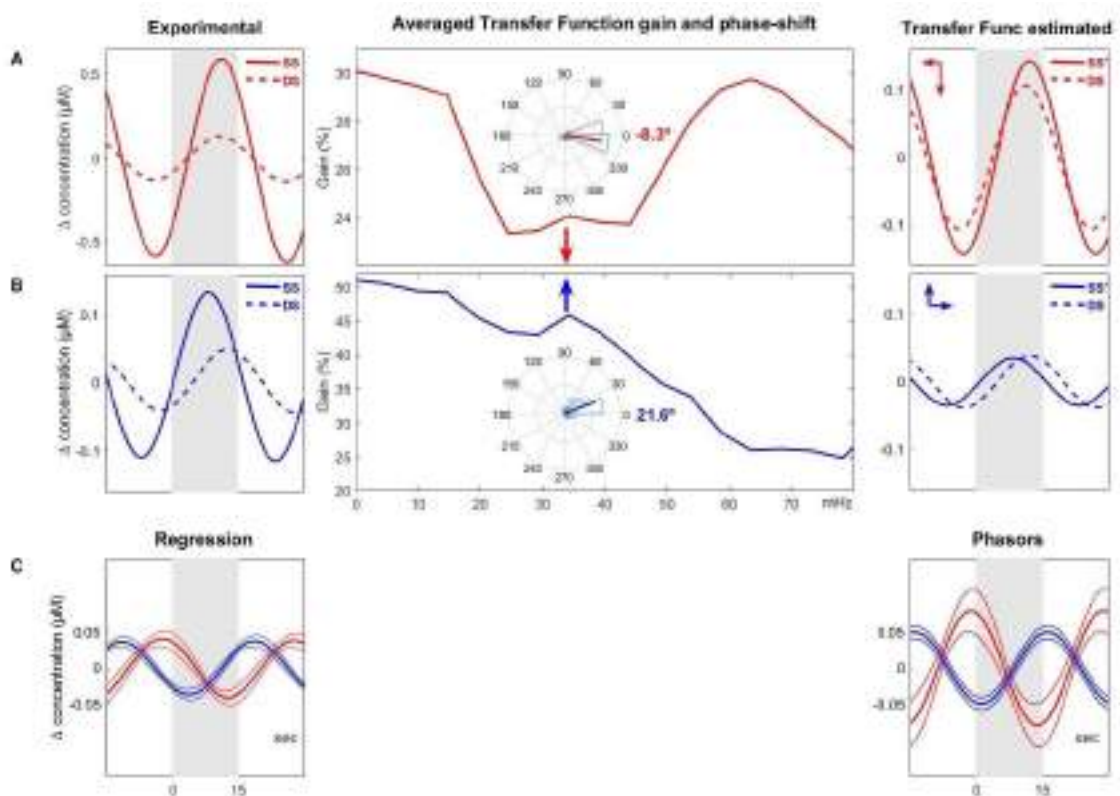


Figure 41. Illustrative comparison of neural signal estimation by regression and phasor analysis in the medial-ROI. Left plot a shows the grand averaged time courses across all the trials for HbO, comparing the experimental SS (solid trace) and DS (dashed trace). Similarly, left plot (b) shows the results for HbR. Right plot a compares the experimental DS for HbO (dashed) with the theoretical DS that should be observed if SS were the only contribution (solid). Arrows illustrate the amplitude and time shifts of the observed DS relative to the theoretical one. Right plot (b) shows the case of HbR. The central plots depict the averaged gain along frequencies for HbO (a) and HbR (b) with arrows indicating the direction of change at ft and the corresponding circular histograms of phase angles at that frequency. C plots show the averages of neural signals estimated by regression (left) and phasors (right) respectively. Thin lines represent SEMs.

As a representative example, Figure 41 compares the CS obtained by regression with that estimated from transfer function data in the medial ROI. As reported in section 4.2.3., the transfer function of HbO showed a clear decrease in magnitude around f_t in parallel with a phase-shift of about -8° , which is illustrated in the middle-plot of Figure 41A. The left-hand plot shows the grand-average of the experimentally obtained trials, comparing SS (solid line) and DS (dashed line). It can be seen the smaller amplitude of DS and the slight shift to the left with respect to SS. The right-hand plot shows what SS should look like in DS in the absence of any other interfering component, according to the magnitude estimate obtained at rest (see Section 3.5.7.). As the red arrows indicate, the magnitude and phase differences of the observed DS (dashed line) related to the predicted SS (solid line) are now more apparent.

After performing the phasor subtraction, the interfering deep component emerged as the sinusoid depicted by the red trace in the plot to the right of Figure 41C. In the case of the HbR, a small increase in magnitude and a phase-shift of about 22° were measured at $\sim f_t$. Similarly, the right-hand plot of Figure 41B illustrates the differences between the predicted (solid line) and observed (dashed line) DS. Phasor algebra pointed to the blue sinusoid drawn to the right of Figure 41C as responsible for the disturbances. The left-hand plot of Figure 41C shows the CSs obtained by means of regression. It can be seen the good match with the deep components estimated by phasors. For the three ROIs (right, medial and left), the estimated time lags between SS and CS were on average 11.5, 13 and 10.7 sec for HbO, and -9.9, -9.5 and -9.5 sec for HbR (Figure 50 in 8.1. section). Phasor analysis corroborates that the task induced deep hemodynamic fluctuations in form of an inverted HbO/HbR response, which from now on we will consider as the neural signal we were looking for. Despite individual differences, accounting for the inter-subject variability, we found that 90% of the participants ($n = 18$) showed this type of response in at least one ROI (Figure 47 in 8.1. section).

3.2.5 Simulation results

Figure 42A shows a segment of the bandpass filtered SS, simulated DS and synthetic neural response for each chromophore of a representative participant. Simple visual inspection reveals time courses comparable to the group-averaged experimental signals shown in Figure 39. The recovered signals averaged across all participants are shown in Figure 42B for each estimation method. In the case of HbO, it can be seen that the shapes of the recovered signals are very similar for both methods, but the phasors fit better to the true synthetic signal showing

significantly lower RMSE values (paired t-test, $p < 0.01$). HbR time courses were also comparable, but again phasors performed better ($p < 0.01$).

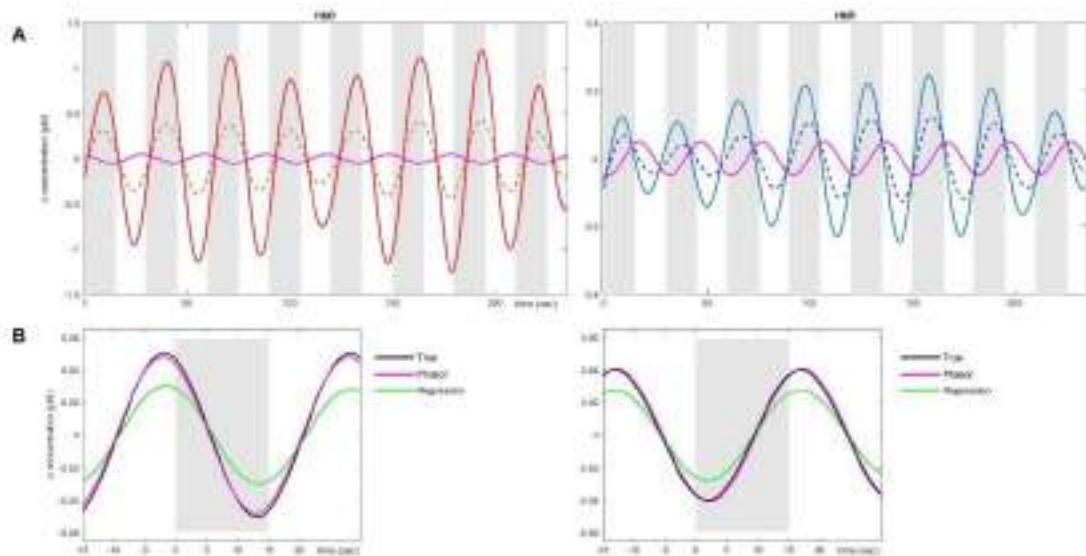


Figure 42. Construction of synthetic data and simulation results. (a) Simulated DS time courses for HbO (left) and HbR (right) data of a representative participant. DSs (dashed traces) were constructed by adding a synthetic neural signal (magenta traces) to the theoretical scaled version of the observed SS (solid traces in red and blue). (b) Averaged recovered signals across all participants for HbO (left) and HbR (right) by regression (green) and phasors (magenta), compared to the true synthetic signal (black).

These findings suggest that, compared to phasors, regression underestimates amplitude, mainly for HbO. Here, we found higher SS-DS coherence for HbO than for HbR, indicating a strong correlation that could affect more regression performance. Overall, phasors seem to work as well as or even better than regression and could help to independently verify the results in any case.

3.2.6 HbO/HbR coupling

During the task, CPSDs showed a significant peak of shared power at f_t in both SS (Figure 43SS, left axis, red trace) and CS (Figure 43CS, left axis, red trace) over all ROIs. MSC measures revealed significant frequency-domain correlation levels at several frequencies, as indicated by the asterisks along the MSC curves drawn in the right-axis of the spectral plots. It can also be seen that MSC levels were higher during the task (red trace) than at rest (black trace),

suggesting that the task increased coupling not only in its frequency but also beyond. Since interpreting coherence when spectral power is very low could be risky and results outside the task specific frequency were beyond the scope of the present work, here we focus solely on the peak of interest.

MSC also peaked around f_t , reaching the highest levels in the medial and left ROIs (MSC > 0.9, $p < 0.01$), which suggest strong correlation between HbO and HbR. Concerning temporal coupling for SS, circular histograms show how phase differences at f_t significantly concentrate during task around -39° , -39° and -47° in the right, medial and left ROIs respectively (Rayleigh test, $p < 0.01$), with HbR leading HbO by 3.2 to 3.9 sec (Figure 43SS, circular plots at bottom). For baseline data, phase analysis was not significant for any ROI (Figure 43SS, circular plots at top). Notably, CS revealed that, on average, HbO and HbR oscillate almost in phase-opposition in the medial and left ROIs (-162° and 176° respectively, $p < 0.01$), showing a time lag around 15-sec but with an unclear precedence. In the right ROI the significance level was not reached in any case. These results imply that the task induced coherent fluctuations between HbO and HbR in both shallow and deep layers, but with some differences. For SS, the temporal coupling was consistent across participants over all the ROIs, showing an out-of-phase relationship. However, CS phases were consistent at the group level only in the middle and left regions, moreover showing counter-phase fluctuations, in line with an inverted hemodynamic response.

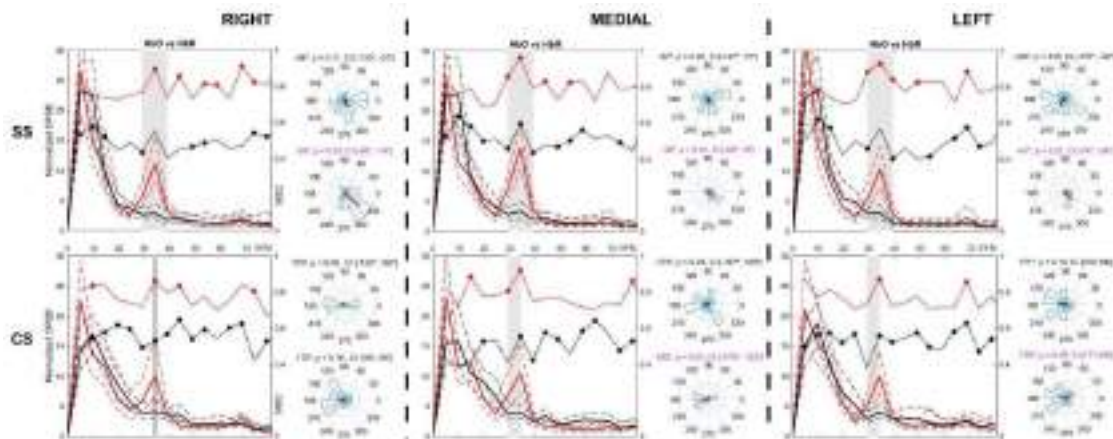


Figure 43. Averaged CPSDs, MSCs and phases between HbO and HbR for each ROI, comparing baseline and task. (SS) results for shallow-signals. CPSDs are drawn on the left axis for baseline (black curves) and task (red curves), dashed lines depict the 95% CI of the mean. Gray boxes indicate the frequencies that showed significantly higher cross-power during task. MSCs are shown on the right axis; asterisks indicate frequencies with significant coherence. Circular histograms show phase differences at f_t during baseline (top) and task (bottom); significant

phase concentration statistical values are labeled in magenta text. (CS) results for regression-estimated clean-signals.

3.2.7 HbO / Heart rate coupling

CPSD and MSC measures were also performed to investigate HbO and heart rate couplings. We focused solely on significant peaks in shallow signals. As illustrated in Figure 44, a peak of shared power was located in the three ROIs at f_t . In parallel, MSC also peaked at the same frequency, indicating strong correlation at the task frequency ($p < 0.01$). Notably, the phase mean did not reach significant levels in any case ($p > 0.05$). These results indicate that at the single-subject level HbO and heart rate oscillate well coupled, resulting in significant coherence at the averaged group level. However, individual phase values were different enough to disperse the angular mean, reflecting an evident inter-subject variability in the temporal coupling of the two signals (Figure 45 o 8.1. section). Figure 44 also shows the averaged fluctuations of the band-pass filtered HbO (bottom plots, red trace) and heart rate (bottom plots, black trace). The grand average of trials across participants (small plots next to time courses) also revealed that both signals start to increase few seconds before the trial onset.

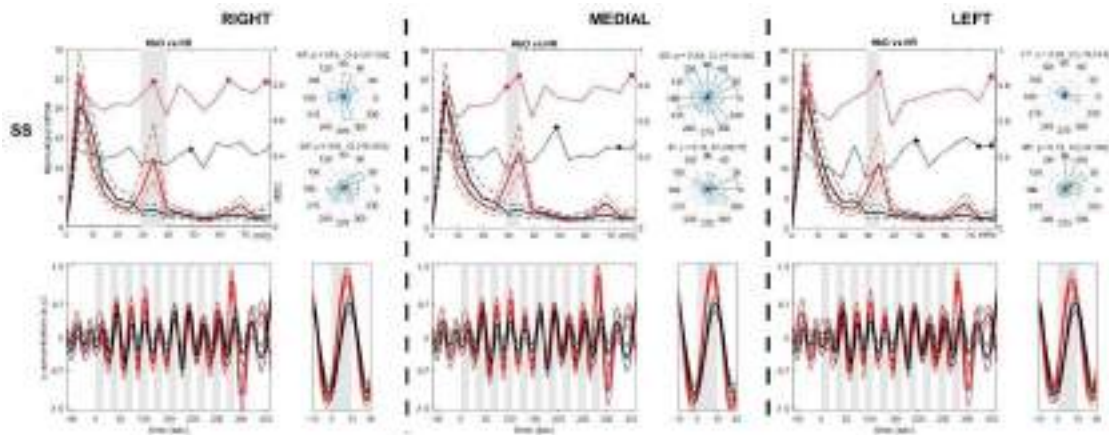


Figure 44. Averaged time courses, CPSDs, MSCs and phases between superficial HbO and heart rate (HR) for each ROI, comparing baseline and task. Top row plots show the CPSDs (left axis), MSCs (right axis) and circular histograms of phase differences at f_t . Baseline values are drawn in black and task values in red. Gray boxes delimit the frequencies with significant higher cross-power during task. Bottom row plots show HbO (red) and heart rate (black) time courses along the entire task; gray boxes mark the 15-s of mental math of each trial. The small plots next to time courses show the grand average of trials. Thin lines depict SEM.

4.1 Initial testing

Our first objective was to check whether Theia accomplished certain aspects typical of the validation of any new NIRS device. We demonstrated the performance of Theia device has been optimal in the spectral calibration of LEDs, detection of well-known spontaneous oscillations, cross-talk assessment and limb vascular occlusion test. Specifically, regarding light sources, the results have indicated that the LEDs emit light sharply peaked and invariant to power modifications, which is a vital prerequisite for the rest of the tests that have been carried out. In a further step, we investigated whether Theia fNIRS recording contained the well-known spontaneous oscillations. Our results have shown that we have found evidence of the presence of the three most relevant systemic oscillations in NIRS measurements. In fact, not only cardiac pulsation has been identified, which is simple because it is very intense, but we have also shown the presence of other challenging frequencies such as respiration and Mayer's waves, confirming the basic function of the Theia device. Interestingly, cardiac pulsations power was much greater than Mayer or respiratory waves, which agrees with previously reported works (Fekete et al., 2011; Obrig et al., 2000; Orihuela-Espina et al., 2010; Pinti et al., 2019; Pollonini et al., 2016; von Lüthmann et al., 2015). Furthermore, comparing chromophores we find that HbO dominates the cardiac and Mayer bands, while the oscillation of respiration shows greater power in HbR. Far from being a disconcerting result, this observation is supported by many previous works that have indicated that heart and Mayer fluctuations were primarily related to the arterial compartment and therefore especially affect HbO (Fantini, et al., 2018; Jones et al., 2016; Kirilina et al., 2013; Lynch et al., 2014; Reddy et al., 2021; Zhang et al., 2005, 2015). Because respiratory oscillations are caused by venous changes, they affect HbR to a greater extent (Fantini, et al., 2018; Kirilina et al., 2013; Lynch et al., 2014; Reddy et al., 2021; Zhang et al., 2005, 2015). Therefore, the heterogeneous presence of well-known spontaneous oscillations between the two chromophores is further confirmation of the quality of our measurements.

On the other hand, our results suggest that changes in inter-chromophores are independent, supporting the idea that cross-talk is low. This fact is based on the presence of different PSD profiles between HbO and HbR, which has already been commented on previously. Furthermore, in cardiac pulsation HbO and HbR signals are highly coherent and oscillate close to contraphase. It is known that in a minimum cross-talk condition, the periodic and spontaneous oscillations related to systole-diastole must produce opposite responses in both

chromophores, as we observed in our data (Fantini, et al., 2018b; Jones et al., 2016). Therefore, taking together these data support the idea that Theia's light source wavelengths have been chosen correctly.

Finally, the vascular occlusion test yields HbO and HbR typical courses described in previous literature (Barstow, 2019; Bezemer et al., 2009; Casavola et al., 2000; Dennis et al., 2021; Gerovasili et al., 2010; Jeffries et al., 2018; Jones et al., 2016; Kooijman et al., 1997; Lacroix et al., 2012; Lima & Bakker, 2005; Martin et al., 2013; Nioka et al., 2006; Zhang et al., 2020). In fact, our arterial and venous occlusion curves are identical to those displayed by Jones et al., (2016) and Kooijman et al., (1997), confirming that fNIRS Theia measurements are sensitive to pressure changes. Therefore, we can conclude that Theia instrument complies with all current technical validation standards for fNIRS system.

4.2 Experimental validation through a paradigm of mental arithmetic.

We found that mental arithmetic successfully evoked cyclic changes in NIRS signals measured in the frontopolar region, in the form of highly characteristic spectral peaks centered on the task frequency (i.e. 0.033 Hz), which provides evidence of the correct Theia instrument functioning in the context of cognitive paradigm. These peaks are clearly discernible from spontaneous activity in resting-state and apparently independent of a stress response. Since mental arithmetic tasks have been used frequently as stressors (Al-Shargie et al., 2016; Hakimi, 2018; Takamoto et al., 2013), and mental overload increases stress (Mandrick et al., 2016; Tao et al., 2019), the experimental protocol used here was tailored to minimize such an effect. Taken together, these data indicate that the rhythmic cognitive task proposed here is feasible to induce periodic hemodynamic fluctuations suitable for effective frequency-resolved measurements.

Predictably, we corroborated the strong influence of surface hemodynamics on deep fNIRS signals, as reflected by the high coherence levels found between signals obtained from multi-distance recordings. In this study, rather than simply considering the surface contribution as unwanted noise, we took advantage of the shared oscillatory state imposed by the task to extract amplitude and phase data, and use it to separate the true DS from that originating in extracerebral tissues. Notably, our results revealed that the deep signals extracted follow a pattern of HbO decrease accompanied by HbR increase, which is reversed (i.e. symmetrically opposite) with respect to the canonical brain activation response.

Previous works have reported that fNIRS signals oscillate close to the experimental stimulation frequency (Franceschini, Fantini, Toronov, Filiaci, & Gratton, 2000), for instance, using a motor task comprising sequences of 10 seconds of tapping and 17 seconds of rest, found spectral peaks at the frequency of the 27-s task period (0.037 Hz). Schroeter, Schmiedel, & Von Cramon, (2004), exploring the visual cortex, identified spectral peaks for HbO and HbR at 0.023 Hz, close to the 0.028 Hz corresponding to the visual stimulation cycle of 35 seconds (18-s of stimulation plus 17-s of rest). Likewise, Zhang, Brown, & Strangman (2007) also found a peak in visual cortex related to the stimulation frequency of 0.033 Hz. Regarding mental tasks, Kirilina et al. (2012) observed periodic changes in fNIRS, fMRI and other physiological signals, coupled to the single block period of an n-back (30-s) and a semantic task (34-s). Also using a semantic categorization task, Kirilina et al., (2013) identified coherent oscillations between skin blood flow and HbO corresponding to the 34-s period of stimulation. Nonetheless, with the exception of

Zhang et al. (2007), none of the cited studies used task / rest intervals of the same duration. We argued that a block-design consisting of exactly regular cycles would better induce an oscillatory state, stationary enough throughout the duration of the task to allow reliable measurements. Although no consensus exists as to the most appropriate stimulus interval in block-design experiments, fNIRS studies often fall in the range of very low frequencies (0.02 to 0.08 Hz), referred as “activation-band” by Kirilina et al. (2013). However, for frequency-analysis purposes, large task cycles lead to extremely low frequencies, which are difficult to identify and could overlap with spontaneous very slow waves (Stefanovska et al., 1999). For example, Vermeij, Meel-van den Abeelen, Kessels, van Beek, & Claassen, (2014), using a verbal n-back working-memory task of 180 seconds (0.005 Hz), only reported fluctuations in the range 0.02 to 0.07 Hz, correctly concluding that they could not be attributed to the task cycle. Likewise, Obrig et al. (2000) used similarly large periods of 120 seconds, finding peaks at 0.1-0.04 Hz, far from the 0.008 Hz predicted by the task frequency. On the contrary, short periods could fall within the range of spontaneous blood pressure waves (i.e. Mayer waves) that could obfuscate (or override) the functional response (Yücel et al., 2016). Furthermore, it might also be desirable to choose periods shorter enough to accommodate a single response (i.e. not several successively overlapped). Here, we used repetitive 15-s cycles of mental math plus 15-s pause, highlighting the oscillatory activity of 30-s period. We successfully found significant task-locked oscillations, separable from spontaneous activity, and showing time courses compatible with isolated, single responses. Further research is needed to test other stimulation periods that might be even more appropriate.

In almost all the aforementioned studies, the authors discussed the contribution of non-neural components to the observed fNIRS changes, stressing the importance of separating brain activation from these potential confounders. This concern should be particularly addressed when exploring the frontopolar region due to the influence of task-related skin blood flow changes, mainly on HbO signals (Haeussinger et al., 2014; Sato et al., 2013; Takahashi et al., 2011). It seems that, in most functional experiments, the superposition of extracerebral and cerebral hemodynamic responses could not be avoided, since they are not independent but inter-related processes (Caldwell et al., 2016; Tachtsidis & Scholkmann, 2016). Our results validate these considerations by showing that, on the frontopolar region, Theia deep-recordings are strongly influenced by superficial activity. In fact, by solely analyzing deep-signals without applying proper corrections, an activation response evoked by the task can be erroneously deduced. Such a misinterpretation is more likely when only HbO is taken into account, for example as seen in Figure 39DS where HbO shows a clear increase/decrease pattern locked to

the task. However, the HbR time course is less conclusive, not supporting a typical activation response and underscoring the need to assess both chromophores to convey more realistic interpretations (Fantini, et al., 2018). Our results also provide complementary evidence that surface hemodynamic influences the different haemoglobin species in a differential way, with HbO being more affected than HbR. This confirms the basic function of the Theia device since it agrees with previous studies that report a stronger influence of confounding factors on HbO (Bauernfeind et al., 2014; Gagnon et al., 2011; Heinzel et al., 2013; Kirilina et al., 2012).

To address the contamination issue, we employed a multi-distance approach in which each deep-recording was cleaned from surface influence by using two specific short-recordings as reference, thus controlling for inhomogeneous hemodynamic activity in the scanned surface area. As commented in Section 3.5.1., such a strategy is commonly accepted as very effective to remove noise, and even considered as a gold standard (Zhou et al., 2020). After performing conventional linear regression, we obtained a clean deep-signal for each ROI that also oscillates at the task frequency, but apparently showing deactivation instead of an expected activation (Figure 39CS). In view of this unusual pattern, and despite the thickness of the tissues that cover and protect the brain (see Section 3.5.6.), it was necessary to verify whether our short 14 mm recordings were also picking up cortical signals, leading to poorly estimated regression residuals. By exploiting the induced oscillatory state, we employed the empirical transfer function and phasor representation of HbO and HbR fluctuations (Figure 41) to explain the amplitude and phase disturbances observed in deep-signals. The results confirmed the presence of deep HbO and HbR components that fluctuate coupled to the task, following an inverted pattern with both chromophores almost in counter-phase. The convergence of two independent analysis, regression and transfer function, strongly supports the finding of a putative cortical response in the form of deoxygenation/oxygenation cycles; noteworthy, it was found in 90% of our sample, a considerable higher occurrence than those reported in, for example, motor imagery fNIRS studies (Abdalmalak et al., 2020; Holper, Shalóm, Wolf, & Sigman, 2011). Therefore, we demonstrated that Theia device short- and deep-recordings captured different hemodynamic components.

Moreover, simulated data revealed that combining transfer functions and phasors might provide better estimates of the amplitude of functional cortical responses. It is worth noting that if shallow and neural signals had oscillated highly correlated (positive or negatively), the regression could have failed because the scaling factor (beta) would have caused the subtraction to flatten the residuals, leading to accidental removal of the cerebral signal. This drawback could

be avoided using the method proposed here. Phasors were first proposed by Zheng, Sassaroli and Fantini (2010) to explain the phase relationships between hemoglobin species but, to our knowledge, this is the first time they have been used to analyze multi-distance fNIRS recordings. Further improvements on the method are currently under way.

Far from being a disconcerting result that casts doubt on the validity of the Theia system, the observation of the reverse oxygenation response is supported by many previous fNIRS studies that reported its occurrence using different task modalities, such as motor imagery (Abdalmalak et al., 2020; Holper et al., 2011), visual stimulation (Maggioni et al., 2015), working memory n-back (Haeussinger et al., 2014; Kirilina et al., 2012), emotional stimulation (Matsukawa et al., 2018) and mental arithmetic (Günther Bauernfeind, Leeb, Wriessnegger, & Pfurtscheller, 2008; Pfurtscheller, Bauernfeind, Wriessnegger, & Neuper, 2010).

This phenomenon has only been partially explained so far, being of considerable interest to understand the underlying neuro-vascular mechanisms and gain insight into the negative BOLD response observed in fMRI studies (see Holper et al. (2011) and Maggioni et al. (2015) for in-depth discussions of possible explanations). Regarding fNIRS studies probing the PFC during working memory tasks, some researchers found a decrease in HbO in frontopolar region using fixed inter-optode distances (i.e. no multi-distance correction), while they found no significant HbR changes (Haeussinger et al., 2014; Kirilina et al., 2012). They suggested that task-evoked sympathetic vasoconstriction drives skin blood flow changes, which in turn impair fNIRS long-recordings, leading to an apparent decrease in oxygenation response. Noteworthy, in both studies, fMRI data showed deactivation in the medial region of the PFC. In contrast, (Takahashi et al., 2011) found a positive pattern (i.e. increased oxygenation) using a verbal-fluency task, which they attributed to skin vessels dilatation by comparing short- (5 mm) and long-distance (30 mm) signals and showing that the effect disappears when pressure is applied to the skin. In the present work, we used two SCs to clean each long recording, which is a very effective method to remove the components (of local or systemic origin) that are common to the shallow and deep-signals (Fantini, et al., 2018). However, if a systemic component appears at different times in the surface and deep layers (e.g. blood flow delay), the regression itself may render a false neuronal response. Time differences in vascular reactivity driven by the task (e.g. delayed autonomic mediation) may also cause delays between layers. (Wyser et al., 2020) reported an average time lag of ~ 0.51 sec between shallow and deep signals for Mayer pressure waves, similar to the values found by (Kirilina et al., 2013). Tong & Frederick, (2010) estimated a time of ~ 6 sec for a pressure wave to pass the whole brain. Using nose tip temperature as a proxy to

assess autonomic activity during a mental math task, Pinti, Cardone, & Merla, (2015) found mean time lags of less than 4 sec, albeit showing significant individual variability, between changes of cutaneous blood flow and prefrontal fNIRS signals. During a cognitive task, a mean time lag of ~6 sec between skin blood flow and prefrontal fNIRS signals was found in Kirilina et al., (2013). The phasor method do not solve the problem of different timing either, but they provide independent information about the delays between signals and avoid regression constraints. We found clearly longer delays than those we have mentioned (see Section 4.2.4. and Figure 50 in supplementary figures), and we believe that they are unlikely to be due to a delayed physiological response, otherwise they would reflect a considerable lack of coordination between autonomic and prefrontal activity. Assuming that the observed response is an artifact due to time delays, it can be expected that for a specific individual the delay will be the same in the three ROIs of the narrow frontopolar region explored. However, we found that in some participants showing consistent surface signals across ROIs, the estimated neural signal was clearly different depending on the region (e.g. participants 1, 2, 3 and 4, Figures 45 and 47 in 8.1. section). Therefore, we conclude that such an inverted pattern actually represents the functional cortical response. However, the existence of some delay cannot be fully ignored and follow-up work is required.

Overall, our results are more in line with those reported by Pfurtscheller et al., (2010). Using a similar task, they also found an HbO decrease in the medial area of the PFC, but no significant changes for HbR. They corrected for extracerebral contamination by employing a common average reference spatial filter, which relies on subtracting the averaged signals from each fNIRS channel. After correction, we found significant fluctuations for both HbO and HbR, which is of great interest for interpretation purposes and implies that our methodological approach is better suited to discriminate the functional brain response. Other fNIRS studies have reported reduced activation in medial areas of the frontal cortex related to arithmetic subtraction in adolescents (Artemenko et al., 2018) or to task difficulty (Verner et al., 2013). However, since they did not use multi-distance corrections, comparing results could be risky.

Currently, fNIRS inverse oxygenation response remains an open topic, as the underlying neurovascular mechanisms are only partially understood. Some studies have been devoted to relating it with the fMRI negative BOLD response (NBR) in visual (Maggioni et al., 2015) and motor cortices (Abdalmalak et al., 2020), investigating its potential cause. Maggioni et al., (2015) found a consistent spatial correlation between NBR and inverse fNIRS response, while Abdalmalak et al., (2020) attribute the phenomenon to motion artifacts. The first discuss in-

depth on the origin of NBR, favoring the idea of neural deactivation (Mullinger et al., 2014) against the “blood stealing” explanation promoted by other authors (Shmuel et al., 2002). Pfurtscheller et al., (2010) also explained the inverse response in terms of a “focal activation/surround deactivation” pattern. Since we did not find any delay in the hemodynamic response, our results also speak against a sequestration of blood from neighboring areas to active areas. Our NIRS probe covered a relatively small area of the PFC, so our data are insufficient to support or reject the idea of concurrently activated and deactivated areas. However, based on the delay need to reach consistent counter-phase changes in HbO/HbR and the strong rhythmicity imposed by the task, we suggest a simpler explanation. It may be plausible that such an inverted response actually expresses a cyclical brain activation state, which after reaching stability appears as a period of oxygen consumption (during mental effort) in a previously well oxygenated brain area, followed by a subsequent re-oxygenation (during the pause). Thus, in the steady-state, the mental effort period starts under a condition of O₂ excess (or compensated) that leads to use the currently available O₂ until a new supply of fresh blood is needed. In this line, Wylie et al. (2009) proposed that different HbO/HbR (and total Hb) combinations might be present in activated visual cortex areas. Nevertheless, more research is needed to fully elucidate the complex coupling between O₂ consumption and blood flow/volume changes in the PFC.

We also found that only the medial and left ROIs showed a consistent inverse response at the group level, which is supported by the significant concentration of HbO/HbR phase angles around 180° (Figure 43CS) and the stronger disturbances in gain and phase detected by transfer function during the task (Figure 40). This finding suggests that, on average, frontopolar activity was slightly lateralized to the left. A meta-analysis conducted by Arsalidou and Taylor, (2011) indicates that, among others, frontopolar area seems to be generically engaged in mental arithmetic, sustaining working memory functions that are necessary to achieve good mathematical performance. They proposed that, for calculation tasks, this area manages the successive executive steps that can lead to the final calculated result. Noteworthy, they also reported that activity in the left part of FPC was concordant among studies involving calculation tasks. The characteristics of our arithmetic task fit with that functional specialization since it is necessary to coordinate each of the iterative subtractions (steps), while holding the result of the previous operation in the working memory, and then combining both to obtain the final result (main goal). Nonetheless, since we did not control for task difficulty or used calculation modalities other than subtraction, we acknowledge that complementary research is needed for more rigorous comparisons and interpretations. In any case, an important point to be also

considered is whether the observed response can be attributed to the "task-negative" activity of the default-mode network (DMN) (Raichle et al., 2001; Raichle & Snyder, 2007). As the brain region interrogated by our NIRS probe overlaps with the medial PFC (DMN-associated region), our findings could reflect decreased neuronal activity in this key region due to task engagement. Since DMN also include deeper structures, unreachable for fNIRS, exploring this possibility will require further research using fMRI imaging methods.

Concerning shallow hemodynamic, we found a consistent task-locked pattern of monotonic HbO increase followed by a decrease during the task pause, which was shortly preceded by similar HbR changes of lesser amplitude. As previously discussed, these fluctuations greatly impair the deep-recordings and potentially lead to their misinterpretation as brain activation, especially when only accounting for HbO. Therefore, we suggest special caution should be taken when interpreting HbO changes reported by fNIRS studies employing mental arithmetic tasks and using only long-recordings (Çiftçi et al., 2008; Tanida et al., 2004; Verner et al., 2013; Yang et al., 2009).

Aiming to elucidate the origin and influence of the extracranial confounds present in fNIRS signals, some studies monitored concurrently skin blood flow, heart rate and arterial blood pressure during cognitive tasks (Haeussinger et al., 2014; Kirilina et al., 2012; Takahashi et al., 2011). Although with variable results, they suggested that task-induced sympathetic outflow (leading to increased cardiac output and arterial blood pressure), together with skin blood flow/volume changes due to local vasomotion (constriction and/or dilatation), are the mechanisms responsible for these extracranial hemodynamic changes. In our work here, we consider that skin blood flow contribution has been small or negligible due to: (i) the optode-skin interface of our NIRS device reduces the skin blood flow (see Section 3.2.), and (ii) our short-channels are long enough (14 mm) to allow light penetrate deeper into the subcutaneous and muscle tissues of the forehead (perhaps even the skull), with little contribution of the skin compared with the volume illuminated. Therefore, albeit we cannot exclude local vasodynamics effects, we point to a systemic drive as the major cause. Our findings revealed that the task induced highly coherent heart/HbO fluctuations at the single-subject level, but with considerable individual variability in their temporal coupling, which leads to inconsistent phase values at the group level (Figure 44). Many studies have emphasized the link between fNIRS signals, heart rate and blood pressure during rest and under functional stimulation (Franceschini et al., 2000, 2006; Kirilina et al., 2012; Minati et al., 2011; Tachtsidis et al., 2008, 2009; Takahashi et al., 2011). In our work, we did not monitor blood pressure, thus preventing the possibility of

linking it with heart rate and HbO. However, based on the aforementioned studies, we reasonably assume that the task used here may also have induced blood pressure oscillations contributing to HbO fluctuations.

The observed HbO/HbR surface pattern seems compatible with an oxygenation effect due to an increased arterial inflow in the micro-vascular bed, which in turn leads to parallel HbR changes. Thus, the phase difference between HbO and HbR (-39° to 47°) would reflect the complex contribution of capillary transit time, blood flow and blood volume changes in shallow layers (Elting et al., 2020; Zheng et al., 2010). However, mainly for HbR, other mechanisms as forehead venous volume changes (Kirilina et al., 2012) or even superficial O₂ consumption could overlap. Another interesting possibility is that surface signals also overlap changes in CBF arising from increasing metabolic demands and cerebral autoregulation. This is plausible since we placed the NIRS probe over a forehead region mainly supplied by the supraorbital and supratrochlear arteries that ultimately connect (via the ophthalmic artery) to the frontopolar branch of the anterior cerebral artery, which plays a key role in blood supply to the frontal lobes. Prior studies have suggested that blood pressure measured from the supraorbital artery may reflect cerebral perfusion pressure (Lee & Westenskow, 1998; Narus et al., 1995), or that the clamping of the internal carotid affects both supraorbital blood flow and frontal lobe oxygenation (Hove et al., 2006). Jenkins and Brown (2014) also postulated the relationship between frontal activity asymmetry and forehead blood flow in a study using EEG and infrared thermography.

Another interesting finding was that the HbO response precedes the trial onset by some seconds. Previous studies reported that the PFC increases oxygenation a few seconds prior to the onset of voluntary exercise, independently of its actual intensity (Asahara et al., 2018; Ishii et al., 2018; Matsukawa et al., 2015). It has been hypothesized that a feedforward mechanism (termed 'central command'), involving higher brain centres, sends descending signals that adjust physiological systems, as the cardiovascular one, to the upcoming effort (Goodwin et al., 1972; Williamson, 2010). Furthermore, there is growing evidence that preparing for a mental challenge induces activity in certain cerebral areas as the anterior cingulate cortex and PFC (Sohn et al., 2007; Vassena et al., 2014, 2019). We suggest that, here, the anticipatory effect may have been enhanced by the use of such a rhythmic and predictable task. It is tempting to speculate that the aforementioned studies and our results point to the same task-related arousal mechanism that brings fresh arterial blood, full of oxygen to the cortex in preparation for upcoming cognitive demands.

Task-related arousal mechanisms requires a close interaction between cognitive function and autonomic control (Forte, et al., 2019; Forte, et al., 2019; Nicolini et al., 2014; Thayer & Lane, 2009; Wang et al., 2016). Thus, the autonomic control appears to be associated with activity levels in executive brain regions, which allows an adaptive response to environmental demands. Conversely, autonomic dysfunctions may be related to the deterioration of certain cognitive functions, specifically of executive functions (Forte, et al., 2019; Forte, et al., 2019). This close coordination of extracerebral and cerebral responses with the task period may have great functional value. The correct coupling between physiological resources may be the sign of proper cognitive and/or cardiovascular function and, its disruption, a potential early marker of cognitive decline and/or cardiovascular disease.

The fNIRS system and the analysis methods presented in this work open up a wide range of possible applications both in research and in clinical diagnosis. The following serve as examples: (i) the result of technology transfer reflected in the USA patent "Method for obtaining near-infrared spectroscopy cerebral signal", application NO.17/720.914,2022, which has already received the "Notice of allowance" and will be posted soon; (ii) and the researchs titled "Identifying ADHD boys by very-low frequency prefrontal fNIRS fluctuations during a rhythmic mental arithmetic task" (Ortuño-Miró, Molina-Rodríguez, Belmonte & Ibáñez-Ballesteros, 2023) and "Stress estimation by the prefrontal cortex asymmetry: Study on fNIRS signals" (Molina-Rodríguez, Hidalgo-Muñoz, Ibáñez-Ballesteros & Tabernero, 2023).

5 Conclusions

- 1) The device has proven to be a valid instrument to assess the functional activity of the PFC, since it has fulfilled all the requirements stipulated in the previous literature regarding the validation of the new fNIRS instruments.
- 2) The mental arithmetic task proposed here is reliable to induce periodic hemodynamic fluctuations suitable for effective frequency-resolved approaches.
- 3) The approximation based on transfer function and phasor algebra has shown to be useful in estimating the putative functional brain activity and assessing the timed-coordination between extracerebral and cerebral responses.
- 4) Two independent methods to estimate the neural signal (linear regression and transfer function) have pointed out that mental arithmetic yields deoxygenation/oxygenation cycles.
- 5) There is a large contribution of superficial tissues to NIRS signals (especially in HbO).
- 6) The absence of measures to control the extracortical contamination can lead to serious misinterpretations.

6 Conclusiones

- 1) El dispositivo Theia ha probado ser un instrumento válido para evaluar la actividad funcional de la CPF, ya que ha cumplido con todos los requisitos estipulados en la literatura previa relativa a la validación de nuevos instrumentos fNIRS.
- 2) La tarea de aritmética mental propuesta aquí es fiable para la inducción de fluctuaciones hemodinámicas periódicas adecuadas para enfoques efectivos de resolución de frecuencia.
- 3) La aproximación basada en la función de transferencia y el álgebra fasorial ha mostrado utilidad en la estimación de la supuesta actividad cerebral funcional y en la evaluación de la coordinación temporal entre las respuestas cerebrales y extracerebrales.
- 4) Dos métodos independientes para la estimación de la señal neuronal (regresión lineal y función de transferencia) han señalado que la aritmética mental produce ciclos de desoxigenación/oxigenación.
- 5) Hay una gran contribución de los tejidos superficiales a las señales NIRS (especialmente en la HbO).
- 6) La ausencia de medidas de control de la contaminación extracortical podría producir serias malinterpretaciones.

7 References

- Aarabi, A., & Huppert, T. J. (2016). Characterization of the relative contributions from systemic physiological noise to whole-brain resting-state functional near-infrared spectroscopy data using single-channel independent component analysis. *Neurophotonics*, 3(2), 025004. <https://doi.org/10.1117/1.nph.3.2.025004>
- Aarabi, A., Osharina, V., & Wallois, F. (2017). Effect of confounding variables on hemodynamic response function estimation using averaging and deconvolution analysis: An event related NIRS study. *NeuroImage*, 155, 25–49. <https://doi.org/10.1016/j.neuroimage.2017.04.048>
- Aaslid, R., Blaha, M., Sviri, G., Douville, C. M., & Newell, D. W. (2007). Asymmetric dynamic cerebral autoregulatory response to cyclic stimuli. *Stroke*, 38(5), 1465–1469. <https://doi.org/10.1161/STROKEAHA.106.473462>
- Aasted, C. M., Yücel, M. A., Cooper, R. J., Dubb, J., Tsuzuki, D., Becerra, L., Petkov, M. P., Borsook, D., Dan, I., & Boas, D. A. (2015). Anatomical guidance for functional near-infrared spectroscopy: AtlasViewer tutorial. *Neurophotonics*, 2(2), 020801. <https://doi.org/10.1117/1.nph.2.2.020801>
- Abdalmalak, A., Milej, D., Cohen, D. J., Anazodo, U., Ssali, T., Diop, M., Owen, A. M., & Lawrence, K. (2020). Using fMRI to investigate the potential cause of inverse oxygenation reported in fNIRS studies of motor imagery. *Neuroscience Letters*, 714, 134607. <https://doi.org/10.1016/j.neulet.2019.134607>
- Abramo, A. C. (1995). Anatomy of the Forehead Muscles: The Basis for the Videoendoscopic Approach in Forehead Rhytidoplasty. *Plastic and Reconstructive Surgery*, 95(7), 1170–1177. <https://doi.org/10.1097/00006534-199506000-00005>
- Agorgianitis, L., Panagouli, E., Tsakotos, G., Tsoucalas, G., & Filippou, D. (2020). The supratrochlear artery revisited: an anatomic review in favor of modern cosmetic applications in the area. *Cureus*, 12(2) <https://doi.org/10.7759/cureus.7141>
- Almajidy, R. K., Mankodiya, K., Abtahi, M., & Hofmann, U. G. (2020). A newcomer's guide to functional near infrared spectroscopy experiments. *IEEE Reviews in Biomedical Engineering*, 13, 292–308. <https://doi.org/10.1109/RBME.2019.2944351>

- Al-Rawi, P. G., Smielewski, P., & Kirkpatrick, P. J. (2001). Evaluation of a near-infrared spectrometer (NIRO 300) for the detection of intracranial oxygenation changes in the adult head. *Stroke*, 32(11), 2492-2500. <https://doi.org/10.1161/hs1101.098356>
- Al-Shargie, F., Kiguchi, M., Badruddin, N., Dass, S. C., Hani, A. F. M., & Tang, T. B. (2016). Mental stress assessment using simultaneous measurement of EEG and fNIRS. *Biomedical Optics Express*, 7(10), 3882. <https://doi.org/10.1364/boe.7.003882>
- Amaro, E., & Barker, G. J. (2006). Study design in fMRI: Basic principles. *Brain and Cognition*, 60(3), 220–232. <https://doi.org/10.1016/j.bandc.2005.11.009>
- Arsalidou, M., & Taylor, M. J. (2011). Is 2+2=4? Meta-analyses of brain areas needed for numbers and calculations. *NeuroImage*, 54(3), 2382–2393. <https://doi.org/10.1016/j.neuroimage.2010.10.009>
- Artemenko, C., Soltanlou, M., Ehlis, A. C., Nuerk, H. C., & Dresler, T. (2018). The neural correlates of mental arithmetic in adolescents: A longitudinal fNIRS study. *Behavioral and Brain Functions*, 14(1), 1–13. <https://doi.org/10.1186/s12993-018-0137-8>
- Asahara, R., Endo, K., Liang, N., & Matsukawa, K. (2018). An increase in prefrontal oxygenation at the start of voluntary cycling exercise was observed independently of exercise effort and muscle mass. *European Journal of Applied Physiology*, 118(8), 1689–1702. <https://doi.org/10.1007/s00421-018-3901-4>
- Atsumori, H., Kiguchi, M., Obata, A., Sato, H., Katura, T., Funane, T., & Maki, A. (2009). Development of wearable optical topography system for mapping the prefrontal cortex activation. *Review of Scientific Instruments*, 80(4). <https://doi.org/10.1063/1.3115207>
- Bale, G., Elwell, C. E., & Tachtsidis, I. (2016). From Jöbsis to the present day: a review of clinical near-infrared spectroscopy measurements of cerebral cytochrome-c-oxidase. *Journal of Biomedical Optics*, 21(9), 091307. <https://doi.org/10.1117/1.jbo.21.9.091307>
- Barstow, T. J. (2019). Understanding near infrared spectroscopy and its application to skeletal muscle research. *Journal of Applied Physiology*, 126(5), 1360-1376. <https://doi.org/10.1152/jappphysiol.00166.2018.-Near>
- Bauernfeind, G., Böck, C., Wriessnegger, S. C., & Müller-Putz, G. R. (2013). Physiological Noise Removal from fNIRS Signals. *Biomedical Engineering*, 58, 2–3. <https://doi.org/10.1515/bmt-2013-4430>

- Bauernfeind, G., Leeb, R., Wriessnegger, S. C., & Pfurtscheller, G. (2008). Development, set-up and first results for a one-channel near-infrared spectroscopy system / Entwicklung, Aufbau und vorläufige Ergebnisse eines Einkanal- Nahinfrarot-Spektroskopie-Systems. *Biomedizinische Technik/Biomedical Engineering*, 53(1), 36–43.
<https://doi.org/10.1515/BMT.2008.005>
- Bauernfeind, G., Wriessnegger, S. C., Daly, I., & Müller-Putz, G. R. (2014). Separating heart and brain: On the reduction of physiological noise from multichannel functional near-infrared spectroscopy (fNIRS) signals. *Journal of Neural Engineering*, 11(5).
<https://doi.org/10.1088/1741-2560/11/5/056010>
- Beer. (1852). Bestimmung der Absorption des rothen Lichts in farbigen Flüssigkeiten. *Annalen Der Physik Und Chemie*, 162(5), 78–88. <https://doi.org/10.1002/andp.18521620505>
- Bell, A. H., Miller, S. L., Castillo-Melendez, M., & Malhotra, A. (2020). The Neurovascular Unit: Effects of Brain Insults During the Perinatal Period. *Frontiers in Neuroscience*, 13, 1452.
<https://doi.org/10.3389/fnins.2019.01452>
- Bendall, R. C. A., Eachus, P., & Thompson, C. (2016). A brief review of research using near-infrared spectroscopy to measure activation of the prefrontal cortex during emotional processing: The importance of experimental design. *Frontiers in Human Neuroscience*, 10, 529. <https://doi.org/10.3389/fnhum.2016.00529>
- Berens, P. (2009). CircStat: A MATLAB Toolbox for Circular Statistics. *Journal of Statistical Software*, 31(10), 1–21.
- Bergersen, T. (1993). A search for arteriovenous anastomoses in human skin using ultrasound Doppler. *Acta Physiologica Scandinavica*, 147(2), 195–201.
<https://doi.org/10.1111/j.1748-1716.1993.tb09489.x>
- Bezemer, R., Lima, A., Myers, D., Klijn, E., Heger, M., Goedhart, P. T., Bakker, J., & Ince, C. (2009). Assessment of tissue oxygen saturation during a vascular occlusion test using near-infrared spectroscopy: the role of probe spacing and measurement site studied in healthy volunteers. *Critical Care*, 13 (1), 1-2. <https://doi.org/10.1186/cc8002>
- Bludau, S., Eickhoff, S. B., Mohlberg, H., Caspers, S., Laird, A. R., Fox, P. T., Schleicher, A., Zilles, K., & Amunts, K. (2014). Cytoarchitecture, probability maps and functions of the human frontal pole. *NeuroImage*, 93, 260–275.
<https://doi.org/10.1016/j.neuroimage.2013.05.052>

- Boas, D. A., Gaudette, T., Strangman, G., Cheng, X., Marota, J. J. A., & Mandeville, J. B. (2001). The accuracy of near infrared spectroscopy and imaging during focal changes in cerebral hemodynamics. *NeuroImage*, *13*(1), 76–90. <https://doi.org/10.1006/nimg.2000.0674>
- Boly, M., Gosseries, O., Massimini, M., & Rosanova, M. (2015). Functional Neuroimaging Techniques. In S. Laureys, G. Gosseries, & S. Tononi (Eds.), *The Neurology of Consciousness: Cognitive Neuroscience and Neuropathology* (pp. 31-45) Academic Press. <https://doi.org/10.1016/B978-0-12-800948-2.00002-9>
- Boschin, E. A., Piekema, C., & Buckley, M. J. (2015). Essential functions of primate frontopolar cortex in cognition. *Proceedings of the National Academy of Sciences of the United States of America*, *112*(9), E1020–E1027. <https://doi.org/10.1073/pnas.1419649112>
- Bouguer, P. (1729). *Essai d'optique, sur la gradation de la lumière*. Light zoom Lumière.
- Bracken, B. K., Festa, E. K., Sun, H. M., Leather, C., & Strangman, G. (2019). Validation of the fNIRS Pioneer™, a portable, durable, rugged functional near-infrared spectroscopy (fNIRS) Device. *HEALTHINF 2019 - 12th International Conference on Health Informatics, Proceedings; Part of 12th International Joint Conference on Biomedical Engineering Systems and Technologies (BIOSTEC)*, 521–531. <https://doi.org/10.5220/0007471405210531>
- Brigadoi, S., & Cooper, R. J. (2015). How short is short? Optimum source–detector distance for short-separation channels in functional near-infrared spectroscopy. *NeuroPhotonics*, *2*(2), 025005. <https://doi.org/10.1117/1.nph.2.2.025005>
- Bunge, S. A., & Kahn, I. (2009). Cognition: An overview of neuroimaging techniques. In L.R. Squire (Ed.), *Encyclopedia of Neuroscience* (pp 1063-1067). Academic Press. <https://doi.org/10.1016/B978-008045046-9.00298-9>
- Burgess, P., Burgess, & P. W., Wu (2013). Rostral prefrontal cortex (Brodmann area 10): metacognition in the brain. In D.T. Stuss & R.T. Knight (Eds.) *Principles of Frontal Lobe Function* (pp.524-534). Oxford University Press. <https://doi.org/10.1093/med/9780199837755.001.0001>
- Burgess, P. W., Veitch, E., de Lacy Costello, A., & Shallice, T. (2000). The cognitive and neuroanatomical correlates of multitasking. *Neuropsychologia*, *38*(6), 848–863. [https://doi.org/10.1016/S0028-3932\(99\)00134-7](https://doi.org/10.1016/S0028-3932(99)00134-7)

- Buxton, R. B., Uludağ, K., Dubowitz, D. J., & Liu, T. T. (2004). Modeling the hemodynamic response to brain activation. *NeuroImage*, *23*, S220-S233.
<https://doi.org/10.1016/j.neuroimage.2004.07.013>
- Cafardi, J. A. (2012). *The Manual of Dermatology*. Springer US. <https://doi.org/10.1007/978-1-4614-0938-0>
- Caldwell, M., Scholkmann, F., Wolf, U., Wolf, M., Elwell, C., & Tachtsidis, I. (2016). Modelling confounding effects from extracerebral contamination and systemic factors on functional near-infrared spectroscopy. *NeuroImage*, *143*, 91–105.
<https://doi.org/10.1016/j.neuroimage.2016.08.058>
- Carlén, M. (2017). What constitutes the prefrontal cortex? *Science*, *358*(6362), 478–482.
<https://doi.org/10.1126/science.aan8868>
- Carruthers, J. D. A., & Carruthers, J. A. (2018). Appreciation of the Vascular Anatomy of Aesthetic Forehead Reflation. *Dermatologic Surgery*, *44*(1), S2–S4.
<https://doi.org/10.1097/DSS.0000000000001688>
- Casavola, C., Paunescu, L. A., Fantini, S., & Gratton, E. (2000). Blood flow and oxygen consumption with near-infrared spectroscopy and venous occlusion: spatial maps and the effect of time and pressure of inflation. *Journal of Biomedical Optics*, *5*(3), 269.
<https://doi.org/10.1117/1.429995>
- Chance, B., Anday, E., Nioka, S., Zhou, S., Hong, L., Worden, K., Li, C., Murray, T., Ovetsky, Y., Pidikiti, D., & Thomas, R. (1998). A novel method for fast imaging of brain function, non-invasively, with light. *Optics Express*, *2*(10), 411. <https://doi.org/10.1364/OE.2.000411>
- Chance, B., Zhuang, Z., UnAh, C., Alter, C., & Lipton, L. (1993). Cognition-activated low-frequency modulation of light absorption in human brain. *Proceedings of the National Academy of Sciences*, *90*(8), 3770–3774. <https://doi.org/10.1073/pnas.90.8.3770>
- Charles, R. L., & Nixon, J. (2019). Measuring mental workload using physiological measures: A systematic review. *Applied Ergonomics*, *74*, 221–232.
<https://doi.org/10.1016/j.apergo.2018.08.028>
- Chiarelli, A. M., Perpetuini, D., Croce, P., Greco, G., Mistretta, L., Rizzo, R., Vinciguerra, V., Romeo, M. F., Zappasodi, F., Merla, A., Fallica, P. G., Edlinger, G., Ortner, R., & Giaconia, G. C. (2020). Fiberless, multi-channel fNIRS-EEG system based on silicon

photomultipliers: Towards sensitive and ecological mapping of brain activity and neurovascular coupling. *Sensors*, 20(10). <https://doi.org/10.3390/s20102831>

Chitnis, D., Cooper, R. J., Dempsey, L., Powell, S., Quaggia, S., Highton, D., Elwell, C., Hebden, J. C., & Everdell, N. L. (2016). Functional imaging of the human brain using a modular, fiberless, high-density diffuse optical tomography system. *Biomedical Optics Express*, 7(10), 4275. <https://doi.org/10.1364/boe.7.004275>

Choi, J. K., Kim, J. M., Hwang, G., Yang, J., Choi, M. G., & Bae, H. M. (2016). Time-Divided Spread-Spectrum Code-Based 400 fW-Detectable Multichannel fNIRS IC for Portable Functional Brain Imaging. *IEEE Journal of Solid-State Circuits*, 51(2), 484–495. <https://doi.org/10.1109/JSSC.2015.2504412>

Christoff, K., & Gabrieli, J. D. E. (2000). The frontopolar cortex and human cognition: Evidence for a rostrocaudal hierarchical organization within the human prefrontal cortex. *Psychobiology*, 28(2), 168–186. <https://doi.org/10.3758/BF03331976>

Çiftçi, K., Sankur, B., Kahya, Y. P., & Akin, A. (2008). Functional clusters in the prefrontal cortex during mental arithmetic. In *16th European Signal Processing Conference*, (pp 1-4). IEEE

Cinciute, S. (2019). Translating the hemodynamic response: why focused interdisciplinary integration should matter for the future of functional neuroimaging. *PeerJ*, 7, e6621. <https://doi.org/10.7717/peerj.6621>

Claassen, J. A. H. R., Thijssen, D. H. J., Panerai, R. B., & Faraci, F. M. (2021). Regulation of cerebral blood flow in humans: physiology and clinical implications of autoregulation. *Physiological Reviews*, 101(4), 1487–1559. <https://doi.org/10.1152/physrev.00022.2020>

Claassen, J. A., Levine, B. D., & Zhang, R. (2009). Dynamic cerebral autoregulation during repeated squat-stand maneuvers. *Journal of Applied Physiology*, 106(1), 153–160. <https://doi.org/10.1152/jappphysiol.90822.2008>

Claassen, J. A., Meel-Van Den Abeelen, A. S., Simpson, D. M., Panerai, R. B., Alexander Caicedo Dorado, Mitsis, G. D., Brassard, P., Ainslie, P. N., Summers, P., Iwasaki, K., Ragauskas, A., Tzeng, Y. C., Müller, M., Wang, C. Y., Hu, H. H., Meel-Van Den Abeelen, A. S. S., Gommer, E., Karemaker, J. M., Aries, M., ... Novak, V. (2015). Transfer function analysis of dynamic cerebral autoregulation: A white paper from the International Cerebral Autoregulation

- Research Network. *Journal of Cerebral Blood Flow and Metabolism*, 36(4), 665–680.
<https://doi.org/10.1177/0271678X15626425>
- Cooper, R. J., Selb, J., Gagnon, L., Phillip, D., Schytz, H. W., Iversen, H. K., Ashina, M., & Boas, D. A. (2012). A systematic comparison of motion artifact correction techniques for functional near-infrared spectroscopy. *Frontiers in Neuroscience*, 6, 147.
<https://doi.org/10.3389/fnins.2012.00147>
- Crum, J. E. (2020). Future Applications of Real-World Neuroimaging to Clinical Psychology. *Psychological Reports*, 124(6), 2403–2426. <https://doi.org/10.1177/0033294120926669>
- Cui, X., Bray, S., Bryant, D. M., Glover, G. H., & Reiss, A. L. (2011). A quantitative comparison of NIRS and fMRI across multiple cognitive tasks. *NeuroImage*, 54(4), 2808–2821.
<https://doi.org/10.1016/j.neuroimage.2010.10.069>
- Dale, A. M. (1999). Optimal experimental design for event-related fMRI. *Human Brain Mapping*, 8(2–3), 109–114. [https://doi.org/10.1002/\(SICI\)1097-0193\(1999\)8:2/3<109::AID-HBM7>3.0.CO;2-W](https://doi.org/10.1002/(SICI)1097-0193(1999)8:2/3<109::AID-HBM7>3.0.CO;2-W)
- Dashtestani, H., Zaragoza, R., Kermanian, R., Condy, E., Anderson, A., Chowdhry, F., Karamzadeh, N. S., Miguel, H., Aram, S., & Gandjbakhche, A. (2019). The Quest for Functional Biomarkers in the Prefrontal Cortex Using Functional Near-Infrared Spectroscopy (fNIRS). In R.R. Alfano & L. Shi (Eds.), *Neurophotonic and Biomedical Spectroscopy* (pp. 123–136). Elsevier. <https://doi.org/10.1016/B978-0-323-48067-3.00006-8>
- de Roeve, I., Bale, G., Cooper, R. J., & Tachtsidis, I. (2017). Functional NIRS Measurement of Cytochrome-C-Oxidase Demonstrates a More Brain-Specific Marker of Frontal Lobe Activation Compared to the Haemoglobins. In W.E. Crusio, H. Dong, H.H. Radake, N. Rezaei, O. Steinlein, & J. Xiao (Eds), *Advances in Experimental Medicine and Biology* (pp. 141–147). Springer. https://doi.org/10.1007/978-3-319-55231-6_19
- Delpy, D. T., & Cope, M. (1997). Quantification in tissue near-infrared spectroscopy. *Philosophical Transactions of the Royal Society B: Biological Sciences*, 352(1354), 649–659. <https://doi.org/10.1098/rstb.1997.0046>
- Delpy, D. T., Cope, M., Van Der Zee, P., Arridge, S., Wray, S., & Wyatt, J. (1988). Estimation of optical pathlength through tissue from direct time of flight measurement. *Physics in Medicine and Biology*, 33(12), 1433–1442. <https://doi.org/10.1088/0031-9155/33/12/008>

- Dennis, J. J., Wiggins, C. C., Smith, J. R., Isautier, J. M. J., Johnson, B. D., Joyner, M. J., & Cross, T. J. (2021). Measurement of muscle blood flow and O₂ uptake via near-infrared spectroscopy using a novel occlusion protocol. *Scientific Reports*, *11*(1).
<https://doi.org/10.1038/s41598-020-79741-w>
- Diamond, S. G., Huppert, T. J., Kolehmainen, V., Franceschini, M. A., Kaipio, J. P., Arridge, S. R., & Boas, D. A. (2006). Dynamic physiological modeling for functional diffuse optical tomography. *NeuroImage*, *30*(1), 88–101.
<https://doi.org/10.1016/j.neuroimage.2005.09.016>
- Doi, H., Nishitani, S., & Shinohara, K. (2013). NIRS as a tool for assaying emotional function in the prefrontal cortex. *Frontiers in Human Neuroscience*, *7*, 770.
<https://doi.org/10.3389/fnhum.2013.00770>
- Donaldson, D. I. (2004). Parsing brain activity with fMRI and mixed designs: What kind of a state is neuroimaging in? *Trends in Neurosciences*, *27* (8), 442–444.
<https://doi.org/10.1016/j.tins.2004.06.001>
- Drake, R., Mitchell, A., & Vogl, W. (2020). *Anatomía para estudiantes*. Elsevier.
- Drummond. (1996). Adrenergic receptors in the forehead microcirculation. *Clinical Autonomic Research*, *6*(1), 23–27. <https://doi.org/10.1007/BF02291402>
- Drummond, P. (1997). The effect of adrenergic blockade on blushing and facial flushing. *Psychophysiology*, *34*(2), 163–168. <https://doi.org/10.1111/j.1469-8986.1997.tb02127.x>
- Drummond, P. D. (1994). The effect of anger and pleasure on facial blood flow. *Australian Journal of Psychology*, *46*(2), 95–99. <https://doi.org/10.1080/00049539408259479>
- Drummond, P. D. (2009). Psychophysiology of the blush. In W.R. Crozier & P.J. de Jong (Eds.), *The Psychological Significance of the Blush* (pp. 15–38). Cambridge University Press.
<https://doi.org/10.1017/CBO9781139012850.004>
- Drummond, P. D., & Lacnce, J. (1987). Facial flushing and sweating mediated by the sympathetic nervous system. *Brain*, *110*(3), 793–803. <https://doi.org/10.1093/brain/110.3.793>
- Dumontheil, I., Burgess, P. W., & Blakemore, S.-J. (2008). Development of rostral prefrontal cortex and cognitive and behavioural disorders. *Developmental Medicine & Child Neurology*, *50*(3), 168–181. <https://doi.org/10.1111/j.1469-8749.2008.02026.x>

- Duncan, A., Meek, J. H., Clemence, M., Elwell, C. E., Tyszczyk, L., Cope, M., & Delpy, D. (1995). Optical pathlength measurements on adult head, calf and forearm and the head of the newborn infant using phase resolved optical spectroscopy. *Physics in Medicine and Biology*, 40(2), 295–304. <https://doi.org/10.1088/0031-9155/40/2/007>
- Elting, J. W. J., Tas, J., Aries, M. J. H., Czosnyka, M., & Maurits, N. M. (2020). Dynamic cerebral autoregulation estimates derived from near infrared spectroscopy and transcranial Doppler are similar after correction for transit time and blood flow and blood volume oscillations. *Journal of Cerebral Blood Flow and Metabolism*, 40(1), 135–149. <https://doi.org/10.1177/0271678X18806107>
- Erdoğan, S. B., Yücel, M. A., & Akin, A. (2014). Analysis of task-evoked systemic interference in fNIRS measurements: Insights from fMRI. *NeuroImage*, 87, 490–504. <https://doi.org/10.1016/j.neuroimage.2013.10.024>
- Erdogmus, S., & Govsa, F. (2007). Anatomy of the supraorbital region and the evaluation of it for the reconstruction of facial defects. *Journal of Craniofacial Surgery*, 18(1), 104–112. <https://doi.org/10.1097/01.scs.0000246498.39194.20>
- Everdell, N. L., Airantzis, D., Kolvya, C., Suzuki, T., & Elwell, C. E. (2013). A portable wireless near-infrared spatially resolved spectroscopy system for use on brain and muscle. *Medical Engineering and Physics*, 35(11), 1692–1697. <https://doi.org/10.1016/j.medengphy.2013.04.011>
- Faes, L., Pinna, G. D., Porta, A., Maestri, R., & Nollo, G. (2004). Surrogate data analysis for assessing the significance of the coherence function. *IEEE Transactions on Biomedical Engineering*, 51(7), 1156–1166. <https://doi.org/10.1109/TBME.2004.827271>
- Fantini, S., Frederick, B., & Sassaroli, A. (2018). Perspective: Prospects of non-invasive sensing of the human brain with diffuse optical imaging. *APL Photonics*, 3(11), 110901. <https://doi.org/10.1063/1.5038571>
- Fantini, S., Ruesch, A., & Kainerstorfer, J. M. (2018). Noninvasive optical studies of the brain. In R.R. Alfano & L. Shi (Eds.), *Neurophotonics and Biomedical Spectroscopy* (pp. 25–52). Elsevier. <https://doi.org/10.1016/B978-0-323-48067-3.00002-0>
- Fekete, T., Rubin, D., Carlson, J. M., & Mujica-Parodi, L. R. (2011). The nirs analysis package: Noise reduction and statistical inference. *PLoS ONE*, 6(9). <https://doi.org/10.1371/journal.pone.0024322>

- Ferrari, M. (2007). Progress of near-infrared spectroscopy and topography for brain and muscle clinical applications. *Journal of Biomedical Optics*, 12(6), 062104.
<https://doi.org/10.1117/1.2804899>
- Ferrari, M., & Quaresima, V. (2012a). Near Infrared Brain and Muscle Oximetry: From the Discovery to Current Applications. *Journal of Near Infrared Spectroscopy*, 20(1), 1–14.
<https://doi.org/10.1255/jnirs.973>
- Ferrari, M., & Quaresima, V. (2012b). A brief review on the history of human functional near-infrared spectroscopy (fNIRS) development and fields of application. *NeuroImage*, 63(2), 921–935. <https://doi.org/10.1016/j.neuroimage.2012.03.049>
- Finn, E. S., Corlett, P. R., Chen, G., Bandettini, P. A., & Constable, R. T. (2018). Trait paranoia shapes inter-subject synchrony in brain activity during an ambiguous social narrative. *Nature Communications*, 9(1), 1–13. <https://doi.org/10.1038/s41467-018-04387-2>
- Florian, G., & Pfurtscheller, G. (1997). Elimination von Atmungseffekten auf bewegungsinduzierte Änderungen der Herzrate - Elimination of Respiratory Effects on Movement-induced Cardiac Response. *Biomedizinische Technik/Biomedical Engineering*, 42(7–8), 203–206. <https://doi.org/10.1515/bmte.1997.42.7-8.203>
- Forte, G., De Pascalis, V., Favieri, F., & Casagrande, M. (2019). Effects of Blood Pressure on Cognitive Performance: A Systematic Review. *Journal of Clinical Medicine*, 9(1), 34.
<https://doi.org/10.3390/jcm9010034>
- Forte, G., Favieri, F., & Casagrande, M. (2019). Heart rate variability and cognitive function: A systematic review. *Frontiers in Neuroscience*, 13, 710.
<https://doi.org/10.3389/fnins.2019.00710>
- Franceschini, M. A., Fantini, S., Toronov, V., Filiaci, M. E., & Gratton, E. (2000). Cerebral hemodynamics measured by near-infrared spectroscopy at rest and during motor activation. *Proceedings of the Optical Society of America In Vivo Optical Imaging Workshop*, 73–80.
- Franceschini, M. A., Fantini, S., Toronov, V., Filiaci, M. E., & Gratton, E. (2000). Cerebral hemodynamics measured by near-infrared spectroscopy at rest and during motor activation. In *Proceedings of the Optical Society of America: Vivo Optical Imaging Workshop* (pp. 73-80). Optical Society of America. Optica Publishing Group

- Franceschini, M. A., Joseph, D. K., Huppert, T. J., Diamond, S. G., & Boas, D. A. (2006). Diffuse optical imaging of the whole head. *Journal of Biomedical Optics*, 11(5), 054007. <https://doi.org/10.1117/1.2363365>
- Friston, K., Ashburner, J., Kiebel, S., & Nichols, T. (2007). *Statistical Parametric Mapping: The Analysis of Functional Brain Images*. Elsevier <https://doi.org/10.1016/B978-0-12-372560-8.X5000-1>
- Friston, K. J., Josephs, O., Rees, G., & Turner, R. (1998). Nonlinear event-related responses in fMRI. *Magnetic Resonance in Medicine*, 39(1), 41–52. <https://doi.org/10.1002/mrm.1910390109>
- Gagnon, L., Cooper, R. J., Yücel, M. A., Perdue, K. L., Greve, D. N., & Boas, D. A. (2012). Short separation channel location impacts the performance of short channel regression in NIRS. *NeuroImage*, 59(3), 2518–2528. <https://doi.org/10.1016/j.neuroimage.2011.08.095>
- Gagnon, L., Perdue, K., Greve, D. N., Goldenholz, D., Kaskhedikar, G., & Boas, D. A. (2011). Improved recovery of the hemodynamic response in diffuse optical imaging using short optode separations and state-space modeling. *NeuroImage*, 56(3), 1362–1371. <https://doi.org/10.1016/j.neuroimage.2011.03.001>
- Gagnon, L., Yücel, M. A., Boas, D. A., & Cooper, R. J. (2014). Further improvement in reducing superficial contamination in NIRS using double short separation measurements. *NeuroImage*, 85, 127–135. <https://doi.org/10.1016/j.neuroimage.2013.01.073>
- Gagnon, L., Yücel, M. A., Dehaes, M., Cooper, R. J., Perdue, K. L., Selb, J., Huppert, T. J., Hoge, R. D., & Boas, D. A. (2012). Quantification of the cortical contribution to the NIRS signal over the motor cortex using concurrent NIRS-fMRI measurements. *NeuroImage*, 59(4), 3933–3940. <https://doi.org/10.1016/j.neuroimage.2011.10.054>
- Garritano, F. G., & Quatela, V. C. (2018). Surgical Anatomy of the Upper Face and Forehead. *Facial Plastic Surgery*, 34(2), 109–113. <https://doi.org/10.1055/s-0038-1637727>
- Gerovasili, V., Dimopoulos, S., Tzani, G., Anastasiou-Nana, M., & Nanas, S. (2010). Utilizing the vascular occlusion technique with NIRS technology. *International Journal of Industrial Ergonomics*, 40(2), 218–222. <https://doi.org/10.1016/j.ergon.2009.02.004>
- Gilroy, A. M., MacPherson, B. R., & Ross, L. M. (2013). *Prometheus, atlas de anatomía*. Panamericana.

- Goodwin, G. M., McCloskey, D. I., & Mitchell, J. H. (1972). Cardiovascular and respiratory responses to changes in central command during isometric exercise at constant muscle tension. *The Journal of Physiology*, *226*(1), 173–190.
<https://doi.org/10.1113/jphysiol.1972.sp009979>
- Gratton, G., & Corballis, P. M. (1995). Removing the heart from the brain: Compensation for the pulse artifact in the photon migration signal. *Psychophysiology*, *32*(3), 292–299.
<https://doi.org/10.1111/j.1469-8986.1995.tb02958.x>
- Guyton, A. C., Guyton, A. C., & Hall, J. E. (2011). *Tratado de fisiología médica*. Elsevier.
- Haeussinger, F. B., Dresler, T., Heinzl, S., Schecklmann, M., Fallgatter, A. J., & Ehlis, A. C. (2014). Reconstructing functional near-infrared spectroscopy (fNIRS) signals impaired by extra-cranial confounds: An easy-to-use filter method. *NeuroImage*, *95*, 69–79.
<https://doi.org/10.1016/j.neuroimage.2014.02.035>
- Haeussinger, F. B., Heinzl, S., Hahn, T., Schecklmann, M., Ehlis, A. C., & Fallgatter, A. J. (2011). Simulation of near-infrared light absorption considering individual head and prefrontal cortex anatomy: Implications for optical neuroimaging. *PLoS ONE*, *6*(10).
<https://doi.org/10.1371/journal.pone.0026377>
- Hakimi, N. (2018). Stress assessment by means of heart rate derived from functional near-infrared spectroscopy. *Journal of Biomedical Optics*, *23*(11), 1.
<https://doi.org/10.1117/1.jbo.23.11.115001>
- Hamel, E. (2006). Perivascular nerves and the regulation of cerebrovascular tone. *Journal of Applied Physiology*, *100*(3), 1059–1064.
<https://doi.org/10.1152/jappphysiol.00954.2005>
- Harris DN, Cowans FM, Wertheim DA. NIRS in the temporal region--strong influence of external carotid artery. *Advances in Experimental Medicine and Biology*, *345*, 825-828.
https://doi.org/10.1007/978-1-4615-2468-7_107
- Hasson, U., Nir, Y., Levy, I., Fuhrmann, G., & Malach, R. (2004). Intersubject Synchronization of Cortical Activity during Natural Vision. *Science*, *303*(5664), 1634–1640.
<https://doi.org/10.1126/science.1089506>
- Heinzl, S., Haeussinger, F. B., Hahn, T., Ehlis, A. C., Plichta, M. M., & Fallgatter, A. J. (2013). Variability of (functional) hemodynamics as measured with simultaneous fNIRS and fMRI

during intertemporal choice. *NeuroImage*, 71, 125–134.

<https://doi.org/10.1016/j.neuroimage.2012.12.074>

Herold, F., Wiegel, P., Scholkmann, F., & Müller, N. (2018). Applications of Functional Near-Infrared Spectroscopy (fNIRS) Neuroimaging in Exercise–Cognition Science: A Systematic, Methodology-Focused Review. *Journal of Clinical Medicine*, 7(12), 466.

<https://doi.org/10.3390/jcm7120466>

Hock, C., Villringer, F., Muller-Spahn, F., Hofmann, M., Schuh-Hofer, S., Heekeren, HWenzel, R., Dirnagl, U., & Villringer, A. (1996). Near Infrared Spectroscopy in the diagnosis of Alzheimer's Disease. *Annals of the New York Academy of Sciences*, 1, 22–29.

Holland, P. W., & Welsch, R. E. (1977). Robust regression using iteratively reweighted least-squares. *Communications in Statistics - Theory and Methods*, 6(9), 813–827.

<https://doi.org/10.1080/03610927708827533>

Holmgaard, F., Vedel, A. G., Langkilde, A., Nilsson, J. C., & Ravn, H. B. (2016). Does depth of the frontal sinus affect near-infrared spectroscopy measurement? *Perfusion*, 31(8), 659–661.

<https://doi.org/10.1177/0267659116649425>

Holper, L., Shalóm, D. E., Wolf, M., & Sigman, M. (2011). Understanding inverse oxygenation responses during motor imagery: A functional near-infrared spectroscopy study. *European Journal of Neuroscience*, 33(12), 2318–2328.

<https://doi.org/10.1111/j.1460-9568.2011.07720.x>

Hosaka, F., Yamamoto, M., Cho, K. H., Jang, H. S., Murakami, G., & Abe, S. I. (2016). Human nasociliary nerve with special reference to its unique parasympathetic cutaneous innervation. *Anatomy and Cell Biology*, 49(2), 132–137.

<https://doi.org/10.5115/acb.2016.49.2.132>

Hoshi, Y. (2016). Hemodynamic signals in fNIRS. In K. Masamoto, H. Hirase, & K. Yamada (Eds.), *Progress in Brain Research. New Horizons in neurovascular coupling: a bridge between brain circulation and neural plasticity*. (pp. 153–179). Elsevier.

<https://doi.org/10.1016/bs.pbr.2016.03.004>

Hoshi, Y., & Tamura, M. (1993). Detection of dynamic changes in cerebral oxygenation coupled to neuronal function during mental work in man. *Neuroscience Letters*, 150(1), 5–8.

[https://doi.org/10.1016/0304-3940\(93\)90094-2](https://doi.org/10.1016/0304-3940(93)90094-2)

- Hove, J. D., Rosenberg, I., Sejrsen, P., Hove, K. D., & Secher, N. H. (2006). Supraorbital cutaneous blood flow rate during carotid endarterectomy. *Clinical Physiology and Functional Imaging*, 26(6), 323–327. <https://doi.org/10.1111/j.1475-097X.2006.00697.x>
- Hu, Z., Liu, G., Dong, Q., & Niu, H. (2020). Applications of Resting-State fNIRS in the Developing Brain: A Review from the Connectome Perspective. *Frontiers in Neuroscience*, 14. <https://doi.org/10.3389/fnins.2020.00476>
- Hughson, R. L., Edwards, M. R., O’Leary, D. D., & Shoemaker, J. K. (2001). Critical analysis of cerebrovascular autoregulation during repeated head-up tilt. *Stroke*, 32(10), 2403–2408. <https://doi.org/10.1161/hs1001.097225>
- Huppert, T. J. (2016). Commentary on the statistical properties of noise and its implication on general linear models in functional near-infrared spectroscopy. *Neurophotonics*, 3(1), 010401. <https://doi.org/10.1117/1.nph.3.1.010401>
- Huppert, T. J., Diamond, S. G., Franceschini, M. A., & Boas, D. A. (2009). HomER: A review of time-series analysis methods for near-infrared spectroscopy of the brain. *Applied Optics*, 48(10), 0–33. <https://doi.org/10.1364/AO.48.00D280>
- Ilvedson, C. R. (1998). *Transfer Function Estimates Using Time-Frequency Analysis* [Doctoral dissertation, [Massachusetts Institute of Technology]]. <https://dspace.mit.edu/handle/1721.1/50472>
- Ishii, K., Liang, N., Asahara, R., Takahashi, M., & Matsukawa, K. (2018). Feedforward- and motor effort-dependent increase in prefrontal oxygenation during voluntary one-armed cranking. *Journal of Physiology*, 596(21), 5099–5118. <https://doi.org/10.1113/JP276956>
- Issard, C., & Gervain, J. (2018). Variability of the hemodynamic response in infants: Influence of experimental design and stimulus complexity. In M. Byrne, K. Mills, J. Pfeifer, & N. Allen (Eds.), *Developmental Cognitive Neuroscience. Methodological challenges in developmental neuroimaging: contemporary approaches and solutions* (pp. 182–193). Elsevier. <https://doi.org/10.1016/j.dcn.2018.01.009>
- Izzetoglu, K., Ayaz, H., Merzagora, A., Izzetoglu, M., Shewokis, P. A., Bunce, S. C., Pourrezaei, K., Rosen, A., & Onaral, B. (2011). The evolution of field deployable fNIR spectroscopy from bench to clinical settings. *Journal of Innovative Optical Health Sciences*, 4(3), 239–250. <https://doi.org/10.1142/S1793545811001587>

- Jeffries, O., Waldron, M., Pattison, J. R., & Patterson, S. D. (2018). Enhanced local skeletal muscle oxidative capacity and microvascular blood flow following 7-day ischemic preconditioning in healthy humans. *Frontiers in Physiology*, *9*, 463.
<https://doi.org/10.3389/fphys.2018.00463>
- Jelzow, A., Tachtsidis, I., Kirilina, E., Niessing, M., Brühl, R., Wabnitz, H., Heine, A., Ittermann, B., & Macdonald, R. (2011). Simultaneous measurement of time-domain fNIRS and physiological signals during a cognitive task. In A. H. Hielscher & P. Taroni (Eds.), *Optics InfoBase Conference Papers* (pp. 808-803). Optica Publishing Group.
<https://doi.org/10.1117/12.889484>
- Jenkins, S. D., & Brown, R. D. H. (2014). A correlational analysis of human cognitive activity using Infrared Thermography of the supraorbital region, frontal EEG and self-report of core affective state. *Proceedings of the 2014 International Conference on Quantitative InfraRed Thermography*. <https://doi.org/10.21611/qirt.2014.131>
- Jöbsis, F. (1977). Noninvasive, infrared monitoring of cerebral and myocardial oxygen sufficiency and circulatory parameters. *Science*, *198*(4323), 1264–1267.
<https://doi.org/10.1126/science.929199>
- Jones, S., Chiesa, S. T., Chaturvedi, N., & Hughes, A. D. (2016). Recent developments in near-infrared spectroscopy (NIRS) for the assessment of local skeletal muscle microvascular function and capacity to utilize oxygen. *Artery Research* *16*, 25–33.
<https://doi.org/10.1016/j.artres.2016.09.001>
- Julien, C. (2006). The enigma of Mayer waves: Facts and models. *Cardiovascular Research*, *70*(1), 12–21. <https://doi.org/10.1016/j.cardiores.2005.11.008>
- Kainerstorfer, J. M., Sassaroli, A., & Fantini, S. (2014). Coherent hemodynamics spectroscopy in a single step. *Biomedical Optics Express*, *5*(10), 3403.
<https://doi.org/10.1364/boe.5.003403>
- Kamran, M. A., Mannann, M. M. N., & Jeong, M. Y. (2018). Differential path-length factor's effect on the characterization of brain's hemodynamic response function: A functional near-infrared study. *Frontiers in Neuroinformatics*, *12*, 1–15.
<https://doi.org/10.3389/fninf.2018.00037>
- Kanat, A., Yazar, U., Ozdemir, B., Coskun, Z. O., & Erdivanli, O. (2015). Frontal sinus asymmetry: Is it an effect of cranial asymmetry? X-ray analysis of 469 normal adult human frontal

sinus. *Journal of Neurosciences in Rural Practice*, 6(4), 511–514.

<https://doi.org/10.4103/0976-3147.168436>

Kassab, A., le Lan, J., Tremblay, J., Vannasing, P., Dehbozorgi, M., Pouliot, P., Gallagher, A., Lesage, F., Sawan, M., & Nguyen, D. K. (2018). Multichannel wearable fNIRS-EEG system for long-term clinical monitoring. *Human Brain Mapping*, 39(1), 7–23.

<https://doi.org/10.1002/hbm.23849>

Kato, T., Kamei, A., Takashima, S., & Ozaki, T. (1993). Human Visual Cortical Function during Photic Stimulation Monitoring by Means of near-Infrared Spectroscopy. *Journal of Cerebral Blood Flow & Metabolism*, 13(3), 516–520.

<https://doi.org/10.1038/jcbfm.1993.66>

Katura, T., Tanaka, N., Obata, A., Sato, H., & Maki, A. (2006). Quantitative evaluation of interrelations between spontaneous low-frequency oscillations in cerebral hemodynamics and systemic cardiovascular dynamics. *NeuroImage*, 31(4), 1592–1600.

<https://doi.org/10.1016/j.neuroimage.2006.02.010>

Kelly, C. P., Yavuzer, R., Keskin, M., Bradford, M., Govila, L., & Jackson, I. T. (2008). Functional anastomotic relationship between the supratrochlear and facial arteries: An anatomical study. *Plastic and Reconstructive Surgery*, 121(2), 458–465.

<https://doi.org/10.1097/01.prs.0000297651.52729.ec>

Khan, T. T., Colon-Acevedo, B., Mettu, P., DeLorenzi, C., & Woodward, J. A. (2017). An Anatomical Analysis of the Supratrochlear Artery: Considerations in Facial Filler Injections and Preventing Vision Loss. *Aesthetic Surgery Journal*, 37(2), 203–208.

<https://doi.org/10.1093/asj/sjw132>

Kirilina, E., Jelzow, A., Heine, A., Niessing, M., Wabnitz, H., Brühl, R., Ittermann, B., Jacobs, A. M., & Tachtsidis, I. (2012). The physiological origin of task-evoked systemic artefacts in functional near infrared spectroscopy. *NeuroImage*, 61(1), 70–81.

<https://doi.org/10.1016/j.neuroimage.2012.02.074>

Kirilina, E., Yu, N., Jelzow, A., Wabnitz, H., Jacobs, A. M., & Tachtsidis, L. (2013). Identifying and quantifying main components of physiological noise in functional near infrared spectroscopy on the prefrontal cortex. *Frontiers in Human Neuroscience*, 7, 864.

<https://doi.org/10.3389/fnhum.2013.00864>

- Kirschbaum, C., Pirke, K., & Hellhammer, D. (1993). The 'Trier Social Stress Test' - A tool for investigating psychobiological stress responses in a laboratory setting. *Neuropsychobiology*, 36(4), 76–81. <https://doi.org/10.16309/j.cnki.issn.1007-1776.2003.03.004>
- Kishi, K., Kawaguchi, M., Yoshitani, K., Nagahata, T., & Furuya, H. (2003). Influence of Patient Variables and Sensor Location on Regional Cerebral Oxygen Saturation Measured by INVOS 4100 Near-Infrared Spectrophotometers. *Journal of Neurosurgical Anesthesiology*, 15(4), 302–306. <https://doi.org/10.1097/00008506-200310000-00002>
- Kleintjes, W. G. (2007). Forehead anatomy: Arterial variations and venous link of the midline forehead flap. *Journal of Plastic, Reconstructive and Aesthetic Surgery*, 60(6), 593–606. <https://doi.org/10.1016/j.bjps.2006.12.006>
- Kocsis, L., Herman, P., & Eke, A. (2006). The modified Beer-Lambert law revisited. *Physics in Medicine and Biology*, 51(5). <https://doi.org/10.1088/0031-9155/51/5/N02>
- Koechlin, E., Basso, G., Pietrini, P., Panzer, S., & Grafman, J. (1999). The role of the anterior prefrontal cortex in human cognition. *Nature*, 399(6732), 148–151. <https://doi.org/10.1038/20178>
- Koechlin, E., & Hyafil, A. (2007). Anterior Prefrontal Function and the Limits of Human Decision-Making. *Science*, 318(5850), 594–598. <https://doi.org/10.1126/science.1142995>
- Koh, P. H., Glaser, D. E., Flandin, G., Kiebel, S., Butterworth, B., Maki, A., Delpy, D. T., & Elwell, C. E. (2007). Functional optical signal analysis: a software tool for near-infrared spectroscopy data processing incorporating statistical parametric mapping. *Journal of Biomedical Optics*, 12(6), 064010. <https://doi.org/10.1117/1.2804092>
- Kohno, S., & Hoshi, Y. (2016). Spatial distributions of hemoglobin signals from superficial layers in the forehead during a verbal-fluency task. *Journal of biomedical optics*, 21(6), 066009 <https://doi.org/10.1117/1>
- Kohno, S., Miyai, I., Seiyama, A., Oda, I., Ishikawa, A., Tsuneishi, S., Amita, T., & Shimizu, K. (2007). Removal of the skin blood flow artifact in functional near-infrared spectroscopic imaging data through independent component analysis. *Journal of Biomedical Optics*, 12(6), 062111. <https://doi.org/10.1117/1.2814249>

- Kolehmainen, V., Prince, S., Arridge, S. R., & Kaipio, J. P. (2003). State-estimation approach to the nonstationary optical tomography problem. *Journal of the Optical Society of America*, 20(5), 876. <https://doi.org/10.1364/JOSAA.20.000876>
- Kooijman, H. M., Hopman, M. T., Colier, W. N., van der Vliet, J. A., & Oeseburg, B. (1997). Near infrared spectroscopy for noninvasive assessment of claudication. *Journal of Surgical Research*, 72(1), 1-7. <https://doi.org/10.1006/jsre.1997.5164>
- Koziej, M., Polak, J., Hołda, J., Trybus, M., Hołda, M., Kluza, P., Moskała, A., Chrapusta, A., Walocha, J., & Woźniak, K. (2019). The Arteries of the Central Forehead: Implications for Facial Plastic Surgery. *Aesthetic Surgery Journal*, 40 (10), 1043-1050. <https://doi.org/10.1093/asj/sjz295/5607055>
- Kroger, J., & Kim, C. (2022). Frontopolar Cortex Specializes for Manipulation of Structured Information. *Frontiers in Systems Neuroscience*, 16. <https://doi.org/10.3389/fnsys.2022.788395>
- Kudielka Kudielka, B. M., Hellhammer, D. H., & Kirschbaum, C. (2007). Ten Years of Research with the Trier Social Stress Test--Revisited. In E. Harmon-Jones & P. Winkielman (Eds.), *Social neuroscience: Integrating biological and psychological explanations of social behavior* (pp. 56–83). The Guilford Press.
- Kumar, V., Shivakumar, V., Chhabra, H., Bose, A., Venkatasubramanian, G., & Gangadhar, B. N. (2017). Functional near infra-red spectroscopy (fNIRS) in schizophrenia: A review. *Asian Journal of Psychiatry*, 27(2017), 18–31. <https://doi.org/10.1016/j.ajp.2017.02.009>
- Kurihara, K., Kawaguchi, H., Obata, T., Ito, H., Sakatani, K., & Okada, E. (2012). The influence of frontal sinus in brain activation measurements by near-infrared spectroscopy analyzed by realistic head models. *Biomedical Optics Express*, 3(9), 2121. <https://doi.org/10.1364/BOE.3.002121>
- Lacroix, S., Gayda, M., Gremeaux, V., Juneau, M., Tardif, J.C., & Nigam, A. (2012). Reproducibility of near-infrared spectroscopy parameters measured during brachial artery occlusion and reactive hyperemia in healthy men. *Journal of Biomedical Optics*, 17(7), 0770101. <https://doi.org/10.1117/1.jbo.17.7.077010>
- Lambert, J. H. (1760). *Photometria sive de mensura et gradibus luminis, colorum et umbrae*. Nabu Press.

- Lareau, E., Lesage, F., Pouliot, P., Nguyen, D., le Lan, J., & Sawan, M. (2011). Multichannel wearable system dedicated for simultaneous electroencephalography/near-infrared spectroscopy real-time data acquisitions. *Journal of Biomedical Optics*, 16(9), 096014. <https://doi.org/10.1117/1.3625575>
- Lee, T. K., & Westenskow, D. R. (1998). Comparison of blood pressure measured by oscillometry from the supraorbital artery and invasively from the radial artery. *Journal of Clinical Monitoring and Computing*, 14(2), 113–117. <https://doi.org/10.1023/A:1007481416222>
- León-Carrión, J., & León-Domínguez, U. (2012). Functional near-infrared spectroscopy (fNIRS): principles and neuroscientific applications. In P. Bright (Ed.), *Neuroimaging - Methods* (pp. 48-74). In Tech. <https://doi.org/10.5772/23146>
- Liang, Z., Gu, Y., Duan, X., Cheng, L., Liang, S., Tong, Y., & Li, X. (2016). Design of multichannel functional near-infrared spectroscopy system with application to propofol and sevoflurane anesthesia monitoring. *Neurophotonics*, 3(4), 045001. <https://doi.org/10.1117/1.nph.3.4.045001>
- Lima, A., & Bakker, J. (2006). Noninvasive monitoring of peripheral perfusion. Applied physiology in intensive care medicine. In M.R. Pinsky, L Bronchard & J. Mancebo (Eds.), *Applied Physiology in Intensive Care Medicine* (pp. 131-141). Springer. <https://doi.org/10.1007/s00134-005-2790-2>
- Liu, G., Cui, W., Hu, X., Xiao, R., Zhang, S., Cai, J., Qiu, J., & Qi, Y. (2022). Development of a miniaturized and modular probe for fNIRS instrument. *Lasers in Medical Science*, 37(4), 2269–2277. <https://doi.org/10.1007/s10103-021-03493-w>
- Liu, H., Chance, B., Hielscher, A. H., Jacques, S. L., & Tittel, F. K. (1995). Influence of blood vessels on the measurement of hemoglobin oxygenation as determined by time-resolved reflectance spectroscopy. *Medical Physics*, 22(8), 1209–1217. <https://doi.org/10.1118/1.597520>
- Liu, T., Pelowski, M., Pang, C., Zhou, Y., & Cai, J. (2016). Near-infrared spectroscopy as a tool for driving research. *Ergonomics*, 59(3), 368–379. <https://doi.org/10.1080/00140139.2015.1076057>
- Liu, X., Gu, Y., Huang, C., Zhao, M., Cheng, Y., Jawdeh, E. G. A., Bada, H. S., Chen, L., & Yu, G. (2021). Simultaneous measurements of tissue blood flow and oxygenation using a

wearable fiber-free optical sensor. *Journal of Biomedical Optics*, 26(01).

<https://doi.org/10.1117/1.jbo.26.1.012705>

Lozano-Teruel, J. A. (1995). *Bioquímica para ciencias de la salud*. McGraw-Hil.

Lu, C.M., Zhang, Y.-J., Biswal, B. B., Zang, Y.-F., Peng, D.-L., & Zhu, C.-Z. (2010). Use of fNIRS to assess resting state functional connectivity. *Journal of Neuroscience Methods*, 186(2), 242–249. <https://doi.org/10.1016/j.jneumeth.2009.11.010>

Lynch, J. M., Buckley, E. M., Schwab, P. J., Busch, D. R., Hanna, B. D., Putt, M. E., Licht, D. J., & Yodh, A. G. (2014). Noninvasive Optical Quantification of Cerebral Venous Oxygen Saturation in Humans. *Academic Radiology*, 21(2), 162–167. <https://doi.org/10.1016/j.acra.2013.10.013>

Maestú-Unturbe, F., Ríos-Lago, M., & Cabestero, R. (2007). *Neuroimagen: técnicas y procesos cognitivos*. Elsevier Masson.

Maggioni, E., Molteni, E., Zucca, C., Reni, G., Cerutti, S., Triulzi, F. M., Arrigoni, F., & Bianchi, A. M. (2015). Investigation of negative BOLD responses in human brain through NIRS technique. A visual stimulation study. *NeuroImage*, 108, 410–422. <https://doi.org/10.1016/j.neuroimage.2014.12.074>

Mandrick, K., Peysakhovich, V., Rémy, F., Lepron, E., & Causse, M. (2016). Neural and psychophysiological correlates of human performance under stress and high mental workload. *Biological Psychology*, 121, 62–73. <https://doi.org/10.1016/j.biopsycho.2016.10.002>

Maris, E., & Oostenveld, R. (2007). Nonparametric statistical testing of EEG- and MEG-data. *Journal of Neuroscience Methods*, 164(1), 177–190. <https://doi.org/10.1016/j.jneumeth.2007.03.024>

Martin, D. S., Levett, D. Z. H., Bezemer, R., Montgomery, H. E., & Grocott, M. P. W. (2013). The use of skeletal muscle near infrared spectroscopy and a vascular occlusion test at high altitude. *High Altitude Medicine and Biology*, 14(3), 256–262. <https://doi.org/10.1089/ham.2012.1109>

Matsubayashi, T., Cho, K. H., Jang, H. S., Murakami, G., Yamamoto, M., & Abe, S.-I. (2016). Significant Differences in Sympathetic Nerve Fiber Density Among the Facial Skin Nerves: A Histologic Study Using Human Cadaveric Specimens. *The Anatomical Record*, 299(8), 1054–1059. <https://doi.org/10.1002/ar.23347>

- Matsukawa, K., Asahara, R., Yoshikawa, M., & Endo, K. (2018). Deactivation of the prefrontal cortex during exposure to pleasantly-charged emotional challenge. *Scientific Reports*, 8(1). <https://doi.org/10.1038/s41598-018-32752-0>
- Matsukawa, K., Ishii, K., Liang, N., Endo, K., Ohtani, R., Nakamoto, T., Wakasugi, R., Kadowaki, A., & Komine, A. H. (2015). Increased oxygenation of the cerebral prefrontal cortex prior to the onset of voluntary exercise in humans. *Journal of Applied Physiology*, 119(5), 452–462. <https://doi.org/10.1152/jappphysiol.00406.2015>
- McLaughlin, R. B., Rehl, R. M., & Lanza, D. C. (2001). Clinically relevant frontal sinus anatomy and physiology. *Otolaryngologic Clinics of North America*, 34(1), 1–22. [https://doi.org/10.1016/S0030-6665\(05\)70291-7](https://doi.org/10.1016/S0030-6665(05)70291-7)
- Meltzer, J. A., Negishi, M., & Constable, R. T. (2008). Biphasic hemodynamic responses influence deactivation and may mask activation in block-design fMRI paradigms. *Human Brain Mapping*, 29(4), 385–399. <https://doi.org/10.1002/hbm.20391>
- Miezin, F. M., Maccotta, L., Ollinger, J. M., Petersen, S. E., & Buckner, R. L. (2000). Characterizing the hemodynamic response: Effects of presentation rate, sampling procedure, and the possibility of ordering brain activity based on relative timing. *NeuroImage*, 11(6), 735–759. <https://doi.org/10.1006/nimg.2000.0568>
- Minati, L., Jones, C. L., Gray, M. A., Medford, N., Harrison, N. A., & Critchley, H. D. (2009). Emotional modulation of visual cortex activity: A functional near-infrared spectroscopy study. *NeuroReport*, 20(15), 1344–1350. <https://doi.org/10.1097/WNR.0b013e328330c751>
- Minati, L., Kress, I. U., Visani, E., Medford, N., & Critchley, H. D. (2011). Intra- and extra-cranial effects of transient blood pressure changes on brain near-infrared spectroscopy (NIRS) measurements. *Journal of Neuroscience Methods*, 197(2), 283–288. <https://doi.org/10.1016/j.jneumeth.2011.02.029>
- Miyazawa, T., Horiuchi, M., Komine, H., Sugawara, J., Fadel, P. J., & Ogoh, S. (2013). Skin blood flow influences cerebral oxygenation measured by near-infrared spectroscopy during dynamic exercise. *European Journal of Applied Physiology*, 113(11), 2841–2848. <https://doi.org/10.1007/s00421-013-2723-7>

- Mohamed, M., Jo, E., Mohamed, N., Kim, M., Yun, J. D., & Kim, J. G. (2021). Development of an integrated EEG/fNIRS brain function monitoring system. *Sensors*, 21(22). <https://doi.org/10.3390/s21227703>
- Molina-Rodríguez, S., Hidalgo-Muñoz, A. R., Ibáñez-Ballesteros, J., & Taberero, C. (2023). Stress estimation by the prefrontal cortex asymmetry: Study on fNIRS signals. *Journal of Affective Disorders*, 325, 151-157. <https://doi.org/10.1016/j.jad.2023.01.018>
- Morais, G. A. Z., Scholkmann, F., Balardin, J. B., Furucho, R. A., de Paula, R. C. V., Biazoli, C. E., & Sato, J. R. (2017). Non-neuronal evoked and spontaneous hemodynamic changes in the anterior temporal region of the human head may lead to misinterpretations of functional near-infrared spectroscopy signals. *Neurophotonics*, 5(1), 011002. <https://doi.org/10.1117/1.nph.5.1.011002>
- Morren, G., Wolf, M., Lemmerling, P., Wolf, U., Choi, J. H., Gratton, E., de Lathauwer, L., & van Huffel, S. (2004). Detection of fast neuronal signals in the motor cortex from functional near infrared spectroscopy measurements using independent component analysis. *Medical and Biological Engineering and Computing*, 42(1), 92–99. <https://doi.org/10.1007/BF02351016>
- Müller, T., Lauk, M., Reinhard, M., Hetzel, A., Lücking, C. H., & Timmer, J. (2003). Estimation of Delay Times in Biological Systems. *Annals of Biomedical Engineering*, 31(11), 1423–1439. <https://doi.org/10.1114/1.1617984>
- Müller-Esterl, Werner., & Brandt, U. (2020). *Bioquímica : fundamentos para Medicina y Ciencias de la vida (1st ed.)*. Reverté.
- Mullinger, K. J., Mayhew, S. D., Bagshaw, A. P., Bowtell, R., & Francis, S. T. (2014). Evidence that the negative BOLD response is neuronal in origin: A simultaneous EEG-BOLD-CBF study in humans. *NeuroImage*, 94, 263–274. <https://doi.org/10.1016/j.neuroimage.2014.02.029>
- Muoio, V., Persson, P. B., & Sendeski, M. M. (2014). The neurovascular unit - concept review. *Acta Physiologica*, 210(4), 790–798. <https://doi.org/10.1111/apha.12250>
- Murkin, J. M., & Arango, M. (2009). Near-infrared spectroscopy as an index of brain and tissue oxygenation. *British Journal of Anaesthesia*, 103, i3–i13. <https://doi.org/10.1093/bja/aep299>

- Narus, S., Egbert, T., Lee, T. K., Lu, J., & Westenskow, D. (1995). Noninvasive blood pressure monitoring from the supraorbital artery using an artificial neural network oscillometric algorithm. *Journal of Clinical Monitoring*, *11*(5), 289–297.
<https://doi.org/10.1007/BF01616986>
- Näsi, T., Virtanen, J., Noponen, T., Toppila, J., Salmi, T., & Ilmoniemi, R. J. (2011). Spontaneous hemodynamic oscillations during human sleep and sleep stage transitions characterized with near-infrared spectroscopy. *PLoS ONE*, *6*(10).
<https://doi.org/10.1371/journal.pone.0025415>
- Nastase, S. A., Gazzola, V., Hasson, U., & Keysers, C. (2019). Measuring shared responses across subjects using intersubject correlation. *Social Cognitive and Affective Neuroscience*, *14*(6), 669–687. <https://doi.org/10.1093/scan/nsz037>
- Nguyen, H. D., Yoo, S. H., Bhutta, M. R., & Hong, K. S. (2018). Adaptive filtering of physiological noises in fNIRS data. *BioMedical Engineering Online*, *17*(1).
<https://doi.org/10.1186/s12938-018-0613-2>
- Nicolini, P., Ciulla, M. M., Malfatto, G., Abbate, C., Mari, D., Rossi, P. D., Pettenuzzo, E., Magrini, F., Consonni, D., & Lombardi, F. (2014). Autonomic Dysfunction in Mild Cognitive Impairment: Evidence from Power Spectral Analysis of Heart Rate Variability in a Cross-Sectional Case-Control Study. *PLoS ONE*, *9*(5), e96656.
<https://doi.org/10.1371/journal.pone.0096656>
- Nioka, S., Kime, R., Sunar, U., Im, J., Izzetoglu, M., Zhang, J., Alacam, B., & Chance, B. (2006). A novel method to measure regional muscle blood flow continuously using NIRS kinetics information. *Dynamic Medicine*, *5*. <https://doi.org/10.1186/1476-5918-5-5>
- Nishiyasu, Tan, Kondo, Nishiyasu, & Ikegami. (1999). Near-infrared monitoring of tissue oxygenation during application of lower body pressure at rest and during dynamical exercise in humans. *Acta Physiologica Scandinavica*, *166*(2), 123–130.
<https://doi.org/10.1046/j.1365-201x.1999.00548.x>
- Nolano, M., Provitera, V., Caporaso, G., Stancanelli, A., Leandri, M., Biasiotta, A., Cruccu, G., Santoro, L., & Truini, A. (2013a). Cutaneous innervation of the human face as assessed by skin biopsy. *Journal of Anatomy*, *222*(2), 161–169. <https://doi.org/10.1111/joa.12001>

- Nordin, M. (1990). Sympathetic discharges in the human supraorbital nerve and their relation to sudo- and vasomotor responses. *The Journal of Physiology*, 423(1), 241–255. <https://doi.org/10.1113/jphysiol.1990.sp018020>
- Nozawa, T., Sasaki, Y., Sakaki, K., Yokoyama, R., & Kawashima, R. (2016). Interpersonal frontopolar neural synchronization in group communication: An exploration toward fNIRS hyperscanning of natural interactions. *NeuroImage*, 133, 484–497. <https://doi.org/10.1016/j.neuroimage.2016.03.059>
- Obrig, H., Neufang, M., Wenzel, R., Kohl, M., Steinbrink, J., Einhäupl, K., & Villringer, A. (2000). Spontaneous low frequency oscillations of cerebral hemodynamics and metabolism in human adults. *NeuroImage*, 12(6), 623–639. <https://doi.org/10.1006/nimg.2000.0657>
- Obrig, H., & Villringer, A. (2003). Beyond the Visible—Imaging the Human Brain with Light. *Journal of Cerebral Blood Flow & Metabolism*, 23(1), 1–18. <https://doi.org/10.1097/01.WCB.0000043472.45775.29>
- Oden, N. (1983). Circular Statistics in Biology . Edward Batschelet. *The Quarterly Review of Biology*, 58(2), 312–312. <https://doi.org/10.1086/413381>
- Okada, E., Firbank, M., Schweiger, M., Arridge, S. R., Cope, M., & Delpy, D. T. (1997). Theoretical and experimental investigation of near-infrared light propagation in a model of the adult head. *Applied Optics*, 36(1), 21. <https://doi.org/10.1364/ao.36.000021>
- Okada, F., Tokumitsu, Y., Hoshi, Y., & Tamura, M. (1993). Gender- and handedness-related differences of forebrain oxygenation and hemodynamics. *Brain Research*, 601(1–2), 337–342. [https://doi.org/10.1016/0006-8993\(93\)91733-9](https://doi.org/10.1016/0006-8993(93)91733-9)
- Okada, F., Tokumitsu, Y., Hoshi, Y., & Tamura, M. (1994). Impaired interhemispheric integration in brain oxygenation and hemodynamics in schizophrenia. *European Archives of Psychiatry and Clinical Neuroscience*, 244(1), 17–25. <https://doi.org/10.1007/BF02279807>
- Öngür, D., Ferry, A. T., & Price, J. L. (2003). Architectonic subdivision of the human orbital and medial prefrontal cortex. *The Journal of Comparative Neurology*, 460(3), 425–449. <https://doi.org/10.1002/cne.10609>
- Orihuela-Espina, F., Leff, D. R., James, D. R. C., Darzi, A. W., & Yang, G. Z. (2010). Quality control and assurance in functional near infrared spectroscopy (fNIRS) experimentation. *Physics*

in Medicine and Biology, 55(13), 3701–3724. <https://doi.org/10.1088/0031-9155/55/13/009>

Ortuño-Miró, S., Molina-Rodríguez, S., Belmonte, C., & Ibáñez-Ballesteros, J. (2023). Identifying ADHD boys by very-low frequency prefrontal fNIRS fluctuations during a rhythmic mental arithmetic task. *Journal of Neural Engineering* (in press). <https://doi.org/10.1088/1741-2552/acad2b>

Paluš, M. (1997). Detecting phase synchronization in noisy systems. *Physics Letters, Section A: General, Atomic and Solid State Physics*, 235(4), 341–351. [https://doi.org/10.1016/S0375-9601\(97\)00635-X](https://doi.org/10.1016/S0375-9601(97)00635-X)

Pan, J., & Tompkins, W. J. (1985). Real-Time QRS Detection Algorithm. In *IEEE Transactions on Biomedical Engineering* (pp. 230-236). <https://doi.org/10.1109/TBME.1985.325532>

Patel, S., Katura, T., Maki, A., & Tachtsidis, I. (2011). Quantification of systemic interference in optical topography data during frontal lobe and motor cortex activation: an independent component analysis. In J.C. LaManna, M.A. Puchowicz, K. Xu, D.K. Harrison, & D.F.B. Bruley (Eds.), *Advances in experimental medicine and biology: Oxygen Transport to Tissue XXXII* (pp. 45-51). Springer. https://doi.org/10.1007/978-1-4419-7756-4_7

Peng, K., Steele, S. C., Becerra, L., & Borsook, D. (2018). Brodmann area 10: collating, integrating and high level processing of nociception and pain. *Progress in neurobiology*, 161, 1-22. <https://doi.org/10.1016/j.pneurobio.2017.11.004>

Petersen, S. E., & Dubis, J. W. (2012). The mixed block/event-related design. *NeuroImage*, 62 (2), 1177–1184. <https://doi.org/10.1016/j.neuroimage.2011.09.084>

Peterson, E. C., Wang, Z., & Britz, G. (2011). Regulation of Cerebral Blood Flow. *International Journal of Vascular Medicine*, 2011, 1–8. <https://doi.org/10.1155/2011/823525>

Pfeifer, M. D., Scholkmann, F., & Labruyère, R. (2018). Signal processing in functional near-infrared spectroscopy (fNIRS): Methodological differences lead to different statistical results. *Frontiers in Human Neuroscience*, 11. <https://doi.org/10.3389/fnhum.2017.00641>

Pfurtscheller, G., Bauernfeind, G., Wriessnegger, S. C., & Neuper, C. (2010). Focal frontal (de)oxyhemoglobin responses during simple arithmetic. *International Journal of Psychophysiology*, 76(3), 186–192. <https://doi.org/10.1016/j.ijpsycho.2010.03.013>

- Piantadosi, C. A. (2007). Early development of near-infrared spectroscopy at Duke University. *Journal of Biomedical Optics*, 12(6), 062102. <https://doi.org/10.1117/1.2804925>
- Pierro, M. L., Hallacoglu, B., Sassaroli, A., Kainerstorfer, J. M., & Fantini, S. (2014). Validation of a novel hemodynamic model for coherent hemodynamics spectroscopy (CHS) and functional brain studies with fNIRS and fMRI. *NeuroImage*, 85(1), 222–233. <https://doi.org/10.1016/j.neuroimage.2013.03.037>
- Pinti, P., Aichelburg, C., Gilbert, S., Hamilton, A., Hirsch, J., Burgess, P., & Tachtsidis, I. (2018). A Review on the Use of Wearable Functional Near-Infrared Spectroscopy in Naturalistic Environments. *Japanese Psychological Research*, 60(4), 347–373. <https://doi.org/10.1111/jpr.12206>
- Pinti, P., Cardone, D., & Merla, A. (2015). Simultaneous fNIRS and thermal infrared imaging during cognitive task reveal autonomic correlates of prefrontal cortex activity. *Scientific reports*, 5(1), 1-14. <https://doi.org/10.1038/srep17471>
- Pinti, P., Scholkmann, F., Hamilton, A., Burgess, P., & Tachtsidis, I. (2019). Current Status and Issues Regarding Pre-processing of fNIRS Neuroimaging Data: An Investigation of Diverse Signal Filtering Methods Within a General Linear Model Framework. *Frontiers in Human Neuroscience*, 12. <https://doi.org/10.3389/fnhum.2018.00505>
- Pinti, P., Tachtsidis, I., Hamilton, A., Hirsch, J., Aichelburg, C., Gilbert, S., & Burgess, P. W. (2018). The present and future use of functional near-infrared spectroscopy (fNIRS) for cognitive neuroscience. *Annals of the New York Academy of Sciences*, 1464(1), 291–25. <https://doi.org/10.1111/nyas.13948>
- Plichta, M. M., Heinzel, S., Ehlis, A. C., Pauli, P., & Fallgatter, A. J. (2007). Model-based analysis of rapid event-related functional near-infrared spectroscopy (NIRS) data: A parametric validation study. *NeuroImage*, 35(2), 625–634. <https://doi.org/10.1016/j.neuroimage.2006.11.028>
- Plichta, M. M., Herrmann, M. J., Baehne, C. G., Ehlis, A. C., Richter, M. M., Pauli, P., & Fallgatter, A. J. (2006). Event-related functional near-infrared spectroscopy (fNIRS): Are the measurements reliable? *NeuroImage*, 31(1), 116–124. <https://doi.org/10.1016/j.neuroimage.2005.12.008>

- Pollonini, L., Bortfeld, H., & Oghalai, J. S. (2016). PHOEBE: a method for real time mapping of optodes-scalp coupling in functional near-infrared spectroscopy. *Biomedical Optics Express*, 7(12), 5104. <https://doi.org/10.1364/boe.7.005104>
- Pondé, J. M., Metzger, P., Amaral, G., Machado, M., & Prandini, M. (2003). Anatomic Variations of the Frontal Sinus. *Minimally Invasive Neurosurgery*, 46(1), 29–32. <https://doi.org/10.1055/s-2003-37956>
- Racah, O., Block, N., & Fox, K. C. (2021). Does the prefrontal cortex play an essential role in consciousness? Insights from intracranial electrical stimulation of the human brain. *Journal of Neuroscience*, 41(10), 2076-2087. <https://doi.org/10.1523/JNEUROSCI.1141-20.2020>
- Raggam, P., Bauernfeind, G., & Wriessnegger, S. C. (2020). NICA: A Novel Toolbox for Near-Infrared Spectroscopy Calculations and Analyses. *Frontiers in Neuroinformatics*, 14. <https://doi.org/10.3389/fninf.2020.00026>
- Raichle, M. E. (2010). Two views of brain function. *Trends in Cognitive Sciences*, 14(4), 180–190. <https://doi.org/10.1016/j.tics.2010.01.008>
- Raichle, M. E., MacLeod, A. M., Snyder, A. Z., Powers, W. J., Gusnard, D. A., & Shulman, G. L. (2001). A default mode of brain function. *Proceedings of the National Academy of Sciences of the United States of America*, 98(2), 676–682. <https://doi.org/10.1073/pnas.98.2.676>
- Raichle, M. E., & Snyder, A. Z. (2007). A default mode of brain function: A brief history of an evolving idea. *NeuroImage*, 37(4), 1083–1090. <https://doi.org/10.1016/j.neuroimage.2007.02.041>
- Ramnani, N., & Owen, A. M. (2004). Anterior prefrontal cortex: Insights into function from anatomy and neuroimaging. *Nature Reviews Neuroscience*, 5(3), 184–194. <https://doi.org/10.1038/nrn1343>
- Rasmussen, P., Dawson, E. A., Nybo, L., van Lieshout, J. J., Secher, N. H., & Gjedde, A. (2007). Capillary-Oxygenation-Level-Dependent Near-Infrared Spectrometry in Frontal Lobe of Humans. *Journal of Cerebral Blood Flow & Metabolism*, 27(5), 1082–1093. <https://doi.org/10.1038/sj.jcbfm.9600416>

- Reddy, P., Izzetoglu, M., Shewokis, P. A., Sangobowale, M., Diaz-Arrastia, R., & Izzetoglu, K. (2021). Evaluation of fNIRS signal components elicited by cognitive and hypercapnic stimuli. *Scientific Reports*, *11*(1). <https://doi.org/10.1038/s41598-021-02076-7>
- Reinhard, M., Wehrle-Wieland, E., Grabiak, D., Roth, M., Guschlbauer, B., Timmer, J., Weiller, C., & Hetzel, A. (2006). Oscillatory cerebral hemodynamics-the macro- vs. microvascular level. *Journal of the Neurological Sciences*, *250*(1–2), 103–109.
<https://doi.org/10.1016/j.jns.2006.07.011>
- Saager, R. B., & Berger, A. (2008). Measurement of layer-like hemodynamic trends in scalp and cortex: implications for physiological baseline suppression in functional near-infrared spectroscopy. *Journal of Biomedical Optics*, *13*(3), 034017.
<https://doi.org/10.1117/1.2940587>
- Saager, R. B., & Berger, A. J. (2005). Direct characterization and removal of interfering absorption trends in two-layer turbid media. *Journal of the Optical Society of America*, *22*(9), 1874.
<https://doi.org/10.1364/josaa.22.001874>
- Saager, R. B., Telleri, N. L., & Berger, A. J. (2011). Two-detector Corrected Near Infrared Spectroscopy (C-NIRS) detects hemodynamic activation responses more robustly than single-detector NIRS. *NeuroImage*, *55*(4), 1679–1685.
<https://doi.org/10.1016/j.neuroimage.2011.01.043>
- Saikia, M. J., Besio, W. G., & Mankodiya, K. (2018). WearLight: toward a wearable, configurable functional nir spectroscopy system for noninvasive neuroimaging. *IEEE Transactions on Biomedical Circuits and Systems*, *13*(1), 91-102.
<https://doi.org/10.1109/TBCAS.2018.2876089>
- Salvesen, R. (2001). Innervation of sweat glands in the forehead. A study in patients with Horner's syndrome. *Journal of the neurological sciences*, *183*(1), 39-42.
[https://doi.org/10.1016/s0022-510x\(00\)00479-2](https://doi.org/10.1016/s0022-510x(00)00479-2)
- Sassaroli, A., Pierro, M., Bergethon, P. R., & Fantini, S. (2012). Low-Frequency Spontaneous Oscillations of Cerebral Hemodynamics Investigated With Near-Infrared Spectroscopy: A Review. *IEEE Journal of Selected Topics in Quantum Electronics*, *18*(4), 1478–1492.
<https://doi.org/10.1109/JSTQE.2012.2183581>

- Sassaroli, A., Tgavalekos, K., & Fantini, S. (2018). The meaning of “coherent” and its quantification in coherent hemodynamics spectroscopy. *Journal of Innovative Optical Health Sciences*, 11(6), 1850036. <https://doi.org/10.1142/S1793545818500360>
- Sato, H., Yahata, N., Funane, T., Takizawa, R., Katura, T., Atsumori, H., Nishimura, Y., Kinoshita, A., Kiguchi, M., Koizumi, H., Fukuda, M., & Kasai, K. (2013). A NIRS–fMRI investigation of prefrontal cortex activity during a working memory task. *NeuroImage*, 83, 158–173. <https://doi.org/10.1016/j.neuroimage.2013.06.043>
- Sato, T., Nambu, I., Takeda, K., Aihara, T., Yamashita, O., Isogaya, Y., Inoue, Y., Otaka, Y., Wada, Y., Kawato, M., Sato, M. aki, & Osu, R. (2016). Reduction of global interference of scalp-hemodynamics in functional near-infrared spectroscopy using short distance probes. *NeuroImage*, 141, 120–132. <https://doi.org/10.1016/j.neuroimage.2016.06.054>
- Scarpa, F., Brigadoi, S., Cutini, S., Scatturin, P., Zorzi, M., Dell’Acqua, R., & Sparacino, G. (2013). A reference-channel based methodology to improve estimation of event-related hemodynamic response from fNIRS measurements. *NeuroImage*, 72, 106–119. <https://doi.org/10.1016/j.neuroimage.2013.01.021>
- Schaeffer, J. D., Yennu, A. S., Gandy, K. C., Tian, F., Liu, H., & Park, H. (2014). An fNIRS investigation of associative recognition in the prefrontal cortex with a rapid event-related design. *Journal of Neuroscience Methods*, 235, 308–315. <https://doi.org/10.1016/j.jneumeth.2014.07.011>
- Schaeffer, S., & Iadecola, C. (2021). Revisiting the neurovascular unit. *Nature Neuroscience*, 24(9), 1198–1209. <https://doi.org/10.1038/s41593-021-00904-7>
- Schecklmann, M., Ehlis, A. C., Plichta, M. M., & Fallgatter, A. J. (2008). Functional near-infrared spectroscopy: A long-term reliable tool for measuring brain activity during verbal fluency. *NeuroImage*, 43(1), 147–155. <https://doi.org/10.1016/j.neuroimage.2008.06.032>
- Schmid-Schönbein, G. W. (1999). Biomechanics of Microcirculatory Blood Perfusion. *Annual Review of Biomedical Engineering*, 1(1), 73–102. <https://doi.org/10.1146/annurev.bioeng.1.1.73>
- Scholkmann, F., Gerber, U., Wolf, M., & Wolf, U. (2013). End-tidal CO₂: An important parameter for a correct interpretation in functional brain studies using speech tasks. *NeuroImage*, 66, 71–79. <https://doi.org/10.1016/j.neuroimage.2012.10.025>

- Scholkmann, F., Kleiser, S., Metz, A. J., Zimmermann, R., Mata Pavia, J., Wolf, U., & Wolf, M. (2014). A review on continuous wave functional near-infrared spectroscopy and imaging instrumentation and methodology. *NeuroImage*, *85*, 6–27.
<https://doi.org/10.1016/j.neuroimage.2013.05.004>
- Scholkmann, F., & Wolf, M. (2013). General equation for the differential pathlength factor of the frontal human head depending on wavelength and age. *Journal of Biomedical Optics*, *18*(10), 105004. <https://doi.org/10.1117/1.jbo.18.10.105004>
- Scholkmann, F., Wolf, M., & Wolf, U. (2013). The Effect of Inner Speech on Arterial CO₂ and Cerebral Hemodynamics and Oxygenation: A Functional NIRS Study. *Advances in Experimental Medicine and Biology*, *789*, 81-87. https://doi.org/10.1007/978-1-4614-7411-1_12
- Scholkmann, F., Wolf, M., & Wolf, U. (2013). The effect of inner speech on arterial CO₂ and cerebral hemodynamics and oxygenation: a functional NIRS study. In S. Van Huffel, G. Naulaers, A. Caicedo, D.F. Bruley, & D.K. Harrison (Eds.), *Avances in experimental medicines and biology: Oxygen Transport to Tissue XXXV* (pp. 81-87). Springer.
https://doi.org/10.1007/978-1-4614-7411-1_12
- Schroeter, M. L., Bücheler, M. M., Müller, K., Uludağ, K., Obrig, H., Lohmann, G., Tittgemeyer, M., Villringer, A., & Von Cramon, D. Y. (2004). Towards a standard analysis for functional near-infrared imaging. *NeuroImage*, *21*(1), 283–290.
<https://doi.org/10.1016/j.neuroimage.2003.09.054>
- Schroeter, M. L., Schmiedel, O., & Von Cramon, D. Y. (2004). Spontaneous low-frequency oscillations decline in the aging brain. *Journal of Cerebral Blood Flow and Metabolism*, *24*(10), 1183–1191. <https://doi.org/10.1097/01.WCB.0000135231.90164.40>
- Shimizu, Y., Imanishi, N., Nakajima, T., Nakajima, H., Aiso, S., & Kishi, K. (2013). Venous architecture of the glabellar to the forehead region. *Clinical Anatomy*, *26*(2), 183–195.
<https://doi.org/10.1002/ca.22143>
- Shmuel, A., Yacoub, E., Pfeuffer, J., Van de Moortele, P. F., Adriany, G., Hu, X., & Ugurbil, K. (2002). Sustained negative BOLD, blood flow and oxygen consumption response and its coupling to the positive response in the human brain. *Neuron*, *36*(6), 1195–1210.
[https://doi.org/10.1016/S0896-6273\(02\)01061-9](https://doi.org/10.1016/S0896-6273(02)01061-9)

- Skaria, A. M. (2015). The median forehead flap reviewed: a histologic study on vascular anatomy. *European Archives of Oto-Rhino-Laryngology*, 272(5), 1231–1237. <https://doi.org/10.1007/s00405-014-3027-1>
- Sohn, M. H., Albert, M. V., Jung, K., Carter, C. S., & Anderson, J. R. (2007). Anticipation of conflict monitoring in the anterior cingulate cortex and the prefrontal cortex. *Proceedings of the National Academy of Sciences of the United States of America*, 104(25), 10330–10334. <https://doi.org/10.1073/pnas.0703225104>
- Stefanovska, A., Bracic, M., & Kvernmo, H. D. (1999). Wavelet analysis of oscillations in the peripheral blood circulation measured by laser Doppler technique. *IEEE Transactions on Biomedical Engineering*, 46(10), 1230–1239. <https://doi.org/10.1109/10.790500>
- Steinbrink, J., Villringer, A., Kempf, F., Haux, D., Boden, S., & Obrig, H. (2006). Illuminating the BOLD signal: combined fMRI-fNIRS studies. *Magnetic Resonance Imaging*, 24(4), 495–505. <https://doi.org/10.1016/j.mri.2005.12.034>
- Strong, E. B. (2009). Frontal Sinus Fractures: Current Concepts. *Craniofacial Trauma & Reconstruction*, 2(3–4), 161–175. <https://doi.org/10.1055/s-0029-1234020>
- Tachtsidis, I., Koh, P. H., Stubbs, C., & Elwell, C. E. (2010). Functional optical topography analysis using statistical parametric mapping (SPM) methodology with and without physiological confounds. In S. Van Huffel, G. Naulaers, A. Caicedo, D.F. Bruley, & D.K. Harrison (Eds). *Advances in experimental medicine and biology: Oxygen Transport to Tissue XXXI* (pp. 237-243). Springer. https://doi.org/10.1007/978-1-4419-1241-1_34
- Tachtsidis, I., Leung, T. S., Chopra, A., Koh, P. H., Reid, C. B., & Elwell, C. E. (2009). False positives in functional near-infrared topography. *Advances in Experimental Medicine and Biology*, 645, 307–314. https://doi.org/10.1007/978-0-387-85998-9_46
- Tachtsidis, I., Leung, T. S., Devoto, L., Delpy, D. T., & Elwell, C. E. (2008). Measurement of frontal lobe functional activation and related systemic effects: A near-infrared spectroscopy investigation. *Advances in Experimental Medicine and Biology*, 614, 397–403. https://doi.org/10.1007/978-0-387-74911-2_44
- Tachtsidis, I., & Scholkmann, F. (2016). False positives and false negatives in functional near-infrared spectroscopy: issues, challenges, and the way forward. *Neurophotonics*, 3(3), 031405. <https://doi.org/10.1117/1.NPh.3.3.031405>

- Tak, S., Uga, M., Flandin, G., Dan, I., & Penny, W. D. (2016). Sensor space group analysis for fNIRS data. *Journal of Neuroscience Methods*, 264, 103–112.
<https://doi.org/10.1016/j.jneumeth.2016.03.003>
- Tak, S., & Ye, J. C. (2014). Statistical analysis of fNIRS data: A comprehensive review. *NeuroImage*, 85, 72–91. <https://doi.org/10.1016/j.neuroimage.2013.06.016>
- Takahashi, T., Takikawa, Y., Kawagoe, R., Shibuya, S., Iwano, T., & Kitazawa, S. (2011). Influence of skin blood flow on near-infrared spectroscopy signals measured on the forehead during a verbal fluency task. *NeuroImage*, 57(3), 991–1002.
<https://doi.org/10.1016/j.neuroimage.2011.05.012>
- Takamoto, K., Hori, E., Urakawa, S., Katayama, M., Nagashima, Y., Yada, Y., Ono, T., & Nishijo, H. (2013). Thermotherapy to the facial region in and around the eyelids altered prefrontal hemodynamic responses and autonomic nervous activity during mental arithmetic. *Psychophysiology*, 50(1), 35–47. <https://doi.org/10.1111/j.1469-8986.2012.01488.x>
- Tan, K. S., Oh, S.-R., Priel, A., Korn, B. S., & Kikkawa, D. O. (2011). Surgical Anatomy of the Forehead, Eyelids, and Midface for the Aesthetic Surgeon. In G.G. Massry, M.R. Murphy, & B. Azizzadeh (Eds.), *Master Techniques in Blepharoplasty and Periorbital Rejuvenation* (pp. 11–24). Springer. https://doi.org/10.1007/978-1-4614-0067-7_2
- Tanida, M., Sakatani, K., Takano, R., & Tagai, K. (2004). Relation between asymmetry of prefrontal cortex activities and the autonomic nervous system during a mental arithmetic task: Near infrared spectroscopy study. *Neuroscience Letters*, 369(1), 69–74.
<https://doi.org/10.1016/j.neulet.2004.07.076>
- Tao, D., Tan, H., Wang, H., Zhang, X., Qu, X., & Zhang, T. (2019). A systematic review of physiological measures of mental workload. *International Journal of Environmental Research and Public Health*, 16(15), 1–23. <https://doi.org/10.3390/ijerph16152716>
- Thayer, J. F., & Lane, R. D. (2009). Claude Bernard and the heart-brain connection: Further elaboration of a model of neurovisceral integration. *Neuroscience and Biobehavioral Reviews*, 33(2), 81–88. <https://doi.org/10.1016/j.neubiorev.2008.08.004>
- Tong, Y., & Frederick, B. de B. (2010). Time lag dependent multimodal processing of concurrent fMRI and near-infrared spectroscopy (NIRS) data suggests a global circulatory origin for low-frequency oscillation signals in human brain. *NeuroImage*, 53(2), 553–564.
<https://doi.org/10.1016/j.neuroimage.2010.06.049>

- Torricelli, A., Contini, D., Pifferi, A., Caffini, M., Re, R., Zucchelli, L., & Spinelli, L. (2014). Time domain functional NIRS imaging for human brain mapping. *NeuroImage*, *85*, 28–50. <https://doi.org/10.1016/j.neuroimage.2013.05.106>
- Tsow, F., Kumar, A., Hosseini, S. H., & Bowden, A. (2021). A low-cost, wearable, do-it-yourself functional near-infrared spectroscopy (DIY-fNIRS) headband. *HardwareX*, *10*, e00204. <https://doi.org/10.1016/j.ohx.2021.e00204>
- Van Beek, A. H. E. A., Claassen, J. A. H. R., Rikkert, M. G. M. O., & Jansen, R. W. M. M. (2008). Cerebral autoregulation: An overview of current concepts and methodology with special focus on the elderly. *Journal of Cerebral Blood Flow and Metabolism*, *28*(6), 1071–1085. <https://doi.org/10.1038/jcbfm.2008.13>
- Vassena, E., Gerrits, R., Demanet, J., Verguts, T., & Siugzdaite, R. (2019). Anticipation of a mentally effortful task recruits Dorsolateral Prefrontal Cortex: An fNIRS validation study. *Neuropsychologia*, *123*, 106–115. <https://doi.org/10.1016/j.neuropsychologia.2018.04.033>
- Vassena, E., Silvetti, M., Boehler, C. N., Achten, E., Fias, W., & Verguts, T. (2014). Overlapping neural systems represent cognitive effort and reward anticipation. *PLoS ONE*, *9*(3). <https://doi.org/10.1371/journal.pone.0091008>
- Vermeij, A., Meel-van den Abeelen, A. S., Kessels, R. P., van Beek, A. H., & Claassen, J. A. (2014). Very-low-frequency oscillations of cerebral hemodynamics and blood pressure are affected by aging and cognitive load. *Neuroimage*, *85*, 608–615. <https://doi.org/10.1016/j.neuroimage.2013.04.107>
- Verner, M., Herrmann, M. J., Troche, S. J., Roebbers, C. M., & Rammsayer, T. H. (2013). Cortical oxygen consumption in mental arithmetic as a function of task difficulty: a near-infrared spectroscopy approach. *Frontiers in Human Neuroscience*, *7*, 1–9. <https://doi.org/10.3389/fnhum.2013.00217>
- Villringer, A., Planck, J., Stodieck, S., Bötzel, K., Schleinkofer, L., & Dirnagl, U. (1994). Noninvasive assessment of cerebral hemodynamics and tissue oxygenation during activation of brain cell function in human adults using near infrared spectroscopy. In P. Vaupel, R. Zander, & D.F. Bruley, *Advances in experimental medicine and biology: Oxygen Transport to Tissue XV* (pp. 559–565). Springer. https://doi.org/10.1007/978-1-4615-2468-7_74

- Volkening, N., Unni, A., Löffler, B. S., Fudickar, S., Rieger, J. W., & Hein, A. (2016). Characterizing the Influence of Muscle Activity in fNIRS Brain Activation Measurements. *IFAC-PapersOnLine*, 49(11), 84–88. <https://doi.org/10.1016/j.ifacol.2016.08.013>
- von Lüthmann, A., Herff, C., Heger, D., & Schultz, T. (2015). Toward a wireless open source instrument: Functional near-infrared spectroscopy in mobile neuroergonomics and BCI applications. *Frontiers in Human Neuroscience*, 9. <https://doi.org/10.3389/fnhum.2015.00617>
- Wabnitz, H., Moeller, M., Liebert, A., Obrig, H., Steinbrink, J., & Macdonald, R. (2010). Time-resolved near-infrared spectroscopy and imaging of the adult human brain. In E. Takahashi & D.F. Bruley (Eds.), *Advances in experimental medicine and biology: Oxygen transport to tissue XXXI* (pp. 143-148). Springer. https://doi.org/10.1007/978-1-4419-1241-1_20
- Walsh, N. D., Seal, M. L., Williams, S. C. R., & Mehta, M. A. (2009). An investigation of cognitive “branching” processes in major depression. *BMC Psychiatry*, 9, 69. <https://doi.org/10.1186/1471-244X-9-69>
- Wang, X., Liu, B., Xie, L., Yu, X., Li, M., & Zhang, J. (2016). Cerebral and neural regulation of cardiovascular activity during mental stress. *BioMedical Engineering Online*, 15, 335–347. <https://doi.org/10.1186/s12938-016-0255-1>
- Watanabe, E., Yamashita, Y., Maki, A., Ito, Y., & Koizumi, H. (1996). Non-invasive functional mapping with multi-channel near infra-red spectroscopic topography in humans. *Neuroscience Letters*, 205(1), 41–44. [https://doi.org/10.1016/0304-3940\(96\)12376-](https://doi.org/10.1016/0304-3940(96)12376-)
- Welch, P. (1967). The use of fast Fourier transform for the estimation of power spectra: A method based on time averaging over short, modified periodograms. *IEEE Transactions on Audio and Electroacoustics*, 15(2), 70–73. <https://doi.org/10.1109/TAU.1967.1161901>
- Wieder, J. M., & Moy, R. L. (1998). Understanding botulinum toxin: Surgical anatomy of the frown, forehead, and periocular region. *Dermatologic Surgery*, 24(11), 1172–1174. <https://doi.org/10.1111/j.1524-4725.1998.tb04093.x>
- Williams, L. R., & Leggett, R. W. (1989). Reference values for resting blood flow to organs of man. *Clinical Physics and Physiological Measurement*, 10(3), 187–217. <https://doi.org/10.1088/0143-0815/10/3/001>

- Williamson, J. W. (2010). The relevance of central command for the neural cardiovascular control of exercise. *Experimental Physiology*, *95*(11), 1043–1048.
<https://doi.org/10.1113/expphysiol.2009.051870>
- Willie, C. K., Tzeng, Y. C., Fisher, J. A., & Ainslie, P. N. (2014). Integrative regulation of human brain blood flow. *Journal of Physiology*, *592*(5), 841–859.
<https://doi.org/10.1113/jphysiol.2013.268953>
- Wolf, M., Wolf, U., Toronov, V., Michalos, A., Paunescu, L. A., Choi, J. H., & Gratton, E. (2002). Different Time Evolution of Oxyhemoglobin and Deoxyhemoglobin Concentration Changes in the Visual and Motor Cortices during Functional Stimulation: A Near-Infrared Spectroscopy Study. *NeuroImage*, *16*(3), 704–712.
<https://doi.org/10.1006/nimg.2002.1128>
- Wylie, G. R., Graber, H. L., Voelbel, G. T., Kohl, A. D., DeLuca, J., Pei, Y., Xu, Y., & Barbour, R. L. (2009). Using co-variations in the Hb signal to detect visual activation: A near infrared spectroscopic imaging study. *NeuroImage*, *47*(2), 473–481.
<https://doi.org/10.1016/j.neuroimage.2009.04.056>
- Wyser, D. G., Kanzler, C. M., Salzmann, L., Lambercy, O., Wolf, M., Scholkmann, F., & Gassert, R. (2022). Characterizing reproducibility of cerebral hemodynamic responses when applying short-channel regression in functional near-infrared spectroscopy. *Neurophotonics*, *9*(01). <https://doi.org/10.1117/1.nph.9.1.015004>
- Wyser, D., Lambercy, O., Scholkmann, F., Wolf, M., & Gassert, R. (2017). Wearable and modular functional near-infrared spectroscopy instrument with multidistance measurements at four wavelengths. *Neurophotonics*, *4*(04), 1. <https://doi.org/10.1117/1.nph.4.4.041413>
- Wyser, D., Mattille, M., Wolf, M., Lambercy, O., Scholkmann, F., & Gassert, R. (2020). Short-channel regression in functional near-infrared spectroscopy is more effective when considering heterogeneous scalp hemodynamics. *Neurophotonics*, *7*(03).
<https://doi.org/10.1117/1.nph.7.3.035011>
- Yang, H., Wang, Y., Zhou, Z., Gong, H., Luo, Q., Wang, Y., & Lu, Z. (2009). Sex differences in prefrontal hemodynamic response to mental arithmetic as assessed by near-infrared spectroscopy. *Gender Medicine*, *6*(4), 565–574.
<https://doi.org/10.1016/j.genm.2009.11.003>

- Yaqub, M. A., Woo, S. W., & Hong, K. S. (2020). Compact, Portable, High-Density Functional Near-Infrared Spectroscopy System for Brain *Imaging*. *IEEE Access*, 8, 128224–128238. <https://doi.org/10.1109/ACCESS.2020.3008748>
- Yücel, M. A., Selb, J., Aasted, C. M., Lin, P.-Y., Borsook, D., Becerra, L., & Boas, D. A. (2016). Mayer waves reduce the accuracy of estimated hemodynamic response functions in functional near-infrared spectroscopy. *Biomedical Optics Express*, 7(8), 3078. <https://doi.org/10.1364/boe.7.003078>
- Yücel, M. A., Selb, J., Aasted, C. M., Petkov, M. P., Becerra, L., Borsook, D., & Boas, D. A. (2015). Short separation regression improves statistical significance and better localizes the hemodynamic response obtained by near-infrared spectroscopy for tasks with differing autonomic responses. *Neurophotonics*, 2(3), 035005. <https://doi.org/10.1117/1.nph.2.3.035005>
- Yücel, M. A., Selb, J. J., Huppert, T. J., Franceschini, M. A., & Boas, D. A. (2017). Functional Near Infrared Spectroscopy: Enabling routine functional brain imaging. *Current Opinion in Biomedical Engineering*, 4, 78–86. <https://doi.org/10.1016/j.cobme.2017.09.011>
- Zarei, M., Ansari, M. A., & Zare, K. (2019). The temporal confounding effects of extra-cerebral contamination factors on the hemodynamic signal measured by functional near-infrared spectroscopy. *Journal of Lasers in Medical Sciences*, 10(4), S73–S81. <https://doi.org/10.15171/jlms.2019.S14>
- Zhang, C., Hodges, B., & McCully, K. K. (2020). Reliability and reproducibility of a four arterial occlusions protocol for assessing muscle oxidative metabolism at rest and after exercise using near-infrared spectroscopy. *Physiological Measurement*, 41(6). <https://doi.org/10.1088/1361-6579/ab921c>
- Zhang, F., Cheong, D., Khan, A. F., Chen, Y., Ding, L., & Yuan, H. (2021). Correcting physiological noise in whole-head functional near-infrared spectroscopy. *Journal of Neuroscience Methods*, 360, 109262. <https://doi.org/10.1016/j.jneumeth.2021.109262>
- Zhang, Q., Brown, E. N., & Strangman, G. E. (2007). Adaptive filtering to reduce global interference in evoked brain activity detection: a human subject case study. *Journal of Biomedical Optics*, 12(6), 064009. <https://doi.org/10.1117/1.2804706>

- Zhang, Q., Strangman, G. E., & Ganis, G. (2009). Adaptive filtering to reduce global interference in non-invasive NIRS measures of brain activation: How well and when does it work? *NeuroImage*, 45(3), 788–794. <https://doi.org/10.1016/j.neuroimage.2008.12.048>
- Zhang, R., Zuckerman, J. H., Giller, C. A., & Levine, B. D. (1998). Transfer function analysis of dynamic cerebral autoregulation in humans. *American Journal of Physiology-Heart and Circulatory Physiology*, 274(1), H233–H241. <https://doi.org/10.1152/ajpheart.1998.274.1.H233>
- Zhang, R., Zuckerman, J. H., Iwasaki, K., Wilson, T. E., Crandall, C. G., & Levine, B. D. (2002). Autonomic Neural Control of Dynamic Cerebral Autoregulation in Humans. *Circulation*, 106(14), 1814–1820. <https://doi.org/10.1161/01.CIR.0000031798.07790.FE>
- Zhang, Y., Brooks, D. H., Franceschini, M. A., & Boas, D. A. (2005a). Eigenvector-based spatial filtering for reduction of physiological interference in diffuse optical imaging. *Journal of Biomedical Optics*, 10(1), 011014. <https://doi.org/10.1117/1.1852552>
- Zhang, Y., Tan, F., Xu, X., Duan, L., Liu, H., Tian, F., & Zhu, C.-Z. (2015a). Multiregional functional near-infrared spectroscopy reveals globally symmetrical and frequency-specific patterns of superficial interference. *Biomedical Optics Express*, 6(8), 2786. <https://doi.org/10.1364/boe.6.002786>
- Zhao, H., Brigadoi, S., Chitnis, D., Vita, E. de, Castellaro, M., Powell, S., Everdell, N. L., & Cooper, R. J. (2020). A wide field-of-view, modular, high-density diffuse optical tomography system for minimally constrained three-dimensional functional neuroimaging. *Biomedical Optics Express*, 11(8), 4110. <https://doi.org/10.1364/boe.394914>
- Zhao, H., & Cooper, R. J. (2017). Review of recent progress toward a fibreless, whole-scalp diffuse optical tomography system. *Neurophotonics*, 5(1), 011012. <https://doi.org/10.1117/1.nph.5.1.011012>
- Zheng, F., Sassaroli, A., & Fantini, S. (2010). Phasor representation of oxy- and deoxyhemoglobin concentrations: what is the meaning of out-of-phase oscillations as measured by near-infrared spectroscopy? *Journal of Biomedical Optics*, 15(4), 040512. <https://doi.org/10.1117/1.3483466>
- Zhou, X., Sobczak, G., McKay, C. M., & Litovsky, R. Y. (2020). Comparing fNIRS signal qualities between approaches with and without short channels. *PLOS ONE*, 15(12), e0244186. <https://doi.org/10.1371/journal.pone.0244186>

Zonta, M., Angulo, M. C., Gobbo, S., Rosengarten, B., Hossmann, K.-A., Pozzan, T., & Carmignoto, G. (2003). Neuron-to-astrocyte signaling is central to the dynamic control of brain microcirculation. *Nature Neuroscience*, 6(1), 43–50. <https://doi.org/10.1038/nn980>

8.1 Offprint of Frequency-domain analysis of fNIRS fluctuations induced by rhythmic mental arithmetic.

ORIGINAL ARTICLE

Frequency-domain analysis of fNIRS fluctuations induced by rhythmic mental arithmetic

Sergio Molina-Rodríguez¹ | Marcos Mirete-Fructuoso¹ | Luis M. Martínez¹ | Joaquín Ibañez-Ballesteros² 

¹Cellular and Systems Neurobiology, Institute of Neurosciences, Spanish National Research Council-Miguel Hernandez University, Alicante, Spain

²Department of Physiology, Miguel Hernandez University, Alicante, Spain

Correspondence

Joaquín Ibañez-Ballesteros, Department of Physiology, Miguel Hernandez University, Santiago Ramon y Cajal, 03550-San Joan d'Alacant, Alicante, Spain.

Email: charly.joa@umh.es

Abstract

Functional near-infrared spectroscopy (fNIRS) is an increasingly used technology for imaging neural correlates of cognitive processes. However, fNIRS signals are commonly impaired by task-evoked and spontaneous hemodynamic oscillations of non-cerebral origin, a major challenge in fNIRS research. In an attempt to isolate the task-evoked cortical response, we investigated the coupling between hemodynamic changes arising from superficial and deep layers during mental effort. For this aim, we applied a rhythmic mental arithmetic task to induce cyclic hemodynamic fluctuations suitable for effective frequency-resolved measurements. Twenty university students aged 18–25 years (eight males) underwent the task while hemodynamic changes were monitored in the forehead using a newly developed NIRS device, capable of multi-channel and multi-distance recordings. We found significant task-related fluctuations for oxy- and deoxy-hemoglobin, highly coherent across shallow and deep tissue layers, corroborating the strong influence of surface hemodynamics on deep fNIRS signals. Importantly, after removing such surface contamination by linear regression, we show that the frontopolar cortex response to a mental math task follows an unusual inverse oxygenation pattern. We confirm this finding by applying for the first time an alternative method to estimate the neural signal, based on transfer function analysis and phasor algebra. Altogether, our results demonstrate the feasibility of using a rhythmic mental task to impose an oscillatory state useful to separate true brain functional responses from those of non-cerebral origin. This separation appears to be essential for a better understanding of fNIRS data and to assess more precisely the dynamics of the neuro-visceral link.

KEYWORDS

extra-cranial contamination, fNIRS, forehead, frequency-domain analysis, mental arithmetic

This is an open access article under the terms of the [Creative Commons Attribution-NonCommercial](https://creativecommons.org/licenses/by-nc/4.0/) License, which permits use, distribution and reproduction in any medium, provided the original work is properly cited and is not used for commercial purposes.

© 2022 The Authors. *Psychophysiology* published by Wiley Periodicals LLC on behalf of Society for Psychophysiological Research.

1 | INTRODUCTION

Based on the neurovascular coupling principle, functional near-infrared spectroscopy (fNIRS) aims at detecting the hemodynamic changes evoked by neuronal oxygen consumption. NIRS is a non-invasive optical imaging technology and it has been widely used to measure brain, mostly cortical, activity through relative concentration changes in oxygenated (HbO) and deoxygenated (HbR) hemoglobin (for reviews see: Obrig & Villringer, 2003; Pinti et al., 2020).

A major challenge in fNIRS research is to reliably disentangle the hemodynamic response due to neurovascular coupling from other confounding components (Tachtsidis & Scholkmann, 2016). fNIRS changes caused by brain activity are naturally low in amplitude and unfortunately also overlap with other fluctuations that do not originate in the cerebral cortex, mainly: (i) systemic hemodynamic activity detectable in both cerebral and extracerebral regions (Bauernfeind et al., 2014; Minati et al., 2011; Tachtsidis et al., 2009), (ii) local blood flow changes in superficial tissue layers across the head (Kirilina et al., 2012), and (iii) instrumental noise and other artifacts. The first two, far from being simply spontaneously generated, can also be evoked by cognitive, emotional or physical tasks. If the modulation of these non-cortical task-related components of the signal mimics the dynamics of the brain activation of interest they could become an important source of interference and noise (Nambu et al., 2017; Näsi et al., 2013; Zimeo Morais et al., 2017). So much so that Takahashi et al. (2011) showed that the task-related skin blood flow changes could explain over 90% of the NIRS signal on a verbal fluency experiment, while Minati et al. (2011) further demonstrated the strong confounding effect of arterial blood pressure fluctuations.

To better infer the presence of a functional response, experimental protocols attempt to increase statistical power by repeating the stimuli a sufficient number of times, interspersed with contrast conditions in which a different response (or none) is expected. To this end, fNIRS experiments often used blocked or event-related designs, depending on whether one wants to analyze sustained or transient responses, respectively (Pinti et al., 2020). Event-designs use short-duration stimuli, normally randomized in order and separated by a constant or jittered inter-stimulus interval. Block-designs attempt to maintain mental engagement by presenting stimuli within a condition for a long enough time interval, followed by a different condition or a resting inter-stimulus interval (Amaro & Barker, 2006). To investigate the interaction between “sustained” and “transient” responses, mixed designs can also be used (Petersen & Dubis, 2012).

Depending on the stimulus presentation strategy, different analysis methods have been developed to make

inference about the functional hemodynamic response and isolate it from confounding interferences (for a review see Tak & Ye, 2014). Although classic averaging strategies provide robust results, the usual averaged-based statistical tests, such as *t* test or ANOVA, do not allow estimating the shape or time-course of fNIRS signals, so they have been progressively replaced by more powerful methods. These include the general linear model (GLM) framework (Friston et al., 2007; Schroeter, Bücheler, et al., 2004), data-driven approaches as principal component analysis and independent component analysis (Kohno et al., 2007; Zhang et al., 2005) and dynamic state-space modeling (Diamond et al., 2006; Kolehmainen et al., 2003). GLM is one of the most widely adopted statistical framework to quantify how well the measured fNIRS signals fit a hemodynamic model that reflects the expected neural response. It exploits the good temporal resolution of fNIRS and allows to include different covariates within the regression model (e.g., physiological signals). In its most basic form, the model is obtained by convolving a hemodynamic response function (HRF) with a stimuli function that encodes the hypothesized time course of the neuronal response (Koh et al., 2007; Tak & Ye, 2014). Therefore, GLM is a hypothesis-driven approach that requires the combination of a specific HRF (often taken from fMRI studies) and other nuisance regressors to construct the linear model, which might not be obvious depending on the task type, brain region and participant’s idiosyncrasy. Moreover, GLM demands special caution when applied to fNIRS signals due to some statistical issues (Huppert, 2016; Huppert et al., 2009; Koh et al., 2007). In contrast, “principal” and “independent” component analysis methods only rely on general statistical assumptions as orthogonality and independence, respectively. Although useful for separating the mixed components that make up the fNIRS signals, they require additional processing to elucidate which of them are task-related and which are not, particularly difficult when extracerebral and cerebral responses are correlated (Zhou et al., 2020). State-space models, mainly based on the Kalman filter, allow building complex hemodynamic models to describe the time varying characteristics of the fNIRS signals and estimate the HRF. Although dynamic analysis appears to provide better estimates of the HRF and better account for non-stationary signals, it still requires improvements in model specifications and state-space estimators.

Regardless of the strengths and weaknesses of each experimental method, all benefit from the inclusion of short-distance recordings to obtain a reference of the contribution of superficial layers to fNIRS signals (for reviews see: Fantini et al., 2018; Tachtsidis & Scholkmann, 2016; Tak & Ye, 2014). Multi-distance measurements are considered particularly effective in isolating the actual cerebral

response. Nevertheless, some open questions remain regarding, for example, the ideal range for source-detector distances, the optimal number of short-channels and their arrangement relative to long-channels. Ideally, and because there is growing evidence of the heterogeneous nature of surface hemodynamics (Wyser et al., 2020), each long-channel should be paired with at least one nearby short-channel. Unfortunately, such a precise spatial configuration of the paired measurements is not currently possible with the most commonly used NIRS devices today.

Our interest is focused on investigating the coupling between hemodynamic changes arising from the superficial and deep layers during mental effort, and isolating the task-evoked cortical response from other confounders. The rationale behind is the assumption that extracerebral and cerebral responses are the result of a coordinated effect product of different inter-related processes (Caldwell et al., 2016; Tachtsidis & Scholkmann, 2016). Rather than viewing surface fluctuations only as annoying confounders that must be removed, we regard them as carriers of valuable information. Information, that might prove essential not only to gain a better understanding of the fNIRS data but also, and perhaps as important, to more accurately assess the full dynamics of the neuro-visceral link. This goal, however, is hampered by the inherent difficulty in differentiating spontaneous from task-locked fluctuations. One possible solution is to deliberately induce periodic oscillations, so that they can be easily located and analyzed by using well-established frequency-domain methods.

In previous studies, a number of protocols have been used to generate hemodynamic oscillations at particular frequencies to investigate cerebrovascular regulation, including cuff inflation-deflation (Aaslid et al., 2007; Kainerstorfer et al., 2014), head-up tilting (Hughson et al., 2001), squat-stand exercises (Claassen et al., 2009), paced breathing (Pierro et al., 2014), and even in visual and motor studies (Obrig et al., 2000; Schroeter, Bücheler, et al., 2004; Wolf et al., 2002).

Here, we hypothesized that performing a cyclic cognitive task would also induce periodic hemodynamic fluctuations measurable in fNIRS recordings. To test this hypothesis, the current study was designed to generate an oscillatory state suitable for effective analysis in the frequency-domain. To this end, we employed a mental arithmetic task within a cyclic block-design at a specific frequency, while performing dense multi-distance recordings on the forehead using a newly developed multi-channel NIRS device. Concurrently, we recorded cardiac activity by continuously monitoring heart rate.

The analysis of the magnitude and phase relationships between signals in the frequency-domain would allow to: (i) identify common task-related oscillatory activity,

(ii) estimate the contribution of shallow and deep tissue layers to fNIRS signals, (iii) separate task-related surface hemodynamics from the putative cortical response, and (iv) measure the relative timing between HbO and HbR changes to better interpret the underlying physiological processes. Furthermore, we used the empirical transfer function as an alternative method to estimate the functional brain activity and assess the timed-coordination between extracerebral and cerebral responses. To our knowledge, such an approach has never been previously tested in fNIRS studies.

2 | METHOD

All data processing was done off-line with MATLAB (Version R2019a, Mathworks, Natick, MA, USA), using native functions, self-made scripts and open source packages.

2.1 | Participants

All procedures performed in this study were approved by the Ethics Committee of the University Miguel Hernandez, in accordance with the declarations of Helsinki. Participants did not receive any remuneration. A total of twenty-four healthy young adults volunteered, 10 males and 14 females (mean age: 22.3; *SD*: 4.2), were recruited for this study. All of them were instructed beforehand about the purpose of the experiment and provided informed written consent prior to study enrollment. After that, the participants practiced the task for 10–15 min to make sure they understood and got used to it (to minimize stress responses). They were seated in a comfortable position while performing the task.

2.2 | Mental task

In this work, the task was based on a block protocol designed as a cyclical pattern of mental effort, alternating phases of mental math with phases of pause of the same duration, that is, regular repetitions of activation-rest. The idea behind this was to induce periodic hemodynamic changes in the form of cycles of some kind of response followed by a return to basal levels. In this way, such an oscillatory pattern may be analyzed by conventional spectral methods. As illustrated in Figure 1, the experimental session was organized into three consecutive uninterrupted recordings: (i) 300 s of baseline in resting condition, (ii) 300 s of task, and (iii) 300 s of recovery in a relaxed state. Participants were asked to keep their eyes



FIGURE 1 Schematic representation of the experimental procedure

on the screen throughout the experiment. During specific time intervals, an image was presented on the screen to instruct the participants to relax mentally. This image was a soft-colored paint depicting an inanimate scene (it was rated as neutral by the participants in a parallel study with affective pictures; results not shown here). The NIRS probe remained in the same position throughout the session. The task consisted of 10 consecutive 30-s trials. Each trial began with 15 s of mental calculation, followed by a 15-s pause of relaxation. To perform the mental math participants were asked to iteratively subtract a small number (between 5 and 9) from a three-digit number (between 100 and 199), as fast as possible. Both numbers, chosen randomly in each trial, were presented on a 21.5" display monitor, 80 cm. away from the participants' eyes. Afterwards, the pause started by presenting the question "Result?" for 5 s, which prompted the participants to inform verbally of the final result of their mental calculations (to allow scoring the performance and ensuring that the participants were paying attention), followed by the "relax" image. Two seconds before presenting the subtraction operands, a fixation cross was displayed in the middle of the computer screen to announce the beginning of the mental calculation. Note that the 30-s period of the trials corresponds to a frequency of 0.033 Hz, which we will refer to as f_t (task frequency) throughout this manuscript. This frequency was chosen so that it did not overlap with well-known spontaneous fluctuations such as blood pressure (0.08–0.12 Hz) (Huppert et al., 2009; Julien, 2006), or very slow endothelial activity (0.01–0.02 Hz) (Stefanovska et al., 1999). Furthermore, the 15-s duration of mental effort accommodates that of a typical hemodynamic response (Buxton et al., 2004; Friston et al., 1998), while the next 15-s pause allows a return to baseline levels, being an optimal inter-event interval to minimize overlaps between consecutive hemodynamic responses (Aarabi et al., 2017; Dale, 1999). Here, we tried to minimize the generation of distress by using a subtraction arithmetic task that was cognitively challenging, but did not exceed the participants' mental abilities. Further, we constantly emphasized the importance of the mental effort, and not the amount or accuracy of the operations performed.

2.3 | Heart rate measurement

ECG was registered using a BIOPAC MP36 physiological monitoring system and the AcqKnowledge software 4.1 (Biopac Systems, Inc., Goleta, CA, USA) at a sampling rate of 500 Hz. ECG was recorded in lead II configuration with disposable electrodes. The MP36R device was digitally synchronized through the I/O port with the PC running the stimuli presentation, so event markers were recorded as well. At the end of the experiment, the raw data were post-processed with AcqKnowledge to: (i) create an R-R tachogram from the ECG signal, using the implemented Pan–Tompkins algorithm (Pan & Tompkins, 1985) for R wave detection, and (ii) extract the instantaneous heart rate from the reciprocal of the tachogram. Finally, the data was exported to MATLAB and then resampled to 10 Hz using cubic spline interpolation.

2.3.1 | Heart rate exclusion criteria

Many studies have investigated how cognitive performance correlates with the stress level induced by mental workload, in most cases through different physiological measures, heart rate being one of common use (Charles & Nixon, 2019; Hakimi, 2018; Mandrick et al., 2016; Tao et al., 2019). However, there is not a clear threshold to differentiate between heart rate changes due to a pure mental effort and those due to a stressful situation. As the present work focuses on the first, it was necessary to estimate a maximum increase in heart rate, beyond which the influence of stress was considered disproportionate. We took as a reference the results of other studies that applied the Trier Social Stress Test, a standard protocol for stress induction in healthy people (Kudielka et al., 2007). In their review work, Kudielka et al. (Kudielka et al., 2007) reported that the mean heart rate increases to the test are about 15–25 bpm. Kirschbaum et al. (1993), found increases about 26 bpm during the test. On the basis of the aforementioned literature, we decided to apply a limit well below the reported values. Compared to the mean heart rate at baseline, the threshold was set to a maximum

increase of 12 beats per minute (bpm) during the task. Two participants were excluded for exceeding this limit, leaving a sample of $N = 22$. Thus, only those participants showing reasonably stable heart rate throughout the baseline and task periods were further considered. The Wilcoxon-signed rank test was used to resolve for differences between the maximum heart rate reached during baseline and task.

2.4 | fNIRS recordings

In this study we used a multichannel, wireless, continuous-wave NIRS device (Brainspy28, Newmanbrain, S.L., Elche, Spain), which employs four sources and ten detectors forming a rectangular grid of 80x20 mm. Each source housed two light-emitting-diodes (LED) at wavelengths 740 nm and 850 nm. Through a precise switching cycle, the device combines pairs of optodes at different separation distances, providing 16 short-channels and 12 long-channels that corresponds to a source-detector distance of 14 and 32 mm, respectively (Figure 2a). Moreover, the device measures and corrects the ambient light contribution.

Also it incorporates a 3-axis accelerometer to account for head motion. It transfers data wirelessly (via Bluetooth) at a sample rate of 10 Hz. The NIRS probe was placed onto the forehead, centered on AFpz according to the international 10–5 system, mainly covering the frontopolar area of the prefrontal cortex (PFC) (Figure 2b). The optodes contact the skin through an intermediate convex lens pressing the skin when the probe is held firmly, in order to reduce cutaneous blood flow and, therefore, its hemodynamic interference (Takahashi et al., 2011).

2.4.1 | Signal quality check—Channels and participants exclusion criteria

To ensure that only clean signals pass to further analysis, we conducted some preliminary quality tests. To account for instrumental noise (Huppert et al., 2009; Orihuela-Espina et al., 2010) we evaluated first the raw optical data to identify channels exhibiting extreme values (below 5% or above 95% of the device dynamic range), or an excessive coefficient of variation $>7.5\%$ (calculated as the percentage ratio between the standard deviation and the mean)

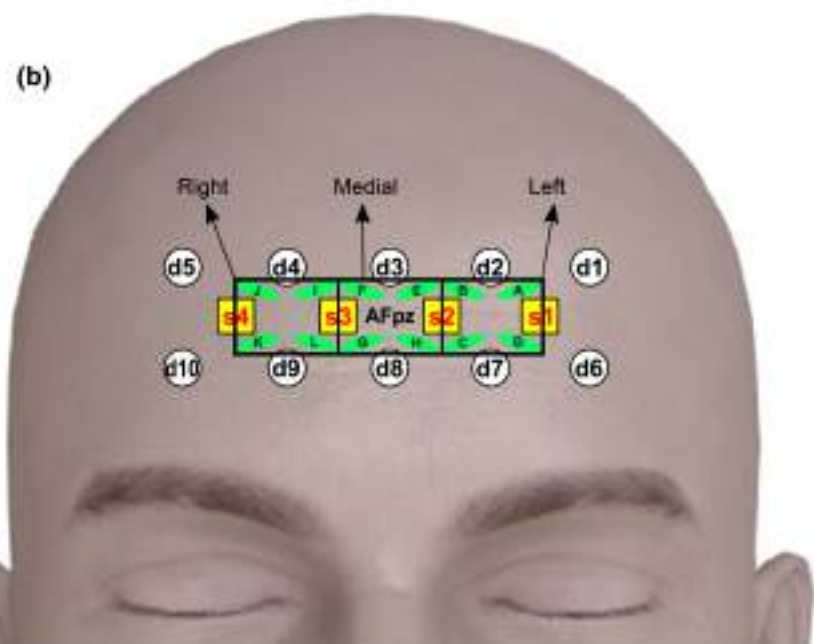
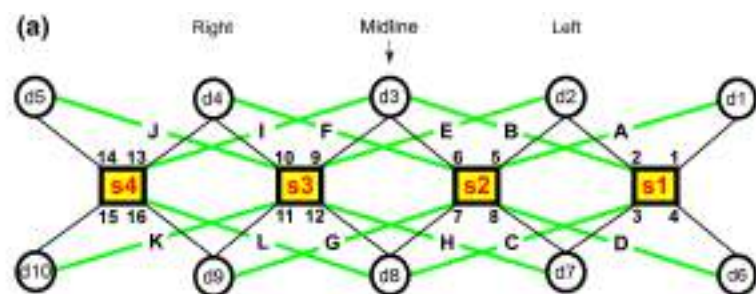


FIGURE 2 Probe geometry and placement. (a) Optode arrangement (yellow squares: Sources; white circles: Detectors). Sixteen short-channels (black lines with numbers) and twelve long-channels (green lines with letters). (b) Probe position on the forehead. Green shaded areas roughly mark the regions explored by the long-channels. Black rectangles outline the long-channels averaged within each ROI (right, medial and left)

(Zimeo Morais et al., 2017). Thus, we discarded the recordings suffering from poor signal to noise ratio, saturation or unphysiological noise contamination. By visual inspection, we rejected recordings affected by motion artifacts by identifying sharp changes in the fNIRS signals aligned with abrupt shifts in the accelerometer data. Two participants were excluded after the quality check. Therefore, the final sample consisted of $N = 20$ participants (8 males and 12 females; mean age: 21.7; SD : 3.8).

2.4.2 | fNIRS data preprocessing

Preprocessing was carried out using the Homer2 NIRS package (Huppert et al., 2009) based in MATLAB. The raw optical data were converted to optical density, and then into oxy- ([HbO]) and deoxyhemoglobin ([HbR]) relative concentration changes via the modified Beer–Lambert law (Delpy et al., 1988; Kocsis et al., 2006). We used a differential pathlength factor calculated in accordance with the general equation described in Scholkmann and Wolf (2013), which takes into account the participant’s age and the wavelength. No partial volume correction was used.

The fNIRS data were digitally low-pass filtered by using a zero-phase, 5th-order Butterworth filter, cut-off 2.5 Hz (MATLAB Signal Processing Toolbox); no high-pass filtering was applied. Therefore, we remove only high-frequency noise while preserving cardiac, respiratory, blood pressure and vasomotor components. After preprocessing, for each chromophore we obtained 16 time-series from the short-channels plus 12 from the long-channels that we refer to as “shallow-” and “deep-signals”, respectively, to indicate how much the light penetrated during their corresponding records. Thus, we had a set of multi-distance recordings to effectively address the problem of extracerebral contamination (Pfeifer et al., 2018; Saager & Berger, 2005; Scholkmann et al., 2014; Yücel et al., 2015), by assuming that short-separation recordings are sensitive only to extra-cerebral changes, while long-separation recordings are sensitive to both extracerebral and cerebral activity (Brigadoi & Cooper, 2015; Saager & Berger, 2005; Scarpa et al., 2013; Yücel et al., 2017).

When using multi-distance recordings regression can be performed assuming that the physiological noise has comparable time courses in both shallow- and deep-signals, and that the focal, task-evoked, cerebral hemodynamics is independent, that is, uncorrelated (Saager et al., 2011; Saager & Berger, 2008). However, the heterogeneous nature of the local superficial fluctuations cannot be dismissed, which raises the need to collect the shallow-signals at recording sites as close as possible to the deep-signal to be decontaminated from surface hemodynamics (Gagnon et al., 2012). Here, we used a NIRS device that

allows each deep-signal to have three shallow-signals that meet the proximity requirements: two obtained close to the long-channel’s detector and source, respectively, and one close to its center (see Figure 2a). Adopting the “double short separation measurements” approach recommended in (Gagnon et al., 2014), we used the combination (the sum) of the two shallow-signals recorded near the detector and source to estimate the extracerebral component to be suppressed from the corresponding deep-signal. Thus, for example, the signal from long-channel “A” was regressed on the sum of the signals from the short-channels 1 and 5 (Figure 2). Over the entire time courses, for all the deep-signals we computed:

$$S_{clean} = S_{deep} - (\beta_0 + \beta_1 S_{shallow}),$$

where β_0 and β_1 are the regression coefficients, S_{deep} is the deep-signal, $S_{shallow}$ is the combined shallow-signal and S_{clean} the desired “clean signal” (in fact, the raw residuals). We solved linear regression by applying the MATLAB function “robustfit”, which uses an iteratively reweighted least squares algorithm and is less sensitive to outliers than ordinary least-squares (Holland & Welsch, 1977). After regression, each S_{deep} has its associated pair S_{clean} and $S_{shallow}$ making a total of 12 signal triplets for each chromophore. Noteworthy, although S_{clean} probably represents the neural component, at this point we prefer the term “clean” without making assumptions about its actual origin. This precaution is based on the fact that, because our mental task attempts to induce periodic oscillations the requirement of non-correlation between extracerebral and cerebral hemodynamics may not be met, compromising the performance of regression (Fantini et al., 2018; Saager & Berger, 2008). Later, in this work, we will apply additional analysis to verify the nature of these regression-estimated signals.

Finally, as the channel positions are not fully consistent across individuals due to the variability in head shape and size (Tak et al., 2016), the signal-to-noise ratio and signal reliability can be improved by spatial clustering (Plichta et al., 2006; Schecklmann et al., 2008). To this end and to avoid interpreting isolated channels, for every single participant we averaged across the signals belonging to three regions of interest (ROI), left, medial, and right (Figure 2b). As such, the signal triplets associated with the four leftmost long-channels (A, B, C, D) yield the corresponding averages of $S_{shallow}$, S_{deep} and S_{clean} . The same procedure was applied for the medial (E, F, G, H) and the rightmost (I, J, K, L) four long-channels. Thus, each of the three ROIs now reduces to just three average signals that, from now on, we denote by SS (shallow), DS (deep), and CS (clean). All further processing was done on these signals, which display comparable signal-to-noise ratio across the three ROIs because they have been obtained by averaging the

same number of neighboring signals in each frontopolar region. For each ROI, we computed the averaged time courses of HbO and HbR for the three signals across all the participants. Furthermore, we obtained the grand average of the trials epoched in the interval -15 to 30 s relative to the onset (10 trials \times 20 participants = 200 trials). Standard error of the mean (*SEM*) was calculated as well.

2.5 | Identification of task-induced frequencies

Firstly, we evaluated if the task successfully induced oscillations by estimating the power spectral density (PSD) of each participant's NIRS data during the task and the baseline condition. The PSDs were computed using Welch's averaged periodogram method (Welch, 1967) with a hamming window of length 2000 samples and 50% of overlap to achieve a good frequency resolution (0.005 Hz), spectral smoothness, and reduced noise variance (Ilvedson, 1998). To allow comparisons, the PSDs were normalized to relative percentage values by calculating the power ratio of each frequency bin to the total power of the entire spectrum (Aarabi & Huppert, 2016). For further analysis, we focused on the frequency range 0.005 to 0.08 Hz under the assumption that the expected task-induced oscillations would fall within that range.

We assessed the presence of significant task-induced oscillations by contrasting the PSDs during task and baseline. Along frequency bins we performed one-tail paired *t*-tests to check whether within-subject PSD values were statistically higher for the task compared with baseline. The observed *t*-statistics were corrected for multiple comparisons by following the cluster-based nonparametric approach given in (Maris & Oostenveld, 2007). We computed Monte Carlo cluster tests over 1000 permutations of the same *t*-test where the condition, that is, task and baseline, was randomly shuffled within subject. Then, we estimated the so-called permutation *p*-value from the proportion of random realizations that have larger cluster-statistic than the observed one. We set a critical alpha-level = 0.01 to identify the frequency bins that showed significantly higher PSD values during the task. Finally, the PSDs were averaged across participants ($N = 20$) to obtain the average normalized PSD of HbO and HbR for each signal type and ROI. In addition, the 95% confidence interval (CI) for the mean at each frequency bin was calculated by bootstrapping over 1000 resamples.

2.6 | SS and DS relationships

Here, SS data were obtained from fNIRS channels exploring the frontopolar region with a source-detector distance of

14 mm. The scalp-cortex distance is known to be increased in this region (15 mm to 17 mm) compared to more lateral frontal areas (Cui et al., 2011; Haeussinger et al., 2011) which, together with the presence of the frontal sinuses, decreases the cerebral fNIRS sensitivity (Haeussinger et al., 2014). Moreover, as pointed out by Zhang et al. (2015), short-channels with a source-detector distance in the range of 14 to 16 mm have a sensitivity to the brain of only about 0.47% . Although it is unlikely that SS picked up cortical signals, it was still important to examine the commonalities and differences between SS and DS to reasonably ensure that SS data are primarily dominated by shallow hemodynamics, while DS also contain deeper components that, likely, stem from the cortical layer. The rationale for this analysis was to demonstrate that the link SS-DS would be altered at the task frequency if another deep oscillatory process (e.g., neurovascular response) appears in the DS signal. To this end, for the time-series pairs HbO_{SS}/HbO_{DS} and HbR_{SS}/HbR_{DS} we performed the following within-subject analysis: (i) cross-spectrum to identify shared fluctuations, (ii) frequency-domain correlation to identify significant covariation, and (iii) transfer function to evaluate the relationship in magnitude and phase. Following the recommendations given in (Claassen et al., 2015) for transfer function analysis, neither detrending nor high-pass filtering was used, and a triangular smoothing window (coefficients $1/4, 1/2, 1/4$) was applied to both auto- and cross-spectra.

To identify synchrony (or shared fluctuations) in the frequency-domain between shallow and deep signals, a cross-spectrum analysis was performed to compare the two signals. We computed the cross-power spectral density (CPSD) of the bivariate time-series using the MATLAB function "cpsd", based on the Welch's averaged periodogram method (Welch, 1967); as for PSD we set a hamming window of length 2000 samples and 50% of overlap. From the complex-valued result, we obtained the magnitude and phase values to find the shared power and phase shift between both signals at particular frequencies. The magnitude peaks that showed significantly higher values during the task were located by following the same approach as for PSD in Section 2.5; the values were normalized and averaged in the same way.

To ensure the reliability of the cross-spectral estimates, we evaluated whether the signals showed significant stability in their relative amplitude and phase at particular frequencies. To this end, we estimated their frequency-domain correlation by computing the magnitude-squared coherence (MSC) as a function of the PSDs and the CPSD (Zhang et al., 1998):

$$MSC_{ssds}(f) = \frac{|CPSD_{ssds}(f)|^2}{PSD_{ss}(f) PSD_{ds}(f)}$$

Coherence values vary between 0 (no correlation) and 1 (perfect correlation), describing the linearity of the relationship between both signals in the frequency domain. The coherence values were also averaged across participants for each signal pair and ROI. Only if significant coherence exists, the cross-spectral estimates have a useful meaning (Claassen et al., 2015). Values of about 0.5 have been commonly considered as a threshold for significance (Sassaroli et al., 2018) but, as the threshold may depend on the frequency, a better alternative for assessing significance is the surrogate data approach (Faes et al., 2004; Paluš, 1997). In this work, following the nomenclature given in (Paluš, 1997), we chose the FT1 surrogates method as it conserves the power spectrum of the original signals (Faes et al., 2004). FT1 surrogates were constructed by substituting the phase of the Fourier transform of the original signals with random values in the range $[-\pi, \pi]$ while the modulus is preserved, and then returning to time-domain by inverting the Fourier transform. We generate 1000 surrogate series and for each one the averaged MSC was computed as for the original signals, realizing the null hypothesis that the averaged MSC stem from pairs of signals that fluctuate asynchronously at the same frequencies of the experimental signals. Afterwards, the mean MSC values obtained from the actual signals were compared with the FT1 distribution to estimate the MSC threshold levels for each frequency bin at $\alpha = .05$.

A transfer function describes the dynamic relationship between the output signal of a system and the input signal. Under the assumption of linearity, the transfer function can be estimated from the frequency-domain representation of the experimental input-output signals. Transfer function models have become a popular approach to investigate the dynamic of cerebrovascular autoregulation (Claassen et al., 2015; Van Beek et al., 2008), and they have also been used to remove systemic physiological noise from fNIRS signals (Bauernfeind et al., 2013; Florian & Pfurtscheller, 1997). In this work, assuming that SS has energy in the frequency range of interest and contain quasi-periodic oscillations, the transfer function $H(f)$ was approximated from the experimental fNIRS data as (Zhang et al., 1998):

$$H(f) = \frac{CPSD_{ssds}(f)}{PSD_{ss}(f)}$$

For each time-series pair, shallow and deep signals were, respectively, the input and output data used to obtain an approximation of the transfer function at particular frequencies (e.g., input HbO_{ss} , output HbO_{ds}). From the complex-valued result, we obtained the magnitude (gain), which represents the relative change in μM between input and output, and the phase that carries their temporal coupling (phase difference or time-lag), while coherence

values indicate the reliability of these measures. For reporting, the gain data were converted into percentage values. Then, at the group level and for each signal pair and ROI, we computed the averages of gain and circular phase angle; phase statistics were managed by means of the Matlab Toolbox CircStat (Berens, 2009). In addition, we calculated the 95% confidence interval (CI) band around the mean by bootstrapping over 2000 resamples. Finally, to assess whether the task induced a consistent phase coupling across participants, we applied a bootstrapped Rayleigh test (Oden, 1983) on the phase values at the task frequency. Consistent coupling should be reflected as a narrow distribution of phase values around a preferred angle. On the contrary, a poor inter-subject synchronization should display a more uniform distribution throughout the 360° circle.

2.7 | Estimating deep component from transfer function

We previously expressed some concerns relating to the reliability of the regression-estimated CS signals. To address them, we applied an alternative novel approach to estimate CS from the transfer function. Supposing that DS solely contains the same fluctuations seen in SS, the relation between both signals should be highly linear and coherent, only altered by the small differences in the volume sampled by our short- and long-channels. Therefore, the transfer function should yield fairly constant gain values across frequencies (depending of the fractional part of DS power that is produced by SS) and a phase shift close to zero (in-phase). Furthermore, coherence values should be close to one. However, when another oscillatory process is added to DS we can expect some level of disturbance in gain and/or phase at certain frequencies. At a specific frequency, cyclic hemodynamic oscillations can be approximated as sinusoids, completely defined by their values of amplitude, phase and frequency. Adding two sinusoids of common frequency results in a sinusoid with same frequency but with amplitude and/or phase altered. In our case, if the task elicits independent cyclic oscillations in both shallow and deep layers, the observed deep sinusoid $X_{ds}(t)$ at the task-frequency would result from the sum of the two contributing sinusoids $X_{ss}(t)$ and $X_{uk}(t)$, that is:

$$X_{ds}(t) = X_{ss}(t) + X_{uk}(t),$$

where $X_{ss}(t)$ is the observed shallow sinusoid and $X_{uk}(t)$ is the unknown deep component. All of these sinusoids are characterized by their values of amplitude A , angular frequency ω and phase ϕ , thus, in sinusoidal form:

$$A_{ds} \cos(\omega_{ds} t + \phi_{ds}) = A_{ss} \cos(\omega_{ss} t + \phi_{ss}) + A_{uk} \cos(\omega_{uk} t + \phi_{uk}).$$

Because they represent harmonic oscillations of common frequency (i.e., $\omega_{ds} = \omega_{ss} = \omega_{uk} = \text{task frequency}$), they do not depend on ω or t , but only on A and ϕ , which makes it possible to convert them into phasors (or complex numbers). In exponential form would be:

$$\bar{X}_{ds} = A_{ds} e^{j\phi_{ds}}, \bar{X}_{ss} = A_{ss} e^{j\phi_{ss}} \text{ and } \bar{X}_{uk} = A_{uk} e^{j\phi_{uk}},$$

where $j = \sqrt{-1}$, while \bar{X}_{ds} , \bar{X}_{ss} and \bar{X}_{uk} are the phasor representation of $X_{ds}(t)$, $X_{ss}(t)$ and $X_{uk}(t)$ respectively. According to phasor algebra:

$$\bar{X}_{ds} = \bar{X}_{ss} + \bar{X}_{uk},$$

hence, we can estimate the unknown component by computing the subtraction of the two complex numbers corresponding to the known phasors, that is:

$$\bar{X}_{uk} = \bar{X}_{ds} - \bar{X}_{ss}. \quad (1)$$

To this end, we firstly obtained the phasors' values for phase and amplitude as follows: (1) We designated \bar{X}_{ss} as the "reference phasor" and, hence, $\phi_{ss} = 0$. (2) From the transfer function we obtained the phase value between SS and DS at the task frequency f_t , so $\phi_{ds} = \arg(H(f_t))$, which indicates the phase-shift of \bar{X}_{ds} with respect to \bar{X}_{ss} . (3) A_{ds} was obtained from the PSD by calculating the RMS amplitude at f_t and converting it to the peak amplitude of a sinusoid that is, $A_{ds} = \sqrt{2} \sqrt{\text{PSD}(f_t) \text{FR}}$, where FR is the frequency resolution (0.005 Hz in our case). Due to spectral leakage, better amplitude estimates are obtained by summing the PSD values within the frequency interval $[f_t - \text{FR}, f_t + \text{FR}]$. (4) A_{ss} was estimated in the same way and then scaled to the theoretical value that it should reach in DS by itself. This is a crucial step in the procedure. The scaling factor was the gain value of the transfer function at f_t but during "baseline", which represents the fraction of SS magnitude present in DS when no significant deep component contributes. Thus, A_{ss} was multiplied by the baseline gain to yield its scaled amplitude. Then, we performed the phasor subtraction (Equation 1) to obtain the amplitude A_{uk} and the phase ϕ_{uk} of the phasor \bar{X}_{uk} . Finally, \bar{X}_{uk} was converted to a sinusoid, which represents the alternative CS estimated by transfer function. This procedure was performed for every single-participant's signals and averages were computed for each ROI and chromophore.

2.8 | Simulations

To assess the feasibility of CS estimation by phasors, we performed a fairly realistic simulation by using the actual

data during task rather than artificial or baseline signals. SS was used as is. DS was obtained by scaling SS to the amplitude that it should reach in the deep-recording, that is, multiplying by the transfer function gain during baseline (See Section 2.7, step 4). We generated a synthetic neural signal as a sinusoidal wave oscillating at 0.033 Hz, with amplitude and phase obtained from the averaged CSs estimated by regression (amplitude = 0.05 μM and 0.04 μM , time-lag = 13 and -9.5 s for HbO and HbR, respectively, and relative to CS) (See Results 3.1 and Figure 4). Then, the sinusoid was added to DS to build the simulated deep-signal. This procedure was applied to the medial-ROI data of every participant and then subjected to both regression and phasor estimation of the neural component. Because phasor-estimated result represents the average over the task, the regression-estimated signal was averaged across trials to allow intra-subject comparisons. The quality of the neural estimates was quantified using the root mean square error (RMSE) between the true synthetic signal and the recovered one. A paired t test was applied to resolve for statistical differences.

2.9 | Measuring HbO/HbR coupling

To investigate significant frequency-domain correlation between HbO and HbR, we computed their MSC and CPSD during the baseline and task conditions. In this case, we were only interested in the SS and CS signals because we assume that DS is nothing more than the linear combination of the first two. MSC and CPSD data, as well as their averages and significance thresholds, were obtained by the same procedure previously detailed. In addition, from the complex-valued CPSD we extracted the phase data (Müller et al., 2003; Reinhard et al., 2006) at the task-frequency to assess the temporal relation (time-shift) between both chromophores. As usual, this procedure was applied for every single participant. Next, we computed the circular mean of phase angles at the group level and then, to assess whether it was significantly oriented in a preferred direction, we applied a bootstrapped Rayleigh test (Oden, 1983) through 2000 resamples. The 95% CI was also computed by bootstrapping.

2.10 | Measuring HbO/heart rate coupling

As in Section 2.9, we investigated the relationships between HbO and heart rate by MSC and CPSD. We only used the HbO data of the SS signals because the coupling between heart rate and the rest of signals can be inferred from the results obtained in other previously performed tests.

3 | RESULTS

We analyzed how fNIRS signals fluctuate in response to a cyclic mental arithmetic task, which can induce physiological stress responses (Charles & Nixon, 2019; Kudielka et al., 2007). To reduce any putative stress response that could have influenced our results we have taken several cautions. First, we have used a non-strenuous task duration, only 30 s, including a calculation and a recovery phase. Second, volunteers practiced the task for 10–15 min to make sure they understood and got used to it and the experimental setting. Third, the participants included in this study had a stable mental performance and reasonably low heart-rate fluctuations during the entire experimental session. In fact, they showed no significant differences between their heart rate values across the two conditions (baseline and task) of the experiment, (Wilcoxon's signed rank test, $p = .091$). On average, during task, the mean heart rate increased only slightly, 7 bpm (9%), with respect to the baseline (Table 1).

3.1 | Oscillations alignment to the task frequency

fNIRS signals showed clear oscillations in accordance with the task frequency and such oscillations were consistently observed, over multiple ROIs, on both shallow and deep layers. Figure 3 shows the results of the PSD analysis at the group level. The normalized PSDs were averaged across participants for each of the three ROIs, for each signal type and for each condition (baseline and task). The DC component (frequency = 0) was set to zero and the upper value of the displayed frequency range was limited to 0.08 Hz. A ubiquitous peak can be seen at ~0.01 Hz both at rest (Figure 3, black traces) and during mental task (Figure 3, colored traces), although the cluster-permutation test found no significant differences between both conditions. However, a clear peak at f_t was detected exclusively during the task and marked as significant by the cluster-test ($p < .01$) (Figure 3, shaded vertical rectangles). This peak corresponds closely to the task frequency and was observed in all ROIs and signal types. In some cases, a secondary peak around 0.066 Hz was also found, which most likely represents a harmonic of the fundamental task-frequency. It seems obvious that

TABLE 1 Averaged heart rate metrics across participants (baseline and task)

All $n = 20$	Maximum (range)	Mean (range)
Baseline	98 (62–127)	77 (53–104)
Task	103 (66–140)	84 (55–116)

the task successfully induced cyclic fluctuations of the HbO and HbR, which were present in the shallow-signals (Figure 3SS), deep-signals (Figure 3DS) and in clean-signals (Figure 3CS).

Figure 4 shows the group-level averaged temporal traces of HbO and HbR after band-pass filtering around the task frequency, using a filter width of 0.015 Hz. It can be seen how SSs (Figure 4SS) start to oscillate in sync with the task-trials, although showing an evident time-shift between both chromophores. Figure 4 also depicts the grand averages of the trials across participants (smaller plots next to temporal traces), which for SS display a common response consisting of: (i) shortly before the trial onset, the HbO strongly increases reaching a maximum at ~11.2 s, (ii) then HbO gently returns to previous levels during the subsequent rest, and (iii) HbR changes were less pronounced and lead HbO by ~4 s. Regarding the DSs, a similar periodic response can be observed (Figure 4DS), but HbO peaks are slightly anticipated to SS (~0.3 s) while HbR lags SS by ~2 s. Finally, CSs also show cyclic fluctuations aligned to the task (Figure 5CS), but in this case HbO oscillates in counter-phase with respect to SS. Furthermore, HbO and HbR show similar amplitudes (~0.05 μM) and evolve anti-correlated with each other, HbO showing a valley at ~12.6 s and HbR a peak at ~18.5 s. At this point, it seems likely that the observed time-shift in DS, relative to SS, is due to the summation of the CS component. Interestingly, the pattern seen in CS would correspond to an inverted HbO/HbR response, that is, decrease in HbO together with an increase in HbR. Noteworthy, the inverted pattern does not appear immediately but progressively reaches stability during the first few trials. This observation might be of interest for a tentative physiological interpretation (see Discussion).

Because fNIRS signals can be highly individual-specific, we have provided additional information about hemodynamic response and spectral data for each participant in the Supplementary Material, with the aim of illustrating the individual differences and the variable contribution of surface tissues to the fNIRS signals in different regions of the forehead.

3.2 | SS/DS relationships

To answer the question of to what extent shallow fluctuations contribute to deep-signals, we performed coherence, cross-spectra and a transfer function estimate between SS and DS data (Figure 5). The analysis revealed a significant cross-spectral peak during the task centered at f_t ($p < .01$), and that was present in all ROIs for HbO and HbR (Figure 5a, left axis). These peaks indicate that SS and DS oscillate at the task frequency with a remarkable shared

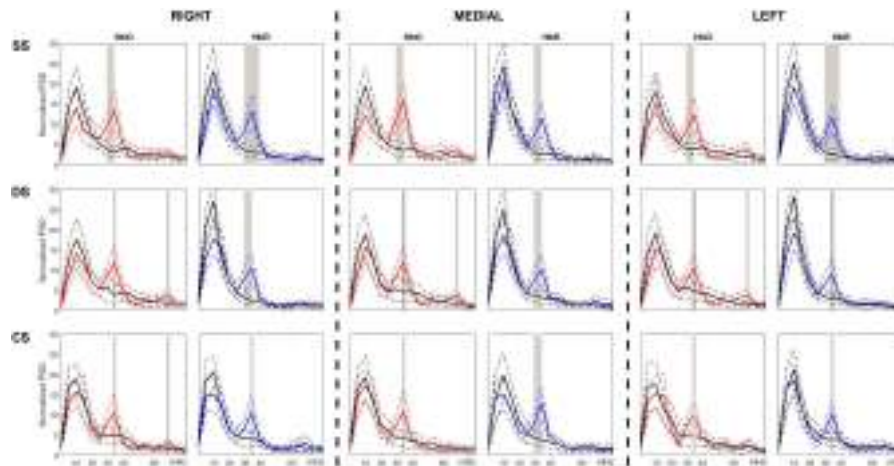


FIGURE 3 Grand average (20 participants) of the normalized PSDs for each ROI (right, medial and left), chromophore and signal type in the frequency range 0.005 to 0.08 Hz. Solid black curves refer to baseline and colored curves to task. Dashed lines represent the 95% CI of the mean. Shaded rectangles delimit the frequency ranges that show significantly higher power during task. (SS) results for shallow-signals. (DS) deep-signals. (CS) clean-signals

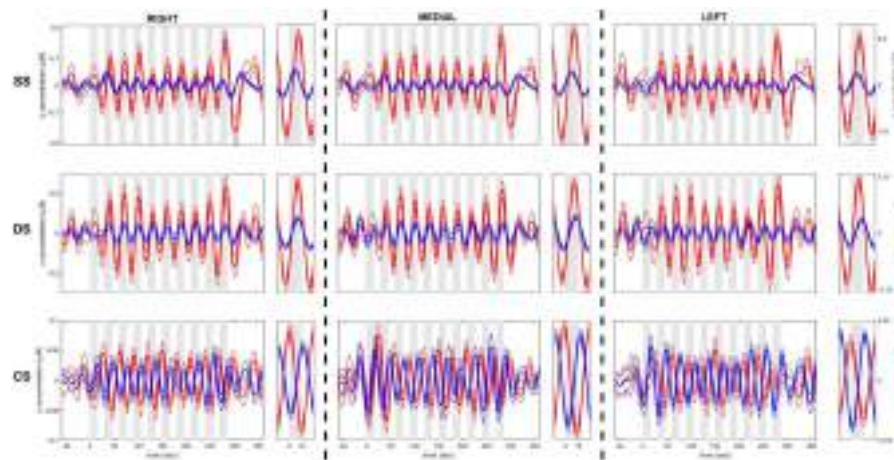


FIGURE 4 Averaged time courses of HbO (red traces) and HbR (blue traces) across participants during task (plus a portion of baseline and recovery to the left and right respectively) for each ROI and signal type. The small plots next to time courses show the grand average of trials. SEMs are depicted by thin lines. Gray boxes mark the 15-sec of mental math of each trial. Each row show the results for shallow (SS), deep (DS) and clean-signals (CS) for the three ROIs (right, medial and left).

power. Moreover, a higher peak was located at ~ 0.01 Hz but showing no differences during task compared to baseline.

Coherence values were above the significance threshold along the entire range of explored frequencies in both conditions (Figure 5a, right axis), describing a consistent linear relationship between SS and DS in the frequency domain. Coherence levels were particularly high for HbO (on average > 0.8), indicating a stronger correlation and, likely, that HbO is more influenced by shallow hemodynamics than HbR. It should be noted that coherence also peak during the task around f_t (quite evident for HbR), meaning that the task-induced oscillations were more coherent than the spontaneous ones.

During the task, transfer function analysis revealed a decrease in magnitude around f_t for HbO, especially

pronounced in the medial ROI (Figure 5b). Phase values also showed certain perturbation at the same frequency (Figure 5c). HbR exhibited a slight increase in magnitude, mainly observed in the medial and left ROIs (Figure 5b), in parallel with strong disturbances in the phase values (Figure 5c). Again, the resting condition did not show such changes. A t test revealed no differences at the group-level between gain values of HbO and HbR during rest ($p = 0.2$). However, during task the gain values were significantly lower for HbO ($p < .01$) in medial and left ROIs, which agrees with the decreasing gain values shown in Figure 5b. The paired t test showed no differences for either HbO or HbR when comparing task with rest, indicating that on average the change during task is very subtle.

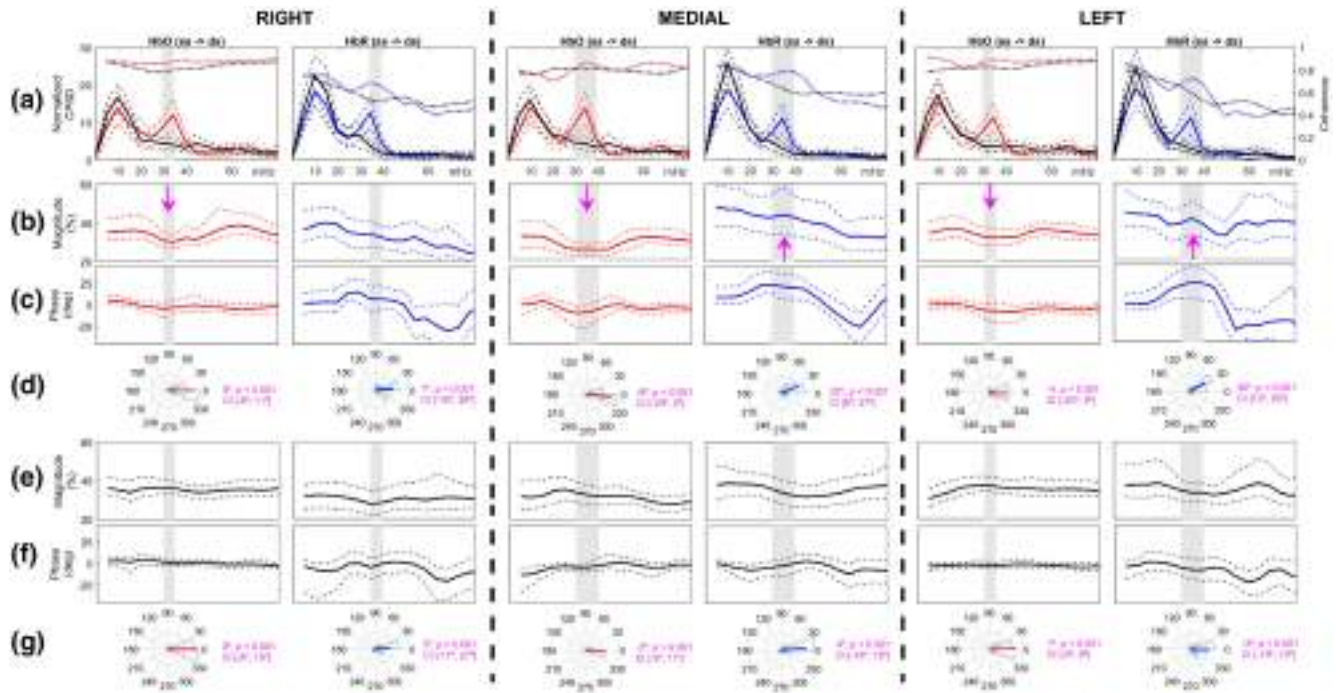


FIGURE 5 Averaged results across participants of CPSD, MSC and transfer function data between SS and DS for each ROI, comparing baseline and task. (a) CPSDs are drawn on the left axis and MSC on the right axis. Thick black curves correspond to baseline and the colored ones to task (HbO in red and HbR in blue). Dashed lines depict the 95% CI of the mean. Gray boxes indicate the frequencies that showed significantly higher cross-power during task. (b) Averaged gain values for task. Arrows point to frequencies showing clear disturbances in gain. (c) Averaged phase values for task. (d) Circular histograms of phase angles for task plus mean angles, p -values for the bootstrapped Rayleigh test and 95% CIs. (e–g) same as (b)–(d) but for baseline results

Circular histograms show that during rest the phase angles concentrate around 0° at the task frequency in all the cases (Figure 5g), being the Rayleigh test highly significant ($p < .01$) and the 95% CI quite narrow. This implies that SS and DS oscillate almost in-phase at that frequency (no time-lags). However, during the task the phases of HbR were shifted clearly to positive values (DS lags SS) in the medial and left ROIs by 22° and 30° , respectively (Rayleigh test, $p < .01$), which correspond to time-lags of 1.8 and 2.5 s at f_t (Figure 5d). Phase changes in HbO were less apparent than those of HbR, a slight shift to negative values (DS leads SS) was observed in the same ROIs (-8° and -4° , time-lags 0.6 and 0.3 s). Noteworthy, the time-lags calculated from the phase values coincide with those obtained from the averaged time-series (see Figure 4).

As expected, these results corroborate that shallow- and deep-signals are highly correlated, underlining the strong influence of surface hemodynamics on deep recordings, which is particularly true for HbO (also observable within a single individual, compare Figures S1 and S2 of supplementary material). Fortunately, the analysis also disclosed changes in magnitude and phase related to the task, pointing to the contribution of a deep component, uniquely present in DS, as responsible for the observed disturbances. Therefore, these findings confirm that our

deep recordings captured other oscillatory processes that are different from the superficial ones.

3.3 | Neural signal estimation by transfer function

We applied an alternative method to estimate the putative neural signal by using phasor representations of the magnitude and phase data obtained from transfer function. Under the assumption that signals were quasi-stationary over the sort period of time determined by the task, we modeled them as sinusoids oscillating at 0.033 Hz, that is, the task frequency. Phasor algebra was used to extract the hidden deep component that explained the disturbances observed in DS. As a representative example, Figure 6 compares the CS obtained by regression with that estimated from transfer function data in the medial ROI. As reported in Section 3.2, the transfer function of HbO showed a clear decrease in magnitude around f_t in parallel with a phase-shift of about -8° , which is illustrated in the middle-plot of Figure 6a. The left-hand plot shows the grand-average of the experimentally obtained trials, comparing SS (solid line) and DS (dashed line). It can be seen the smaller amplitude of DS and the slight shift to the left with respect to SS. The right-hand plot shows what SS should look like

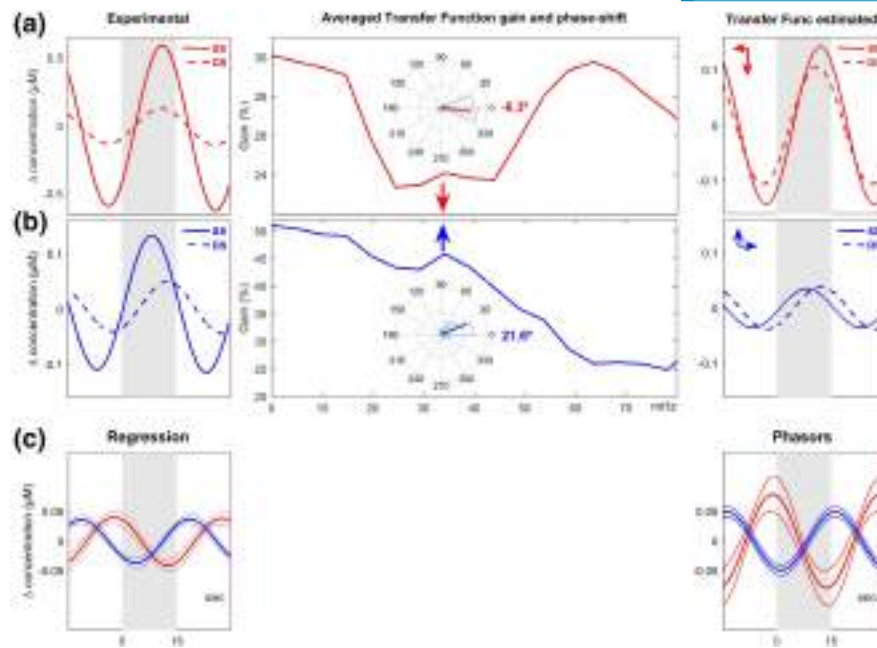


FIGURE 6 Illustrative comparison of neural signal estimation by regression and phasor analysis in the medial-ROI. Left plot (a) shows the grand averaged time courses across all the trials for HbO, comparing the experimental SS (solid trace) and DS (dashed trace). Similarly, left plot (b) shows the results for HbR. Right plot (a) compares the experimental DS for HbO (dashed) with the theoretical DS that should be observed if SS were the only contribution (solid). Arrows illustrate the amplitude and time shifts of the observed DS relative to the theoretical one. Right plot (b) shows the case of HbR. The central plots depict the averaged gain along frequencies for HbO (a) and HbR (b) with arrows indicating the direction of change at f_i and the corresponding circular histograms of phase angles at that frequency. C plots show the averages of neural signals estimated by regression (left) and phasors (right) respectively. Thin lines represent SEMs

in DS in the absence of any other interfering component, according to the magnitude estimate obtained at rest (see Section 2.7). As the red arrows indicate, the magnitude and phase differences of the observed DS (dashed line) related to the predicted SS (solid line) are now more apparent.

After performing the phasor subtraction, the interfering deep component emerged as the sinusoid depicted by the red trace in the plot to the right of Figure 6c. In the case of the HbR, a small increase in magnitude and a phase-shift of about 22° were measured at $\sim f_i$. Similarly, the right-hand plot of Figure 6b illustrates the differences between the predicted (solid line) and observed (dashed line) DS. Phasor algebra pointed to the blue sinusoid drawn to the right of Figure 6c as responsible for the disturbances. The left-hand plot of Figure 6c shows the CSs obtained by means of regression. It can be seen the good match with the deep components estimated by phasors. For the three ROIs (right, medial and left), the estimated time lags between SS and CS were on average 11.5, 13 and 10.7 s for HbO, and -9.9 , -9.5 and -9.5 s for HbR (Figure S6). Phasor analysis corroborates that the task induced deep hemodynamic fluctuations in form of an inverted HbO/HbR response, which from now on we will consider as the neural signal we were looking for. Despite individual differences, accounting for the inter-subject variability,

we found that 90% of the participants ($n = 18$) showed this type of response in at least one ROI (see Figure S3).

3.4 | Simulation results

Figure 7a shows a segment of the bandpass filtered SS, simulated DS and synthetic neural response for each chromophore of a representative participant. Simple visual inspection reveals time courses comparable to the group-averaged experimental signals shown in Figure 4. The recovered signals averaged across all participants are shown in Figure 7b for each estimation method. In the case of HbO, it can be seen that the shapes of the recovered signals are very similar for both methods, but the phasors fit better to the true synthetic signal showing significantly lower RMSE values (paired t test, $p < .01$). HbR time courses were also comparable, but again phasors performed better ($p < .01$).

These findings suggest that, compared to phasors, regression underestimates amplitude, mainly for HbO. Here, we found higher SS-DS coherence for HbO than for HbR, indicating a strong correlation that could affect more regression performance. Overall, phasors seem to work as well as or even better than regression, and could help to independently verify the results in any case.

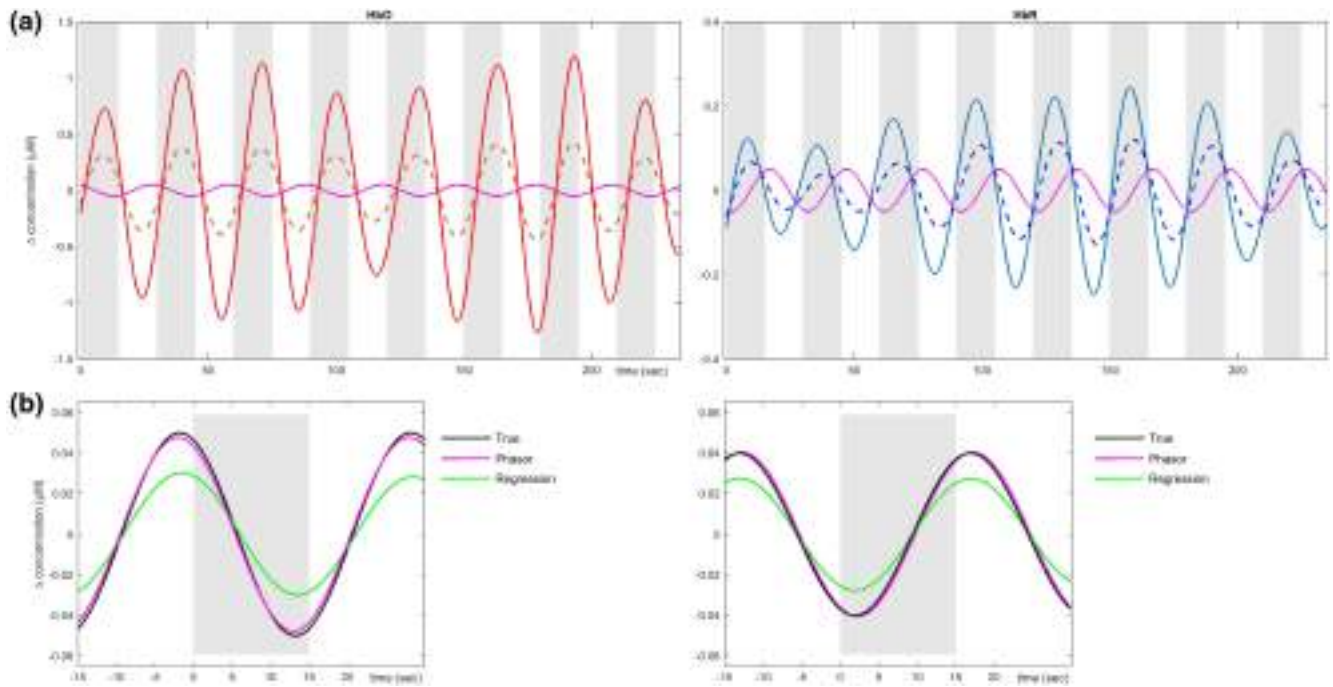


FIGURE 7 Construction of synthetic data and simulation results. (a) Simulated DS time courses for HbO (left) and HbR (right) data of a representative participant. DSs (dashed traces) were constructed by adding a synthetic neural signal (magenta traces) to the theoretical scaled version of the observed SS (solid traces in red and blue). (b) Averaged recovered signals across all participants for HbO (left) and HbR (right) by regression (green) and phasors (magenta), compared to the true synthetic signal (black)

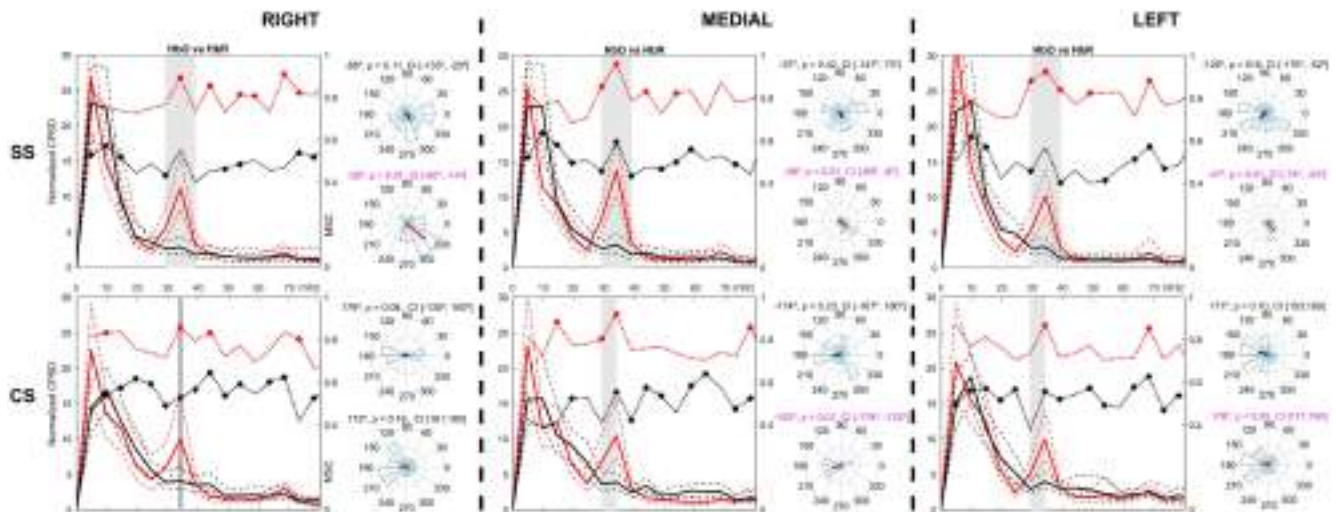


FIGURE 8 Averaged CPSDs, MSCs and phases between HbO and HbR for each ROI, comparing baseline and task. (SS) results for shallow-signals. CPSDs are drawn on the left axis for baseline (black curves) and task (red curves), dashed lines depict the 95% CI of the mean. Gray boxes indicate the frequencies that showed significantly higher cross-power during task. MSCs are shown on the right axis; asterisks indicate frequencies with significant coherence. Circular histograms show phase differences at f_i during baseline (top) and task (bottom); significant phase concentration statistical values are labeled in magenta text. (CS) results for regression-estimated clean-signals

3.5 | HbO/HbR coupling

During the task, CPSDs showed a significant peak of shared power at f_i in both SS (Figure 8SS, left axis, red trace) and CS (Figure 8CS, left axis, red trace) over all ROIs. MSC measures revealed significant frequency-domain correlation levels at several frequencies, as indicated by the

asterisks along the MSC curves drawn in the right-axis of the spectral plots. It can also be seen that MSC levels were higher during the task (red trace) than at rest (black trace), suggesting that the task increased coupling not only in its frequency but also beyond. Since Interpreting coherence when spectral power is very low could be risky and results outside the task specific frequency were beyond the scope

of the present work, here we focus solely on the peak of interest.

MSC also peaked around f_i , reaching the highest levels in the medial and left ROIs (MSC > 0.9, $p < .01$), which suggest strong correlation between HbO and HbR. Concerning temporal coupling for SS, circular histograms show how phase differences at f_i significantly concentrate during task around -39° , -39° and -47° in the right, medial and left ROIs, respectively (Rayleigh test, $p < .01$), with HbR leading HbO by 3.2 to 3.9 s (Figure 8SS, circular plots at bottom). For baseline data, phase analysis was not significant for any ROI (Figure 8SS, circular plots at top). Notably, CS revealed that, on average, HbO and HbR oscillate almost in phase-opposition in the medial and left ROIs (-162° and 176° , respectively, $p < .01$), showing a time lag around 15-s but with an unclear precedence. In the right ROI the significance level was not reached in any case. These results imply that the task induced coherent fluctuations between HbO and HbR in both shallow and deep layers, but with some differences. For SS, the temporal coupling was consistent across participants over all the ROIs, showing an out-of-phase relationship. However, CS phases were consistent at the group level only in the middle and left regions, more-over showing counter-phase fluctuations, in line with an inverted hemodynamic response.

3.6 | HbO/heart rate coupling

CPSD and MSC measures were also performed to investigate HbO and heart rate couplings. We focused solely

on significant peaks in shallow signals. As illustrated in Figure 9, a peak of shared power was located in the three ROIs at f_i . In parallel, MSC also peaked at the same frequency, indicating strong correlation at the task frequency ($p < .01$). Notably, the phase mean did not reach significant levels in any case ($p > .05$). These results indicate that at the single-subject level HbO and heart rate oscillate well coupled, resulting in significant coherence at the averaged group level. However, individual phase values were different enough to disperse the angular mean, reflecting an evident inter-subject variability in the temporal coupling of the two signals (see Figure S1). Figure 9 also shows the averaged fluctuations of the band-pass filtered HbO (bottom plots, red trace) and heart rate (bottom plots, black trace). The grand average of trials across participants (small plots next to time courses) also revealed that both signals start to increase few seconds before the trial onset.

4 | DISCUSSION

The main purpose of this work was to assess the feasibility of using rhythmic cognitive tasks to induce periodic hemodynamic fluctuations suitable for effective frequency-resolved measurements. First, we investigated whether power spectral analysis can distinguish task engagement from rest. Next, we measured the phase-amplitude coupling between different signal pairs to estimate their linear relationship, aiming to differentiate the functional brain response from extra-cerebral confounders and to infer the nature of the underlying processes.

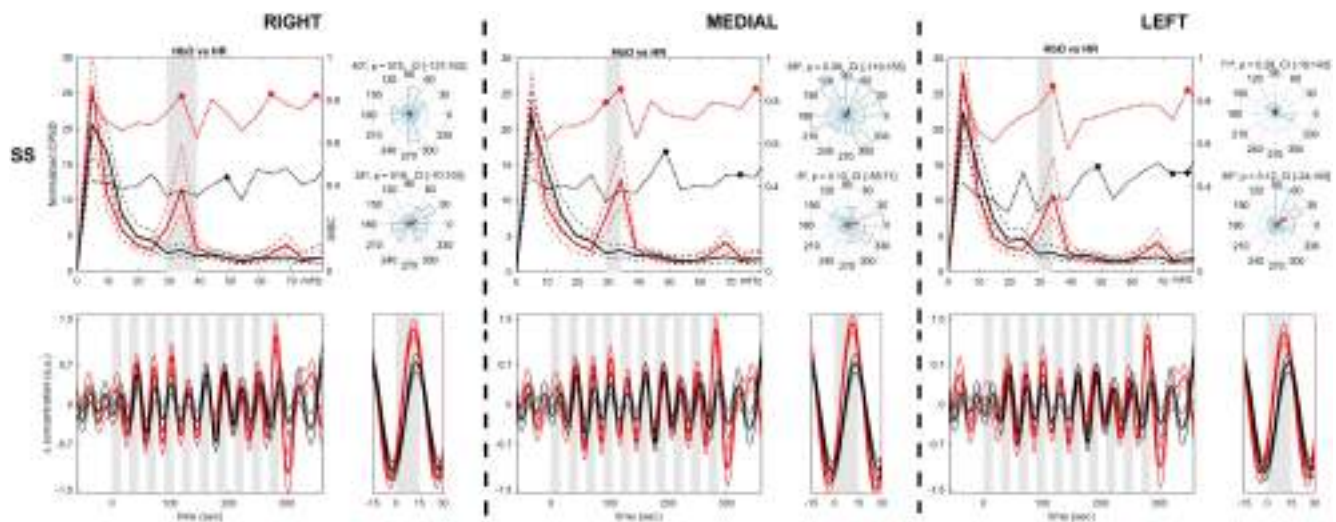


FIGURE 9 Averaged time courses, CPSDs, MSCs and phases between superficial HbO and heart rate (HR) for each ROI, comparing baseline and task. Top row plots show the CPSDs (left axis), MSCs (right axis) and circular histograms of phase differences at f_i . Baseline values are drawn in black and task values in red. Gray boxes delimit the frequencies with significant higher cross-power during task. Bottom row plots show HbO (red) and heart rate (black) time courses along the entire task; gray boxes mark the 15-s of mental math of each trial. The small plots next to time courses show the grand average of trials. Thin lines depict SEMs

We found that mental arithmetic successfully evoked cyclic changes in NIRS signals measured in the frontopolar region of the forehead, in the form of highly characteristic spectral peaks centered on the task frequency (i.e., 0.033 Hz). These peaks are clearly discernible from spontaneous activity in resting-state and apparently independent of a stress response. As mental arithmetic tasks have been used frequently as stressors (Al-Shargie et al., 2016; Hakimi, 2018; Takamoto et al., 2013), and mental overload increases stress (Mandrick et al., 2016; Tao et al., 2019), the experimental protocol used here was tailored to minimize such an effect.

Predictably, we corroborated the strong influence of surface hemodynamics on deep fNIRS signals, as reflected by the high coherence levels found between signals obtained from multi-distance recordings. In this study, rather than simply considering the surface contribution as unwanted noise, we took advantage of the shared oscillatory state imposed by the task to extract amplitude and phase data, and use it to separate the true deep signal from that originating in extracerebral tissues. Notably, our results revealed that the deep signals extracted follow an unusual pattern of HbO decrease accompanied by HbR increase, which is reversed (i.e., symmetrically opposite) with respect to the canonical brain activation response.

Previous works have reported that fNIRS signals oscillate close to the experimental stimulation frequency. Franceschini et al. (2000), for instance, using a motor task comprising sequences of 10 s of tapping and 17 s of rest, found spectral peaks at the frequency of the 27-s task period (0.037 Hz). Schroeter, Schmiedel, et al. (2004), exploring the visual cortex, identified spectral peaks for HbO and HbR at 0.023 Hz, close to the 0.028 Hz corresponding to the visual stimulation cycle of 35 s (18-s of stimulation plus 17-s of rest). Likewise, Zhang et al. (2007) also found a peak in visual cortex related to the stimulation frequency of 0.033 Hz. Regarding mental tasks, Kirilina et al. (2012) observed periodic changes in fNIRS, fMRI and other physiological signals, coupled to the single block period of an n-back (30-s) and a semantic task (34-s). Also using a semantic categorization task, Kirilina et al. (2013) identified coherent oscillations between skin blood flow and HbO corresponding to the 34-s period of stimulation. Nonetheless, with the exception of Zhang et al. (2007), none of the cited studies used task/rest intervals of the same duration. We argued that a block-design consisting of exactly regular cycles would better induce an oscillatory state, stationary enough throughout the duration of the task to allow reliable measurements. Although no consensus exists as to the most appropriate stimulus interval in block-design experiments, fNIRS studies often fall in the range of very low frequencies (0.02 to 0.08 Hz), referred as “activation-band” by Kirilina et al. (2013).

However, for frequency-analysis purposes, large task cycles lead to extremely low frequencies, which are difficult to identify and could overlap with spontaneous very slow waves (Stefanovska et al., 1999). For example, Vermeij et al. (2014), using a verbal n-back working-memory task of 180 s (0.005 Hz), only reported fluctuations in the range 0.02 to 0.07 Hz, correctly concluding that they could not be attributed to the task cycle. Likewise, Obrig et al. (2000) used similarly large periods of 120 s, finding peaks at 0.1–0.04 Hz, far from the 0.008 Hz predicted by the task frequency. On the contrary, short periods could fall within the range of spontaneous blood pressure waves (i.e., Mayer waves) that could obfuscate (or override) the functional response (Yücel et al., 2016). Furthermore, it might also be desirable to choose periods shorter enough to accommodate a single response (i.e., not several successively overlapped). Here, we used repetitive 15-s cycles of mental math plus 15-s pause, highlighting the oscillatory activity of 30-s period. We successfully found significant task-locked oscillations, separable from spontaneous activity, and showing time courses compatible with isolated, single responses. Further research is needed to test other stimulation periods that might be even more appropriate.

In almost all the aforementioned studies, the authors discussed the contribution of non-neural components to the observed fNIRS changes, stressing the importance of separating brain activation from these potential confounders. This concern should be particularly addressed when exploring the frontopolar region due to the influence of task-related skin blood flow changes, mainly on HbO signals (Haeussinger et al., 2014; Sato et al., 2013; Takahashi et al., 2011). It seems that, in most functional experiments, the superposition of extracerebral and cerebral hemodynamic responses could not be avoided, as they are not independent but inter-related processes (Caldwell et al., 2016; Tachtsidis & Scholkmann, 2016). Our results validate these considerations by showing that, on the frontopolar region, deep-recordings are strongly influenced by superficial activity. In fact, by solely analyzing deep-signals without applying proper corrections, an activation response evoked by the task can be erroneously deduced. Such a misinterpretation is more likely when only HbO is taken into account, for example as seen in Figure 4DS where HbO shows a clear increase/decrease pattern locked to the task. However, the HbR time course is less conclusive, not supporting a typical activation response and underscoring the need to assess both chromophores to convey more realistic interpretations (Fantini et al., 2018). Our results also provide complementary evidence that surface hemodynamics influences the different hemoglobin species in a differential way, with HbO being more affected than HbR. This is in agreement with previous studies reporting a stronger influence of confounding factors on HbO

(Bauernfeind et al., 2014; Gagnon et al., 2011; Heinzl et al., 2013; Kirilina et al., 2012).

To address the contamination issue, we employed a multi-distance approach in which each deep-recording was cleaned from surface influence by using two specific short-recordings as reference, thus controlling for inhomogeneous hemodynamic activity in the scanned surface area. As commented in Section 2.4.2, such a strategy is commonly accepted as very effective to remove noise, and even considered as a gold standard (Zhou et al., 2020). After performing conventional linear regression, we obtained a clean deep-signal for each ROI that also oscillates at the task frequency, but apparently showing deactivation instead of an expected activation (Figure 4CS). In view of this unusual pattern, and despite the thickness of the tissues that cover and protect the brain (see Section 2.6), it was necessary to verify whether our short 14 mm recordings were also picking up cortical signals, leading to poorly estimated regression residuals. By exploiting the induced oscillatory state, we employed the empirical transfer function and phasor representation of HbO and HbR fluctuations (Figure 6) to explain the amplitude and phase disturbances observed in deep-signals. The results confirmed the presence of deep HbO and HbR components that fluctuate coupled to the task, following an inverted pattern with both chromophores almost in counter-phase. The convergence of two independent analysis, regression and transfer function, strongly supports the finding of a putative cortical response in the form of deoxygenation/oxygenation cycles; noteworthy, it was found in 90% of our sample, a considerable higher occurrence than those reported in, for example, motor imagery fNIRS studies (Abdalmalak et al., 2020; Holper et al., 2011). Therefore, we demonstrated that our short- and deep-recordings captured different hemodynamic components.

Moreover, simulated data revealed that combining transfer functions and phasors might provide better estimates of the amplitude of functional cortical responses. It is worth noting that if shallow and neural signals had oscillated highly correlated (positive or negatively), the regression could have failed because the scaling factor (beta) would have caused the subtraction to flatten the residuals, leading to accidental removal of the cerebral signal. This drawback could be avoided using the method proposed here. Phasors were first proposed by Zheng et al. (2010) to explain the phase relationships between hemoglobin species but, to our knowledge, this is the first time they have been used to analyze multi-distance fNIRS recordings. Further improvements on the method are currently under way.

Inverse oxygenation responses have been previously reported in fNIRS studies using different task modalities, such as motor imagery (Abdalmalak et al., 2020; Holper et al., 2011), visual stimulation (Maggioni et al., 2015),

working memory n-back (Haeussinger et al., 2014; Kirilina et al., 2012), emotional stimulation (Matsukawa et al., 2018), and mental arithmetic (Bauernfeind et al., 2008; Pfurtscheller et al., 2010). This phenomenon has only been partially explained so far, being of considerable interest to understand the underlying neuro-vascular mechanisms and gain insight into the negative BOLD response observed in fMRI studies (see Holper et al. [2011] and Maggioni et al. [2015] for in-depth discussions of possible explanations). Regarding fNIRS studies probing the PFC during working memory tasks, some researchers found a decrease in HbO in frontopolar region using fixed inter-optode distances (i.e., no multi-distance correction), while they found no significant HbR changes (Haeussinger et al., 2014; Kirilina et al., 2012). They suggested that task-evoked sympathetic vasoconstriction drives skin blood flow changes, which in turn impair fNIRS long-recordings, leading to an apparent decrease in oxygenation response. Noteworthy, in both studies, fMRI data showed deactivation in the medial region of the PFC. In contrast, Takahashi et al. (2011) found a positive pattern (i.e., increased oxygenation) using a verbal-fluency task, which they attributed to skin vessels dilatation by comparing short- (5 mm) and long-distance (30 mm) signals and showing that the effect disappears when pressure is applied to the skin. In the present work, we used two short-channels to clean each long recording, which is a very effective method to remove the components (of local or systemic origin) that are common to the shallow and deep-signals (Fantini et al., 2018). However, if a systemic component appears at different times in the surface and deep layers (e.g., blood flow delay), the regression itself may render a false neuronal response. Time differences in vascular reactivity driven by the task (e.g., delayed autonomic mediation) may also cause delays between layers. Wyser et al. (2020) reported an average time lag of ~ 0.51 s between shallow and deep signals for Mayer pressure waves, similar to the values found by Kirilina et al. (2013). Tong and Frederick (2010) estimated a time of ~ 6 s for a pressure wave to pass the whole brain. Using nose tip temperature as a proxy to assess autonomic activity during a mental math task, Pinti et al. (2015) found mean time lags of less than 4 s, albeit showing significant individual variability, between changes of cutaneous blood flow and prefrontal fNIRS signals. During a cognitive task, a mean time lag of ~ 6 s between skin blood flow and prefrontal fNIRS signals was found in (Kirilina et al., 2013). The phasor method do not solve the problem of different timing either, but they provide independent information about the delays between signals and avoid regression constraints. We found clearly longer delays than those we have mentioned (see Section 3.3 and Figure S6), and we believe that they are unlikely to be due to a delayed physiological

response, otherwise they would reflect a considerable lack of coordination between autonomic and prefrontal activity. Assuming that the observed response is an artifact due to time delays, it can be expected that for a specific individual the delay will be the same in the three ROIs of the narrow frontopolar region explored. However, we found that in some participants showing consistent surface signals across ROIs, the estimated neural signal was clearly different depending on the region (e.g., participants 1, 2, 3 and 4, Figures S1 and S3). Therefore, we conclude that such an inverted pattern actually represents the functional cortical response. However, the existence of some delay cannot be fully ignored and follow-up work is required.

Overall, our results are more in line with those reported by Pfurtscheller et al. (2010). Using a similar task, they also found an HbO decrease in the medial area of the PFC, but no significant changes for HbR. They corrected for extracerebral contamination by employing a common average reference spatial filter, which relies on subtracting the averaged signals from each fNIRS channel. After correction, we found significant fluctuations for both HbO and HbR, which is of great interest for interpretation purposes and implies that our methodological approach is better suited to discriminate the functional brain response. Other fNIRS studies have reported reduced activation in medial areas of the frontal cortex related to arithmetic subtraction in adolescents (Artemenko et al., 2018) or to task difficulty (Verner et al., 2013). However, since they did not use multi-distance corrections, comparing results could be risky.

Currently, fNIRS inverse oxygenation response remains an open topic, as the underlying neurovascular mechanisms are only partially understood. Some studies have been devoted to relate it with the fMRI negative BOLD response (NBR) in visual (Maggioni et al., 2015) and motor cortices (Abdalmalak et al., 2020), investigating its potential cause. Maggioni et al. (2015) found a consistent spatial correlation between NBR and inverse fNIRS response, while Abdalmalak et al. (2020) attribute the phenomenon to motion artifacts. The first discuss in-depth on the origin of NBR, favoring the idea of neural deactivation (Mullinger et al., 2014) against the “blood stealing” explanation promoted by other authors (Shmuel et al., 2002). Pfurtscheller et al. (2010) also explained the inverse response in terms of a “focal activation/surround deactivation” pattern. As we did not find any delay in the hemodynamic response, our results also speak against a sequestration of blood from neighboring areas to active areas. Our NIRS probe covered a relatively small area of the PFC, so our data are insufficient to support or reject the idea of concurrently activated and deactivated areas. However, based on the delay need to reach consistent counter-phase changes in HbO/HbR and the strong

rhythmicity imposed by the task, we suggest a simpler explanation. It may be plausible that such an inverted response actually expresses a cyclical brain activation state, which after reaching stability appears as a period of oxygen consumption (during mental effort) in a previously well oxygenated brain area, followed by a subsequent reoxygenation (during the pause). Thus, in the steady-state, the mental effort period starts under a condition of O₂ excess (or compensated) that leads to use the currently available O₂ until a new supply of fresh blood is needed. In this line, Wylie et al. (2009) proposed that different HbO/HbR (and total Hb) combinations might be present in activated visual cortex areas. Nevertheless, more research is needed to fully elucidate the complex coupling between O₂ consumption and blood flow/volume changes in the PFC.

We also found that only the medial and left ROIs showed a consistent inverse response at the group level, which is supported by the significant concentration of HbO/HbR phase angles around 180° (Figure 8CS) and the stronger disturbances in gain and phase detected by transfer function during the task (Figure 5). This finding suggests that, on average, frontopolar activity was slightly lateralized to the left. A meta-analysis conducted by Arsalidou and Taylor (2011) indicates that, among others, frontopolar area seems to be generically engaged in mental arithmetic, sustaining working memory functions that are necessary to achieve good mathematical performance. They proposed that, for calculation tasks, this area manages the successive executive steps that can lead to the final calculated result. Noteworthy, they also reported that activity in the left part of frontopolar cortex was concordant among studies involving calculation tasks. The characteristics of our arithmetic task fit with that functional specialization as it is necessary to coordinate each of the iterative subtractions (steps), while holding the result of the previous operation in the working memory, and then combining both to obtain the final result (main goal). Nonetheless, as we did not control for task difficulty or used calculation modalities other than subtraction, we acknowledge that complementary research is needed for more rigorous comparisons and interpretations. In any case, an important point to be also considered is whether the observed response can be attributed to the “task-negative” activity of the default-mode network (DMN) (Raichle et al., 2001; Raichle & Snyder, 2007). As the brain region interrogated by our NIRS probe overlaps with the medial prefrontal cortex (DMN-associated region), our findings could reflect decreased neuronal activity in this key region due to task engagement. Since DMN also include deeper structures, unreachable for fNIRS, exploring this possibility will require further research using fMRI imaging methods.

Concerning shallow hemodynamic, we found a consistent task-locked pattern of monotonic HbO increase

followed by a decrease during the task pause, which was shortly preceded by similar HbR changes of lesser amplitude. As previously discussed, these fluctuations greatly impair the deep-recordings and potentially lead to their misinterpretation as brain activation, especially when only accounting for HbO. Therefore, we suggest special caution should be taken when interpreting HbO changes reported by fNIRS studies employing mental arithmetic tasks and using only long-recordings, as in (Çiftçi et al., 2008; Tanida et al., 2004; Verner et al., 2013; Yang et al., 2009).

Aiming to elucidate the origin and influence of the extracranial confounds present in fNIRS signals, some studies monitored concurrently skin blood flow, heart rate and arterial blood pressure during cognitive tasks (Haeussinger et al., 2014; Kirilina et al., 2012; Takahashi et al., 2011). Although with variable results, they suggested that task-induced sympathetic outflow (leading to increased cardiac output and arterial blood pressure), together with skin blood flow/volume changes due to local vasomotion (constriction and/or dilatation), are the mechanisms responsible for these extracranial hemodynamic changes. In our work here, we consider that skin blood flow contribution has been small or negligible due to: (i) the optode-skin interface of our NIRS device reduces the skin blood flow (see Section 2.4), and (ii) our short-channels are long enough (14 mm) to allow light penetrate deeper into the subcutaneous and muscle tissues of the forehead (perhaps even the skull), with little contribution of the skin compared with the volume illuminated. Therefore, albeit we cannot exclude local vasodynamics effects, we point to a systemic drive as the major cause. Our findings revealed that the task induced highly coherent heart/HbO fluctuations at the single-subject level, but with considerable individual variability in their temporal coupling, which leads to inconsistent phase values at the group level (Figure 9). Many studies have emphasized the link between fNIRS signals, heart rate and blood pressure during rest and under functional stimulation (Franceschini et al., 2000; Franceschini et al., 2006; Kirilina et al., 2012; Minati et al., 2011; Tachtsidis et al., 2008, 2009; Takahashi et al., 2011). In our work, we did not monitor blood pressure, thus preventing the possibility of linking it with heart rate and HbO. However, based on the aforementioned studies, we reasonably assume that the task used here may also have induced blood pressure oscillations contributing to HbO fluctuations.

The observed HbO/HbR surface pattern seems compatible with an oxygenation effect due to an increased arterial inflow in the micro-vascular bed, which in turn leads to parallel HbR changes. Thus, the phase difference between HbO and HbR (-39° to 47°) would reflect the complex contribution of capillary transit time, blood flow and blood volume changes in shallow layers (Elting

et al., 2020; Zheng et al., 2010). However, mainly for HbR, other mechanisms as forehead venous volume changes (Kirilina et al., 2012) or even superficial O_2 consumption could overlap. Another interesting possibility is that surface signals also overlap changes in cerebral blood flow arising from increasing metabolic demands and cerebral autoregulation. This is plausible as we placed the NIRS probe over a forehead region mainly supplied by the supraorbital and supratrochlear arteries that ultimately connect (via the ophthalmic artery) to the frontopolar branch of the anterior cerebral artery, which plays a key role in blood supply to the frontal lobes. Prior studies have suggested that blood pressure measured from the supraorbital artery may reflect cerebral perfusion pressure (Lee & Westenskow, 1998; Narus et al., 1995), or that the clamping of the internal carotid affects both supraorbital blood flow and frontal lobe oxygenation (Hove et al., 2006). Jenkins and Brown (2014) also postulated the relationship between frontal activity asymmetry and forehead blood flow in a study using EEG and infrared thermography.

Another interesting finding was that the HbO response precedes the trial onset by some seconds. Previous studies reported that the PFC increases oxygenation a few seconds prior to the onset of voluntary exercise, independently of its actual intensity (Asahara et al., 2018; Ishii et al., 2018; Matsukawa et al., 2015). It has been hypothesized that a feedforward mechanism (termed “central command”), involving higher brain centres, sends descending signals that adjust physiological systems, as the cardiovascular one, to the upcoming effort (Goodwin et al., 1972; Williamson, 2010). Furthermore, there is growing evidence that preparing for a mental challenge induces activity in certain cerebral areas as the Anterior Cingulate Cortex and PFC (Sohn et al., 2007; Vassena et al., 2014, 2019). We suggest that, here, the anticipatory effect may have been enhanced by the use of such a rhythmic and predictable task. It is tempting to speculate that the aforementioned studies and our results point to the same task-related arousal mechanism that brings fresh arterial blood, full of oxygen to the cortex in preparation for upcoming cognitive demands.

Task-related arousal mechanisms requires a close interaction between cognitive function and autonomic control (Forte, De Pascalis, et al., 2019; Forte, Favieri, et al., 2019; Nicolini et al., 2014; Thayer & Lane, 2009; Wang et al., 2016). Thus, the autonomic control appears to be associated with activity levels in executive brain regions, which allows an adaptive response to environmental demands. Conversely, autonomic dysfunctions may be related to the deterioration of certain cognitive functions, specifically of executive functions (Forte, De Pascalis, et al., 2019; Forte, Favieri, et al., 2019). This close coordination of extracerebral and cerebral responses with the

task period may have great functional value. The correct coupling between physiological resources may be the sign of proper cognitive and/or cardiovascular function and, its disruption, a potential early marker of cognitive decline and/or cardiovascular disease.

ACKNOWLEDGEMENTS

We wish to thank Professor Carlos Belmonte for continuous support and critical reading of the manuscript. We acknowledge the technical assistance of Mr. Miguel Ibañez and Mr. Alejandro Mendez.

CONFLICT OF INTEREST

This work was conducted in absence of any funding. Joaquín Ibañez-Ballesteros reports that he is inventor of patents licensed to Newmanbrain, SL and co-founder and scientific advisor of Newmanbrain S.L., the company responsible of manufacturing the NIRS device used in this research.

AUTHOR CONTRIBUTIONS

Sergio Molina-Rodriguez: Conceptualization; formal analysis; investigation; methodology; writing – original draft. **Marcos Mirete-Fructuoso:** Formal analysis; investigation; writing – original draft. **Luis M Martinez:** Conceptualization; writing – review and editing. **Joaquín Ibañez-Ballesteros:** Conceptualization; formal analysis; methodology; software; supervision; writing – original draft; writing – review and editing.

ORCID

Joaquín Ibañez-Ballesteros  <https://orcid.org/0000-0001-8606-4221>

REFERENCES

- Aarabi, A., & Huppert, T. J. (2016). Characterization of the relative contributions from systemic physiological noise to whole-brain resting-state functional near-infrared spectroscopy data using single-channel independent component analysis. *Neurophotonics*, 3(2), Article 025004. <https://doi.org/10.1117/1.nph.3.2.025004>
- Aarabi, A., Osharina, V., & Wallois, F. (2017). Effect of confounding variables on hemodynamic response function estimation using averaging and deconvolution analysis: An event-related NIRS study. *NeuroImage*, 155, 25–49. <https://doi.org/10.1016/j.neuroimage.2017.04.048>
- Aaslid, R., Blaha, M., Svirri, G., Douville, C. M., & Newell, D. W. (2007). Asymmetric dynamic cerebral autoregulatory response to cyclic stimuli. *Stroke*, 38(5), 1465–1469. <https://doi.org/10.1161/STROKEAHA.106.473462>
- Abdalmalak, A., Milej, D., Cohen, D. J., Anazodo, U., Ssali, T., Diop, M., Owen A.M., St. Lawrence K. (2020). Using fMRI to investigate the potential cause of inverse oxygenation reported in fNIRS studies of motor imagery. *Neuroscience Letters*, 714, Article 134607. <https://doi.org/10.1016/j.neulet.2019.134607>
- Al-Shargie, F., Kiguchi, M., Badruddin, N., Dass, S. C., Hani, A. F. M., & Tang, T. B. (2016). Mental stress assessment using simultaneous measurement of EEG and fNIRS. *Biomedical Optics Express*, 7(10), 3882–3898. <https://doi.org/10.1364/boe.7.003882>
- Amaro, E., & Barker, G. J. (2006). Study design in fMRI: Basic principles. *Brain and Cognition*, 60(3), 220–232. <https://doi.org/10.1016/j.bandc.2005.11.009>
- Arsalidou, M., & Taylor, M. J. (2011). Is 2+2=4? Meta-analyses of brain areas needed for numbers and calculations. *NeuroImage*, 54(3), 2382–2393. <https://doi.org/10.1016/j.neuroimage.2010.10.009>
- Artemenko, C., Soltanlou, M., Ehli, A. C., Nuerk, H. C., & Dresler, T. (2018). The neural correlates of mental arithmetic in adolescents: A longitudinal fNIRS study. *Behavioral and Brain Functions*, 14(1), 1–13. <https://doi.org/10.1186/s12993-018-0137-8>
- Asahara, R., Endo, K., Liang, N., & Matsukawa, K. (2018). An increase in prefrontal oxygenation at the start of voluntary cycling exercise was observed independently of exercise effort and muscle mass. *European Journal of Applied Physiology*, 118(8), 1689–1702. <https://doi.org/10.1007/s00421-018-3901-4>
- Bauernfeind, G., Böck, C., Wriessnegger, S. C., & Müller-Putz, G. R. (2013). Physiological noise removal from fNIRS signals. *Biomedical Engineering / Biomedizinische Technik*, 58, 2–3. <https://doi.org/10.1515/bmt-2013-4430>
- Bauernfeind, G., Wriessnegger, S. C., Daly, I., & Müller-Putz, G. R. (2014). Separating heart and brain: On the reduction of physiological noise from multichannel functional near-infrared spectroscopy (fNIRS) signals. *Journal of Neural Engineering*, 11(5), 056010. <https://doi.org/10.1088/1741-2560/11/5/056010>
- Bauernfeind, G., Leeb, R., Wriessnegger, S. C., & Pfurtscheller, G. (2008). Development, set-up and first results for a one-channel near-infrared spectroscopy system/Entwicklung, Aufbau und vorläufige Ergebnisse eines Einkanal-Nahinfrarot-Spektroskopie-systems. *Biomedizinische Technik/ Biomedical Engineering*, 53(1), 36–43. <https://doi.org/10.1515/BMT.2008.005>
- Berens, P. (2009). CircStat: A MATLAB toolbox for circular statistics. *Journal of Statistical Software*, 31(10), 1–21.
- Brigadoi, S., & Cooper, R. J. (2015). How short is short? Optimum source–detector distance for short-separation channels in functional near-infrared spectroscopy. *Neurophotonics*, 2(2), Article 025005. <https://doi.org/10.1117/1.nph.2.2.025005>
- Buxton, R. B., Uludağ, K., Dubowitz, D. J., & Liu, T. T. (2004). Modeling the hemodynamic response to brain activation. *NeuroImage*, 23, 220–233. <https://doi.org/10.1016/j.neuroimage.2004.07.013>
- Caldwell, M., Scholkmann, F., Wolf, U., Wolf, M., Elwell, C., & Tachtsidis, I. (2016). Modelling confounding effects from extracerebral contamination and systemic factors on functional near-infrared spectroscopy. *NeuroImage*, 143, 91–105. <https://doi.org/10.1016/j.neuroimage.2016.08.058>
- Charles, R. L., & Nixon, J. (2019). Measuring mental workload using physiological measures: A systematic review. *Applied Ergonomics*, 74, 221–232. <https://doi.org/10.1016/j.apergo.2018.08.028>
- Çiftçi, K., Sankur, B., Kahya, Y. P., & Akin, A. (2008). Functional clusters in the prefrontal cortex during mental arithmetic. In

- 16th European Signal Processing Conference, (Eusipco) (pp. 1–4). IEEE.
- Claassen, J. A. R., Meel-van den Abeelen, A., Simpson, D. M., Panerai, R. B., & international Cerebral Autoregulation Research Network (CARNet). (2015). Transfer function analysis of dynamic cerebral autoregulation: A white paper from the international cerebral autoregulation research network. *Journal of Cerebral Blood Flow and Metabolism*, 36(4), 665–680. <https://doi.org/10.1177/0271678X15626425>
- Claassen, J. A., Levine, B. D., & Zhang, R. (2009). Dynamic cerebral autoregulation during repeated squat-stand maneuvers. *Journal of Applied Physiology*, 106(1), 153–160. <https://doi.org/10.1152/jappphysiol.90822.2008>
- Cui, X., Bray, S., Bryant, D. M., Glover, G. H., & Reiss, A. L. (2011). A quantitative comparison of NIRS and fMRI across multiple cognitive tasks. *NeuroImage*, 54(4), 2808–2821. <https://doi.org/10.1016/j.neuroimage.2010.10.069>
- Dale, A. M. (1999). Optimal experimental design for event-related fMRI. *Human Brain Mapping*, 8(2–3), 109–114. [https://doi.org/10.1002/\(SICI\)1097-0193\(1999\)8:2<3<109::AID-HBM7>3.0.CO;2-W](https://doi.org/10.1002/(SICI)1097-0193(1999)8:2<3<109::AID-HBM7>3.0.CO;2-W)
- Delpy, D. T., Cope, M., Van Der Zee, P., Arridge, S., Wray, S., & Wyatt, J. (1988). Estimation of optical pathlength through tissue from direct time of flight measurement. *Physics in Medicine and Biology*, 33(12), 1433–1442. <https://doi.org/10.1088/0031-9155/33/12/008>
- Diamond, S. G., Huppert, T. J., Kolehmainen, V., Franceschini, M. A., Kaipio, J. P., Arridge, S. R., & Boas, D. A. (2006). Dynamic physiological modeling for functional diffuse optical tomography. *NeuroImage*, 30(1), 88–101. <https://doi.org/10.1016/j.neuroimage.2005.09.016>
- Elting, J. W. J., Tas, J., Aries, M. J. H., Czosnyka, M., & Maurits, N. M. (2020). Dynamic cerebral autoregulation estimates derived from near infrared spectroscopy and transcranial doppler are similar after correction for transit time and blood flow and blood volume oscillations. *Journal of Cerebral Blood Flow and Metabolism*, 40(1), 135–149. <https://doi.org/10.1177/0271678X18806107>
- Faes, L., Pinna, G. D., Porta, A., Maestri, R., & Nollo, G. (2004). Surrogate data analysis for assessing the significance of the coherence function. *IEEE Transactions on Biomedical Engineering*, 51(7), 1156–1166. <https://doi.org/10.1109/TBME.2004.827271>
- Fantini, S., Frederick, B., & Sassaroli, A. (2018). Perspective: Prospects of non-invasive sensing of the human brain with diffuse optical imaging. *APL Photonics*, 3(11), 110901. <https://doi.org/10.1063/1.5038571>
- Florian, G., & Pfurtscheller, G. (1997). Elimination von Atmungseffekten auf bewegungsinduzierte Änderungen der Herzrate [Elimination of respiratory effects on movement-induced cardiac response]. *Biomedizinische Technik/Biomedical Engineering*, 42(7–8), 203–206. <https://doi.org/10.1515/bmte.1997.42.7-8.203>
- Forte, G., De Pascalis, V., Favieri, F., & Casagrande, M. (2019). Effects of blood pressure on cognitive performance: A systematic review. *Journal of Clinical Medicine*, 9(1), 34. <https://doi.org/10.3390/jcm9010034>
- Forte, G., Favieri, F., & Casagrande, M. (2019). Heart rate variability and cognitive function: A systematic review. *Frontiers in Neuroscience*, 13(JUL), 1–11. <https://doi.org/10.3389/fnins.2019.00710>
- Franceschini, M. A., Fantini, S., Toronov, V., Filiaci, M. E., & Gratton, E. (2000). Cerebral hemodynamics measured by near-infrared spectroscopy at rest and during motor activation. In *Proceedings of the Optical Society of America In Vivo Optical Imaging Workshop*, (pp.73–80). Optical Society of America.
- Franceschini, M. A., Joseph, D. K., Huppert, T. J., Diamond, S. G., & Boas, D. A. (2006). Diffuse optical imaging of the whole head. *Journal of Biomedical Optics*, 11(5), Article 054007. <https://doi.org/10.1117/1.2363365>
- Friston, K., Ashburner, J., Kiebel, S., Nichols, T., & Penny, W. D. (2007). *Statistical parametric mapping: The analysis of functional brain images*. Elsevier. <https://doi.org/10.1016/B978-0-12-372560-8.X5000-1>
- Friston, K. J., Josephs, O., Rees, G., & Turner, R. (1998). Nonlinear event-related responses in fMRI. *Magnetic Resonance in Medicine*, 39(1), 41–52. <https://doi.org/10.1002/mrm.1910390109>
- Gagnon, L., Cooper, R. J., Yücel, M. A., Perdue, K. L., Greve, D. N., & Boas, D. A. (2012). Short separation channel location impacts the performance of short channel regression in NIRS. *NeuroImage*, 59(3), 2518–2528. <https://doi.org/10.1016/j.neuroimage.2011.08.095>
- Gagnon, L., Perdue, K., Greve, D. N., Goldenholz, D., Kaskhedikar, G., & Boas, D. A. (2011). Improved recovery of the hemodynamic response in diffuse optical imaging using short optode separations and state-space modeling. *NeuroImage*, 56(3), 1362–1371. <https://doi.org/10.1016/j.neuroimage.2011.03.001>
- Gagnon, L., Yücel, M. A., Boas, D. A., & Cooper, R. J. (2014). Further improvement in reducing superficial contamination in NIRS using double short separation measurements. *NeuroImage*, 85, 127–135. <https://doi.org/10.1016/j.neuroimage.2013.01.073>
- Goodwin, G. M., McCloskey, D. I., & Mitchell, J. H. (1972). Cardiovascular and respiratory responses to changes in central command during isometric exercise at constant muscle tension. *The Journal of Physiology*, 226(1), 173–190. <https://doi.org/10.1113/jphysiol.1972.sp009979>
- Haeussinger, F. B., Dresler, T., Heinzel, S., Schecklmann, M., Fallgatter, A. J., & Ehlis, A.-C. (2014). Reconstructing functional near-infrared spectroscopy (fNIRS) signals impaired by extracranial confounds: An easy-to-use filter method. *NeuroImage*, 95, 69–79. <https://doi.org/10.1016/j.neuroimage.2014.02.035>
- Haeussinger, F. B., Heinzel, S., Hahn, T., Schecklmann, M., Ehlis, A. C., & Fallgatter, A. J. (2011). Simulation of near-infrared light absorption considering individual head and prefrontal cortex anatomy: Implications for optical neuroimaging. *PLoS One*, 6(10), Article e26377. <https://doi.org/10.1371/journal.pone.0026377>
- Hakimi, N. (2018). Stress assessment by means of heart rate derived from functional near-infrared spectroscopy. *Journal of Biomedical Optics*, 23(11), 1. <https://doi.org/10.1117/1.jbo.23.11.115001>
- Heinzel, S., Haeussinger, F. B., Hahn, T., Ehlis, A. C., Plichta, M. M., & Fallgatter, A. J. (2013). Variability of (functional) hemodynamics as measured with simultaneous fNIRS and fMRI during intertemporal choice. *NeuroImage*, 71, 125–134. <https://doi.org/10.1016/j.neuroimage.2012.12.074>
- Holland, P. W., & Welsch, R. E. (1977). Robust regression using iteratively reweighted least-squares. *Communications in Statistics—Theory and Methods*, 6(9), 813–827. <https://doi.org/10.1080/03610927708827533>
- Holper, L., Shalóm, D. E., Wolf, M., & Sigman, M. (2011). Understanding inverse oxygenation responses during motor

- imagery: A functional near-infrared spectroscopy study. *European Journal of Neuroscience*, 33(12), 2318–2328. <https://doi.org/10.1111/j.1460-9568.2011.07720.x>
- Hove, J. D., Rosenberg, I., Sejrsen, P., Hove, K. D., & Secher, N. H. (2006). Supraorbital cutaneous blood flow rate during carotid endarterectomy. *Clinical Physiology and Functional Imaging*, 26(6), 323–327. <https://doi.org/10.1111/j.1475-097X.2006.00697.x>
- Hughson, R. L., Edwards, M. R., O'Leary, D. D., & Shoemaker, J. K. (2001). Critical analysis of cerebrovascular autoregulation during repeated head-up tilt. *Stroke*, 32(10), 2403–2408. <https://doi.org/10.1161/hs1001.097225>
- Huppert, T. J. (2016). Commentary on the statistical properties of noise and its implication on general linear models in functional near-infrared spectroscopy. *Neurophotonics*, 3(1), Article 010401. <https://doi.org/10.1117/1.nph.3.1.010401>
- Huppert, T. J., Diamond, S. G., Franceschini, M. A., & Boas, D. A. (2009). HomER: A review of time-series analysis methods for near-infrared spectroscopy of the brain. *Applied Optics*, 48(10), 0–33. <https://doi.org/10.1364/AO.48.00D280>
- Ilvedson, C. R. (1998). *Transfer function estimates using time-frequency analysis*. Massachusetts Institute of Technology.
- Ishii, K., Liang, N., Asahara, R., Takahashi, M., & Matsukawa, K. (2018). Feedforward- and motor effort-dependent increase in prefrontal oxygenation during voluntary one-armed cranking. *Journal of Physiology*, 596(21), 5099–5118. <https://doi.org/10.1113/JP276956>
- Jenkins, S. D., & Brown, R. D. H. (2014). A correlational analysis of human cognitive activity using infrared thermography of the supraorbital region, frontal EEG and self-report of core affective state. In *Proceedings of the 2014 International Conference on Quantitative InfraRed Thermography*. <https://doi.org/10.21611/qirt.2014.131>
- Julien, C. (2006). The enigma of Mayer waves: Facts and models. *Cardiovascular Research*, 70(1), 12–21. <https://doi.org/10.1016/j.cardiores.2005.11.008>
- Kainerstorfer, J. M., Sassaroli, A., & Fantini, S. (2014). Coherent hemodynamics spectroscopy in a single step. *Biomedical Optics Express*, 5(10), 3403–3416. <https://doi.org/10.1364/boe.5.003403>
- Kirilina, E., Jelzow, A., Heine, A., Niessing, M., Wabnitz, H., Brühl, R., Ittermann, B., Jacobs, A. M., & Tachtsidis, I. (2012). The physiological origin of task-evoked systemic artefacts in functional near infrared spectroscopy. *NeuroImage*, 61(1), 70–81. <https://doi.org/10.1016/j.neuroimage.2012.02.074>
- Kirilina, E., Yu, N., Jelzow, A., Wabnitz, H., Jacobs, A. M., & Tachtsidis, L. (2013). Identifying and quantifying main components of physiological noise in functional near infrared spectroscopy on the prefrontal cortex. *Frontiers in Human Neuroscience*, 7(DEC), 1–17. <https://doi.org/10.3389/fnhum.2013.00864>
- Kirschbaum, C., Pirke, K., & Hellhammer, D. (1993). The 'Trier social stress test'—A toll for investigating psychobiological stress responses in a laboratory setting. *Neuropsychobiology*, 36(4), 76–81. <https://doi.org/10.16309/j.cnki.issn.1007-1776.2003.03.004>
- Kocsis, L., Herman, P., & Eke, A. (2006). The modified beer-Lambert law revisited. *Physics in Medicine and Biology*, 51(5), N91–N98. <https://doi.org/10.1088/0031-9155/51/5/N02>
- Koh, P. H., Glaser, D. E., Flandin, G., Kiebel, S., Butterworth, B., Maki, A., Delpy, D. T., & Elwell, C. E. (2007). Functional optical signal analysis: A software tool for near-infrared spectroscopy data processing incorporating statistical parametric mapping. *Journal of Biomedical Optics*, 12(6), 064010. <https://doi.org/10.1117/1.2804092>
- Kohno, S., Miyai, I., Seiyama, A., Oda, I., Ishikawa, A., Tsuneishi, S., Amita, T., & Shimizu, K. (2007). Removal of the skin blood flow artifact in functional near-infrared spectroscopic imaging data through independent component analysis. *Journal of Biomedical Optics*, 12(6), 062111. <https://doi.org/10.1117/1.2814249>
- Kolehmainen, V., Prince, S., Arridge, S. R., & Kaipio, J. P. (2003). State-estimation approach to the nonstationary optical tomography problem. *Journal of the Optical Society of America A*, 20(5), 876. <https://doi.org/10.1364/JOSAA.20.000876>
- Kudielka, B. M., Hellhammer, D. H., & Kirschbaum, C. (2007). Ten years of research with the trier social stress test—Revisited. In E. Harmon-Jones & P. Winkielman (Eds.), *Social neuroscience: Integrating biological and psychological explanations of social behavior* (pp. 56–83). The Guilford Press.
- Lee, T. K., & Westenskow, D. R. (1998). Comparison of blood pressure measured by oscillometry from the supraorbital artery and invasively from the radial artery. *Journal of Clinical Monitoring and Computing*, 14(2), 113–117. <https://doi.org/10.1023/A:1007481416222>
- Maggioni, E., Molteni, E., Zucca, C., Reni, G., Cerutti, S., Triulzi, F. M., Arrigoni, F., & Bianchi, A. M. (2015). Investigation of negative BOLD responses in human brain through NIRS technique. A visual stimulation study. *NeuroImage*, 108, 410–422. <https://doi.org/10.1016/j.neuroimage.2014.12.074>
- Mandrick, K., Peysakhovich, V., Rémy, F., Lepron, E., & Causse, M. (2016). Neural and psychophysiological correlates of human performance under stress and high mental workload. *Biological Psychology*, 121, 62–73. <https://doi.org/10.1016/j.biopsycho.2016.10.002>
- Maris, E., & Oostenveld, R. (2007). Nonparametric statistical testing of EEG- and MEG-data. *Journal of Neuroscience Methods*, 164(1), 177–190. <https://doi.org/10.1016/j.jneumeth.2007.03.024>
- Matsukawa, K., Asahara, R., Yoshikawa, M., & Endo, K. (2018). Deactivation of the prefrontal cortex during exposure to pleasantly-charged emotional challenge. *Scientific Reports*, 8(1), 452–462. <https://doi.org/10.1038/s41598-018-32752-0>
- Matsukawa, K., Ishii, K., Liang, N., Endo, K., Ohtani, R., Nakamoto, T., Wakasugi, R., Kadowaki, A., & Komine, H. (2015). Increased oxygenation of the cerebral prefrontal cortex prior to the onset of voluntary exercise in humans. *Journal of Applied Physiology*, 119(5), 452–462. <https://doi.org/10.1152/jappphysiol.00406.2015>
- Minati, L., Kress, I. U., Visani, E., Medford, N., & Critchley, H. D. (2011). Intra- and extra-cranial effects of transient blood pressure changes on brain near-infrared spectroscopy (NIRS) measurements. *Journal of Neuroscience Methods*, 197(2), 283–288. <https://doi.org/10.1016/j.jneumeth.2011.02.029>
- Müller, T., Lauk, M., Reinhard, M., Hetszel, A., Lücking, C. H., & Timmer, J. (2003). Estimation of delay times in biological systems. *Annals of Biomedical Engineering*, 31(11), 1423–1439. <https://doi.org/10.1114/1.1617984>
- Mullinger, K. J., Mayhew, S. D., Bagshaw, A. P., Bowtell, R., & Francis, S. T. (2014). Evidence that the negative BOLD response is neuronal in origin: A simultaneous EEG-BOLD-CBF study in humans. *NeuroImage*, 94, 263–274. <https://doi.org/10.1016/j.neuroimage.2014.02.029>
- Nambu, I., Ozawa, T., Sato, T., Aihara, T., Fujiwara, Y., Otaka, Y., Osu, R., Izawa, J., & Wada, Y. (2017). Transient increase in systemic

- interferences in the superficial layer and its influence on event-related motor tasks: A functional near-infrared spectroscopy study. *Journal of Biomedical Optics*, 22(3), 035008. <https://doi.org/10.1117/1.jbo.22.3.035008>
- Narus, S., Egbert, T., Lee, T. K., Lu, J., & Westenskow, D. (1995). Noninvasive blood pressure monitoring from the supraorbital artery using an artificial neural network oscillometric algorithm. *Journal of Clinical Monitoring*, 11(5), 289–297. <https://doi.org/10.1007/BF01616986>
- Näsi, T., Mäki, H., Hiltunen, P., Heiskala, J., Nissilä, I., Kotilahti, K., & Ilmoniemi, R. J. (2013). Effect of task-related extracerebral circulation on diffuse optical tomography: Experimental data and simulations on the forehead. *Biomedical Optics Express*, 4(3), 412–426. <https://doi.org/10.1364/boe.4.000412>
- Nicolini, P., Ciulla, M. M., Malfatto, G., Abbate, C., Mari, D., Rossi, P. D., Petteuzzo, E., Magrini, F., Consonni, D., & Lombardi, F. (2014). Autonomic dysfunction in mild cognitive impairment: Evidence from power spectral analysis of heart rate variability in a cross-sectional case-control study. *PLoS One*, 9(5), Article e96656. <https://doi.org/10.1371/journal.pone.0096656>
- Obrig, H., Neufang, M., Wenzel, R., Kohl, M., Steinbrink, J., Einhäupl, K., & Villringer, A. (2000). Spontaneous low frequency oscillations of cerebral hemodynamics and metabolism in human adults. *NeuroImage*, 12(6), 623–639. <https://doi.org/10.1006/nimg.2000.0657>
- Obrig H., Villringer A. (2003). Beyond the Visible—Imaging the Human Brain with Light. *Journal of Cerebral Blood Flow & Metabolism*, 23(1), 1. –18. <http://dx.doi.org/10.1097/01.wcb.0000043472.45775.29>
- Oden, N. (1983). Circular statistics in biology. Edward Batschelet. *The Quarterly Review of Biology*, 58(2), 312. <https://doi.org/10.1086/413381>
- Orihuela-Espina, F., Leff, D. R., James, D. R. C., Darzi, A. W., & Yang, G. Z. (2010). Quality control and assurance in functional near infrared spectroscopy (fNIRS) experimentation. *Physics in Medicine and Biology*, 55(13), 3701–3724. <https://doi.org/10.1088/0031-9155/55/13/009>
- Paluš, M. (1997). Detecting phase synchronization in noisy systems. *Physics Letters, Section A: General, Atomic and Solid State Physics*, 235(4), 341–351. [https://doi.org/10.1016/S0375-9601\(97\)00635-X](https://doi.org/10.1016/S0375-9601(97)00635-X)
- Pan, J., & Tompkins, W. J. (1985). A real-time QRS detection algorithm. *IEEE Transactions on Biomedical Engineering*, 3, 230–236. <https://doi.org/10.1109/TBME.1985.325532>
- Petersen, S. E., & Dubis, J. W. (2012). The mixed block/event-related design. *NeuroImage*, 62(2), 1177–1184. <https://doi.org/10.1016/j.neuroimage.2011.09.084>
- Pfeifer, M. D., Scholkmann, F., & Labruyère, R. (2018). Signal processing in functional near-infrared spectroscopy (fNIRS): Methodological differences lead to different statistical results. *Frontiers in Human Neuroscience*, 11, 641. <https://doi.org/10.3389/fnhum.2017.00641>
- Pfurtscheller, G., Bauernfeind, G., Wriessnegger, S. C., & Neuper, C. (2010). Focal frontal (de)oxyhemoglobin responses during simple arithmetic. *International Journal of Psychophysiology*, 76(3), 186–192. <https://doi.org/10.1016/j.ijpsycho.2010.03.013>
- Pierro, M. L., Hallacoglu, B., Sassaroli, A., Kainerstorfer, J. M., & Fantini, S. (2014). Validation of a novel hemodynamic model for coherent hemodynamics spectroscopy (CHS) and functional brain studies with fNIRS and fMRI. *NeuroImage*, 85(1), 222–233. <https://doi.org/10.1016/j.neuroimage.2013.03.037>
- Pinti, P., Cardone, D., & Merla, A. (2015). Simultaneous fNIRS and thermal infrared imaging during cognitive task reveal autonomic correlates of prefrontal cortex activity. *Scientific Reports*, 5(1), 1–14. <https://doi.org/10.1038/srep17471>
- Pinti, P., Tachtsidis, I., Hamilton, A., Hirsch, J., Aichelburg, C., Gilbert, S., & Burgess, P. W. (2020). The present and future use of functional near-infrared spectroscopy (fNIRS) for cognitive neuroscience. *Annals of the New York Academy of Sciences*, 1464(1), 5–29. <https://doi.org/10.1111/nyas.13948>
- Plichta, M. M., Herrmann, M. J., Baehne, C. G., Ehlis, A. C., Richter, M. M., Pauli, P., & Fallgatter, A. J. (2006). Event-related functional near-infrared spectroscopy (fNIRS): Are the measurements reliable? *NeuroImage*, 31(1), 116–124. <https://doi.org/10.1016/j.neuroimage.2005.12.008>
- Raichle, M. E., MacLeod, A. M., Snyder, A. Z., Powers, W. J., Gusnard, D. A., & Shulman, G. L. (2001). A default mode of brain function. *Proceedings of the National Academy of Sciences of the United States of America*, 98(2), 676–682. <https://doi.org/10.1073/pnas.98.2.676>
- Raichle, M. E., & Snyder, A. Z. (2007). A default mode of brain function: A brief history of an evolving idea. *NeuroImage*, 37(4), 1083–1090. <https://doi.org/10.1016/j.neuroimage.2007.02.041>
- Reinhard, M., Wehrle-Wieland, E., Grabiak, D., Roth, M., Guschlbauer, B., Timmer, J., Weiller, C., & Hetzel, A. (2006). Oscillatory cerebral hemodynamics—the macro- vs. microvascular level. *Journal of the Neurological Sciences*, 250(1–2), 103–109. <https://doi.org/10.1016/j.jns.2006.07.011>
- Saager, R. B., & Berger, A. (2008). Measurement of layer-like hemodynamic trends in scalp and cortex: Implications for physiological baseline suppression in functional near-infrared spectroscopy. *Journal of Biomedical Optics*, 13(3), Article 034017. <https://doi.org/10.1117/1.2940587>
- Saager, R. B., & Berger, A. J. (2005). Direct characterization and removal of interfering absorption trends in two-layer turbid media. *Journal of the Optical Society of America A*, 22(9), 1874–1882. <https://doi.org/10.1364/josaa.22.001874>
- Saager, R. B., Telleri, N. L., & Berger, A. J. (2011). Two-detector corrected near infrared spectroscopy (C-NIRS) detects hemodynamic activation responses more robustly than single-detector NIRS. *NeuroImage*, 55(4), 1679–1685. <https://doi.org/10.1016/j.neuroimage.2011.01.043>
- Sassaroli, A., Tgavalekos, K., & Fantini, S. (2018). The meaning of “coherent” and its quantification in coherent hemodynamics spectroscopy. *Journal of Innovative Optical Health Sciences*, 11(06), Article 1850036. <https://doi.org/10.1142/S1793545818500360>
- Sato, H., Yahata, N., Funane, T., Takizawa, R., Katura, T., Atsumori, H., Nishimura, Y., Kinoshita, A., Kiguchi, M., Koizumi, H., Fukuda, M., & Kasai, K. (2013). A NIRS-fMRI investigation of prefrontal cortex activity during a working memory task. *NeuroImage*, 83, 158–173. <https://doi.org/10.1016/j.neuroimage.2013.06.043>
- Scarpa, F., Brigadoi, S., Cutini, S., Scatturin, P., Zorzi, M., Dell’Acqua, R., & Sparacino, G. (2013). A reference-channel based methodology to improve estimation of event-related hemodynamic response from fNIRS measurements. *NeuroImage*, 72, 106–119. <https://doi.org/10.1016/j.neuroimage.2013.01.021>
- Schecklmann, M., Ehlis, A. C., Plichta, M. M., & Fallgatter, A. J. (2008). Functional near-infrared spectroscopy: A long-term

- reliable tool for measuring brain activity during verbal fluency. *NeuroImage*, 43(1), 147–155. <https://doi.org/10.1016/j.neuroimage.2008.06.032>
- Scholkmann, F., Kleiser, S., Metz, A. J., Zimmermann, R., Mata Pavia, J., Wolf, U., & Wolf, M. (2014). A review on continuous wave functional near-infrared spectroscopy and imaging instrumentation and methodology. *NeuroImage*, 85, 6–27. <https://doi.org/10.1016/j.neuroimage.2013.05.004>
- Scholkmann, F., & Wolf, M. (2013). General equation for the differential pathlength factor of the frontal human head depending on wavelength and age. *Journal of Biomedical Optics*, 18(10), 105004. <https://doi.org/10.1117/1.jbo.18.10.105004>
- Schroeter, M. L., Bücheler, M. M., Müller, K., Uludağ, K., Obrig, H., Lohmann, G., Tittgemeyer, M., Villringer, A., & von Cramon, D. (2004). Towards a standard analysis for functional near-infrared imaging. *NeuroImage*, 21(1), 283–290. <https://doi.org/10.1016/j.neuroimage.2003.09.054>
- Schroeter, M. L., Schmiedel, O., & Von Cramon, D. Y. (2004). Spontaneous low-frequency oscillations decline in the aging brain. *Journal of Cerebral Blood Flow and Metabolism*, 24(10), 1183–1191. <https://doi.org/10.1097/01.WCB.0000135231.90164.40>
- Shmuel, A., Yacoub, E., Pfeuffer, J., Van de Moortele, P. F., Adriany, G., Hu, X., & Ugurbil, K. (2002). Sustained negative BOLD, blood flow and oxygen consumption response and its coupling to the positive response in the human brain. *Neuron*, 36(6), 1195–1210. [https://doi.org/10.1016/S0896-6273\(02\)01061-9](https://doi.org/10.1016/S0896-6273(02)01061-9)
- Sohn, M. H., Albert, M. V., Jung, K., Carter, C. S., & Anderson, J. R. (2007). Anticipation of conflict monitoring in the anterior cingulate cortex and the prefrontal cortex. *Proceedings of the National Academy of Sciences of the United States of America*, 104(25), 10330–10334. <https://doi.org/10.1073/pnas.0703225104>
- Stefanovska, A., Bracic, M., & Kvernmo, H. D. (1999). Wavelet analysis of oscillations in the peripheral blood circulation measured by laser doppler technique. *IEEE Transactions on Biomedical Engineering*, 46(10), 1230–1239. <https://doi.org/10.1109/10.790500>
- Tachtsidis, I., Leung, T. S., Chopra, A., Koh, P. H., Reid, C. B., & Elwell, C. E. (2009). False positives in functional near-infrared topography. *Advances in Experimental Medicine and Biology*, 645, 307–314. https://doi.org/10.1007/978-0-387-85998-9_46
- Tachtsidis, I., Leung, T. S., Devoto, L., Delpy, D. T., & Elwell, C. E. (2008). Measurement of frontal lobe functional activation and related systemic effects: A near-infrared spectroscopy investigation. *Advances in Experimental Medicine and Biology*, 614, 397–403. https://doi.org/10.1007/978-0-387-74911-2_44
- Tachtsidis, I., & Scholkmann, F. (2016). False positives and false negatives in functional near-infrared spectroscopy: Issues, challenges, and the way forward. *Neurophotonics*, 3(3), 031405. <https://doi.org/10.1117/1.nph.3.3.031405>
- Tak, S., Uga, M., Flandin, G., Dan, I., & Penny, W. D. (2016). Sensor space group analysis for fNIRS data. *Journal of Neuroscience Methods*, 264, 103–112. <https://doi.org/10.1016/j.jneumeth.2016.03.003>
- Tak, S., & Ye, J. C. (2014). Statistical analysis of fNIRS data: A comprehensive review. *NeuroImage*, 85, 72–91. <https://doi.org/10.1016/j.neuroimage.2013.06.016>
- Takahashi, T., Takikawa, Y., Kawagoe, R., Shibuya, S., Iwano, T., & Kitazawa, S. (2011). Influence of skin blood flow on near-infrared spectroscopy signals measured on the forehead during a verbal fluency task. *NeuroImage*, 57(3), 991–1002. <https://doi.org/10.1016/j.neuroimage.2011.05.012>
- Takamoto, K., Hori, E., Urakawa, S., Katayama, M., Nagashima, Y., Yada, Y., Ono, T., & Nishijo, H. (2013). Thermotherapy to the facial region in and around the eyelids altered prefrontal hemodynamic responses and autonomic nervous activity during mental arithmetic. *Psychophysiology*, 50(1), 35–47. <https://doi.org/10.1111/j.1469-8986.2012.01488.x>
- Tanida, M., Sakatani, K., Takano, R., & Tagai, K. (2004). Relation between asymmetry of prefrontal cortex activities and the autonomic nervous system during a mental arithmetic task: Near infrared spectroscopy study. *Neuroscience Letters*, 369(1), 69–74. <https://doi.org/10.1016/j.neulet.2004.07.076>
- Tao, D., Tan, H., Wang, H., Zhang, X., Qu, X., & Zhang, T. (2019). A systematic review of physiological measures of mental workload. *International Journal of Environmental Research and Public Health*, 16(15), 1–23. <https://doi.org/10.3390/ijerph16152716>
- Thayer, J. F., & Lane, R. D. (2009). Claude Bernard and the heart-brain connection: Further elaboration of a model of neurovisceral integration. *Neuroscience and Biobehavioral Reviews*, 33(2), 81–88. <https://doi.org/10.1016/j.neubiorev.2008.08.004>
- Tong, Y., & Frederick, D. B. (2010). Time lag dependent multimodal processing of concurrent fMRI and near-infrared spectroscopy (NIRS) data suggests a global circulatory origin for low-frequency oscillation signals in human brain. *NeuroImage*, 53(2), 553–564. <https://doi.org/10.1016/j.neuroimage.2010.06.049>
- Van Beek, A. H. E. A., Claassen, J. A. H. R., Rikkert, M. G. M. O., & Jansen, R. W. M. M. (2008). Cerebral autoregulation: An overview of current concepts and methodology with special focus on the elderly. *Journal of Cerebral Blood Flow and Metabolism*, 28(6), 1071–1085. <https://doi.org/10.1038/jcbfm.2008.13>
- Vassena, E., Gerrits, R., Demanet, J., Verguts, T., & Siugzdaite, R. (2019). Anticipation of a mentally effortful task recruits dorsolateral prefrontal cortex: An fNIRS validation study. *Neuropsychologia*, 123(October 2017), 106–115. <https://doi.org/10.1016/j.neuropsychologia.2018.04.033>
- Vassena, E., Silvetti, M., Boehler, C. N., Achten, E., Fias, W., & Verguts, T. (2014). Overlapping neural systems represent cognitive effort and reward anticipation. *PLoS One*, 9(3), e91008. <https://doi.org/10.1371/journal.pone.0091008>
- Vermeij, A., Meel-van den Abeelen, A. S. S., Kessels, R. P. C., van Beek, A. H. E. A., & Claassen, J. A. H. R. (2014). Very-low-frequency oscillations of cerebral hemodynamics and blood pressure are affected by aging and cognitive load. *NeuroImage*, 85, 608–615. <https://doi.org/10.1016/j.neuroimage.2013.04.107>
- Verner, M., Herrmann, M. J., Troche, S. J., Roebbers, C. M., & Rammsayer, T. H. (2013). Cortical oxygen consumption in mental arithmetic as a function of task difficulty: A near-infrared spectroscopy approach. *Frontiers in Human Neuroscience*, 7, 217. <https://doi.org/10.3389/fnhum.2013.00217>
- Wang, X., Liu, B., Xie, L., Yu, X., Li, M., & Zhang, J. (2016). Cerebral and neural regulation of cardiovascular activity during mental stress. *Biomedical Engineering Online*, 15(s2), 335–347. <https://doi.org/10.1186/s12938-016-0255-1>
- Welch, P. (1967). The use of fast Fourier transform for the estimation of power spectra: A method based on time averaging over short, modified periodograms. *IEEE Transactions on Audio and Electroacoustics*, 15(2), 70–73. <https://doi.org/10.1109/TAU.1967.1161901>

- Williamson, J. W. (2010). The relevance of central command for the neural cardiovascular control of exercise. *Experimental Physiology*, 95(11), 1043–1048. <https://doi.org/10.1113/expphysiol.2009.051870>
- Wolf, M., Wolf, U., Toronov, V., Michalos, A., Paunescu, L. A., Choi, J. H., & Gratton, E. (2002). Different time evolution of oxyhemoglobin and deoxyhemoglobin concentration changes in the visual and motor cortices during functional stimulation: A near-infrared spectroscopy study. *NeuroImage*, 16(3), 704–712. <https://doi.org/10.1006/nimg.2002.1128>
- Wylie, G. R., Graber, H. L., Voelbel, G. T., Kohl, A. D., DeLuca, J., Pei, Y., Xu, Y., & Barbour, R. L. (2009). Using co-variations in the Hb signal to detect visual activation: A near infrared spectroscopic imaging study. *NeuroImage*, 47(2), 473–481. <https://doi.org/10.1016/j.neuroimage.2009.04.056>
- Wyser, D., Mattille, M., Wolf, M., Lambercy, O., Scholkmann, F., & Gassert, R. (2020). Short-channel regression in functional near-infrared spectroscopy is more effective when considering heterogeneous scalp hemodynamics. *Neurophotonics*, 7(3), 035011. <https://doi.org/10.1117/1.nph.7.3.035011>
- Yang, H., Wang, Y., Zhou, Z., Gong, H., Luo, Q., Wang, Y., & Lu, Z. (2009). Sex differences in prefrontal hemodynamic response to mental arithmetic as assessed by near-infrared spectroscopy. *Gender Medicine*, 6(4), 565–574. <https://doi.org/10.1016/j.genm.2009.11.003>
- Yücel, M. A., Selb, J., Aasted, C. M., Lin, P.-Y., Borsook, D., Becerra, L., & Boas, D. A. (2016). Mayer waves reduce the accuracy of estimated hemodynamic response functions in functional near-infrared spectroscopy. *Biomedical Optics Express*, 7(8), 3078. <https://doi.org/10.1364/boe.7.003078>
- Yücel, M. A., Selb, J., Aasted, C. M., Petkov, M. P., Becerra, L., Borsook, D., & Boas, D. A. (2015). Short separation regression improves statistical significance and better localizes the hemodynamic response obtained by near-infrared spectroscopy for tasks with differing autonomic responses. *Neurophotonics*, 2(3), 035005. <https://doi.org/10.1117/1.nph.2.3.035005>
- Yücel, M. A., Selb, J. J., Huppert, T. J., Franceschini, M. A., & Boas, D. A. (2017). Functional near infrared spectroscopy: Enabling routine functional brain imaging. *Current Opinion in Biomedical Engineering*, 4, 78–86. <https://doi.org/10.1016/j.cobme.2017.09.011>
- Zhang, Q., Brown, E. N., & Strangman, G. E. (2007). Adaptive filtering to reduce global interference in evoked brain activity detection: A human subject case study. *Journal of Biomedical Optics*, 12(6), 064009. <https://doi.org/10.1117/1.2804706>
- Zhang, R., Zuckerman, J. H., Giller, C. A., & Levine, B. D. (1998). Transfer function analysis of dynamic cerebral autoregulation in humans. *American Journal of Physiology-Heart and Circulatory Physiology*, 274(1), H233–H241. <https://doi.org/10.1152/ajpheart.1998.274.1.H233>
- Zhang, Y., Brooks, D. H., Franceschini, M. A., & Boas, D. A. (2005). Eigenvector-based spatial filtering for reduction of physiological interference in diffuse optical imaging. *Journal of Biomedical Optics*, 10(1), Article 011014. <https://doi.org/10.1117/1.1852552>
- Zhang, Y., Tan, F., Xu, X., Duan, L., Liu, H., Tian, F., & Zhu, C.-Z. (2015). Multiregional functional near-infrared spectroscopy reveals globally symmetrical and frequency-specific patterns of superficial interference. *Biomedical Optics Express*, 6(8), 2786. <https://doi.org/10.1364/boe.6.002786>
- Zheng, F., Sassaroli, A., & Fantini, S. (2010). Phasor representation of oxy- and deoxyhemoglobin concentrations: What is the meaning of out-of-phase oscillations as measured by near-infrared spectroscopy? *Journal of Biomedical Optics*, 15(4), Art 040512. <https://doi.org/10.1117/1.3483466>
- Zhou, X., Sobczak, G., McKay, C. M., & Litovsky, R. Y. (2020). Comparing fNIRS signal qualities between approaches with and without short channels. *PLoS One*, 15(12), Article e0244186. <https://doi.org/10.1371/journal.pone.0244186>
- Zimeo Morais, G. A., Scholkmann, F., Balardin, J. B., Furucho, R. A., de Paula, R. C. V., Biazoli, C. E., & Sato, J. R. (2017). Non-neuronal evoked and spontaneous hemodynamic changes in the anterior temporal region of the human head may lead to misinterpretations of functional near-infrared spectroscopy signals. *Neurophotonics*, 5(01), 1. <https://doi.org/10.1117/1.nph.5.1.011002>

SUPPORTING INFORMATION

Additional supporting information may be found in the online version of the article at the publisher's website.

How to cite this article: Molina-Rodríguez, S., Mirete-Fructuoso, M., Martínez, L. M. & Ibañez-Ballesteros, J. (2022). Frequency-domain analysis of fNIRS fluctuations induced by rhythmic mental arithmetic. *Psychophysiology*, 59, e14063. <https://doi.org/10.1111/psyp.14063>

8.2 Supplementary figures

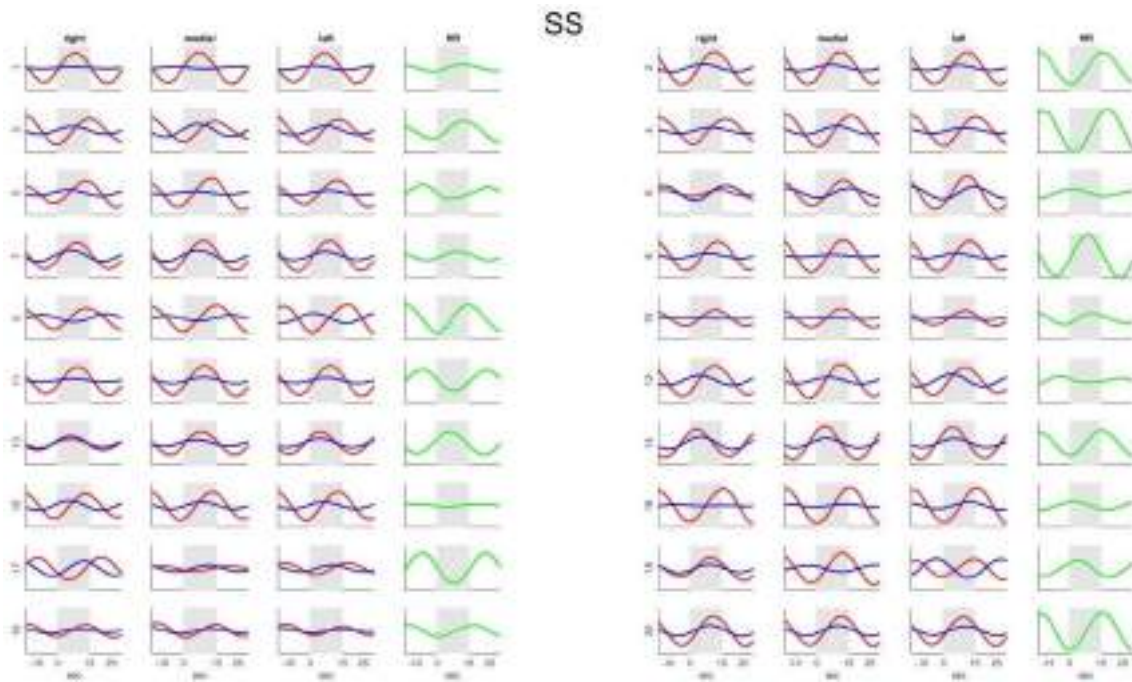


Figure 45. Shallow fNIRS signals and heart rate changes averaged over all task trials for each participant and for each of the three ROIs (HbO in red, HbR in blue and heart rate in green). Gray boxes mark the 15-sec of mental math. The label on the y-axis identifies each participant. For a better comparison, signals have been standardized into Z-scores.

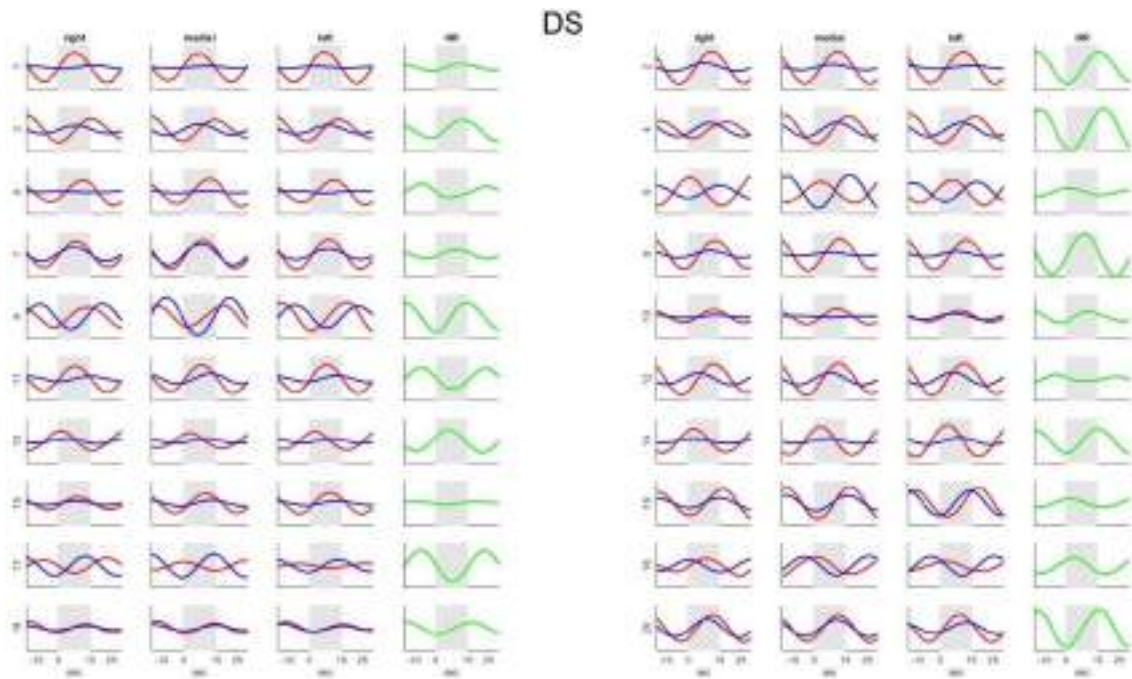


Figure 46. Deep fNIRS signals and heart rate changes averaged over all task trials for each participant and for each of the three ROIs (HbO in red, HbR in blue and heart rate in green). Gray boxes mark the 15-sec of mental math. The label on the y-axis identifies each participant. For a better comparison, signals have been standardized into Z-scores.

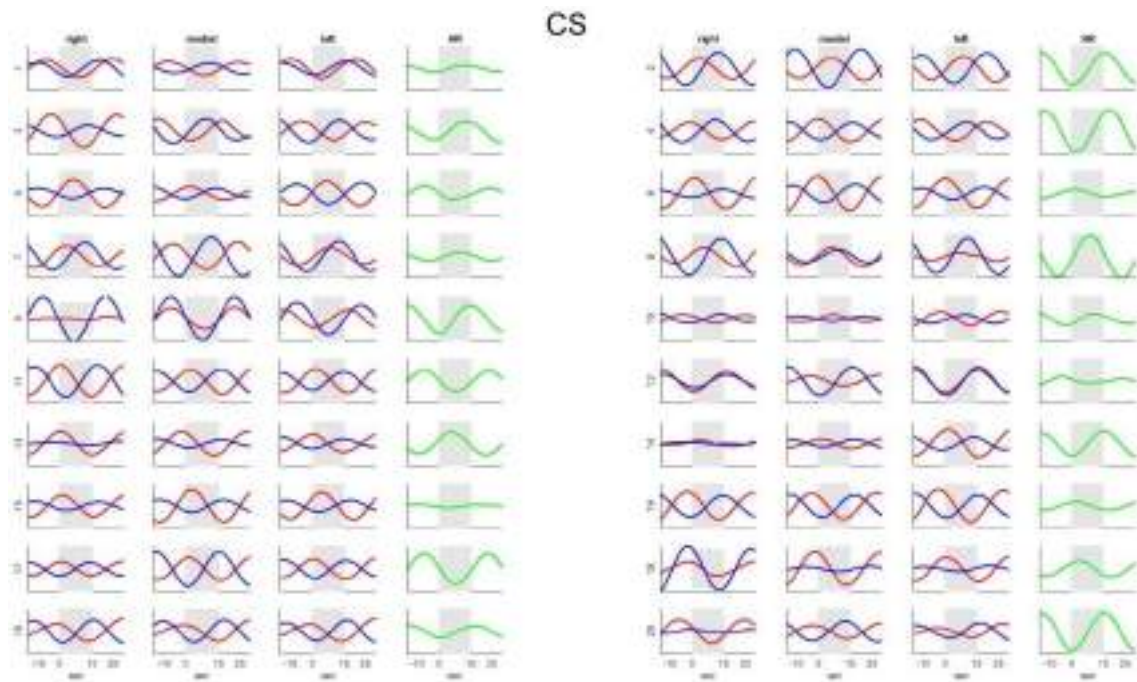


Figure 47. Clean (neural)-signals and heart rate changes averaged over all task trials for each participant and for each of the three ROIs (HbO in red, HbR in blue and heart rate in green). Gray boxes mark the 15-sec of mental math. The label on the y-axis identifies each participant. For a better comparison, signals have been standardized into Z-scores.

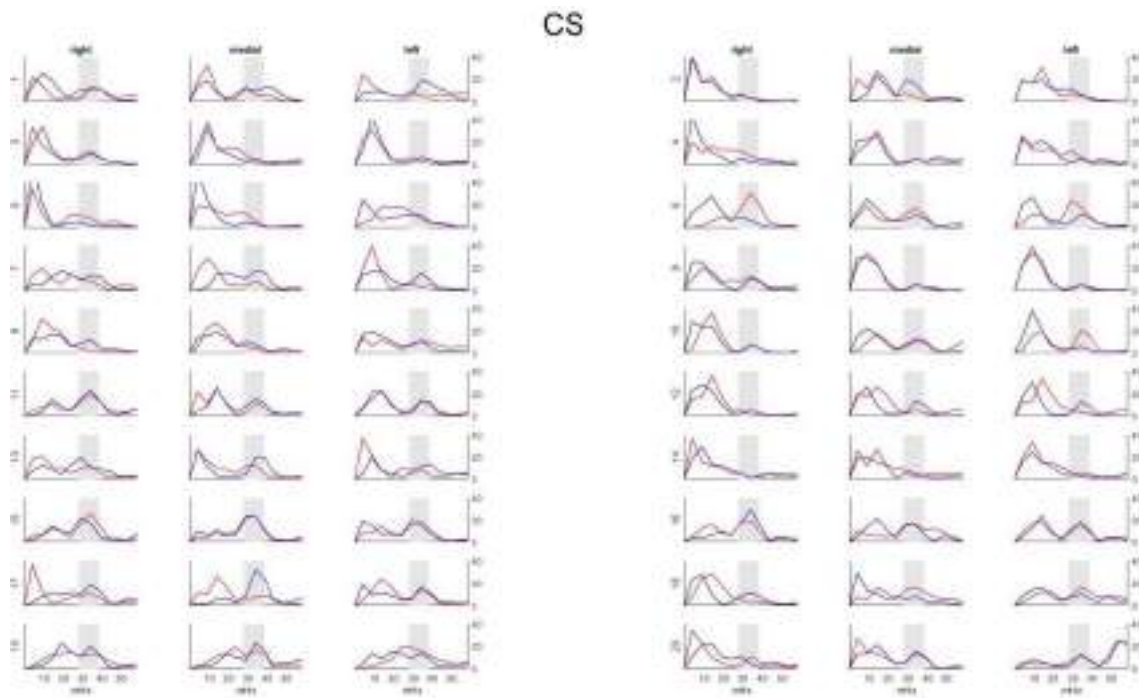


Figure 48. Normalized power spectral density of clean-signals for each participant and for each of the three ROIs during task (HbO in red and HbR in blue). Gray boxes delineate a 10 MHz wide frequency band centered on the 33 MHz task frequency. The label on the y-axis identifies each participant.

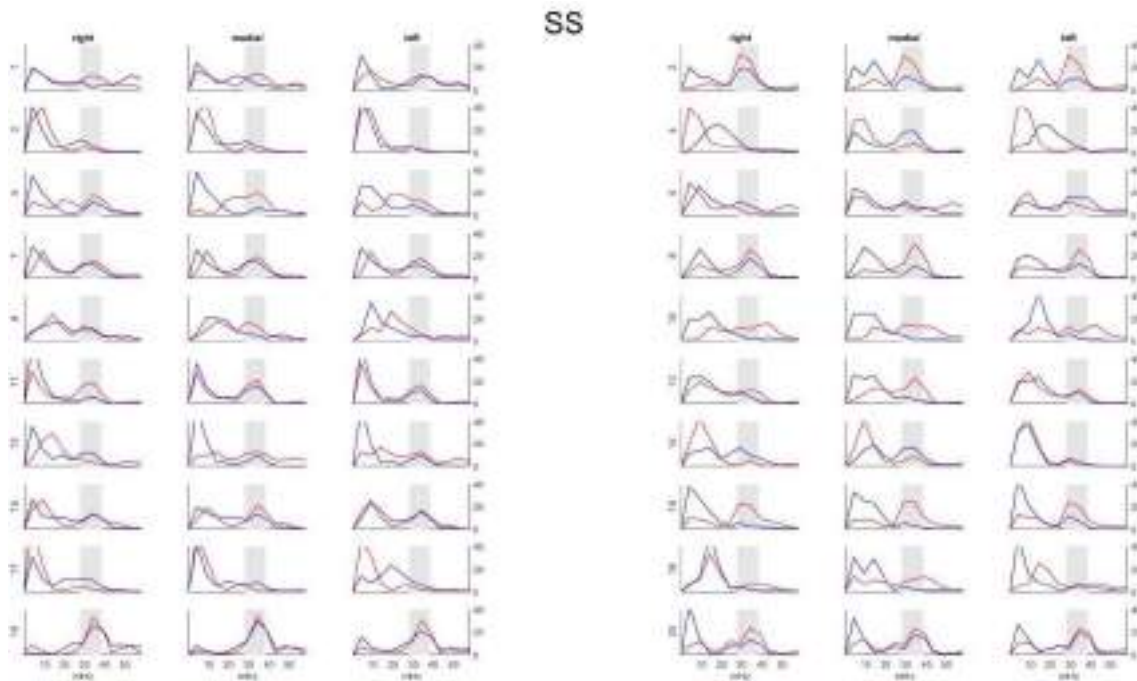


Figure 49. Normalized power spectral density of shallow-signals for each participant and for each of the three ROIs during task (HbO in red and HbR in blue). Gray boxes delineate a 10 mHz wide frequency band centered on the 33 mHz task frequency. The label on the y-axis identifies each participant.

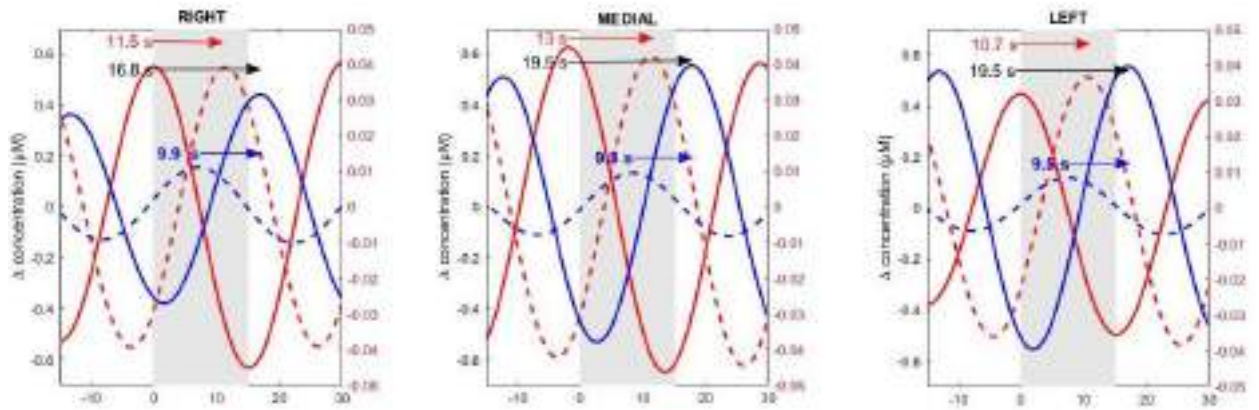


Figure 50. Average time lags across participants between SS (dotted traces) and CS (solid traces) for HbO (red arrows) and HbR (blue arrows). Black arrows show the time lag between HbO and HbR in CS signals. Left and right axis indicate relative concentration changes for SS and CS respectively. Shaded rectangles represent the 15-s of mental calculation.

8.3 Informed consent form

**CONSENTIMIENTO INFORMADO PARA LA MONITORIZACIÓN MULTIMODAL DE LA
RESPUESTA CEREBRAL ANTE ESTÍMULOS COGNITIVOS, SENSORIALES Y EMOCIONALES**

D. , de años de edad, con domicilio en DNI nº

DECLARO:

Que el/la Dr./Dra....., me ha explicado que:

1.- Identificación, descripción y objetivos del procedimiento.

Para llevar a cabo el estudio se necesitan adultos sanos (hombres y mujeres) tanto diestros como zurdos; que no tengan historial de enfermedad grave, especialmente cardiológica, dermatológica, neurológica o psiquiátrica; así como disfunciones visuales o auditivas no corregidas. Si no se cumplen las condiciones anteriores no se puede participar en este estudio.

El presente estudio pretende valorar las relaciones entre la respuesta metabólica cerebral, la respuesta eléctrica cerebral y la respuesta del sistema nervioso autónomo. Para ello, se realizarán registros simultáneos con tres metodologías no-invasivas: fNIR (espectroscopia funcional de infrarrojo cercano), EEG (electroencefalografía) y ECG (electrocardiografía). Todas ellas son de diseño y desarrollo propio (tanto hardware como software) del Departamento de Fisiología.

El objetivo principal es el estudio de la respuesta del sistema nervioso frente a diferentes tipos de estimulación: sensorial, emocional y cognitiva; con la intención de describir los patrones cerebrales característicos del proceso de toma de decisiones.

El estudio se compone de dos fases:

1º Se realizarán registros durante sesiones de estimulación estándar, principalmente sensorial (visual y auditiva), consistentes en la visualización de imágenes y vídeos variados, sin contenido afectivo/emocional especial (por ejemplo caras de hombres y mujeres, alimentos, letras...). La participación del voluntario puede ser pasiva (el participante solo mira las imágenes o vídeos con atención) o activa (durante la visualización se le puede pedir que busque un determinado carácter u objeto en la presentación y pulse un botón cuando lo identifique). El objetivo de esta fase es el estudio y caracterización de la señal cerebral de cada individuo con el fin de seleccionar a aquellos cuya señal esté perfectamente calibrada y caracterizada.

2º El objetivo de la segunda fase es el estudio de la respuesta del sistema nervioso frente a estímulos sensoriales, cognitivos y emocionales en el contexto de la toma de decisiones. En esta fase participarán sólo aquellos individuos que hayan sido seleccionados en la primera fase.

Los procedimientos de estímulo se explican con mayor detalle en el documento adjunto: "Información del procedimiento". Sin embargo, los tipos de estímulos de 'Imágenes de contenido emocional' y 'Estímulos gustativos: sabores', requieren de un consentimiento específico. Por tanto, me explican que:

1) Algunas imágenes pueden herir mi sensibilidad. Por ejemplo, imágenes de contenido violento, traumático o erótico (no pornográfico). Y que puedo decidir no participar en esta parte del estudio. Con respecto a este punto declaro que:

SI deseo participar en esta parte del estudio

NO deseo participar en esta parte del estudio

2) Me darán a probar algunas soluciones inoñas de diferentes sabores así como algunos alimentos comunes adquiridos en establecimientos de alimentación. Me indican que puedo decidir no participar en esta parte del estudio. Además, claramente me advierten de que si padezco alguna alergia o intolerancia alimentaria no debo participar en esta parte del estudio. Con respecto a este punto declaro que:

SI deseo participar en esta parte del estudio y NO padezco ningún tipo de alergia o intolerancia que me impida hacerlo.

NO deseo participar en esta parte del estudio o padezco algún tipo de alergia o intolerancia que me impide hacerlo.

2.- Beneficios que se espera alcanzar

Yo no recibiré ninguna compensación económica ni otros beneficios, sin embargo, si las investigaciones tuvieran éxito, podría ayudar al establecimiento de una nueva técnica no-invasiva de imagen para el estudio de la funcionalidad cerebral en humanos.

3.- Alternativas razonables

La decisión de permitir el análisis de mis datos es totalmente voluntaria, pudiendo negarme e incluso pudiendo revocar mi consentimiento en cualquier momento, sin tener que dar ninguna explicación.

4.- Consecuencias previsibles de su realización y de la no realización

Si decido libre y voluntariamente permitir la evaluación de mis datos, tendré derecho a decidir ser o no informado de los resultados de la investigación, si es que ésta se lleva a cabo.

5.- Riesgos frecuentes y poco frecuentes

La participación en este estudio y la evaluación de mis datos clínicos, demográficos y de antecedentes nunca supondrá un riesgo adicional para mi salud.

6.- Riesgos y consecuencias en función de la situación clínica personal del paciente y con sus circunstancias personales o profesionales

Puesto que declaro no padecer o haber padecido ninguna enfermedad grave, especialmente cardiológica, dermatológica, neurológica o psiquiátrica, ni sufro disfunciones visuales o auditivas no corregidas que desaconsejen participar en este estudio,. Entiendo, y así me lo explican, que en mis condiciones de "buena salud física y mental" no hay riesgos significativos derivados de la participación en este estudio.

7.- Protección de datos personales y confidencialidad.

LA INFORMACIÓN SOBRE MIS DATOS PERSONALES Y DE SALUD NO SERÁ INCORPORADA NI TRATADA EN BASES DE DATOS INFORMATIZADAS. LA INFORMACIÓN QUEDARÁ RESTRINGIDA AL EQUIPO INVESTIGADOR DE ESTE PROYECTO Y SE USARÁ EXCLUSIVAMENTE PARA LOS PROPÓSITOS DE ESTE ESTUDIO.

NO se cederán mis datos a otros centros de investigación o a otros terceros.

Asimismo, se me ha informado que tengo la posibilidad de ejercitar los derechos de acceso, rectificación, cancelación y oposición al tratamiento de datos de carácter personal, en los términos previstos en la normativa aplicable.

Si decidiera revocar el consentimiento que ahora presto, mis datos no serán utilizados en ninguna investigación después de la fecha en que haya retirado mi consentimiento, si bien, los datos científicos obtenidos hasta ese momento seguirán formando parte de la investigación.

Yo entiendo que:

Mi elección es voluntaria, y que puedo revocar mi consentimiento en cualquier momento, sin tener que dar explicaciones.

Declaro que previamente a la firma de este documento:

- 1) He informado al equipo investigador de que no padezco o he padecido ninguna enfermedad grave, especialmente cardiológica, dermatológica, neurológica o psiquiátrica, ni sufro disfunciones visuales o auditivas no corregidas que desaconsejen mi participación en este estudio,
- 2) Se me ha entregado el documento "Información del Procedimiento" en el cual están explicados con detalle los procedimientos que forman parte del estudio, y que lo he leído con atención.
- 3) La "Información del Procedimiento" y el presente documento se me han facilitado con suficiente antelación para reflexionar con calma y tomar mi decisión libre y responsablemente.
- 4) He comprendido las explicaciones que se me han facilitado en un lenguaje claro y sencillo y el personal investigador que me ha atendido me ha permitido realizar todas las observaciones y me ha aclarado todas las dudas que le he planteado

Por todo lo anteriormente expuesto:

ACEPTO participar en este estudio:

() En su totalidad

() Exceptuando las siguientes partes:

() Imágenes de contenido emocional.

() Estímulos gustativos/sabores.

() La parte de

.....

Y OTORGO mi consentimiento para que el Departamento de Fisiología de la Universidad Miguel Hernández utilice mis datos para la investigación que están realizando, manteniendo siempre mi anonimato y la confidencialidad de los datos.

Observaciones:
.....

Por ello, manifiesto que estoy satisfecho con la información recibida y en tales condiciones estoy de acuerdo en **PARTICIPAR** y **CONSIENTO PERMITIR EL USO DE MIS DATOS EXPERIMENTALES Y DEMOGRÁFICOS PARA INVESTIGACIÓN.**

En a de de 20...

Firma del participante

Firma del investigador

DNI:

Fdo.:

Fdo.:.....

(Nombre y dos apellidos)

(Nombre y dos apellidos)

REVOCACIÓN DEL CONSENTIMIENTO

D./D^a como
participante (o representante del participante
D.....), de años de edad, con
domicilio en
..... DNI. nº Revoco el
consentimiento prestado en fecha, que doy con esta fecha por
finalizado, sin tener que dar explicaciones.

En de de 20.....

Firma del participante

Firma del investigador

DNI:

Fdo.:

Fdo.:.....

(Nombre y dos apellidos)

(Nombre y dos apellidos)